WARSAW UNIVERSITY OF TECHNOLOGY

FACULTY OF MATERIAL SCIENCE AND ENGINEERING

Ph.D. THESIS

Agnieszka Chmielewska, M.Sc.

In situ alloying of NiTi using laser powder bed fusion

Supervisor

Wojciech Święszkowski, Professor

WARSAW 2022

The only source of knowledge is experience.

Albert Einstein

ABSTRACT

The emergence of additive manufacturing (AM) technologies has initiated new possibilities for fabricating a wide variety of functional complex three-dimensional parts and alleviating laborious machining operations. Thus, AM has begun its revolution in various high value industry sectors such as aerospace, automotive and medicine. Laser powder bed fusion (LPBF) is one of the fusion-based AM methods allowing fabrication of a wide variety of functional complex shaped three dimensional parts. In this technique, powder layers are melted upon one another locally with laser beam until part completion. Compared to flow-based AM techniques, LPBF has an advantage of building complex geometries with both high resolution and high accuracy relative to the original computer-aided design (CAD) file.

Recently shape memory alloys (SMA) are extensively investigated as the attractive materials for many engineering and medical applications. Nickel-titanium (NiTi) is the most widely used SMA, that demonstrates stable shape memory effect and superelasticity behaviours, low stiffness, biocompatibility, damping characteristics, and corrosion resistance. Moreover, shape memory and superelasticity allow for large recoverable strains of up to 8%. Nevertheless, such unique properties result in the high reactivity and high ductility of the alloy, which generate difficulties in the processing and machining, thus, make fabrication of NiTi parts a hard task. These challenges altogether have limited the starting form of NiTi devices to simple geometries including rod, wire, bar, tube, sheet, and strip. Thus, AM techniques have gained significant attention for processing NiTi since they eliminate many of the challenges associated with the conventional methods. In recent years, AM techniques have been implemented for the direct production of complex NiTi such as lattice-based and hollow structures with the potential use in aerospace and medical applications. However, the high price of NiTi powders, caused by fabrication difficulties, affects the high cost of manufactured objects. A favourable solution of this issue seems to be the use of elemental powders of nickel and titanium, which are nearly three times cheaper than pre-alloyed NiTi powders. This would reduce the price of final objects as well as facilitate the modification of the alloys' chemical composition, i.e., Ni/Ti ratio, which affect phase transition temperature, responsible for its unique shape memory and superelasticity behaviour.

Within the presented PhD thesis, the following objectives are aimed: (1) development of LPBF manufacturing parameters of the NiTi alloy fabricated from elementally blended Ni and Ti powders; (2) determination of the amount of evaporated nickel depending on the initial powder's chemical composition (Ni/Ti ratio) and melting strategy; (3) design of the heat-treatment to improve microstructure homogeneity; (4) development of the chemical polishing post-processing; (5) evaluation of corrosion and biological performance.

The work presents the influence of manufacturing parameters (i.e., laser parameters and scanning strategy) and different melting strategies, including multiple remelting, on printability and microstructure of the LPBF *in situ* alloyed NiTi components. Ni evaporation from manufactured samples was found to ranges from 1.6 to 3.0 wt. %, depending on the initial powder blend composition (53-57 wt.% Ni) and number of melts of a single layer. Remelting was observed to significantly improve the blending of the Ni and Ti elemental powders during LPBF compared with single melt processes; however, it did not eliminate phase composition inhomogeneity entirely. Heat treatment allowed for the significant homogenization of the chemical and phase composition; nevertheless, thermodynamically stable oxygen-rich Ni_2Ti_4O phase that was not eliminated. The low cytotoxicity and high passivation suggest that elementally blended pure Ni and Ti powders merit further investigation for use in biomedical applications.

In summary, the works presents comprehensive study on *in situ* alloying through LPBF from elemental Ni and Ti powders with different chemical composition. It was concluded that the LPBF when combined with properly selected heat treatment a is a promising way of synthesizing a homogenous NiTi alloy from elemental powders. Furthermore, the comparison of the results obtained for samples fabricated from the pre-mixed Ni and Ti powders with those obtained from pre-alloyed NiTi powder showed similar characteristics in terms of corrosion resistance and biological evaluation. The presented results highlight the capabilities of LPBF *in situ* alloying to fabricate NiTi alloy with a potential use for biomedical and industrial applications.

Key words:

NiTi; shape memory alloys (SMA); additive manufacturing (AM); laser powder bed fusion (LPBF); *in situ* alloying; elementally blended powders; pre-mixed powders.

STRESZCZENIE

Technologie wytwarzania przyrostowego zapoczątkowały nowe możliwości wytwarzania szerokiej gamy funkcjonalnych i złożonych części eliminując konieczność stosowania pracochłonnych operacji obróbki mechanicznej. W ten sposób technologie wytwarzania przyrostowego rozpoczęły rewolucję we wiodących sektorach przemysłu: lotniczym, motoryzacyjnym i medycznym. Metoda laserowego topienia w złożu proszku jest techniką wytwarzania przyrostowego pozwalającą na wytwarzanie funkcjonalnych elementów z dużą swobodą geometrii. W tej metodzie wysokoenergetyczna wiązka lesera stapia proszek warstwa po warstwie do momentu wytworzenia całego elementu. W porównaniu z innymi technologiami przyrostowymi wytwarzania metali, metoda laserowego topienia w złożu proszku pozwala na wytwarzanie elementów o złożonej geometrii z wysoką dokładnością odwzorowania modelu komputerowego.

Jednymi z chętnie wykorzystywanych materiałów w aplikacjach medycznych i inżynierskich są stopy z pamięcią kształtu. Najbardziej znanym przedstawicielem tej grupy jest stop tytanu z niklem (NiTi), który posiada dwie niezwykłe cechy funkcjonalne jakimi są pamięć kształtu i supersprężystość. Dzięki nim materiał ten posiada możliwość odkształceń sprężystych do 8%. Ponadto charakteryzuje się niską sztywnością, biokompatybilnością i odpornością korozyjną. Niemniej jednak unikalne właściwości stopu NiTi, jego wysoka reaktywność i ciągliwość powodują trudności w jego wytwarzaniu i obróbce mechanicznej. Z tego względu jest dostępny na rynku jedynie w prostych formach, takich jak druty, pręty, rury, taśmy, blachy itp. Duże możliwości wytwarzania elementów o skomplikowanych geometriach ze stopu NiTi gwarantują technologie przyrostowe, które eliminują konieczność trudnej konwencjonalnej obróbki mechanicznej. W ostatnich latach technologie przyrostowe są wykorzystywane do wytwarzania elementów o skomplikowanej geometrii, takich jak struktury kratownicowe lub porowate, które z powodzeniem stosowane są w aplikacjach lotniczych i medycznych. Ze względu na trudności związanie z wytwarzaniem stopu NiTi w postaci proszku jego cena jest bardzo wysoka, co wpływa także na wysoki koszt wykonanych z niego elementów. Korzystnym rozwiązaniem tego problemu mogłoby być mieszanie proszków elementarnych, niklu i tytanu, których cena jest ponad trzykrotnie niższa niż cena proszku stopu NiTi. Pozwoliłoby to na obniżenie ceny gotowego elementu oraz znacznie ułatwiło modyfikacje składu chemicznego tego materiału, głównie stosunku ilości niklu i tytanu, który determinuje właściwości termosprężyste odpowiadające za pamięć kształtu i supersprężystość.

Celem prowadzanych w niniejszej pracy badań było (1) opracowanie parametrów wytwarzania stopu NiTi z mieszaniny proszków elementarnych Ni i Ti technologią laserowego topienia w złożu proszku; (2) określenie ilości odparowanego niklu w zależności od składu chemicznego (stosunku ilości niklu do tytanu) materiału wsadowego oraz strategii przetapiania; (3) zaprojektowanie obróbki cieplnej zwiększającej ujednorodnienie mikrostruktury; (4) zaprojektowanie chemicznej obróbki poprocesowej; (5) ocena właściwości korozyjnych i biologicznych.

W pracy przedstawiono wpływ parametrów wytwarzania (tj. parametry pracy lasera oraz strategie skanowania) oraz różnych strategii przetapiania, w tym wielokrotnego przetapiania, na możliwość konsolidacji i mikrostrukturę stopu NiTi wytwarzanego *in situ* technologią laserowego topienia w złożu proszku. Wykazano, że odparowanie niklu z wytworzonych próbek wynosi pomiędzy 1.6 a 3.0 % wag. i zależy od wkładu wyjściowego materiału wsadowego (53-57 % wag. Ni) oraz liczby przetopień pojedynczej warstwy. Zaobserwowano, że ponowne przetapianie znacznie poprawia stopień wymieszania składników stopowych, niklu i tytanu, w porównaniu do procesów, gdzie zastosowano pojedyncze topienie, jednak niejednorodność fazowa nie została całkowicie wyeliminowana. Przeprowadzona obróbka cieplna pozwoliła na poprawę jednorodności składu chemicznego i fazowego, niemniej jednak, nie udało się wyeliminować obecności bogatej w tlen termodynamiczne stabilnej fazy Ni_2Ti_4O. Niska cytotoksyczność i wysoki stopień pasywacji badanych materiałów wskazują, że stop NiTi wytwarzany *in situ* zasługuje na uwagę i dalsze badania w kierunku aplikacji biomedycznych.

Podsumowując, w pracy przedstawiono kompleksowe badania nad wytwarzaniem *in situ* stopu NiTi, z mieszaniny proszków elementarnych niklu i tytanu o różnym składzie chemicznym, za pomocą technologii laserowego topienia w złożu proszku. Wykazano, że laserowe topienie w złożu proszku w połączeniu z odpowiednio dobraną obróbką cieplną jest obiecującym sposobem syntezy stopu NiTi z proszków elementarnych. Ponadto porównanie wyników uzyskanych dla próbek wytworzonych z mieszaniny proszków Ni i Ti z wynikami uzyskanymi z proszku stopu NiTi wykazało podobne właściwości obydwu materiałów pod względem odporności korozyjnej i odpowiedzi biologicznej. Uzyskane wyniki wskazują na możliwość zastosowania w aplikacjach biomedycznych stopu NiTi wytworzonego z mieszaniny proszków elementarnych technologią laserowego topienia w złożu proszku.

Słowa kluczowe:

NiTi; stopy z pamięcią kształtu; technologie przyrostowe; laserowe topienie w złożu proszku; stopowanie *in situ*; proszki elementarne;

Table of contest

Chapter I

General introduction/ State of the Art

1.1. Introduction

The exploration and rapid adoption of additive manufacturing (AM) (aka. 3D printing) methods has had the strong influence on a virtually all industry sectors. Recently AM is evolving at an extremely quick pace and revolutionizing manufacturing operations. AM is the only technique which allows production of complexly shaped geometries, often made with lattice structures with pre-defined mechanical properties. Simultaneously, many materials, which were not used or the usage of them was significantly reduced, can be now applied thanks to the possibilities given by AM. The leaders in utilizing amazing capabilities of AM technologies are the aerospace, medical and automotive industry. Nevertheless, AM is in wide interest of the energy sector. The rapid development of AM technologies is driving the need to expand the range of new materials that can be used in an increasingly wide range of applications. However, the need for the use of process-specific materials is the main limitation and critical to the selection requirements for AM technologies. The selected process requires batch material to be formed into a state compatible with particular system. This applies to the state (solid, liquid), size and shape (e.g., powder, wire, liquid, sheet), and properties (e.g., thermal and electrical conductivity, melting point temperature, reflectivity, reactivity) of the material. Therefore, a lot of attention is currently focused on development new materials designed for a wide range of AM technologies [1,2]. Moreover, recent significant advancement in AM is evolving towards multidimensional manufacturing, known as 4D printing, that can be realized with the use of smart materials or multimaterials [3,4].

Shape memory alloys (SMA) show great potential in many industrial and engineering applications [5–7]. NiTi also referred to as Nitinol, is one of the well-known and frequently used SMA. In the in the areas of fixed-wing aircraft, rotorcraft, and spacecraft, it is used for sensors and actuators [8,9]. Furthermore, NiTi is an essential material in the medical device engineer's toolbox. It is widely used in various biomedical engineering applications, such as orthodontic archwires, surgical stents, active catheters, spine-fracture fixations, oral and maxillofacial implants, bone plates, and lumbar vertebral replacements [10,11]. NiTi demonstrates good deformability that is associated with superelastic behaviour. A mechanically imposed strain as high as 8% can be reversibly recovered after unloading. Moreover, it exhibits low stiffness, biocompatibility, and high corrosion resistance [10,12]. The properties of this material, combined with the possibility of fabricating complex geometries with predefined mechanical properties, make it of interest among many world scientists and aspire to be used in medical applications as a material for implants and bone anastomosis hardware. The main limitation of NiTi research and commercial usage is the high cost and excessive difficulty in machining due to the inherent superelasticity or shape memory. For this reason, an extremely important issue is to reduce material cost and eliminate machining, which would initiate lower costs of the fabricated elements.

1.2. Additive manufacturing

Additive manufacturing (AM) is a computer-controlled process that creates objects by depositing materials layer by layer. ASTM F2792-12a defines it as "*a process of joining materials to make objects from 3D model data, usually layer upon layer*"[13]. AM differs from traditional formative technologies and is the opposite of subtractive technologies, which create elements by gradually removing a portion of a material. AM enables manufacturing complex-shaped geometries directly from metal powder in one manufacturing process giving the advantage of significant reduction or even elimination of the machining. Thanks to the possibility of constructional elements production with a wide range of geometrical freedom, AM has been extensively developed during the last few years and has recently become the fastest-growing manufacturing technique. It is especially important in the case of metallic materials. Despite the increasing AM usage in the manufacturing metal, and more recently, metal composite components, there are still many materials seeking further development [14–18].

AM systems can be classified in terms of many categories such as energy source, material feedstock, the method of supplying the material, synthesis technology, etc. AM of metallic materials can be divided into two main categories: flow-based: direct energy deposition (DED) and fusion-based: powder bed fusion (PBF) [13,19–21]. In the flow-based technologies, materials supply can occur via powder or wire feed, through one or more nozzles that directly feed the powder into the laser focus. The fusion-based technologies only utilize powdered materials deposited on a building platform through a roller, blade, or knife, and a focused laser beam melts the powder locally layer by layer. The nature of those methods and properties of the fabricated object differs significantly from each other. PBF technologies provide a good surface finish and are more common for creating small, complex-shaped parts. Nevertheless, size limits, long manufacturing time, and the necessity of the support structures usage for overhanging features are the limiting factors. DED has a faster build rate and the capability to build larger geometries. Due to the possibility of depositing material on an existing part, DED is used to repair worn or defective metal components and hybrid manufacturing. However, they are also typically limited to coarser feature resolution resulting in the poorer surface finish which requires secondary processing [22–24]. Each process has its advantages and disadvantages thus, the selection of the technology depends on a specific application.

1.2.1. Laser powder bed fusion

Laser powder bed fusion (LPBF) is one of the fusion-based AM technologies that use high-power laser as a heat source to selectively fuse regions of a powder bed. There are two distinct types of LPBF technology: selective laser melting (SLM) and direct metal laser sintering (DMLS). SLM is the trademarked term of LPBF technology patented by Fraunhofer Institute, Germany (1994), while DMLS is a name deposited and patented by EOS GmbH, Germany (1995). Both SLM and DMLS technologies belong to the LPBF family and use laser as a source of thermal energy to synthesize powdered material in a powder bed [25].

During the LPBF fabrication process, successive layers of metal powder are fully melted and consolidated on top of each other using thermal energy supplied by a focused and computer-controlled laser energy source. Consequently, dense parts are formed, often without the need for major post-processing other than surface finishing, heat treatments, or adding very fine details such as threads. The quality of fabricated parts depends strongly on the powder properties, such as particle size and morphology and manufacturing parameters. Moreover, other important factors influencing process parameters include, but are not limited to, melting strategy, hatch style, the diameter of the laser spot, bed temperature, and the direction of gas flow. Layer thickness, laser power, scanning velocity, hatch distance are the basic variables that can be defined for devices equipped with a continuous laser, and the distance between successive scanning points and the exposure time can be controlled in for pulsed lasers (Figure I.1) [26–28].

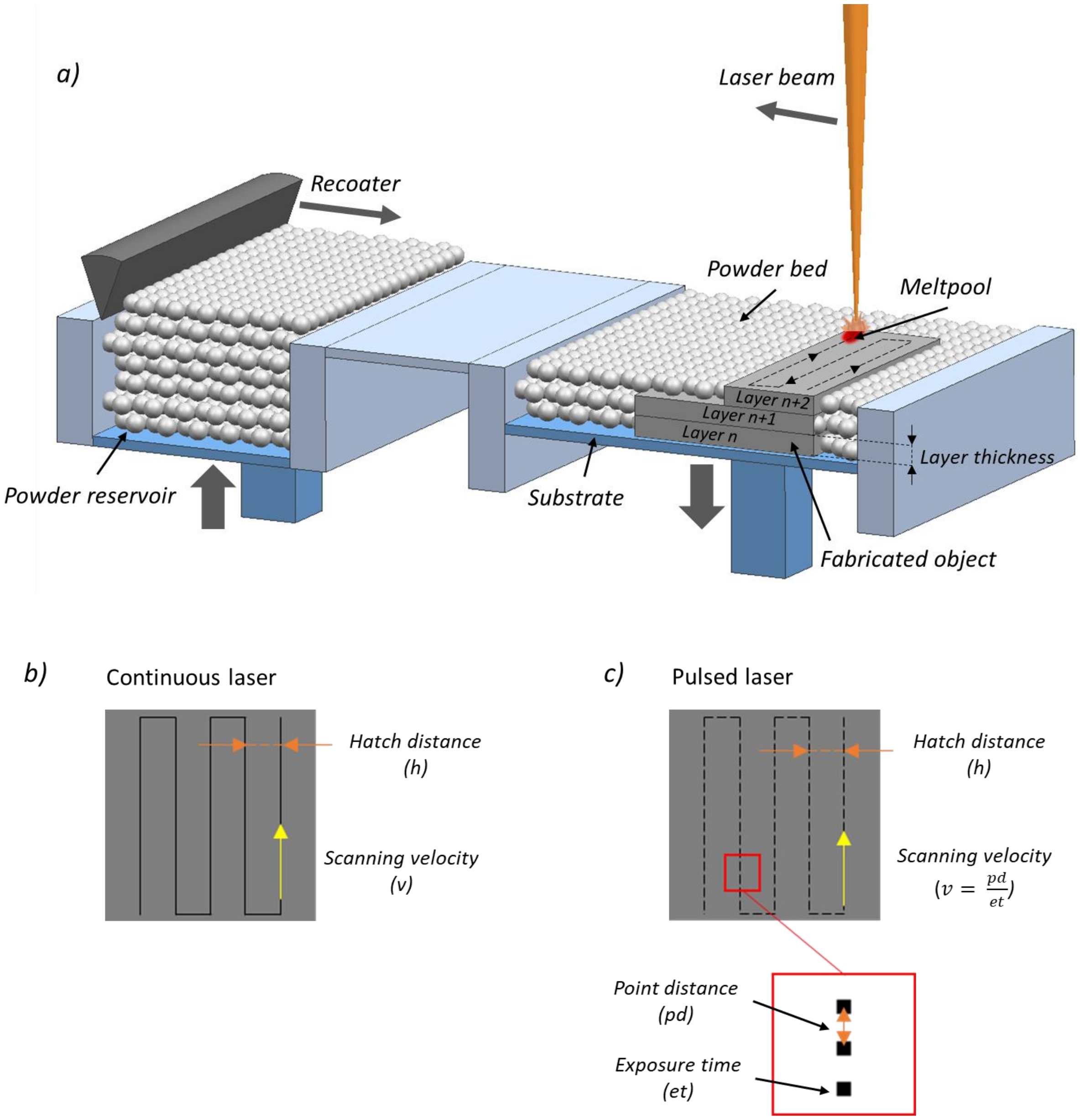

Figure I.1 Schematics of (a) laser powder bed fusion (LPBF) system and process parameters for systems equipped with (b) continuous laser and c) pulsed laser.

The LPBF process is carried out in an inert atmosphere (e.g., argon, helium, nitrogen) to reduce contamination and oxidation as the metal melts and resolidifies. The manufacturing process starts with the distribution of thin layer of powder on the building platform (aka. substrate, base or built plate). The laser beam, controlled by mirrors, moves on the planar (x and y) directions on the designed paths. After completing the scan of the first layer, the building platform is moved down by a certain distance equal to the predefined layer thickness. Subsequently recoating mechanism spray another layer of a fresh powder on top of the previously built surface, and the material is again selectively melted and resolidified. This cycle is repeated until a complete object is formed. The remained unmelted powder in the powder bed can be collected, sieved, and reused for the next process [25,29]. However, due to the increased temperature surrounding the melt pool (heat affected zone), powder particles fuse to all external surfaces of the fabricated part. The additional postprocessing step is required to remove the remaining adhered powder that can cause dimensional inaccuracy between the intended dimensions of the virtual model and the fabricated part. Moreover, the overhanging features require support structures, and postprocessing is necessary to remove them from the part after fabrication [30,31].

To summarize, among the wide range of AM technologies, LPBF gives the advantage of fabrication of complex-shape components with high resolution. However, identifying the optimal parameters is a crucial task for fabricating high-quality parts.

1.2.2. In situ alloying in additive manufacturing

In situ alloying in additive manufacturing is a new approach to fabricate alloys by employing pure elemental blends instead of pre-alloyed ones. This strategy is beneficial to the AM methods due to added flexibility given by the rapid development of new materials. Recently this method has been utilized in both fusion-based and flow-based powder AM techniques [32–35]. *In situ* alloying facilitates tailoring chemical composition and enables the production of new, unconventional alloys (Figure I.2a). Metallic powders can be fabricated by mechanical methods and water or gas atomization. So far, feedstock powders have been made of previously prepared metal alloys, and each powder was fabricated separately. Therefore, *in situ* alloying eliminates the need for complicated, time-consuming, and expensive pre-alloyed powder production since new materials can be prepared by mixing any elementary feedstock powders in any amount and proportion. It is especially important for testing new compositions where the small batch powder is typically utilized. Moreover, it facilitates an approach to control mechanical properties and create novel functionally graded material with controlled composition and properties [36–39].

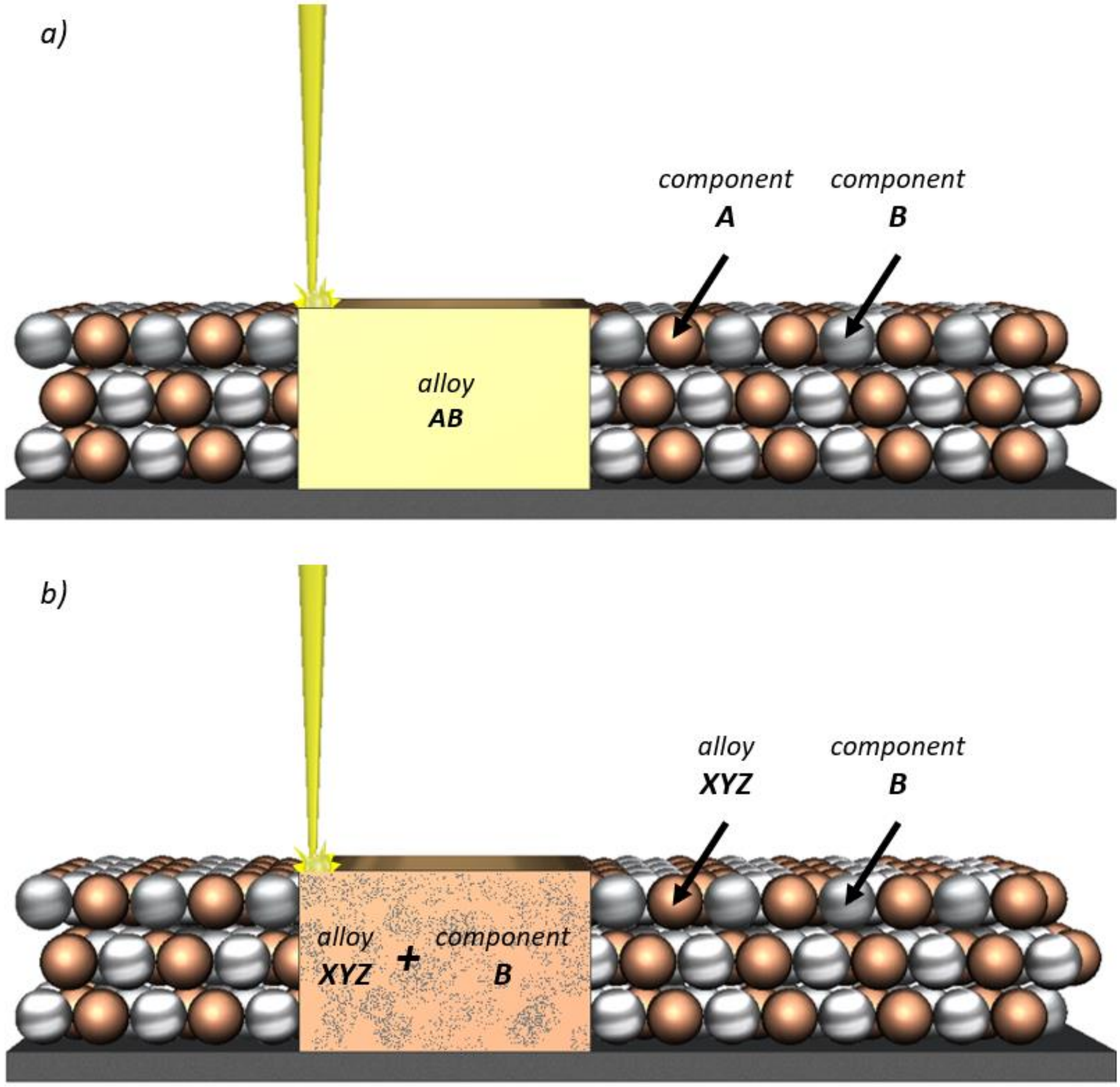

Figure I.2 Schematic illustration of in situ alloying: (a) tailoring chemical composition from blend of components A and B; (b) introduction of an additional component B to feedstock pre-alloyed powder (alloy XYZ) to modify its microstructure and/or properties.

Recent studies on *in situ* alloying focus on the influence of different factors such as mixing methods and LBPF process parameters on chemical and phase homogeneity, microstructure, and mechanical properties. However, the greatest challenge associated with LPBF *in situ* alloying is the uniform blending of the alloying elements in the fabricated material (Figure I.3) [39–41]. In addition to *in situ* alloying by mixing elemental powders, this method has also been utilized to introduce an additional component to feedstock pre-alloyed powder to modify its microstructure or properties (Figure I.2b). Recent studies showed that the added elements might modify microstructure by promoting heterogeneous nucleation and change as-built grain morphology from columnar to equiaxed [42,43]. Yadroitsev et al.[44] and Gue et al.[45] demonstrated that the addition of Cu to Ti-6Al-4V creates novel biomaterial with antibacterial properties. Moreover, it was shown by Vora et al. [46] that additional components introduced to Al-12Si alloy are capable of reducing stress within components during fabrication and reducing the support structures for overhanging geometries. Qiu et al. [47] reported that corrosion resistance of Ti-6Al-4V alloy was improved by Pb addition. Gu et al. [48–50] synthesized TiC/Ti nanocomposites with enhanced wear resistance and TiC/AlSi10Mg nanocomposites with improved tensile strength and microhardness.

The challenges associated with this method may arise in the various stages of manufacturing, i.e., preparation and mixing elemental powders, melting powder blends, and post-processing. The preliminary step is the selection of powders with the desired morphology and their uniform blending, which ensures homogenous distribution of elements and eliminates the formation of agglomerates in the final batch powder mix [47,51,52]. Moreover, powder blend flowability and powder recycling have been reported as the limiting factors [40]. Physical characteristics and thermomechanical properties of powders need to be considered. Differences in energy absorption, optical, and thermal properties between components may lead to problems with uniform melting of all components and achieving a homogeneous distribution of elements in the matrix [39]. In addition, differences in melting point temperatures between compounds may lead to evaporation of some elements and result in changes in chemical composition in the final alloy [51]. Consequently, microstructure inhomogeneity and segregation of the elements create challenges for the post-treatment processes [36–38].

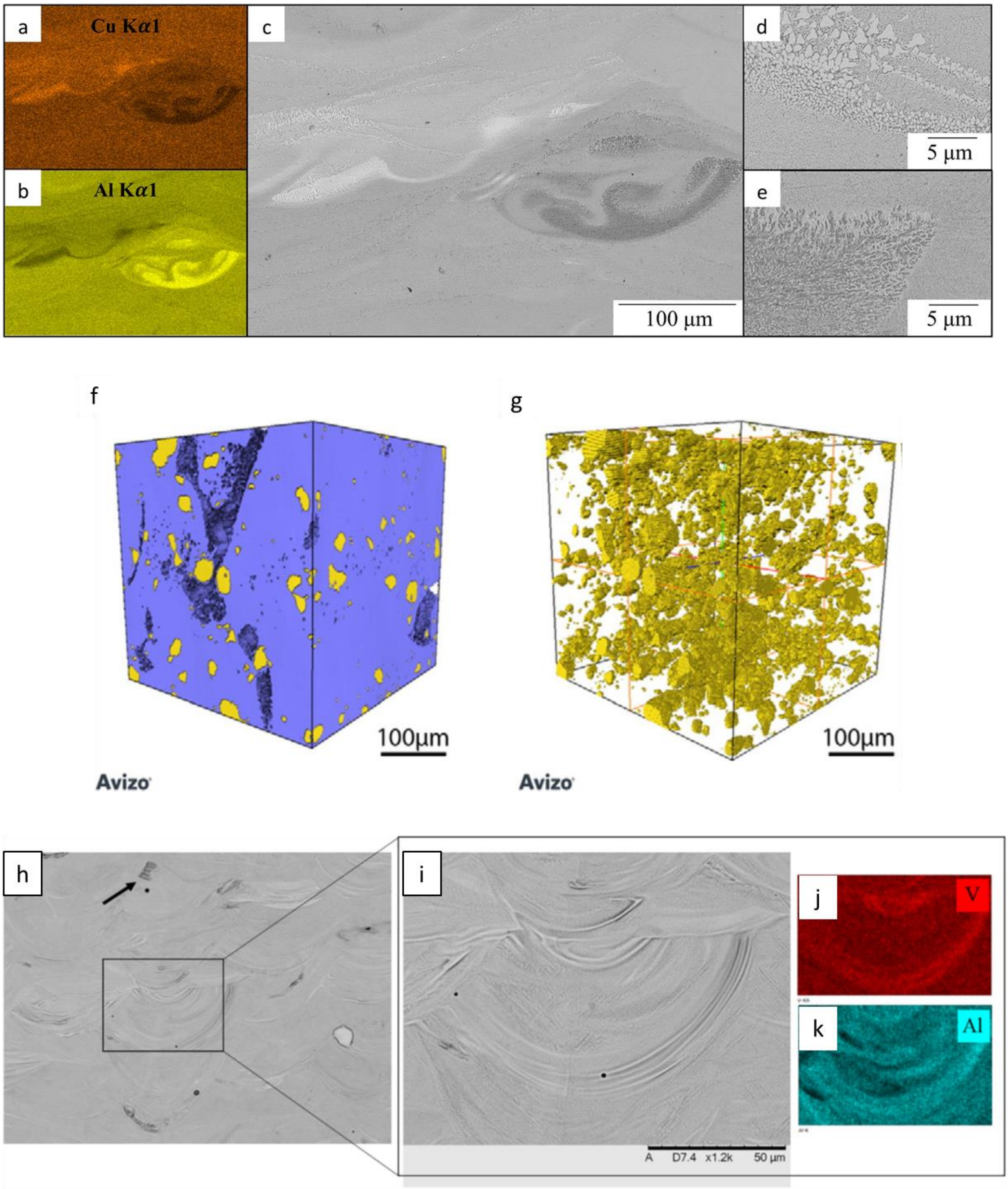

Figure I.3 SEM EDS maps of Cu (a) and Al (b) in a sample made from AlCu powder blend. Light and dark regions in the backscattered micrograph (c-e) correspond to high concentrations of Cu or Al respectively [40]; Tomographic reconstruction of in situ alloyed TiNb: (f) full volume with TiNb alloy (blue), Nb particles (yellow), voids (hollow) and (g) Nb particles in the volume [41]; (h-k) backscatter SEM/EDS showing the general microstructural features of the in situ alloyed Ti6Al4V alloy [39].

1.3. Metallic biomaterials for orthopaedic applications

The metallic biomaterials have been utilized in various orthopaedic, endovascular, and dental applications such as a knee, hip, and joint replacement; spinal fusion cages; fracture fixation plates, screws, and nails; dental implants and abutments; vascular stents, pacemakers, and many others. The principal metallic biomaterials used in medical devices consist of titanium alloys, stainless steel and cobalt alloys [53–55]. Indeed, metallic skeletal devices such as bone implants and bone fixation plates play an important role in most cases of bone injuries. Orthopaedic surgeries are one of the most rapidly growing surgical procedure categories. The number of orthopaedic surgeries performed worldwide in 2017 reached approximately 22.3 million [56]. There is a wide variety of orthopaedic procedures that surgeons perform, which address different parts of the body. The main task of a medical device is to restore bone function by replacing its fragment (implant) or ensure robust healing (fixation devices). In addition to biological properties, the equal significance should be given to the mechanical stability of the device as adequate stabilization preserves the optimal alignment and function of the native bone during physiologic loading. This stability is essential for the formation of a callus that bridges the fracture site allowing loads to be transmitted across the fracture line. The restoration of normal geometry and function in the new bone tissue at the remodelling stage ensures the restoration of proper stress-strain directory and minimizes fracture or bone-implant interface micromotion at the early stage of bone healing [57,58]. Although the standard-of-care skeletal devices ensure many advantages related to faster recovery of patients and improve their comfort of the life the disadvantages of long-term use remain one of the major problems.

1.3.1. Mechanical properties- stiffness and Young’s Modulus

Usually, stiffness is used to describe the mechanical properties of bones since they depend on the type of bone, the work that it does, and its shape. Meanwhile, to describe the property of the metals, it is most common to use Young’s modulus. Stiffness is a structural property, the resistance to elastic deformation, which is influenced by the geometry of the device/object as well as the material of which it is comprised; it is also affected by the way load is applied. Young's modulus (or elastic modulus) is a mechanical property that measures a material’s ability to withstand changes in length when under lengthwise tension or compression. It is intrinsic to a particular material and is not influenced by device/object geometry. However, the Young’s Modulus is, in essence, the stiffness of a device and is proportional to each other (the higher Young’s modulus, the higher stiffness of the object). The bone has an anisotropic structure, which means that its mechanical properties depend on the direction in which the property is measured. This can be explained by the example of the femoral cortical bone. The Young's modulus of femoral cortical bone measured along the longitudinal direction is about 18 GPa, while along transverse direction varies between 5 to 10 GPa. However, in the case of bone, the Young's modulus is not as relevant as stiffness. Stiffness is more representative factor that describes the mechanical properties of the bone since it incorporates bone's structure and geometry and Young's modulus. Many factors influence bone stiffness, such as age, sex, state of health, and anatomical site. The stiffness of the bone varies from well below 3 GPa for the cancellous bone to 20 GPa for the cortical bone [59]. Moreover, in the areas between hard and soft tissue at the interface between cartilage and bone, the structure of the bone can be graduated [60]. The Young's modulus of commonly used metals for long-term skeletal devices such as titanium alloys, cobalt-chromium alloys, and stainless steel are, respectively, about 110, 190, and 210 GPa, which makes them 4-10 times stiffer than the bone which it is permanently attached [61]. Although highly stiff skeletal devices provide strong immobilization immediately after the surgery, the long term usage may lead to disturbing the stress distribution, which can lead to one or more of three poor outcomes: (a) stress shielding and resorption of newly healed bone, (b) stress concentration in the fixation device and device failure (e.g., plate cracking or screw pull-out), and/or (c) failure to restore masticatory muscle power as the reconstructed bone heals.

1.3.2. Stress shielding and stress concentration

It is well known that incorrect bone-skeletal device interaction may affect the healing process and lead to the failure of the implantation. High stress concentration on the device causes accelerated striping wear and fatigue which might consequently result in its fracture or displacement [62,63]. Meanwhile, stress concentration in the surrounding bone results in bone resorption or insufficiency fractures (Figure I.4) [64]. Stress shielding is the reduction of bone density due to the redistribution of load that occurs when a skeletal device takes over the load on the bones. Metallic skeletal devices, such as implants or fixation plates and screws, are used as a joint replacement or to repair bone fractures, respectively. According to Wolff's law, bones undergo the regeneration and remodelling process adapting their architecture, mass, and mechanical properties in response to mechanical loading. The skeletal device, constructed of a material that is much stiffer than surrounding bone, supports major of patient's weight, thereby, demonstrates an unphysiological redistribution of force transmission and prevents the local bone from receiving sufficient mechanical stimulus during remodelling. As a result, the bone will tend to redistribute and resorb [65–68]. A decrease in bone mass and density may contribute to implant loosening and/or failure. The resorptive process generated by stress shielding had been reported as one of the main problems that lead to bone loss and revision surgery in craniofacial [69], knee [70–72], shoulder [73], spine[74], and hip [75] implants, and bone fixation plates [76–78]. Therefore, mechanical properties and geometry are critical factors that should be considered during skeletal device design to address stress shielding and stress concentration.

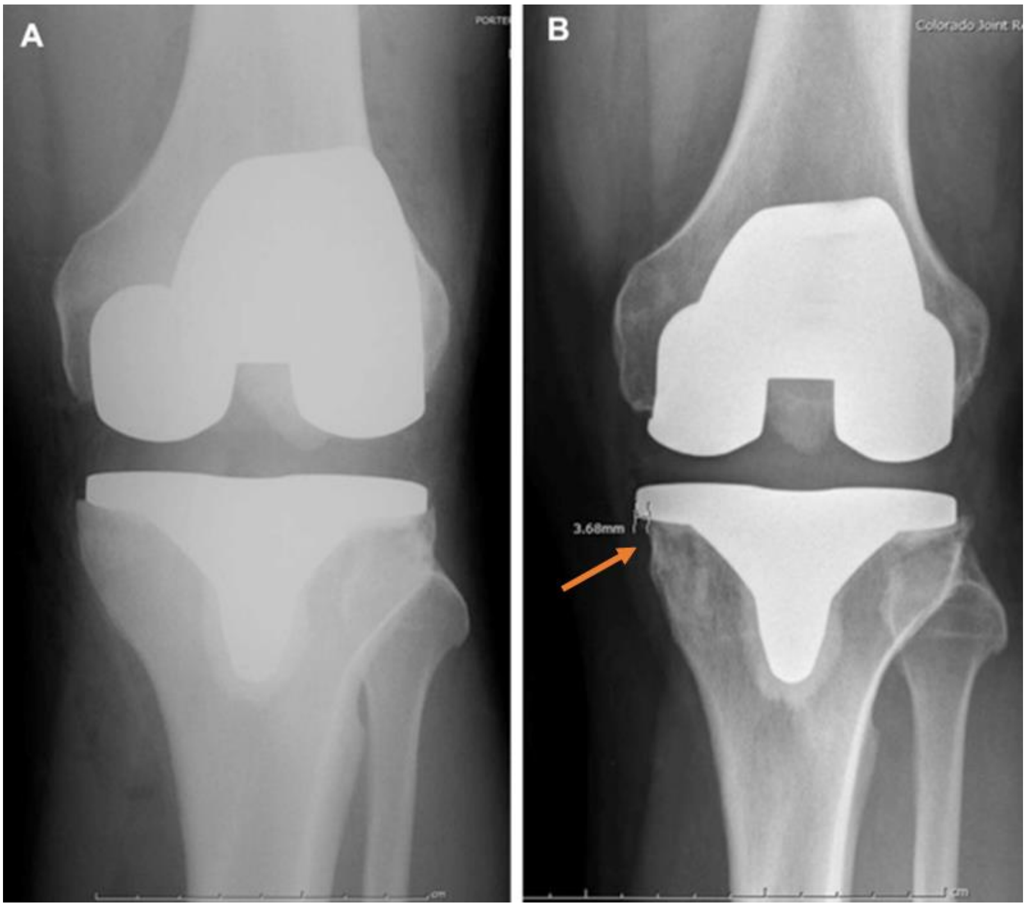

Figure I.4 (a) Immediate AP knee postoperative radiograph; (b) Two-year postoperative AP knee radiographs showing tibial bone loss (arrow) related to the stress shielding effect [72].

1.3.3. Stiffness-matching

The idea of stiffness-matching medical devices is to favour the correct transfer of loads to the tissues surrounding the implant and promote healing. Postoperative complications associated with the long-term use of overly rigid implants generate the need to develop medical devices that would mechanically activate the biological performance of the device, recreate stress-strain trajectory of bone, and match the stiffness with the work performed by the bone. The promising solution that brings many benefits to the healing process is the usage of personalized implants and medical instrumentation that provide desired properties adapted to the anatomy and needs of a particular patient.

The mechanical performance of the device can be modified by the geometry and the employed material. As mentioned before, Young's modulus of metallic materials routinely used for skeletal devices is higher than the modulus of bone. Therefore, recent research focuses on developing materials that have an elastic modulus close to that of the bone tissue to eliminate or mitigate the stress shielding [61,79–81]. Moreover, the geometry of the device might be modified by introducing porosity, hollow, and lattice structures that will allow obtaining geometries with predefined mechanical properties [82–85]. The combination of low modulus metallic materials and the porous geometry can provide promising solutions to design stiffness-matching medical devices that would recreate the desirable stress-strain relationship and avoid a mismatch of the stiffness between the medical device and the surrounding tissues.

1.4. Shape Memory Alloys (SMA)

Shape memory alloys (SMA) are a class of metallic alloys that are able to undergo large reversible deformations under specific external stimuli, such as heat, load, electricity or magnetic field, and immediately return to the undeformed shape when the stimuli is removed. This behaviour is generated by reversible changes of the crystallographic structure, between crystallographic more-ordered parent phase (austenite), to a crystallographic less-ordered product phase (martensite). Wide variety of alloys are known to exhibit shape memory effect such as titanium-, nickel-, and copper-based alloys. In recent years, common SMAs, such as Ni-, Ti-, Cu-, and Au-based, have been introduced via substitution of diversity of additional elements to modify their functional properties [6,86–91]. The exploration of SMA has opened new horizons for a wide variety of applications in various fields and increased demand for technological advancements. SMAs applications include, but are not limited to actuators, sensors, couplings, fasteners, dampers, transducers, cardiovascular devices, and many others. Undoubtedly, SMAs are studied extensively and are still of a great interest.

1.4.1. NiTi alloy

NiTi alloy with a nominal composition in the range of 53-57 wt.% (Figure I.5) is the most commonly used shape memory metal in engineering and medical applications. It was discovered by William J. Buehler and Frederick Wang in early 1960 in Naval Ordnance Laboratory, USA. The NiTi system has been studied extensively and is still of a great interest due to its superior properties of shape memory and superelasticity behaviour. Moreover, the alloy exhibits high corrosion resistance and biocompatibility [5,92–94].

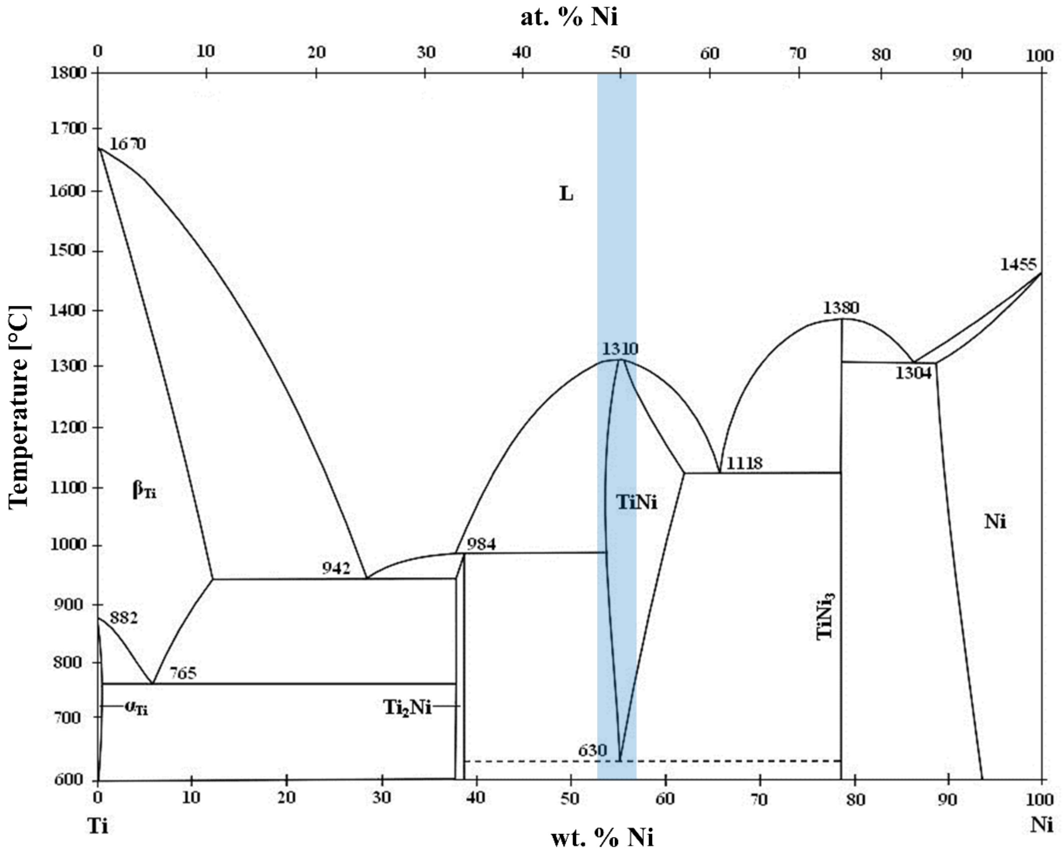

Figure I.5 Phase diagram of the Ti–Ni system [95].

NiTi phase exhibits in two crystal structures: body-cantered cubic (BCC) (B2) with the $Pm\bar{3}m$ space group, referred to as austenite (Figure I.6a), and monoclinic (B19') with a $P2_{1/m}$ space group, referred to as martensite (Figure I.6b). The crystal structure strongly depends on the chemical composition and temperature. In the high temperatures, the parent austenite phase is present, while martensite is the low-temperature phase. Upon cooling NiTi undergoes reversible solid-state diffusionless phase transformation between austenite and martensite (Figure I.7). There are four transformation temperatures associated with NiTi B2 and B19' phases:

- Austenite start temperature (A_s) -"the temperature at which the martensite to austenite transformation begins on heating in a single-stage transformation or the temperature at which the R-phase to austenite transformation begins on heating in a two-stage transformation."
- Austenite finish temperature (A_f) -"the temperature at which the martensite to austenite transformation is completed on heating in a single-stage transformation or the temperature at which the R-phase to austenite transformation is completed on heating in a two-stage transformation."
- Martensite start temperature (M_s) -"the temperature at which the transformation from austenite to martensite begins on cooling in a single-stage transformation or the temperature at which the transformation from R-phase to martensite begins on cooling in a two-stage transformation."
- Martensite finish temperature (M_f) -"the temperature at which the transformation from austenite to martensite is completed on cooling in a single-stage transformation or the temperature at which the transformation from R-phase to martensite is completed on cooling in a two-stage transformation."[96]

Moreover, the occurrence of additional phase in NiTi alloys, referred to as R-Phase, can be observed if the alloy is subjected to specific processing conditions such as annealing, cold working, Ni content variations, or introduction of the ternary element. R-Phase is an intermediate phase that may form upon cooling and heating prior to martensite and austenite transformation, respectively (Figure I.7). It has a rhombohedral distortion of the cubic austenite crystal lattice structure (Figure I.6c). It belongs to space group $P\overline{3}$ [97–100].

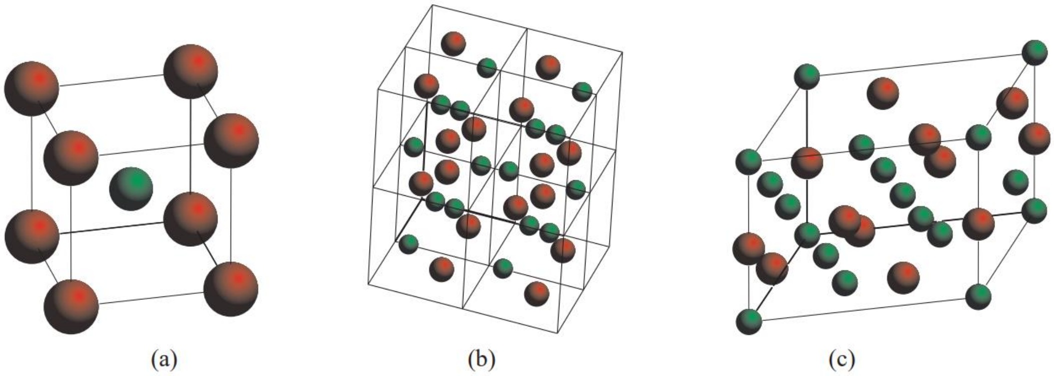

Figure I.6 Graphical representation of NiTi transformation temperatures and phase transformation upon heating and cooling. The unit cells of NiTi phases: (a) body-cantered cubic (BCC) lattice of austenite, (b) monoclinic lattice of martensite, (c) rhombohedral lattice of R-Phase [101].

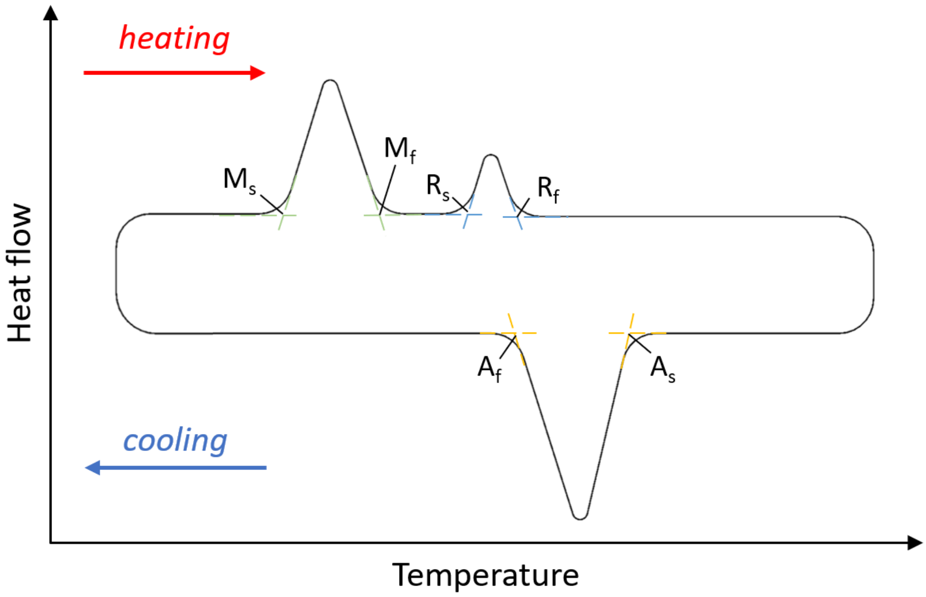

Figure I.7 Graphical representation of NiTi transformation temperatures and phase transformation upon heating and cooling.

Transformation temperatures

The transformation temperatures are influenced by many factors and are highly sensitive to the chemical and phase composition of NiTi alloys. The intermetallic phases, precipitates, and impurities affect the features of the martensitic transformation; thus, they need to be precisely controlled. It is well known that martensitic transformation temperature is strongly dependent on to the alloying ratio, and M_s decreases with the increasing Ni content [102–104]. The Ni content in an alloy is influenced by many factors, among which the most important is the chemical composition of the alloy i.e., the Ni/Ti ratio. However, another factor influencing the changes in the nickel content in the matrix is the precipitates formation such as Ni_3Ti_2, Ni_3Ti_4, or Ni_3Ti. Ni-rich precipitates absorb nickel from the matrix and thus change the Ni/Ti ratio. The M_s temperature changes by approximately 80 degrees Kelvin for every atomic percent change in Ni content. For this reason, great control of the alloy content is required during the manufacturing process [10]. Moreover, the manufacturing history, such as cold or hot-working, and application of external stress also affect transformation temperatures due to the changes in the grain size. The grain size affects transformation temperatures. Along with the increase in the grain size, the M_s and A_s transformation temperatures decreases [105–109].

Mechanical properties- superelasticity and shape memory

NiTi alloys exhibit superelasticity, unidirectional shape memory effect, and bidirectional shape memory effect. These unique properties result from reversible solid-state phase transformation when the material is subject to external stimuli such as a change in temperature or applied stress. The superelastic and shape memory response simply depends on the transformation temperature of the NiTi component coupled with the application temperature. A phase transformation induced by a change in temperature is the mechanism responsible for the shape memory property. However, phase transformation in NiTi alloy might be induced under external stress applied to the material. Transformation induced by stress is the mechanism responsible for the superelastic property. Below the M_f temperature, the NiTi alloys will exhibit shape memory, while above the A_f temperature, the NiTi material will exhibit superelasticity (Figure I.8) [110–112]. Moreover, NiTi exhibit an elastic modulus (austenite:70 GPa; martensite: 28-40 GPa) closer to that of bone (3–20 GPa) than other metallic materials commonly used in medical applications (titanium alloys-110 GPa, cobalt-chromium alloys-190 GPa, stainless steel- 210 GPa) [59,113,114].

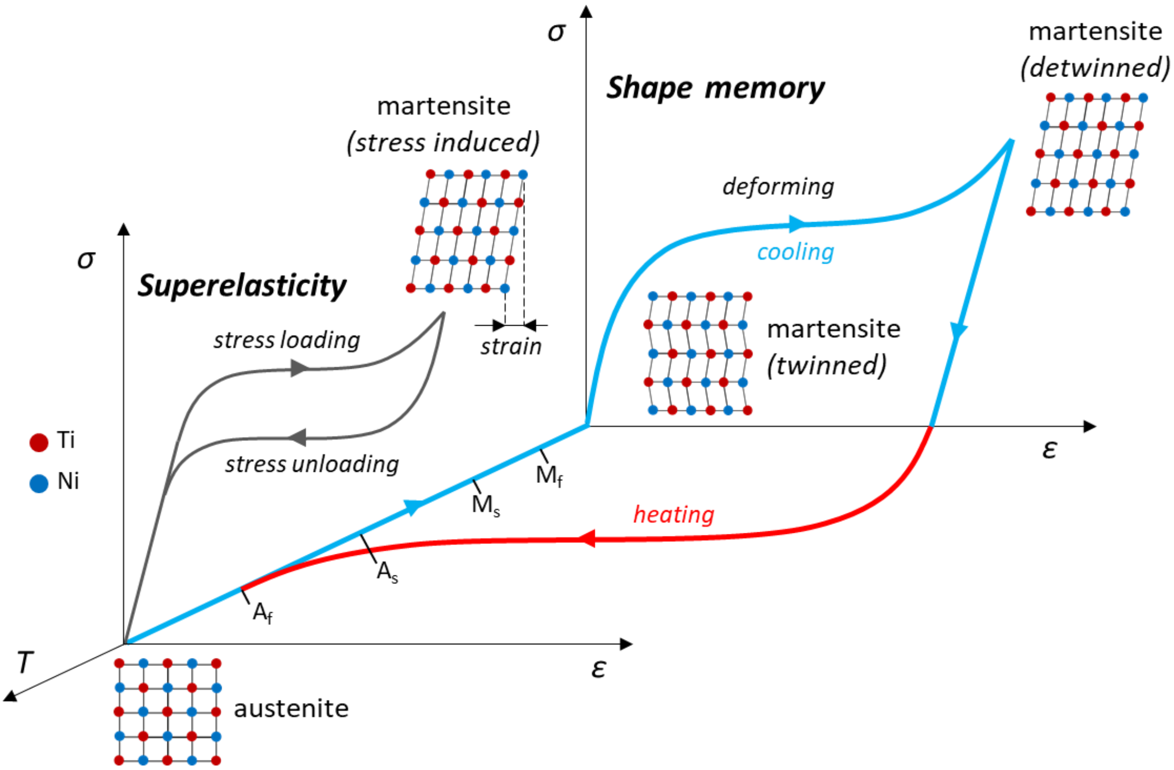

Figure I.8 Stress-strain-temperature diagram of NiTi: the behaviour of superelasticity and shape memory effect according to the phase transformation.

Shape memory

The shape memory effect in NiTi alloys is the material's ability to return from the deformed shape to the original, undeformed shape when heated. The transformation occurs between martensite and austenite. The force applied to the material causes a plastic deformation which is the result of the thermoelastic change in crystal structure due to reorientation and detwinning of twins in martensite. Upon heating, once the temperature reaches above A_f, the crystal structure changes back into austenite, resulting in a recovery of the deformation and restoration of the original shape. In most cases, shape change occurs only once upon heating of previously deformed material, and upon recooling, material does not undergo any shape change, even though the crystal structure changes to martensite. However, through an appropriate combination of mechanical and thermal treatments, SMA alloys can be trained to possess two-way shape memory effect that can be obtained without the help of any mechanical loading. In a two-way shape memory effect, material remembers' two geometrical shapes: shape at high temperature ($T>A_f$) and another shape at low temperature ($T<M_f$). Shape change occurs spontaneously upon both heating and cooling.

Superelasticity

Superelasticity also referred to as pseudoelasticity, is the ability to undergo large deformation under the external load and immediately return to the undeformed shape when the load is removed. Superelasticity is defined by ASTM F2005 as "*nonlinear recoverable deformation behaviour of NiTi SMA at temperatures above the austenite finish temperature* (A_f)*. The nonlinear deformation arises from the stress-induced formation of martensite (stress-induced) on loading and the spontaneous reversion of this crystal structure to austenite upon unloading*" [96]. NiTi demonstrates good deformability that is associated with superelastic behaviour. After unloading, a mechanically imposed strain as high as 8% can be reversibly recovered.

Precipitations

The processing of commercial NiTi alloys generally includes heat treatment such as solution annealing and subsequent aging, which usually result in precipitates formation. The four most common types of precipitates can be distinguished in NiTi alloys: stable $NiTi_2$ and Ni_3Ti, and metastable Ni_4Ti_3 and Ni_3Ti_2 phases [115]. The microstructure, lattice structure, transformation temperatures, and mechanical properties depend on the categories and morphology of the precipitates[116–118]. Based on TTT diagrams, it can be supposed that as aging time and temperature increase the precipitation sequence of Ni-rich NiTi alloys is expected to be Ni_4Ti_3 → Ni_3Ti_2 → Ni_3T [119]. Among precipitates in NiTi alloys, Ni_3Ti_4 has a direct influence on martensitic transformation. Many researchers have studied the influence of Ni_3Ti_4 precipitates on the mechanical and thermomechanical properties of NiTi alloys. It was shown that coherent Ni_3Ti_4 precipitates in the matrix could enhance shape memory behaviour, suppress the occurrence of martensitic transformation, and thus facilitate the formation of R phase, resulting in multistage phase transformation [115,117,118,120,121]. It has been shown that $NiTi_2$, Ni_3Ti_2, and Ni_3Ti_2 precipitates affect the mechanical properties of the material. These incoherent phases can act as effective barriers to a dislocation motion, thus strengthening the material and simultaneously lowering the alloy’s ductility. Moreover, due to their brittle nature, they can initiate crack nucleation/ propagation [115,117,118,122].

Non-metallic inclusions

Oxygen and carbon constitute one of the major impurities in NiTi alloys since they can combine with titanium and lead to the Ti- rich oxides and carbides formation. The presence of oxides and carbides results in Ti depletion in the alloy and can affect chemical balance leading to the change in transformation temperatures generated by the chemical composition changes. Moreover, due to the brittle nature of oxides and carbides, the presence of these small particles can affect fatigue life since these particles can act as crack initiators during the fatigue [123,124]. Moreover, contaminants such as oxygen, carbide, and nitrogen may be responsible for the presence of secondary precipitated phase in the matrix. During the heat treatment of NiTi alloys, oxygen can diffuse and promote the formation of $NiTiO_3$ and Ni_2Ti_4O oxides ascribed to the lower formation enthalpy. The presence of these phases affects the formability, transformation temperatures, and mechanical properties of NiTi alloys [102,125–128].

Passivation

The unique combination of shape memory and superelasticity properties coupled with biocompatibility response has made NiTi an excellent material for medical device applications. On the surface of NiTi, titanium ions interact with oxygen to form an extremely tenacious passive titanium oxide layer (TiO_2), which typically gives the NiTis excellent corrosion resistance and biocompatibility. This oxide layer protects the NiTi materials beneath from the external environment and nickel ion release, which could be hazardous for health. Some research reported that although NiTi alloys have a high percentage of nickel, the quantity of released nickel ions is smaller than released from typical stainless steel for medical application [129–133].

Manufacturing

Due to the high reactivity of NiTi, it is most commonly manufactured using high purity elementary components by vacuum melting techniques such as vacuum induction melting (VIM) or vacuum arc melting (VAM). The commonly available shapes of NiTi products are imitated to simple forms such as sheet, rod, bar, and wire. It is because the inherent properties of NiTis render their machining a challenging task. The drawbacks in machining NiTi include rapid and uncontrollable tool wear, undesirable chip and burr formation, and high cutting forces. Moreover, the phenomena of work hardening combined with high ductility, low elastic modulus, and superelasticity of NiTi alloys contribute to the poor surface quality of machined parts [134,135]. Most machining methods indicate high temperatures and high forces excreted on the workpiece, which influence the thermomechanical properties of the material. Furthermore, solid-state phase transformation that occurs during machining complicates predicting the machining behaviours. Recent studies showed that the machining performance of difficult-to-machine material could be improved by cryogenic machining [136,137]. It was shown that cryogenic machining is effectively reduced progressive tool wear and improves the surface quality of NiTi [138]. To withstand difficulties with NiTi machining, non-traditional/ unconventional machining processes have been established. Laser cutting and electro-discharge machining were found to be more effective alternatives to manufacture NiTi products [139–143]. However, as the laser cuts some of the molten material, it will be recast onto the wall of the component. This part of the heat-affected zone is called "recast layer". The re-cast laser is heavily oxidized and very brittle and typically contains micro-cracks that serve as fracture initiation points. Thus, laser cutting and electric discharge machining parts require post-processing to remove heat-affected zones, recast layers, and slag to achieve acceptable device performance [103,144]. Electrochemical machining is an adaptive approach for efficient machining of NiTi alloys. In this technique, the required shape of the product is obtained by electrolytically dissolving the metal. The elimination of heat input reduces surface oxidation and results in a burr-free finish. Moreover, the electrochemical machining has a beneficial influence on surface texture. Although, this technique is a favourable method for fabricating small intricate geometries, the small size of the part and the need to use thin foils are a significant limitations [145,146]. One unconventional machining extensively used in various industrial applications is abrasive water jet machining. The main advantages of the process are high flexibility and machining versatility, the absence of thermal effects, and minimal stress imposed on the workpiece. The main limitation of the technique is low accuracy compared to other cutting methods; therefore is usually used for rough cutting of thick hard materials [147–149].

Recently additive manufacturing (AM) has gained significant attention for processing NiTi because it eliminates many of the challenges associated with the conventional methods [150,151]. Plenty of publications show studies about NiTi fabrication using many different AM techniques, such as flow-based: laser direct energy deposition (LDED) [152], laser direct metal deposition (DMD) [153,154], laser engineered net shaping (LENS) [155], as well as fusion based: laser powder bed fusion (LPBF) [85,156–158], electron beam melting (EBM) [51,159] and many others. The base material in the additive methods is metallic powder, which can be fabricated via several different techniques such as mechanical attrition, hydriding, water, and gas atomization. Nevertheless, regardless of the powder manufacturing method, great control of the chemical composition and impurity content is required.

Up to now, in terms of mechanical and functional properties, the compressive behaviour of AM NiTis has been extensively investigated with promising results. As mentioned in many works, composition, impurities, texture, and precipitation characteristics of NiTi alloys are all affected by manufacturing methods and parameters. As a result, the structural and functional properties of NiTi alloys fabricated through various routes can be distinct [106,160,161]. Consequently, identifying the optimal manufacturing parameters is a crucial task because these parameters happen to be the most influential on the part’s characteristics. Due to the properties of NiTi alloys, it is challenging to fabricate them in powder forms. It results in high costs and limited availability on the market. NiTi alloy powders are about three times more expensive than the alloying element powders, titanium, and nickel. Hence, *in situ* alloying via AM from elemental powders is a promising, cost-effective alternative, which offers the flexibility to tailor the powder composition, and thus, is a facile approach to control the material properties or create novel alloys. It is particularly true for NiTi alloys, as their phase transformation temperature is susceptible to the alloy composition.

Flow-based AM technologies are commonly used for multi-material fabrication. Thus, in the work presented by Shiva et al. [162], Ni and Ti powder were pre-mixed, and three different weight percentage compositions were selected. The laser-based rapid manufacturing (LRM) method was used. It was developed that Ni/Ti ratio influenced microstructure, mechanical and thermomechanical properties of investigated materials. Halani et al. [163] fabricated pre-mixed Ni and Ti powders with laser direct deposition (LDD) technique, and Bimber et al. [152] implemented laser direct energy deposition (LDED) process. In all these works, the formation of $NiTi_2$, Ni_3Ti, Ni_4Ti_3 phases, and Ni content decrease were observed. A decrease in Ni/Ti ratio can be induced because of a relatively lower nickel evaporation temperature (2732°C) as compared to that of titanium (3287°C). However, powder bed fusion technologies are more common for creating complex parts. Thus far, only four studies, presented by Zhang et al. [164]; Wang et al. [51]; Stoll et al. [165], and Zhao et al. [166]. It was investigated that fabrication parameters influence microstructure and mechanical properties and the heterogeneity of phase distribution. Wang et al. [51] systematically studied the influence of LPBF parameters on phase composition and mechanical properties. However, these studies did not demonstrate the influence of the fabrication process on the chemical composition of final materials. Moreover, in previously mentioned studies, different scanning strategies were used: energy density, scan velocity, and scanning vectors rotation. Nevertheless, the remelting process was not examined. As shown by Zhang et al. [167], in the case of Nb-Mo-Ta-W alloy, fabrication with mixed multi-element powders, the remelting strategy has a positive impact on the material's homogeneity, and this improvement may result from the "*in situ* heat treatment", which occurs during remelting of the solidified layers. In the other works that referred to LPBF *in situ* alloying of different alloys [39,41,79], only basic LPBF parameters were changed during manufacturing process, high inhomogeneity of fabricated materials was found with no remelting or laser focus variations. Therefore, it can be assumed that the remelting of each layer, with the same or different scanning strategy and parameters applied, could help reduce the inhomogeneity of NiTi alloys fabricated from pre-mixed powders. Simultaneously, another important aspect would be the investigation of the impact of suggested scanning strategies on the Ni/Ti ratio in the fabricated alloy. Moreover, the influence of manufacturing parameters on different mixing ratios of Ni/Ti powders and their properties were not investigated in previous works using LPBF technology.

1.5. Summary of state of art

The benefits provided by additive manufacturing (AM) technologies make them more and more frequently used in all areas of our lives. Despite their unquestionable development, there is still a strong need to understand and control their phenomena, which will allow wider use of them. Among existing metal AM technologies, laser powder bed fusion processes (LPBF) are the most frequently investigated due to a large number of process variables and parameters involved in this technique, which enables successfully fabricating fully dense metal parts and controlling their properties. NiTi alloys are widely used for many engineering and medical applications owing to their unique shape memory and superelasticity characteristics. However, the high price and the specific mechanical properties of NiTis make their machining a challenging task, which significantly reduces the field of application and limits the potential of this material. Hence, *in situ* alloying via AM from elemental powders is cost-effective and provides flexibility in tailoring the required chemical composition, i.e., nickel to titanium ratio, and gives the advantage of fabrication complex-shape geometries with high accuracy. Moreover, understanding the impact of the parameters of the LPBF technology fabrication process of the NiTi pre-mixed powders would enable a better understanding of the phenomena accompanying this method and the broadening of the possibility of using it to produce new metallic materials.

Chapter II

Hypothesis, Objective, and Scope of Thesis

2.1. Hypothesis, Objective, and Scope of Thesis

Laser powder bed fusion (LPBF) technology enable complex shape geometries fabrication, while the usage of pre-mixed powders provides a significant price reduction of batch material compared to pre-alloyed powder. Phase transformation temperature of NiTi alloys, which determines its unique shape memory and superelasticity properties, is highly sensitive to the alloy composition. Therefore, it is critical to accurately model the impact of LPBF process parameters on the microstructure, chemical and phase composition of the fabricated material.

Hence, the following **research hypothesis** have been formulated:

The use of laser powder bed fusion technology enables the manufacturing of NiTi alloy from elementally blended Ni and Ti powders, and multiple remelting and designed laser scanning/ melting strategies along with appropriately selected heat treatment increase the homogeneity of the microstructure of the fabricated material.

Taking into consideration research hypothesis, the **objectives of the presented thesis** are as follows:

Objectives:

Utilitarian:

- Development of laser powder bed fusion manufacturing parameters for *in situ* alloying of NiTi from elemental Ni and Ti powders with the use of a remelting and designed scanning strategies
- Development of the heat treatment to homogenize the chemical and phase composition of *in situ* alloyed NiTi powder fabricated by laser powder bed fusion.

Scientific:

- Evaluation of the influence of laser powder bed fusion parameters and melting strategies on the microstructure, chemical and phase composition of *in situ* alloyed NiTi.

- Evaluation of corrosion and biological performance of NiTi alloy fabricated by laser powder bed fusion using elementally blended Ni and Ti powders.

Scope of Thesis

The following scope of thesis have been undertaken to achieve objectives and prove the hypothesis:

1. Optimization of laser powder bed fusion manufacturing parameters for *in situ* alloying of NiTi from elemental Ni and Ti powders with the use of a remelting and designed scanning strategies:

- Investigation of the influence of different parameters and melting strategies on the printability and microstructural defects formation (porosity, cracks).
- Influence of melting strategies on chemical and phase composition homogeneity, residual stresses, and density.

2. Evaluation of chemical and phase composition of NiTi powder blends with chemical compositions of $Ni_{53}Ti_{47}$, $Ni_{55.7}Ti_{43.7}$, and $Ni_{57}Ti_{43}$ (wt.%):
    - Fabrication of solid coupons using powder blends with three different chemical compositions,
    - Investigation of chemical and phase composition homogeneity depending on the initial powder’s chemical composition and the number of melts.
3. Development of the solution heat treatment to improve microstructure homogeneity of *in situ* alloyed NiTi:

- Selection of a heat treatment temperature and time,
- Investigation of a Ni_2Ti_4O phase formation.

4. Development of postprocessing chemical polishing of NiTi alloy fabricated by laser powder bed fusion:
    - Selection of the chemical composition of the solution and polishing time,

  - Investigations of the effects of chemical polishing on the accuracy of the rendered computer-aided design (CAD) model.

5. Evaluation of corrosion and biological performance of *in situ* alloyed NiTi:

    - Comparison of corrosion resistance and biological performance of NiTi coupons fabricated from pre-mixed and pre-alloyed powder,
    - Surface characterisation of chemically polished NiTi coupons fabricated from pre-mixed and pre-alloyed powder,
    - Investigation of Ni ion release.

2.2. Description of chapters

Chapter I describes the additive manufacturing technology, with an emphasis on laser powder bed fusion technique and *in situ* alloying; metallic biomaterials for orthopaedic applications; and shape memory alloys, with an emphasis on NiTi alloy.

Chapter II provides the hypothesis, objectives, and scope of thesis.

Chapter III demonstrates the optimization of laser powder bed fusion manufacturing parameters for *in situ* alloying of NiTi from elemental Ni and Ti powders with the use of a remelting and designed scanning strategies. The chapter focuses on influence of manufacturing parameters and melting strategies on printability, microstructural defects formation, and chemical homogeneity.

Chapter IV presents the laser powder bed fusion fabrication of NiTi coupons using powder blends with chemical compositions of $Ni_{53}Ti_{47}$, $Ni_{55.7}Ti_{43.7}$, and $Ni_{57}Ti_{43}$ (wt.%), and evaluates the influence of manufacturing parameters and scanning strategies on chemical and phase composition of fabricated material depending on the chemical composition of the initial powder blend.

Chapter V demonstrates the development of the solution heat treatment to improve chemical and phase homogeneity of the *in situ* alloyed NiTi fabricated by laser powder bed fusion.

Chapter VI presents postprocessing chemical polishing of NiTi alloy fabricated by laser powder bed fusion and studies the influence of solution composition and time of polishing on the accuracy of the rendered computer-aided design (CAD) model

Chapter VII evaluates the corrosion and biological performance of NiTi alloy fabricated by laser powder bed fusion using two different source materials with the same initial chemical composition: pre-alloyed NiTi powder and elementally blended Ni and Ti powder.

Chapter VIII summarizes obtained results and discusses further research plans.

Chapter III

Laser Powder Bed Fusion (LPBF) of NiTi Alloy Using Elemental Powders: The Influence of Remelting on the Printability and Microstructure

Agnieszka Chmielewska, Bartłomiej Wysocki, Elżbieta Gadalińska, Eric McDonald,
Bogusława Adamczyk-Cieślak, David Dean, Wojciech Święszkowski

Published in: Rapid Prototyping Journal

DOI: 10.1108/RPJ-08-2021-0216

Abstract

Purpose

The purpose of this paper is to investigate the effect of remelting each layer on the homogeneity of NiTi parts fabricated from elemental nickel and titanium powders using Laser Powder Bed Fusion (LPBF). In addition, the influence of manufacturing parameters and different melting strategies, including multiple cycles of remelting, on printability and macro defects, such as pore and crack formation, have been investigated.

Design/ methodology/ approach

An LPBF process was used to manufacture NiTi alloy from elementally blended powders and was evaluated with the use of a remelting scanning strategy to improve the homogeneity of fabricated specimens. Furthermore, both single melt and up to two remeltings were utilized.

Findings

The results indicate that remelting can be beneficial for density improvement as well as chemical and phase composition homogenization. Backscattered Electron (BSE) mode in Scanning Electron Microscopy (SEM) showed a reduction in the presence of unmixed Ni and Ti elemental powders in response to increasing the number of remelts. The microhardness values of NiTi parts for the different numbers of melts studied were similar and ranged from 487 to 495HV. Nevertheless, it was observed that measurement error decreases as the number of remelts increases, suggesting an increase in chemical and phase composition homogeneity. However, X-ray diffraction (XRD) analysis revealed the presence of multiple phases regardless of the number of melt runs.

Originality

For the first time elementally blended NiTi powders were fabricated via LPBF using remelting scanning strategies.

3.1. Introduction

Additive Manufacturing (AM) has now become a cost-effective, energy efficient, and environmentally friendly fabrication process for low volume production. With the ongoing rapid reduction in 3D printing cost, AM could soon become competitive with mainstream manufacturing forming strategies for mid-level runs as well. Due to geometric freedom, AM has been extensively developed during the last few years and has become the fastest growing manufacturing technique recently, particularly important with metallic materials [168–170].The use of AM may significantly reduce or even eliminate the need for machining. Powder Bed Fusion (PBF) technology utilizes a laser or electron beam energy source to build parts by melting a metallic powder in a layer-wise manner. Compared to other non-powder-bed metal AM systems, such as Directed Energy Deposition (DED) or laser engineered net shaping (LENS), PBF has an advantage when sed to fabricate parts with complex, including high porosity, geometries with both high resolution and high accuracy relative to the original computer aided design (CAD) part’s dimensions. However, one of the limitations of PBF is the low availability of suitable metallic powders from the small number of 3D printable alloys.

Shape memory alloys (SMA) show great potential in many aerospace and medical applications, and consequently are proving to be of great interest to AM (Dhanasekaran et al. 2018; Farber et al. 2019). NiTi, also referred to as nitinol, is one of the well-known, and frequently used, SMA materials. Humbeeck (1999) and Sharma and Srinivas (2019) report that in the aerospace industry nitinol has been utilized to produce portions of aircraft wings. Furthermore, as reported by Duerig et al. (1999), Elahinia et al. (2012) and Chen et al. (2019), nitinol is an essential material in the medical device engineer’s toolbox and, is widely used in various biomedical engineering applications, such as orthodontic arch wires, surgical stents, active catheters, spine-fracture fixations, oral and maxillofacial implants, bone plates, and lumbar vertebral replacements.

NiTi’s unique mechanical properties result from reversible, solid-state, phase transformations that occur when the material is subject to external stimuli such as a change in temperature or an applied stress. A phase transformation induced by a change in temperature is the mechanism responsible for the shape memory property while transformation-induced by stress are the mechanisms that initiate a part’s superelastic property. This diffusionless martensitic transformation occurs between the parent B2 austenite phase and the B19’ martensitic phase. The superelastic and shape memory responses simply depend on the transformation temperature of the NiTi component coupled with the ambient temperature. Dadbakhsh et al. (2014) and Frenzel et al. (2010) demonstrated that below the martensite finish (M_f) temperature the NiTi alloys will exhibit shape memory, while above the austenite start (A_f) temperature the NiTi material will exhibit superelasticity. The martensitic transformation temperature is sensitive to the alloying ratio. Khalil-Allafi and Amin-Ahmadi (2009) described, that the martensite start (M_s) temperature varies significantly with atomic percent change in Ni content. For this reason, it is possible to precisely control the transformation temperature by selecting the appropriate chemical composition of the material, as reported by Dadbakhsh et al. (2014) and Frenzel et al. (2010). There are a limited number of NiTi powders with different chemical compositions on the market. Therefore, if there is a need to obtain a material with a specific chemical composition, the powder must be produced, which is a time-consuming and expensive process. Hence, *in situ* alloying via AM from elemental powders is a promising, cost-effective alternative, which offers the flexibility to tailor the powder composition. The enhanced ability to vary and control LPBF nitinol part material properties may lead to the creation of novel alloys.

To overcome the problems related to preparation of the powders with different relative wt. % compositions of either Ni or Ti, AM manufacturing from elementally blended powders has been implemented. Thus far, studies presented by Stoll et al. (2020); Wang et al. (2019); Zhao et al. (2020) and Zhang et al. (2013) have previously shown the potential of using LPBF to synthesize NiTi alloys directly from elementally blended pure nickel and titanium powders. Those studies demonstrated that fabrication parameters influence microstructure and mechanical properties as well as phase formation. Moreover, it was reported by Zhang et al. (2013) and Zhao et al. (2020) that energy input influences phase transition in as-built LPBF-fabricated NiTi parts. Wang et al. (2019) subjected fabricated materials to post-processing heat treatment in order to increase material homogeneity. This indeed reduced presence of unwanted phases and promoted formation of the NiTi phase.

In all of the previously mentioned studies on LPBF of NiTi parts from Ni and Ti elemental powders, different process parameters have been optimized, such as: energy density, scan velocity, and scanning vector rotation. Nevertheless, a remelting process, which is an additional melting process for a consolidated layer, without covering it with new metal powder, has not been yet examined for the LPBF of elemental Ni and Ti powders. Zhang et al. (2019) show that during fabrication of NbMoTaW alloy parts from mixed multi-element powders, use of a remelting strategy has a positive impact on the homogeneity of the material and that homogeneity may be further improved via an "*in situ* heat treatment" which occurs during remelting of already solidified layers before the next layer is printed. Moreover, Wei et al. (2019) report that this phenomenon can eliminate thermal stress and inhibit crack initiation and propagation.

Fischer et al. (2016); Simonelli et al. (2018) and Vrancken et al. (2014), explored LPBF powder mix fabrication of different alloys where only basic PBF parameters were adjusted during the manufacturing process. This resulted in high inhomogeneity of fabricated materials when no remelting or laser focus variation was used. Therefore, given what has previously been studied in regard to LPBF of Ni and Ti elemental powders, the objective of the current study is to investigate the effect of remelting of each layer on the homogeneity NiTi parts fabricated from elemental nickel and titanium powders via LPBF. In addition, the influence of manufacturing parameters (i.e., laser parameters and scanning strategy) and different melting strategies, including multiple remelting, on printability and the occurrence of macroscopic defects, such as pores and cracks, were investigated. Currently, there are two major limitations to using as-cast NiTi, machining difficulties and its high price. One major benefit of AM technologies is the reduction or elimination of the need for machining. Pre-alloyed NiTi powder used for AM is also expensive. Production Ni-Ti components using pre-mixed Ni and Ti elemental powders, instead of pre alloyed powders, would reduce the material costs of fabrication by nearly three times. Consequently, the price of the final part would be significantly reduced, thereby providing the possibility of wider application of this material in many industrial fields.

3.2. Materials and Methods

3.2.1. Powder Preparation

Spherical elemental powders of Ni (TLS Technik, Germany; size range <45µm; D10= 6.57 µm; D50= 19.95 µm; D90= 39.67 µm) and Ti (grade 1 TLS Technik; size range 15-45µm; D10= 14,68 µm; D50= 30.58 µm; D90= 44.24 µm) were used in this study. The Ni:Ti powder blend ratio was Ni 55.7wt% : Ti 44.3wt%. The chemical compositions, including impurities, of Ni and Ti are listed in Table III.1 and Table III.2, respectively. The two powders were dry blended, without any additives or lubricants, in a tumbling mixer for 2h in order to achieve uniform particle distribution. The morphology of the powders, as well as their distribution after blending, was observed in a Hitachi SU-8000 (Hitachi, Japan, Tokyo) scanning electron microscope (SEM).

Table III.1 Chemical composition of nickel powder.

Element	**Ni**	**C**	**Fe**
wt. [%]	99.9	0.017	<0.1

Table III.2 Chemical composition of titanium powder.

Element	**Ti**	**C**	**Fe**	**N**	**H**	**O**
wt. [%]	Bal.	<0.08	<0.20	<0.03	<0.015	<0.18

3.2.2. Manufacturing

Cylindrical parts of dimensions ϕ6 x 4 mm were fabricated in LPBF process using a Realizer SLM50 machine (Realizer GmbH, Borchen, Germany) equipped with a ytterbium fiber laser source with a maximum power output of 120W. The fabrication process was performed under an argon atmosphere while the oxygen content was kept below 0.3 vol. %. The build parts were deposited on a substrate made from bulk NiTi to provide compatibility and wettability with the processed materials. The substrate was preheated and kept at 200°C to ensure building parts remained bonded to the substrate during the process. The process parameters were as follows: laser power (P) of 25-30 W, scanning speed (v) of 500-100 mm/s, hatch spacing (h) of 0.03-0.07 mm and hatch angle of 45° (no contours were applied). The powder layer thickness (t) was set to 25 μm. Based on the equation E=P/(vht), the energy density was calculated and varied in the range of 14-80 J/mm^3. The LPBF parameters optimization procedure (laser parameters and scanning strategies) for the parts fabrication are shown in Appendix 1.

After the first scan, here referred to as a single melting (SM), some sets of parts were subjected to one or two additional remeltings. This means that on each platform every layer of the part was scanned one, two, or three times, as shown in Figure III.1. Each first and second remelting was performed in the same laser scanning direction as was used in the first melt. The remelting was processed with different parameters than the first melt. Two remelting parameters R1 and R2 were used, with scanning speeds of 1000 and 3000mm/s and a laser power of 25 W and 75 W, respectively. Both parameters for remelting resulted in the same energy density of 33 J/mm^3. The use of those three melting strategies allowed to obtain five platforms of parts with the scanning parameters as described in Table III.3.

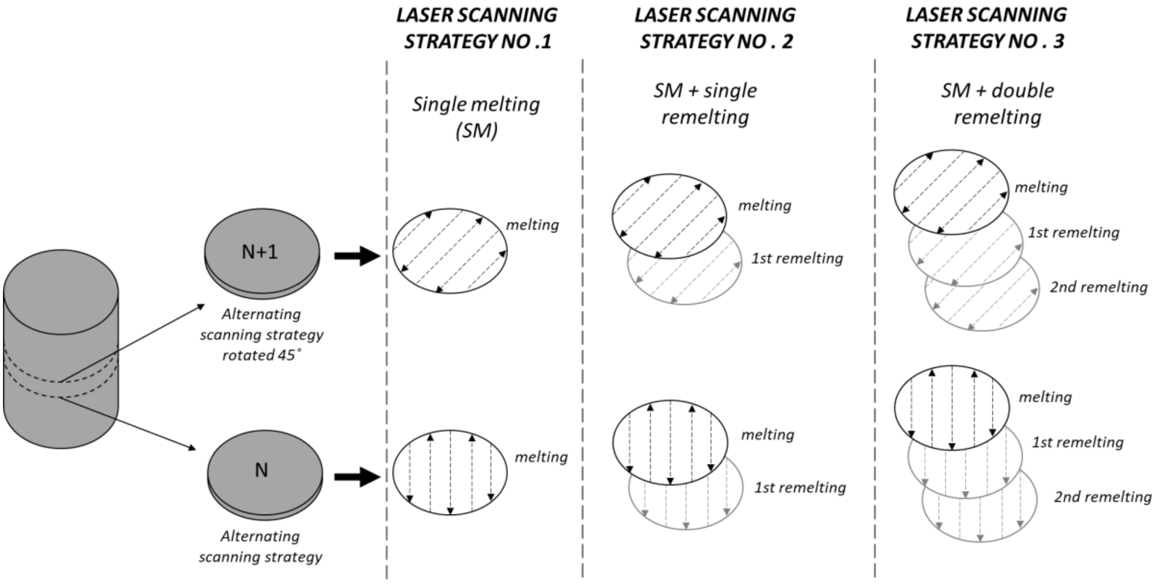

Figure III.1 Scheme of melting strategies utilized, including in some cases up to two remelts.

Table III.3 LPBF process parameters and number of remelts used for processing of blended elemental Ni and Ti powders.

Platform No.	Remelting No.	melting	1st remelting	2nd remelting
1	Single Melting (SM)	14-80J/mm^3 (P=25-30W, v=500-1000mm/s)		
2	Single Melting (SM) + One remelting	14-80J/mm^3 (P=25-30W, v=500-1000mm/s)	33J/mm^3 (R1) (P=25W, v=1000mm/s)	
3	Single Melting (SM) + two remeltings	14-80J/mm^3 (P=25-30W, v=500-1000mm/s)	33 J/mm^3 (R1) (P=25W, v=1000mm/s)	33 J/mm^3 (R1) (P=25W, v=1000mm/s)
4	Single Melting (SM) + One remelting	14-80 J/mm^3 (P=25-30 W, v=500-1000mm/s)	33 J/mm^3 (R2) (P=75W, v=3000mm/s)	
5	Single Melting (SM) + two remeltings	14-80 J/mm^3 (P=25-30 W, v=500-1000mm/s)	33 J/mm^3 (R2) (P=75W, v=3000mm/s)	33 J/mm^3 (R2) (P=75W, v=3000mm/s)

3.2.3. Microstructure Characterization and Phase Identification

After fabrication, parts were removed from the substrate and hot mounted in resin. All parts were mechanically ground and polished for further tests. Pore and crack density were studied on metallographically prepared specimens using light microscopy (Zeiss AxioVision Light Microscope). The relative density of the parts was calculated on the basis of microscopic images using MicroMeter software [180,181].

To reveal Ni and Ti elemental distribution in the 3D printed parts, parts were analyzed using a Hitachi SU-8000 scanning electron microscope (SEM) in the Backscattered Electron (BSE) mode. SEM BSE observations were performed to provide information about the distribution of different elements in the part according to their atomic number. The parts were subjected to scanning electron microscopy with energy dispersive spectroscopy (SEM-EDS) analysis to obtain elements maps for the evaluation of the homogenization ratio.

A qualitative phase analysis was performed by X-ray diffraction (XRD) at room temperature using a Bruker D8 Advance (Bruker, Germany) diffractometer with filtered Cu Kα (λ = 0.154056nm) radiation. The recording conditions of the XRD patterns were as follows: voltage 40kV, current 40mA, angular range 2Θ from 30° to 110°, step $\Delta 2\Theta$ – 0.05°, counting time – 3 s. The XRD patterns were analysed using Bruker EVA software and the PDF-2 database (from the International Centre for Diffraction Data).The diffraction measurements of stress values were performed with a PANalytical Empyrean diffractometer with Cr Kα (λ = 0.228976 nm) radiation. The Kβ component of the radiation was cut off by applying a V filter. The first attempts to obtain diffraction stress measurements were made using Cu Kα radiation for a NiTi (B2) phase reflection with *hkl* Miller coefficients (321), which nominally, according to the 04-017-0804 card of the ICDD PDF4+ libraries, should be at approximate position $2\theta=147.127°$. Unfortunately, the multiplicity of planes with these coefficients turned out to be unsatisfactory to collect reliable stress measurements. When Cr radiation was used, it was possible to obtain higher peak intensities for reflections with *hkl* coefficients (211). The position of the reflex according to the referenced ICDD4+ card was $2\theta=137.881°$. A disadvantage of the measurement for the material under investigation using Cr radiation was the appearance of a high amount of fluorescence. This phenomenon was compensated by using appropriate detector energy thresholds. The incident X-ray beam was collimated and made quasi-parallel using a polycapillary. The incident beam was limited to a size of 1 x 2 mm^2. Stress measurements were carried out in side-inclination geometry. The step for $\sin^2\psi$ was 0.15°, stress measurements were carried out for 3 directions relative to the specimen to obtain the information about the full stress tensor. Each measurement was made by collecting the shape and position of 9 diffraction peaks. Each diffraction peak was observed in the angular range of 9.56°, the measurement step was 0.105° and the measurement for each peak lasted about 2 hours.

The microhardness measurements on all parts were implemented on a polished XY plane using a microhardness tester (Falcon 500, Innovatest, Netherlands). A load of 200g and indentation time of 15s was selected. For each part, 6 load test readings were taken at different locations and the average value was considered as a microhardness value.

A TCH 600 Nitrogen/ Oxygen/ Hydrogen determinator (LECO, St. Joseph, MI, USA) was used to determine the content of oxygen in all fabricated parts. The elements are converted to their oxidized form by utilizing the gas fusion method and the infrared absorption (IR) is used to measure combustion gases within a metallic part.

The chemical composition of the fabricated parts was analysed using a ZSX Primus II (Rigaku, Japan) Wavelength Dispersive X-ray Fluorescence (WDXRF) device.

The density of the selected parts was evaluated by the Archimedes method and µCT analysis. The µCT images were collected on a HeliScan (Thermo Fisher Scientific, Waltham, MA). The voxel size was set to 5.3 µm. A source voltage of 100 kV and a source current of 100 µA were used. A 3-mm aluminium filter material was chosen. The scanning procedure was carried out by rotating an emitted X-ray by 180°, 1800 projections per resolution, and an exposure time of 0.45 s per projection.

3.3. Results and Discussion

3.3.1. Powder Characterization

The powder mixture of elementally blended pure Ni and Ti is shown in Figure III.2. SEM observation using a BSE signal shows Ti particles that are darker with a smooth surface, while Ni particles are brighter, and their surface is more irregular. The particles were uniformly distributed, and no agglomerates were observed.

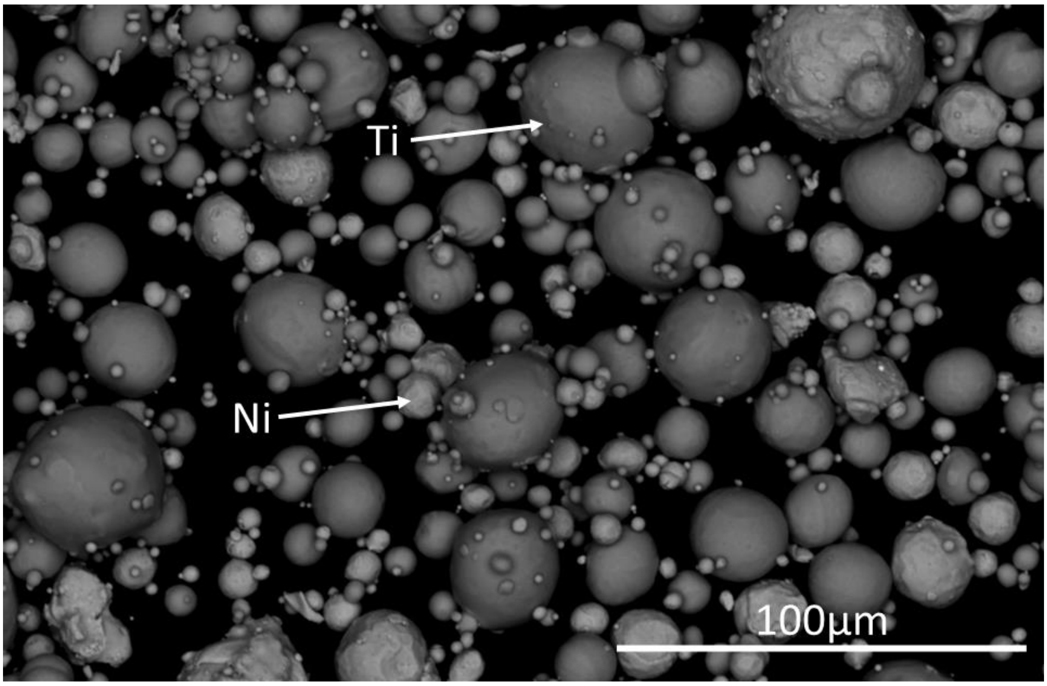

Figure III.2 A powder mixture of elementally blended pure Ni and Ti powders.

3.3.2. Effects of Processing Parameters on Printability

In this study, printability refers to successfully building a part, and concurrently avoiding or minimizing macrocracking defects and delamination. Lu et al. (2020) and Zhang et al. (2019) have reported that in their studies when remelting was done at a different angle than the first scanning, with NiTi elementally blended powders, when changing the direction of remelting, the laser collects welding contaminations on the part surface. That collection of contaminations causes surface roughness and porosity. Liu and Guo (2020) and Sato et al. (2017) studied the occurrence of welding contamination. They found that welding contamination depends on manufacturing conditions, as well as used material and its morphology. In this study, during the first scanning of each layer (single melting - SM), the laser moved aside causing welding contamination, such as spatter particles and balling, and isolated the contaminants at the edge of fabricated layer (Figure III.3a). It was observed, that after the direction of the remelting was changed (rotated in relation to the SM), and the laser approached the edge, where the welding contamination had accumulated, some of the contaminated agglomerations were observed to be collected by the laser and spread over the part's surface (Figure III.3b). Additionally, in the agglomerations caused high surface roughness and porosity in these parts (Appendix 1). However, when the direction of remelting was the same as in a SM fabricated part, the welding contaminations were limited to the edge of the fabricated layer and its surface was smooth (Figure III.3c). Therefore, each first and second remelting was performed in the same direction as the first scan. Moreover, Li et al. (2012) observed that a remelting procedure can also alleviate the balling effect to a certain extent, due to the melting and wetting of metal balls. Thus, remelting can improve surface quality.

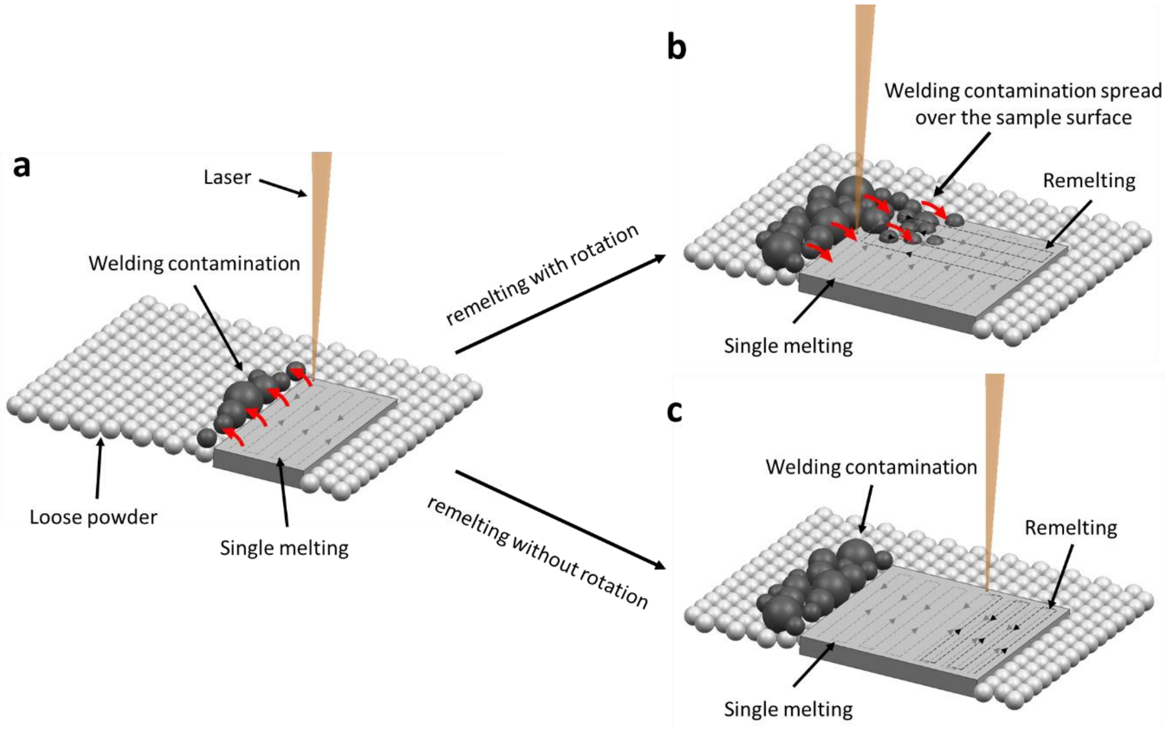

Figure III.3 Schematic illustration of a) the formation of contamination during the scanning and the influence of melting strategy on welding contamination: b) welding contamination collects at the edge of the printed part in each layer, c) the size of welding contamination expands as the part is built.

All of the samples manufactured in the separate substrates are shown in Figure III.4. The manufacturing parameters used for single melting (SM), located on platform 1, enable the fabrication of parts free of macroscopic defects, as well as avoiding delamination and macrocracks. No significant dimensional inaccuracy (in macroscale) due to the powder adhesion was observed. The SM parts also showed no deformation due to high energy input. Therefore, all of the samples from platform 2-5 were subjected to further remelting. Samples remelted with R1 parameters once or twice, shown on platforms 2 and 3, respectively, were free of macroscopic-defects, cracks, or delamination. Instead, R2 remelting parameters induced minor cracks along the build direction. First and second R2 remelting are shown on platforms 4 and 5, respectively. Visible cracks could be the result of high temperature differences, stresses due to phase transitions or the formation of brittle phases, i.e. $NiTi_2$, Ni_3Ti, Ni_4Ti_3 [188–190].

Single melt (SM) parts as well as remelted parts with R1 parameters have smoother top surface, while those remelted with R2 parameters have a more irregular top surface. Moreover, some of the R2 remelted parts failed during the fabrication. The failure of the parts may be caused by the large thermal gradient that generates high thermal stresses as discussed in section 3.3.

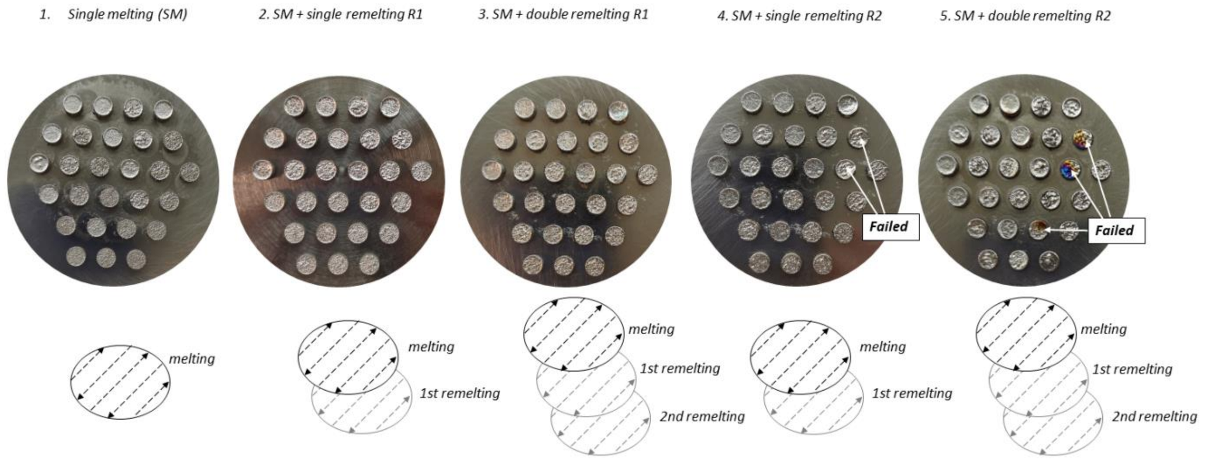

Figure III.4 Results of LPBF parts manufactured with different number of remelts.

3.3.3. Microstructure

Figure III.5 shows optical micrographs of a polished surface of parts fabricated with different energy densities and melting strategies. The presence of pores and cracks in the microstructure of the fabricated parts was observed. The size and distribution of pores, as well as cracks, depend on the manufacturing parameters. The porosity decreases with increasing energy density and with the remelting applied for most parts. Li et al. (2019) and Griffiths et al. (2018) reported that remelting provided good metallurgical bonding between adjacent melt pools and the formation of shallower melt pools. As a result, the density and surface quality was improved. Chen et al. (2018); Griffiths et al. (2018;) and Xiong et al. (2020) discovered similar results in their works, where remelting was applied. It was reported that due to good metallurgical fusion provided by remelting, the pores were successfully reduced. Moreover, the number of pores and their average size were minimized.

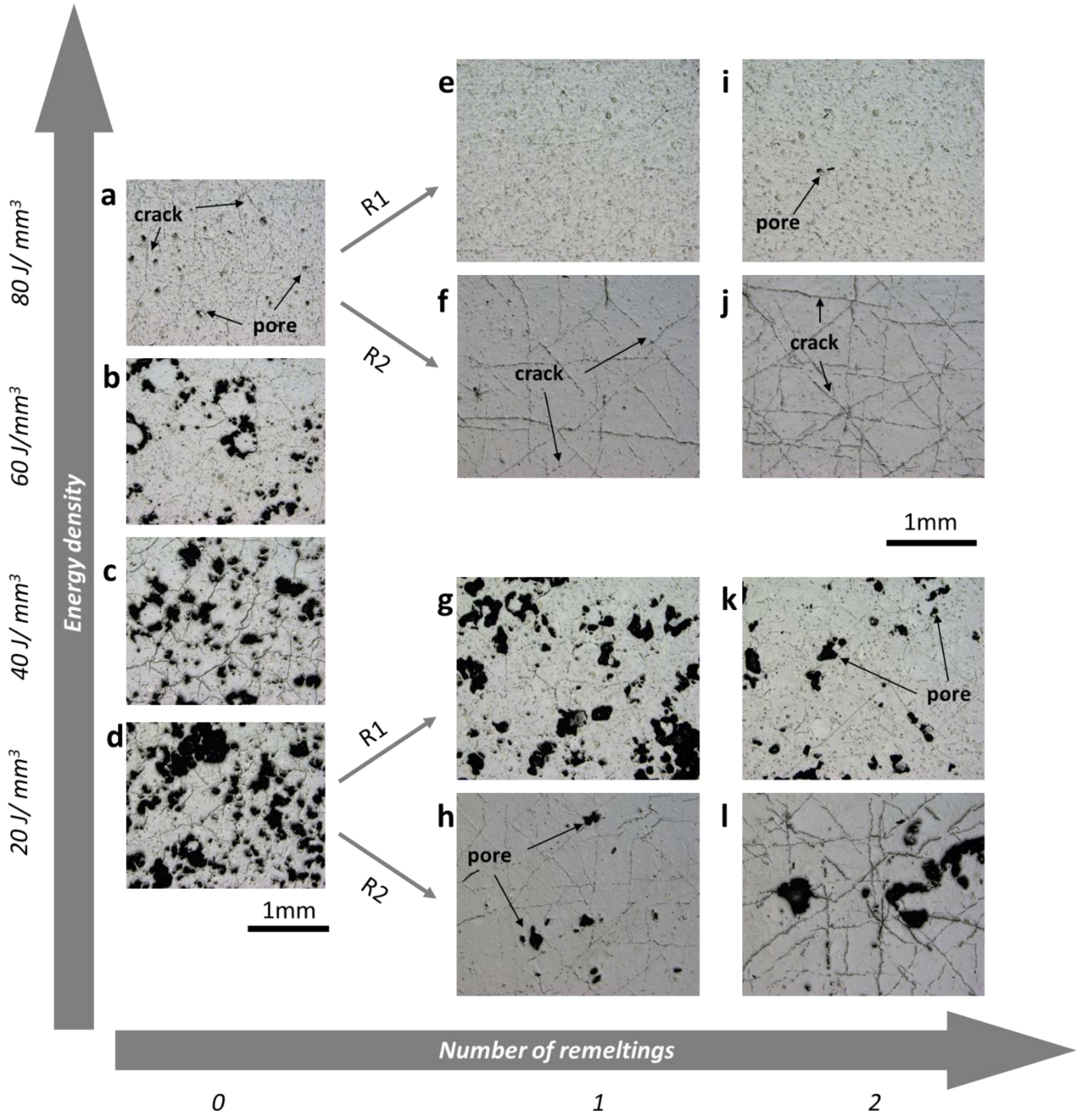

Figure III.5 Light microscopy micrographs of parts manufactured with different process parameters and number of remelts: (a-d)as-built parts; (e) 80 J/mm^3 + R1; (f) 80 J/mm^3 + R2; (g) 20 J/mm^3 + R1; (h) 20 J/mm^3 and + R2; (i) 80 J/mm^3 + 2x R1; (j) 80 J/mm^3 + 2x R2 parameters; (k) 20 J/mm^3 + 2x R1 parameters; (l) 20 J/mm^3 + 2x R2.

For the majority of the parts rendered, the size of the pores decreases with applied remelting strategy. However, some combinations of first melting parameters and additional remelting resulted in a reduction in the number of pores while increasing their size. This phenomenon was mainly observed for parts fabricated at lower energy densities used for SM. It can be explained by the presence of lack-of-fusion zones which are observed for the parts produced with lower energy densities, which is likely due to narrower and shallower melt pools.

It was reported by Dong et al. (2021) and Liu et al. (2021) that relatively low energy densities leads to poor fusion quality of laser tracks and massive lack-of-fusion zones were observed. As a result, the porosity seen in the parts manufactured with low energy densities is generated due to the incomplete fusion of the metal powder during laser scanning and the creation of lack of fusion. Thus, it can be concluded that the observed porosity results from the lack of fusion is correlated with decreasing energy density. This effect is even more obvious for additive manufacturing systems where the laser exposure scanning track in the point distance mode in contrast to systems where the laser is working in a constant mode.

Wang et al. (2019) found that the increase of the energy density enhances microstructural homogeneity of the material and the disappearance of lack-of fusion effects; however, spherical pores arise. High energy densities generate excess heat input that induces material evaporation. When the material evaporates the melt pool collapses, and spherical pores are formed. The process is called key-hole type melting and was previously reported by Ali et al. (2017); Liu et al. (2021); and Trapp et al. (2017). However, high energy input affects dimensional inaccuracy due to the phenomenon of surface adhesion of partially melted powder. Moreover, as described in previous studies by Chmielewska et al. (2019) and Tang et al. (2020), significant deformation of the fabricated parts has been observed under a high energy deposition fabrication process. Therefore, in this study high energy densities have been replaced by remelting scanning strategies in order to eliminate formation of high-temperature defects and prevent dimensional inaccuracy.

Furthermore, cracks are visible for both SM and remelted parts. For R1 parameters, both the first and second remelting cause a significant reduction in the number of cracks or their complete elimination. For R2 parameters, the number of cracks visible in the material increases with an increasing number of remelts. Moreover, the cracks became distinct with large widths and lengths as a result of increasing the number of remelts. The emergence of the cracks may be related to the phenomenon of thermal stress during LPBF fabrication. Ali et al. (2017); Guo et al. (2019); Leuders et al. (2013); and Shi et al. (2020) have observed that when laser power and scanning velocity are high, rapid solidification and a large thermal gradient occur, resulting in high thermal stresses and thus the creation of cracks. With the lower laser power and scanning speed, the solidification rate and thermal gradient are lower, thus lower thermal stresses occur or can be completely eliminated. This phenomenon is noticeable in the applied R1 and R2 remelting with the same energy densities generated by different values of the scanning speed and laser power. The scanning velocity and laser power for R2 was three times higher than in R1. Consequently, in the case of R2 remelting more cracks were generated, while R1 remelting eliminated cracks. It can be concluded that laser power as well as the scanning speed should be well balanced to obtain low porosity and crack-free microstructure.

The densities calculated on the basis of microscopic observations correlates with different energy densities for all melting strategies are presented in Figure III.6. The application of the remelting process improves material density and allows for fabrication of the parts with the density of up to 98.35%. Material density improves with higher energy densities of the first melting.

Remelting R1 resulted in higher densities of parts LPBF fabricated from Ni and Ti elemental powders than R2. This phenomenon may be related to the aforementioned higher temperature gradient in R2 remelting compared with R1. An inverse relationship is observed between the value of energy density and porosity. For the parts fabricated by SM with energy density below 20 J/mm^3 high porosity and low material density, below 75%, was observed. Moreover, the use of R2 remelting resulted in significant cracks expansion, and an increase in cracks with the increasing number of remelts, as depicted Figure III.5. Ali et al. (2017); Guo et al. (2019); Leuders et al. (2013); and Shi et al. (2020) have stated that due to the presence of increased thermal gradient, thermal stresses are generated. As a consequence, cracks generated by the thermal stresses increased significantly and led to part failure. The failed parts were excluded from the studies. Since the R2 remelting strategy did not provide good printability results, it was excluded from further investigation.

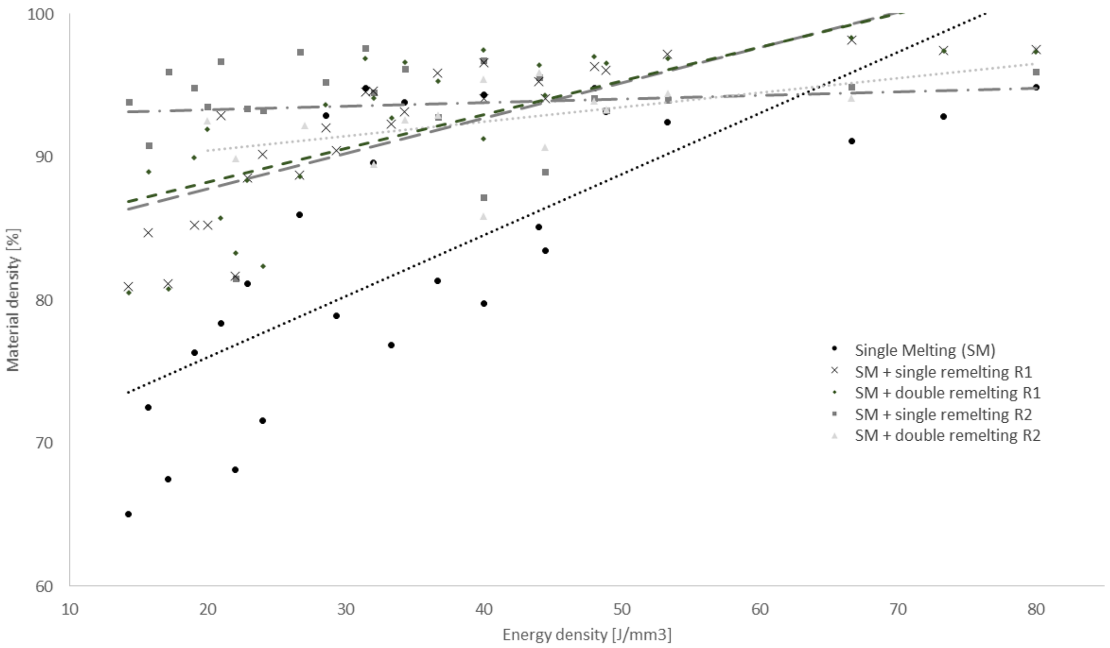

Figure III.6 Relationship between relative density and energy density for NiTi manufactured with elementally blended powders.

3.3.4. Scanning electron microscopy analysis

The chemical composition homogeneity of the parts was further studied with SEM BSE observations and EDS analysis (Figure III.7). The intensity of the BSE signal is strongly related to the atomic number (Z) of the specimen. Brighter BSE intensity correlates with greater average Z in the part, and dark areas have a lower average Z. Accordingly, the bright-shaded regions in Figure III.7 are Ni-rich, while dark-shaded are Ti-rich. Homogeneity in the presented study is defined as the uniform distribution of Ni and Ti elements in the LPBF-rendered part and is observed as lower phase contrast in BSE images. Chemical composition homogeneity was observed to increase with the number of remelts. In order to further determine the chemical homogeneity of specimens, EDS measurements were performed. These measurements are shown in Figure III.7 where Ni and Ti atoms are more homogeneously distributed in a parts remelted twice, relative to the SM parts. The influence of the SM parameters, especially the value of energy density, on the homogeneity of the parts was examined as well. No significant differences in the homogeneity of parts manufactured with different energy densities in the first melting were observed in a range of 80-20 J/mm^3, were observed, for both single melt and remelted parts. It should be noted that inhomogeneity did not disappear completely in any of the remelting processes. That homogeneity increases with increasing energy density was previously described by Zhao et al.(2020) and Wang et al. (2019). Nevertheless, in above-mentioned studies, heat treatment was applied to increase material homogenization and elimination of unwanted phases.

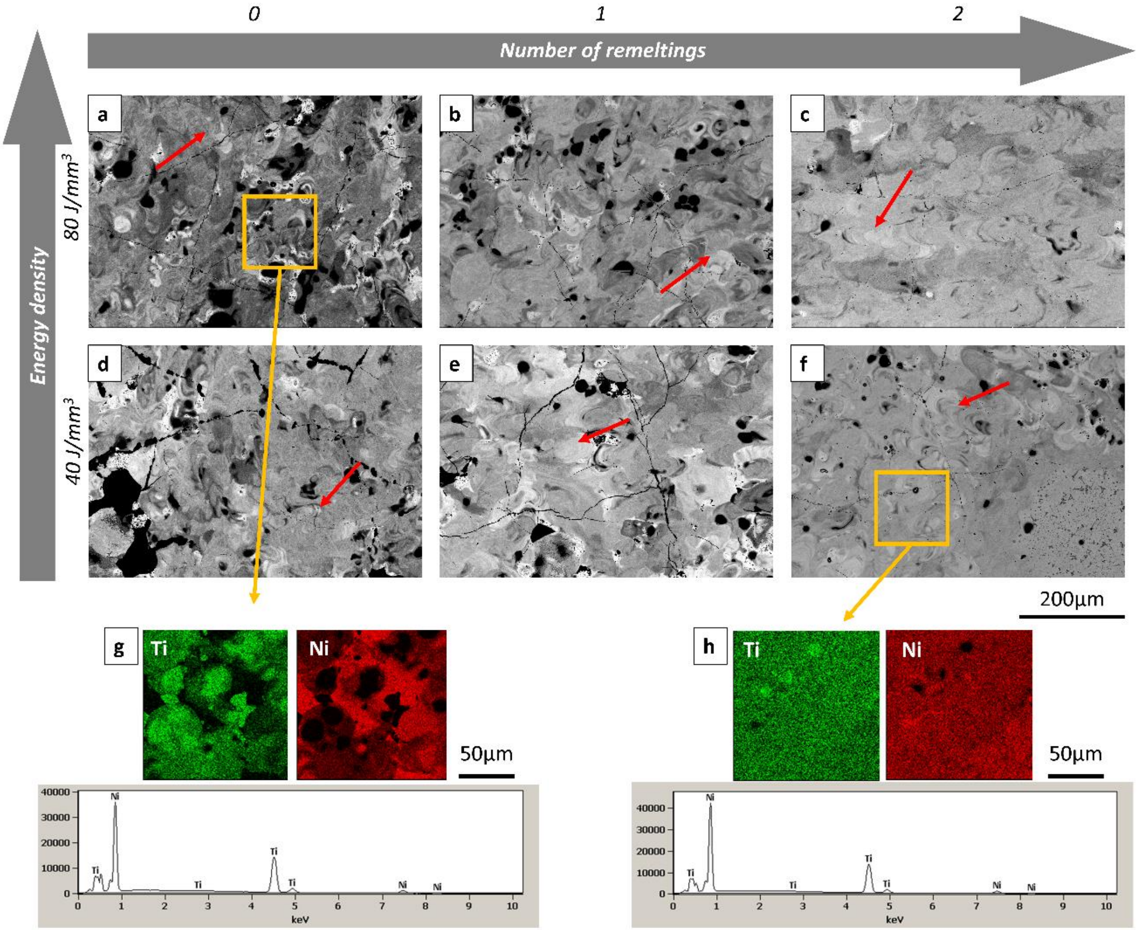

Figure III.7 SEM BSE observations of parts single melt process (a, c) and remelted once (b, e) and twice (c, f) with R1 parameters, EDS maps of parts single melt (g) and remelted twice with R1 parameters (h); red arrows indicate meltpools.

3.3.5. X- ray Diffraction

In order to identify the phases, X-ray diffraction analysis was performed on single melt and remelted parts (Figure III.8 XRD diffractograms of parts fabricated with single melting and R1 single and double remelting.Figure III.8). Multiple phases were identified. This analysis showed that in all parts, regardless of the power and amount of remelting, there are NiTi (B2) and (B19’), $NiTi_2$, Ni_3Ti_4, Ni_3Ti phases. Although, as reported by Halani and Shin (2012) and Wang et al. (2019), the peaks of some phases, as NiTi (B19’) and Ti_2Ni, or NiTi (B2) and Ni_3Ti, overlap each other. The presence of multiple phases is confirmed with the results of the BSE observations and EDS analysis, which revealed high phase contrast and chemical composition differences in the fabricated parts. However, as demonstrated by Zhao et al. (2020), high energy densities, above 375 J/mm^3, applied to fabricate elementally blended NiTi, eliminate the presence of Ni_4Ti_3 and Ni_3Ti unwanted secondary phases. Thus, it can be concluded, that lower energy densities, below 80 J/mm^3, and remelting strategies, are not sufficient to blend the elemental components completely and post- processing heat treatment should be applied.

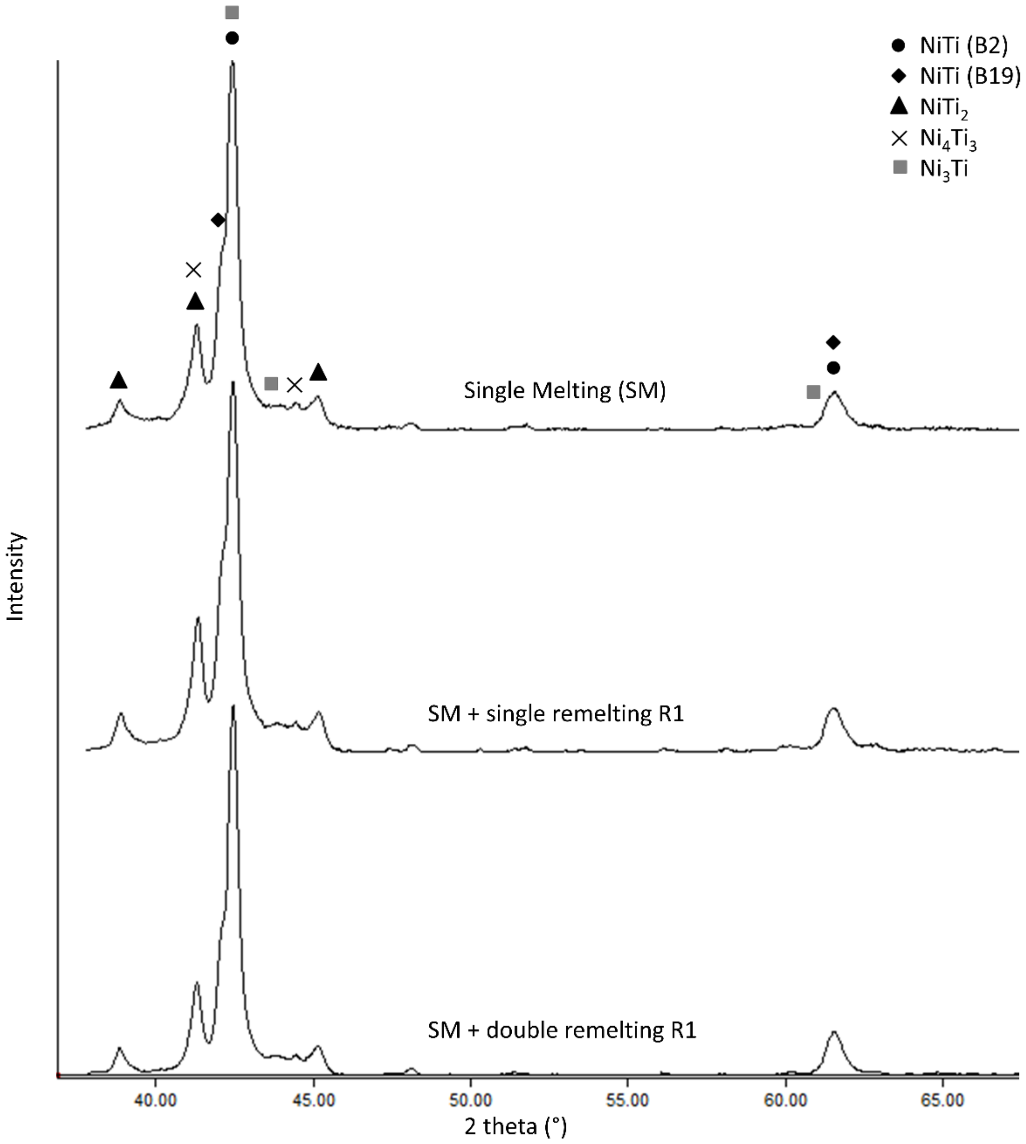

Figure III.8 XRD diffractograms of parts fabricated with single melting and R1 single and double remelting.

Stress measurement was performed on parts fabricated with single melting and R1 single and double remelting. All stress measurements carried out using the diffraction methodology were performed according the EN-15305 standard and were conducted for the austenitic NiTi phase with cubic structure (space group: Pm-3m) and lattice parameter a_0=3.005 Å. The expected penetration depth of Cr radiation into this material was about 20µm. In order to realize the analysis of experimental data, a background cut-off was performed, for which the form of a linear function was adopted. The distribution of the diffracted radiation was approximated by a Gaussian function. In the stress analysis, the following values of elasticity constants were assumed: s_1=-3.98 1/TPa and ½s_2=16.02 1/TPa. The results were calculated to obtain the principal stresses σ_{11} and σ_{22}, their uncertainties $\Delta\sigma_{11}$ and $\Delta\sigma_{22}$ and reduced Huber-von Mises stresses σ_{red} (with uncertainty σ_{red}). The results for these stress measurements are summarized in Table III.4.

The results indicate that the lowest stresses are present in single melted (SM) parts that also have the highest number of cracks and pores (Table III.4). Therefore, it can be concluded that the residual stresses generated by the high thermal gradient (i.e., uneven heat deposition and cooling) between melt pool and powder bed have been released at the location of cracks. Likewise, the lowest residual stresses are presented in double melted (SM+ single remelting R1) part which has the lowest number of cracks and pores, indicating that the remelting closed the cracks but did not increase the stress enough to cause further cracks. Furthermore, a third melting run (SM + double remelting R1) resulted in an increased number of cracks. This was likely due to an increase in the heat input generated by the third melt run as well as reduced residual stresses (stresses were released at the site of cracks).

Table III.4 XRD stress measurement results of parts fabricated with single melting and R1 single and double remelting LPBF.

Part no.	**σ11 [MPa]**	**Δσ11 [MPa]**	**σ22 [MPa]**	**Δσ22 [MPa]**	**σred [MPa]**	**Δσred [MPa]**
Single Melting (SM)	50.10	30.85	1.40	35.88	49.41	13.67
SM + single remelting R1	236.7	31.10	214.20	31.10	226.29	30.98
SM + double remelting R1	181.10	57.35	157.70	63.44	170.61	59.34

3.3.6. Microhardness

Figure III.9 shows the variation of microhardness for SM and R1 remelted parts. The microhardness of the material presented in this study varied in a range from 487 to 495 HV, depending on implemented number of melts. Furthermore, it can be observed that the measurement error decreases as the number of remelts increases and is the lowest for parts remelted twice. This may be due to the fact, that SM parts and parts remelted once can have more unmixed regions which are Ni rich or Ti rich. This reduction in the measurement error is ascribed to the improvement of microstructure homogeneity. Moreover, microhardness of LPBF-rendered parts using elemental Ni and Ti powders is higher than for LPBF parts rendered from pre-alloyed NiTi powders as well as conventional fabrication techniques. The average hardness value for the martensite phase of as-cast NiTi, reported by Shishkovsky et al. (2012), is 340-440 HV, whereas the average hardness for the Ti_2Ni phase, reported by Zhang et al. (2013), is 700 HV. For LPBF-manufactured NiTi, different factors influence the microhardness level, including material composition, powder type (pre-alloyed or elementally blended), laser parameters, and post-heat treatment. Moreover, due to the high cooling rates associated with LPBF, high thermal stresses are known to occur. Elahinia et al. (2016) have stated that thermal stress enhances microhardness significantly. In case of NiTi alloy manufactured by LPBF from elementally blended powders, the presence of many different phases is an additional factor influencing the hardness.

It was reported by Zhang et al. (2013) that parts LPBF-rendered from elementally blended Ni and Ti powders with composition of $Ni_{55}Ti_{45}$ (which is close to our composition) exhibit microhardness that is dependent on scanning parameters, with the scanning parameters values in their studies varied an average of 360-460HV. Research presented by Wysocki et al. (2017), describes an increase of microhardness that they relate to oxygen pick-up during LPBF fabrication. Kwasniak et al. (2016) and Sun et al. (2013) claim that oxygen is responsible for solid solution strengthening, and therefore, can enhance mechanical properties of titanium alloys. The phenomenon of solid solution strengthening of additively manufactured titanium and its alloys was also reported by Wysocki et al. (2018, 2017), Velasco-Castro et al. (2019) and Pauzon et al. (2021).

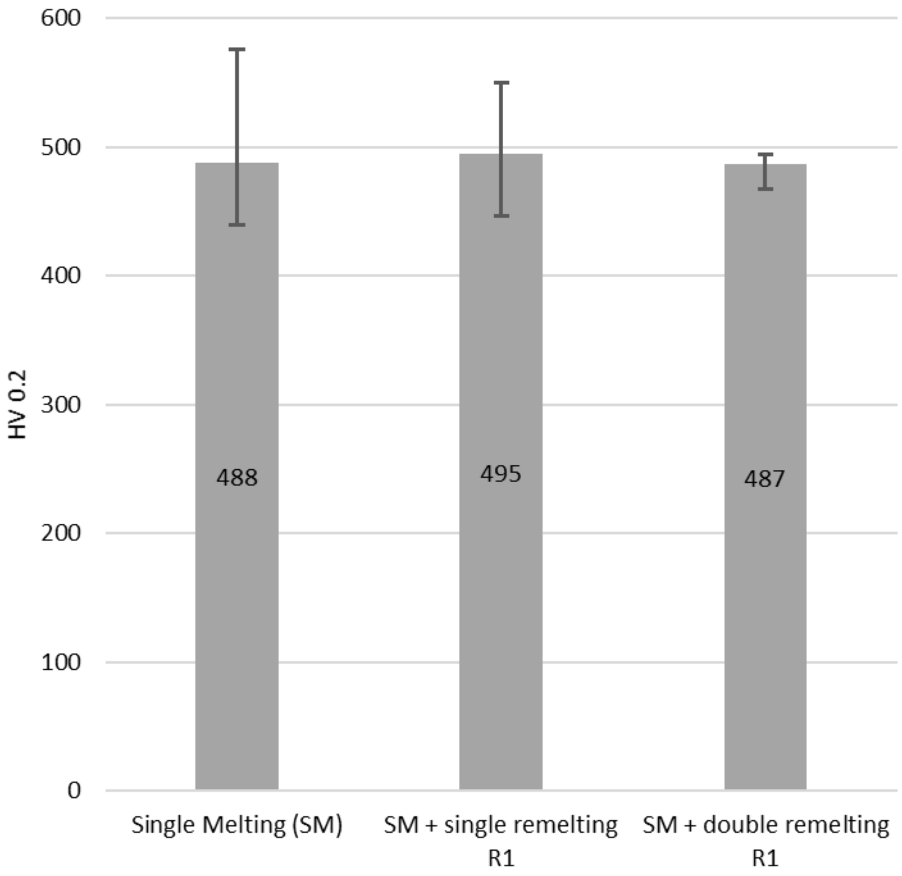

Figure III.9 Microhardness of parts fabricated with single melting and R1 single and double remelting.

3.3.7. Wavelength Dispersive X-ray Fluorescence chemical composition analysis

Chemical composition of parts fabricated with single melting and R1 single and double remelting was analysed using Wavelength Dispersive X-ray Fluorescence (WD-XRF). The influence of the number of melts on the chemical composition (e.g., nickel evaporation) was studied. The initial content of Ni in batch powder was 55.7 wt. %. The WD-XRF data showed that the amount of nickel in the material decreases with an increasing number of melt runs (Figure III.10). The highest decrease in nickel content was observed after the first melting (1.6 wt. %), and each subsequent melt run resulted in a smaller reduction in the amount of nickel, which was 0.6 wt. % and 0.4 wt. % for the first and second remelting, respectively. The decrease in the amount of evaporated nickel might be due to the fact that pure elements were alloyed after first melting (no peaks of pure Ti and Ni were detected on XRD) and were more thoroughly blended after each melt run, and the evaporation of nickel from NiTi alloy is less than that of pure nickel [212]. Moreover, the number of melt runs and Ni evaporation can also affect the changes in martensitic and austenitic transformation temperatures of NiTi. These differences were described by Chmielewska et al. (2021).

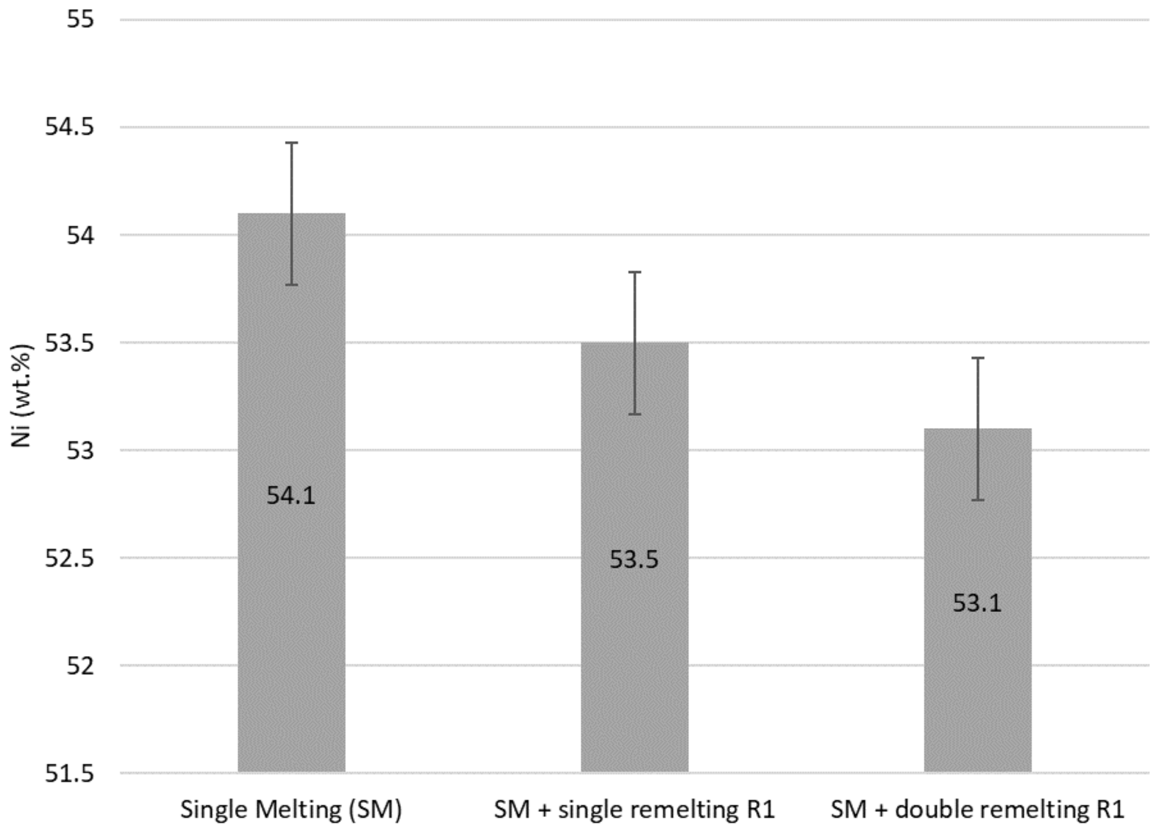

Figure III.10 Chemical composition (Ni content) of parts fabricated with single melting and R1 single and double remelting; the measurement error was ±0.33 wt.%.

3.3.8. Oxygen content analysis

An oxygen content study was performed to determine whether the number of melt runs influences oxygen pick-up. An average presence of 0.54 wt.% of the oxygen is observed across all parts in our study (Table III.5). The oxygen level in the building chamber during the fabrication process was below 0.3 vol. %. Additionally, the elemental nickel elemental powder is claimed to be free of oxygen by the vendor (Table III.1) and titanium elemental powders contain <0.18% of the oxygen (Table III.2). Therefore, it can be concluded that oxygen that was introduced into the parts during the first melt run, and subsequent melt runs did not influence the oxygen level in the material

Table III.5 Oxygen content in parts fabricated with single melting and R1 single and double remelting; the measurement error was ±0.1 wt.%.

	Single Melting (SM)	**SM + single remelting R1**	**SM + double remelting R1**
oxygen content (wt.%)	0.54	0.54	0.54

3.3.9. µCT and Archimedes density measurement

The density of parts fabricated with single melt and R1 single and double remelting was evaluated by Archimedes density measurement (Figure III.11) and µCT (Figure III.12). To provide high quality of µCT scans, a section of 3 x 3 x 3 mm of each part was analysed. Archimedes density measurement showed that parts fabricated with single melting R1 single and R1 double remelting had a density of 95.88, 98.70, and 99.02%, respectively, versus the theoretical value for NiTi alloy. The calculated density based on µCT for these same three study groups was 94.95, 98.33, and 99.17, respectively. Moreover, µCT results showed that pores present in the parts as irregular shapes. The densities measured with both methods did not significantly differ from each other (differences were below 0.93%). Both analyses showed that remelting improves the density of parts fabricated from elemental Ni and Ti powders, and that the density increases with an increasing number of melt runs.

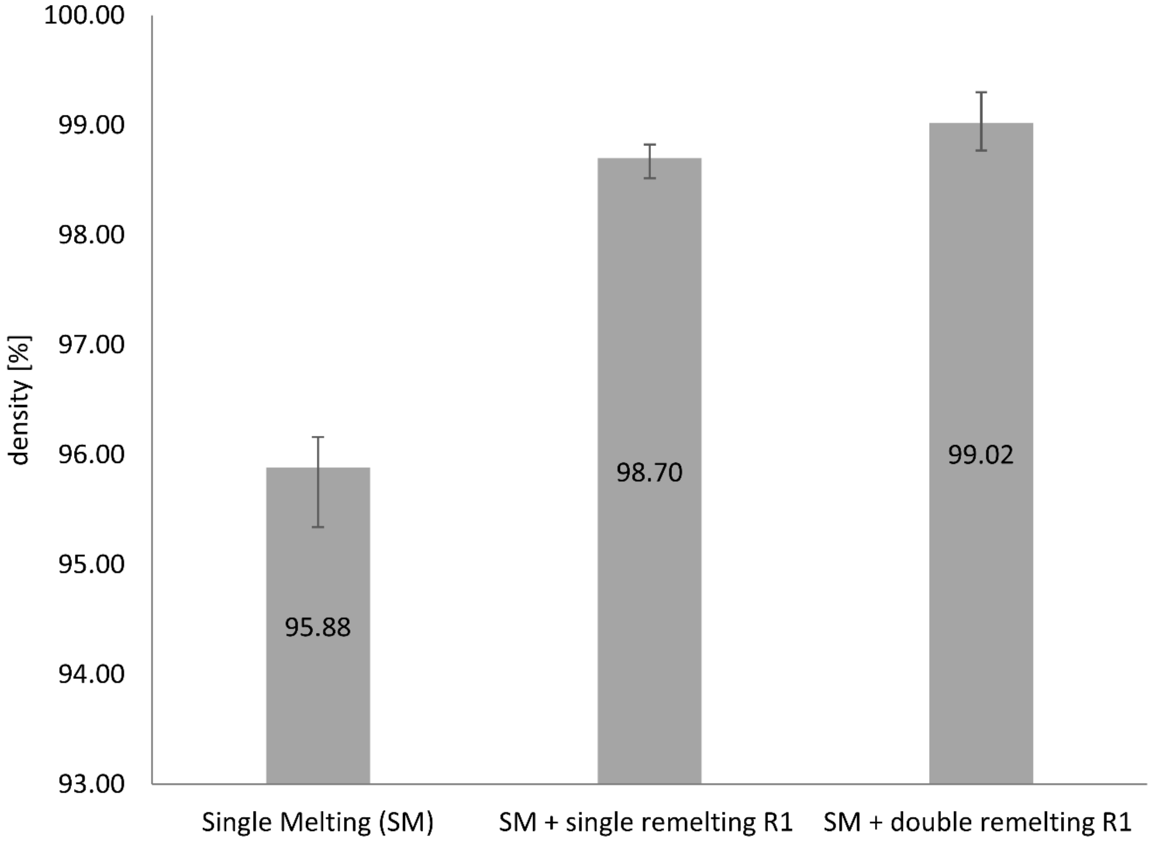

Figure III.11 Archimedes density measurement of parts fabricated with single melting and R1 single and double remelting.

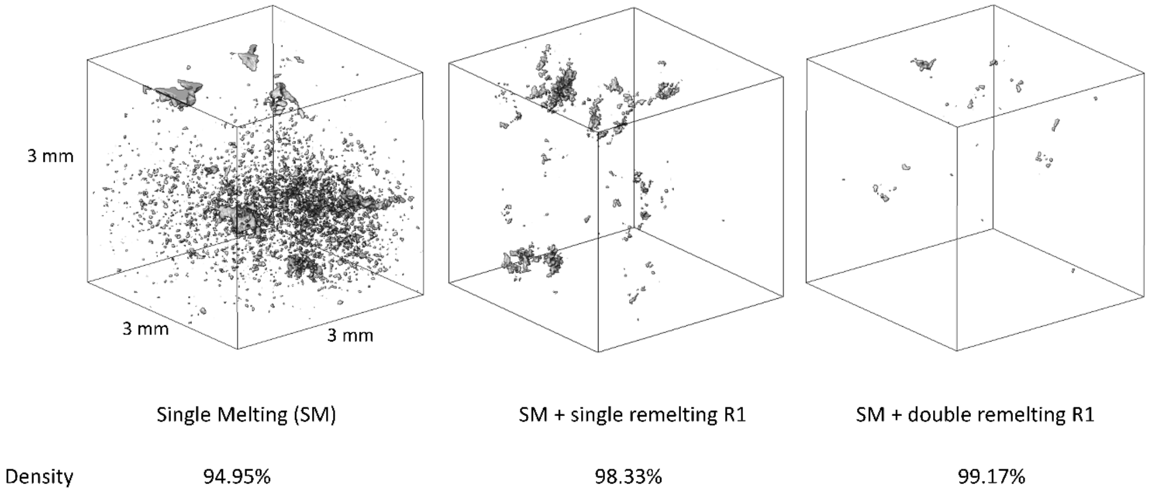

Figure III.12 Density analyses of μCT-scans of sample parts fabricated with single melting and R1 single and double remelting.

3.4. Conclusions

For the first time, Ni and Ti elementally blended powders were used to fabricate NiTi parts via LPBF using remelting strategies. The influence of the number of remelts, with the same energy density (J/mm^3) but obtained with different laser process parameters (i.e., laser power, scanning speed), on final NiTi part homogeneity was studied. The study showed that using remelting parameters with the same value of the energy density but resulting from different values of laser power (25 and 75W) and scanning speed (1000 and 3000 mm/s), give radically different results. Remelting was observed to significantly reduce porosity. The relatively high density, revealed with μCT reconstruction estimated at value at 99.17%, was observed for parts where remelting was applied. Additionally, remelting R1, with lower laser power and scanning speed, eliminated cracks, while remelting R2, with higher laser power and scanning speed, generated a high thermal gradient that is expected to have promoted the formation and growth of cracks. Increased NiTi homogeneity was observed to correlate with increasing number of remelts. However, multiple phases were observed regardless of the number of remelts, thus post-processing heat treatment should be investigated in future research on LPBF remelting of Ni and Ti elemental powders. The microhardness of the parts remelted twice was more uniform than parts produced from a single melt or remelted once. XRD stress measurement suggested that residual stress and crack occurrence was reduced in LPBF processes that include remelting. WD-XRF chemical composition analysis showed that the highest amount of Ni evaporated during first melt run (single melting) and subsequent melt runs did not influence Ni evaporation significantly. In conclusion, remelting was observed to significantly improve the blending of the Ni and Ti elemental powders during LPBF compared with single melt processes; however, it did not eliminate phase composition inhomogeneity entirely.

Appendix 1

Optimization procedure and optimization parameters

The optimization procedure was performed by fabrication of the samples with 5 sets of process parameters stated in Table III.6-13. The first set of process parameters showed in Table III.6. was based on the process parameters used for processing of the pre-alloyed NiTi powder which optimization and characterization are a part of another manuscript submitted to the Journal of Materials Processing Technology.

Parameters no. 1

In the first set of the parameters, single melting of each layer was performed with a wide range of energy densities (17-198 J/mm^3), and low laser powers in a range of 32.5W – 42.5 W. The low laser powers are in our experience beneficial for the defect free fabrication of the titanium alloys, that was described in our previous study [206]. While a few parameters form the set of Parameters no. 1 (energy densities lower than 70 J/mm^3) allowed for fabrication of samples with acceptable quality (Figure III.13), majority of them (fabricated with energy densities higher than 70 J/mm^3) were failed due to the overheating and excessive melting. The dark overheated samples visible on the Realizer SLM50 building platform are shown in Figure III.13. The microstructure of representative samples fabricated with some of Parameters no. 1 (1, 5, 8, 12) are shown in Figure III.14. Based on the obtained results, modification of the Parameters no. 1 was implemented, and new set of parameters (Parameters no. 2) was determined.

Table III.6. A1 Parameters no. 1 (Single Melting - SM).

No.	t [mm]	h [µm]	pd [µm]	ext [µs]	v [mm/s]	P [W]	E [J/mm^3]
1	25	120	10	20	500	32.5	22
2	25	120	10	40	250	32.5	43
3	25	120	10	60	167	32.5	65
4	25	120	10	80	125	32.5	87
5	25	120	10	100	100	32.5	108
6	25	120	10	120	83	32.5	130
7	25	120	10	140	71	32.5	152
8	25	150	10	20	500	32.5	17

9	25	150	10	40	250	32.5	35
10	25	150	10	60	167	32.5	52
11	25	150	10	80	125	32.5	69
12	25	150	10	100	100	32.5	87
13	25	150	10	120	83	32.5	104
14	25	150	10	140	71	32.5	121
15	25	120	10	20	500	42.5	23
16	25	120	10	40	250	42.5	45
17	25	120	10	60	167	42.5	85
18	25	120	10	80	125	42.5	113
19	25	120	10	100	100	42.5	142
20	25	120	10	120	83	42.5	170
21	25	120	10	140	71	42.5	198
22	25	150	10	20	500	42.5	28
23	25	150	10	40	250	42.5	57
24	25	150	10	60	167	42.5	85
25	25	150	10	80	125	42.5	91
26	25	150	10	100	100	42.5	113
27	25	150	10	120	83	42.5	136
28	25	150	10	140	71	42.5	159

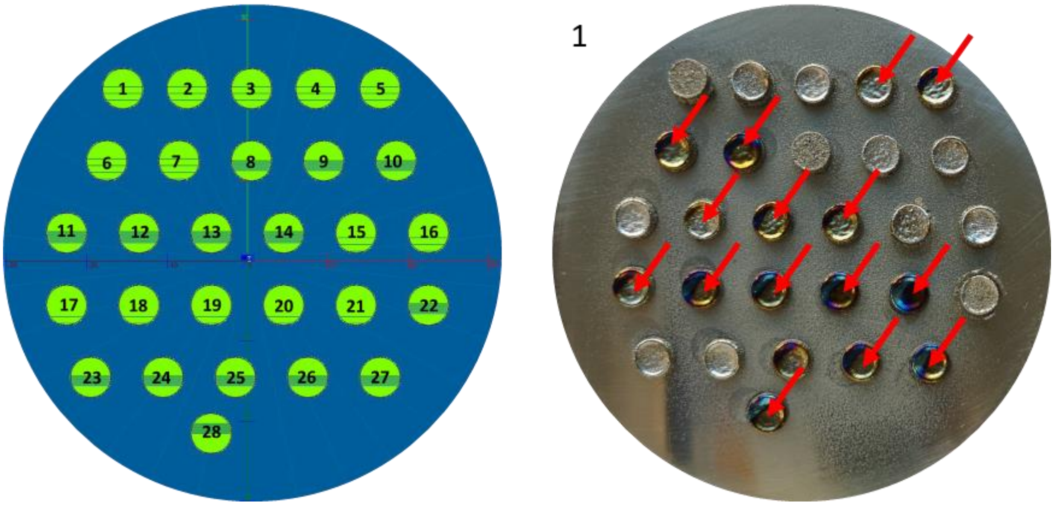

Figure III.13. A1 The Realizer SLM50 building platform with NiTi samples made with Parameters no. 1 set. Majority of samples is overheated (red arrows).

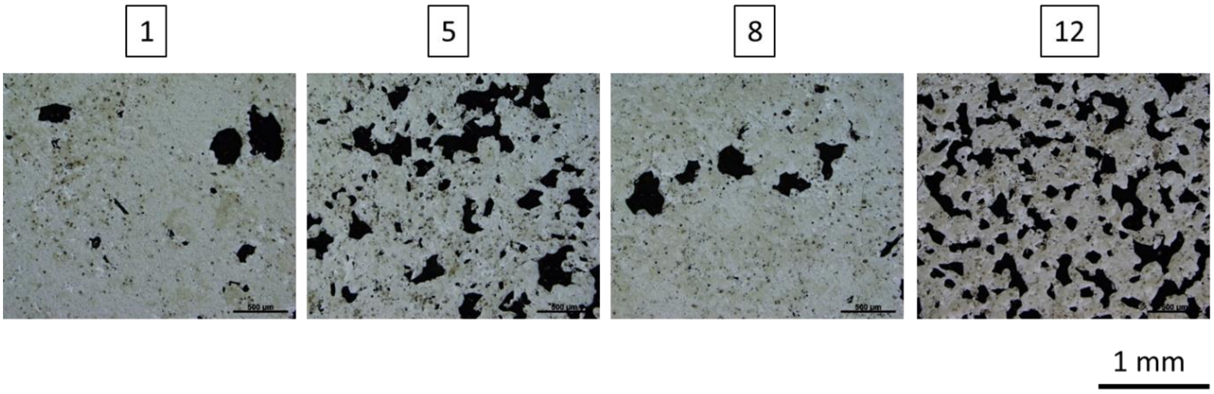

Figure III.14. A1 Microstructure of samples no. 1, 8, 15 and 22 fabricated with Parameters no. 1.

Based on the obtained results, modification of the Parameters no. 1 was implemented.

Parameters no. 2

The results of samples fabricated with Parameters 1. showed that the best quality was obtained for samples fabricated with energy densities below 70 J/mm^2. Thus, the parameters from first set of parameters (Table III.6) were modified by decreasing laser power and increasing point distance to utilise energy densities lower than 70 J/mm^3 (Table III.7). All single melted samples with parameters 2.1. (Single Melting) were successfully fabricated however the porosity of these samples was significant so we have decided to add additional process variations to decrease porosity (additional meltings with rotation within successive melt runs). These process variations (scanning strategies) are sets numbered 2.2-2.5.

List of the variations (scanning strategies) for the Parameters no. 2:

2.1.Single melting

2.2.Double melting: 2x single melting (45° rotation)

2.3.Double melting: Premelting (P/R) and single melting (45° rotation)

2.4.Double melting: Single meltings and remelting (P/R) (45° rotation)

2.5.Double melting: single melting and remelting (P/R) (no rotation)

First variation of the process Parameters 2.1. was adding additional scanning with the same process parameters. The double melting with Parameters no. 2 is 2x single melting (45 rotation) which is noted as Parameters 2.2. The macroscopic observation showed that

Parameters 2.2. caused overheating for the majority of the samples, while microscopic observations of samples made with Parameters 2.2. showed increase in porosity compared to single melted (2.1) samples. Majority of the samples failed in early stage of fabrication. Thus, for the next set of samples (Parameters 2.3-2.5) additional scanning with lower energy density was applied. For samples 2.2-2.4, the rotation of 45° between first and subsequent melt run was applied. The results showed that after producing only a few layers, the surface roughness was very high, and the side cracks presented on some samples caused them to wrap and detach for the substrate. Thus, further production was not possible due to the risk of wiper(coater) damage. Only a few samples were successfully fabricated, however they possessed high porosity (Figure III.16). We have observed the phenomena of welding contamination collection described in the manuscript (section 3.2; Figure III.15). Thus, for the 2.5 set of parameters no rotation was applied. It allowed for successful fabrication of majority of the samples and porosity decrease compared to single melted (2.1) samples. Based on this observation we decided to not apply rotation in further study.

Figure III.15. A1 Parameters no. 2 (scanning strategies 2.1-2.5.)

No.	**t [mm]**	**h [µm]**	**pd [µm]**	**ext [µs]**	**v [mm/s]**	**lp [W]**	**E[J/mm^3]**
1	25	120	20	20	1000	27.5	9
2	25	120	20	40	500	27.5	18
3	25	120	20	60	333	27.5	28
4	25	120	20	80	250	27.5	37
5	25	120	20	100	200	27.5	46
6	25	120	20	120	167	27.5	55
7	25	120	20	140	143	27.5	64
8	25	150	20	20	1000	27.5	7
9	25	150	20	40	500	27.5	15
10	25	150	20	60	333	27.5	22
11	25	150	20	80	250	27.5	29
12	25	150	20	100	200	27.5	37
13	25	150	20	120	167	27.5	44
14	25	150	20	140	143	27.5	51
15	25	120	20	20	1000	37.5	13
16	25	120	20	40	500	37.5	25
17	25	120	20	60	333	37.5	38

18	25	120	20	80	250	37.5	50
19	25	120	20	100	200	37.5	63
20	25	120	20	120	167	37.5	75
21	25	120	20	140	143	37.5	88
22	25	150	20	20	1000	37.5	10
23	25	150	20	40	500	37.5	20
24	25	150	20	60	333	37.5	30
25	25	150	20	80	250	37.5	40
26	25	150	20	100	200	37.5	50
27	25	150	20	120	167	37.5	60
28	25	150	20	140	143	37.5	70

Table III.7. A1 Additional melting applied to Parameters no. 2 (scanning strategies 2.3-2.5)

No.	t [mm]	h [µm]	pd [µm]	ext [µs]	v [mm/s]	P [W]	E[J/mm^3]
(P/R)	25	150	10	20	500	27.5	15

Fabricated samples on the platforms along with platforms numbers and the marking of samples on the platforms are presented in Figure III.15.

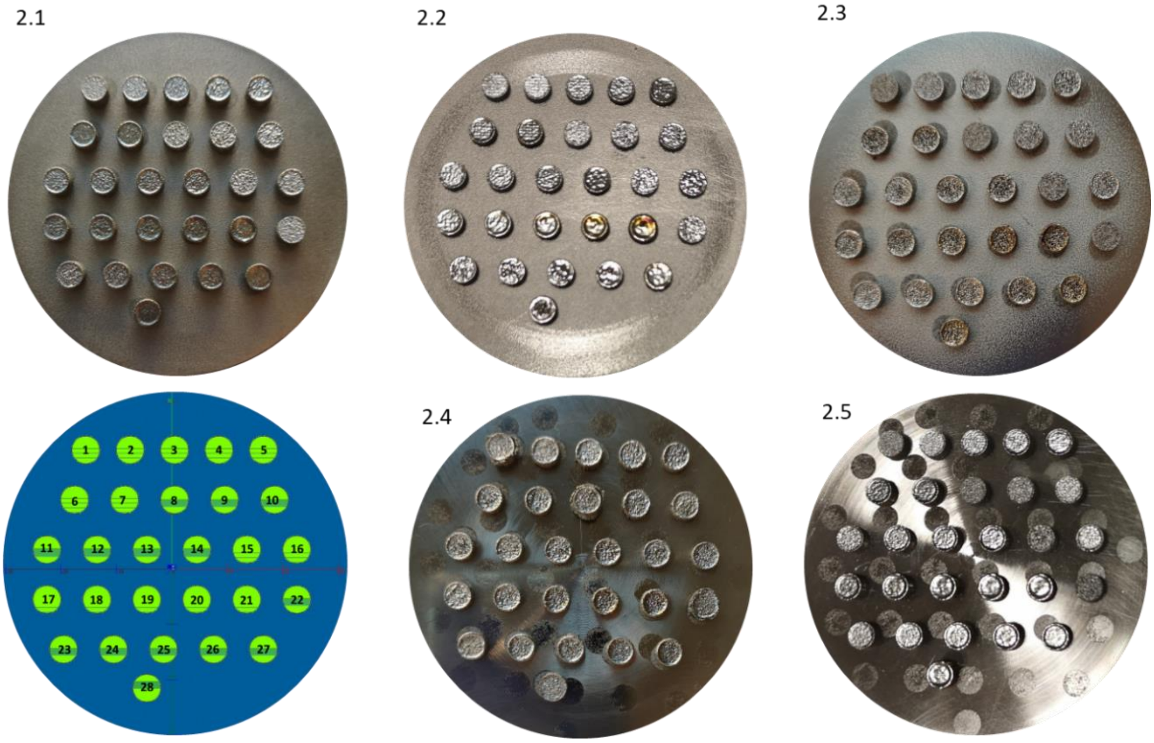

Figure III.16. A1 The Realizer SLM50 building platforms with NiTi samples made with set of Parameters no.2 with scanning strategies 2.1-2.5.

Metallographic observations of polished samples were performed (Figure III.17). Nevertheless, due to the high porosity and delamination some of the samples could not be removed from the platform in a form that allows the preparation of metallographic samples (samples were damaged, when removed from the building platform). The samples that could not be successfully removed from the platform were eliminated from further analysis. Moreover, the samples that failed in early stage of fabrication (after few layers) were not analysed.

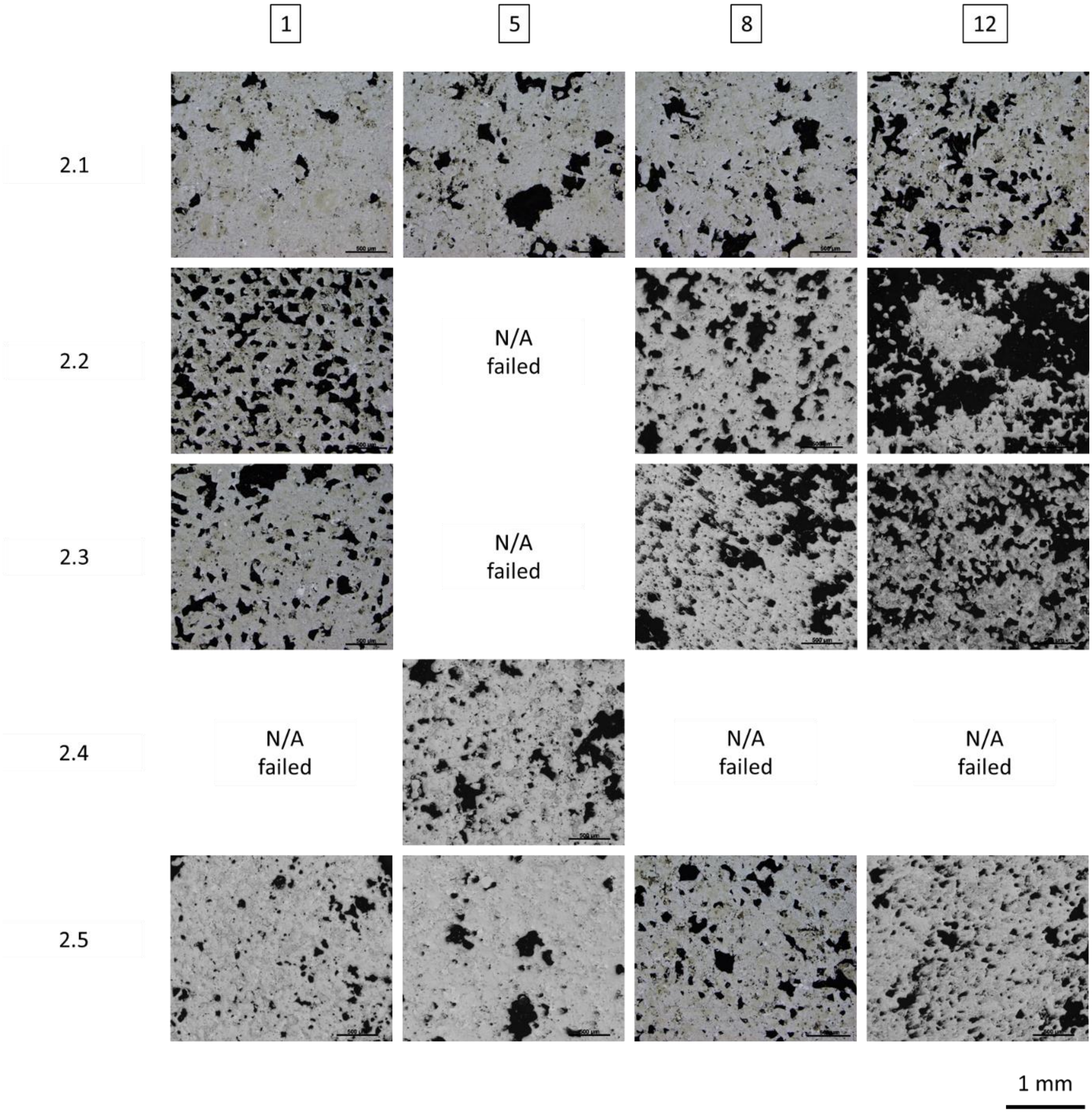

Figure III.17. A1 Microstructure of samples no. 1, 5, 8 and 12 fabricated with Parameters no. 2 and scanning strategies 2.1.-2.5.

Parameters no. 3

Based on obtained results for Parameters no. 1 and no. 2 we have selected new set of parameters. Followed modification compared to Parameters no. 2 was implemented:

- Hatch distance was decreased
- Energy density was decreased (below 60 J/mm^3)
- Scanning speed was increased

Different scanning strategies including single melting and multiple meltings (2-3 scanning of each layer) were applied. No rotation for these additional meltings (remeltings) was applied for Parameters no. 3. The scanning vector rotation of 45° was applied just between successive layers after spreading fresh powder (Figure III.1 in the manuscript). Six sets of platforms with samples were fabricated with Parameters no. 3 presented in Table III.8.

Firstly, single melting was performed (3.1) for 24 samples fabricated with parameters presented in Table III.8. Then, for scanning strategy 3.2 double melting was applied- each layer was scanned twice with the same parameters as first melt run (1-24 Table III.8). Results showed that the energy delivered to the material was to high and resulted in failure of most of the samples (overheating and delamination). Based on those results, we have determined new parameters for additional melting (Table III.9). Additional melting was performed before (premelting: 3.3) and after (remelting: 3.4) melting with the base (single melting) parameters (presented in Table III.8). Moreover, both premelting and remelting was also applied with base (single melting-Table III.8) parameters (3.5). Results showed that premelting did not provide good printability, thus in further studies only remelting was implemented. Triple melting, including single melting (parameters 1-24 Table III.8) and double remelting (parameters P/R Table III.9) was applied (3.6).

List of the variations (scanning strategies) for the Parameters no. 3 (no rotation for additional melting (remelting) before spreading fresh powder):

3.1.Single melting

3.2.Double melting: 2x single melting

3.3.Double melting: Premelting (P/R) and single melting

3.4.Double melting: Single meltings and remelting (P/R)

3.5.Triple melting: Premelting (P/R), single melting and remelting (P/R)

3.6.Triple melting: single melting and 2x remelting (P/R)

Table III.8. A1 Parameters no. 3 (scanning strategies 3.1-3.6).

No.	t [mm]	h [µm]	pd [µm]	ext [µs]	v [mm/s]	P [W]	E [J/mm^3]
1	25	50	10	20	500	37.5	60
2	25	50	20	20	1000	37.5	30
3	25	50	10	20	500	32.5	52
4	25	50	20	20	1000	32.5	26
5	25	50	10	20	500	27.5	44
6	25	50	20	20	1000	27.5	22
7	25	100	10	20	500	37.5	30
8	25	100	20	20	1000	37.5	15
9	25	100	10	20	500	32.5	26
10	25	100	20	20	1000	32.5	13
11	25	100	10	20	500	27.5	22
12	25	100	20	20	1000	27.5	11
13	25	120	10	20	500	37.5	25
14	25	120	20	20	1000	37.5	13
15	25	120	10	20	500	32.5	22
16	25	120	20	20	1000	32.5	11
17	25	120	10	20	500	27.5	18
18	25	120	20	20	1000	27.5	9
19	25	150	10	20	500	37.5	20
20	25	150	20	20	1000	37.5	10
21	25	150	10	20	500	32.5	17
22	25	150	20	20	1000	32.5	9
23	25	150	10	20	500	27.5	15
24	25	150	20	20	1000	27.5	7

Table III.9. A1 Additional melting applied to Parameters no. 3 (scanning strategies 3.3-3.7).

No.	**t [mm]**	**h [µm]**	**pd [µm]**	**ext [µs]**	**v [mm/s]**	**P [W]**	**E[J/mm^3]**
(P/R)	25	150	10	20	500	27.5	15

Fabricated samples on the platforms along with platforms numbers and the marking of samples on the platforms are presented in Figure III.18:

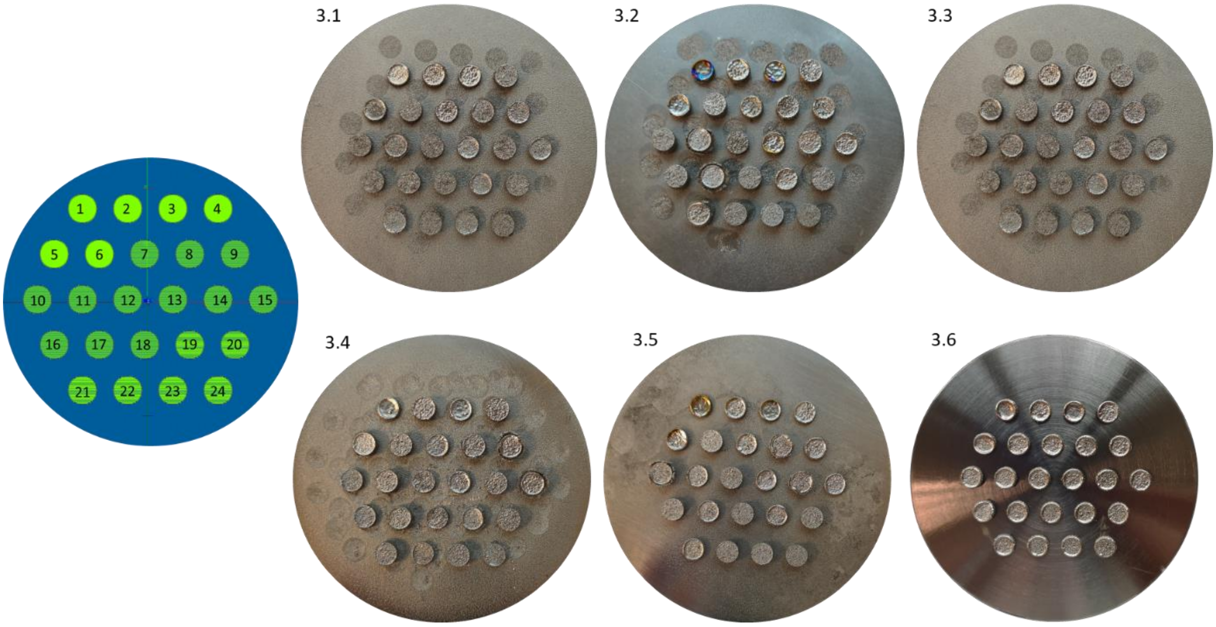

Figure III.18. A1 The Realizer SLM50 building platforms with NiTi samples made with set of Parameters no.3 with scanning strategies 3.1-3.6.

Metallographic observations of polished samples made with Parameters no. 3 and melting strategies 3.1.-3.6. are shown in Figure III.19. Nevertheless, due to the high porosity and delamination some of the samples could not be removed from the platform in a form that allows the preparation of metallographic samples (have been damaged, when removed from the building platform). The samples that could not be successfully removed from the platform were eliminated from further analysis. Moreover, the samples that failed in early stage of fabrication (after few layers) was not analysed.

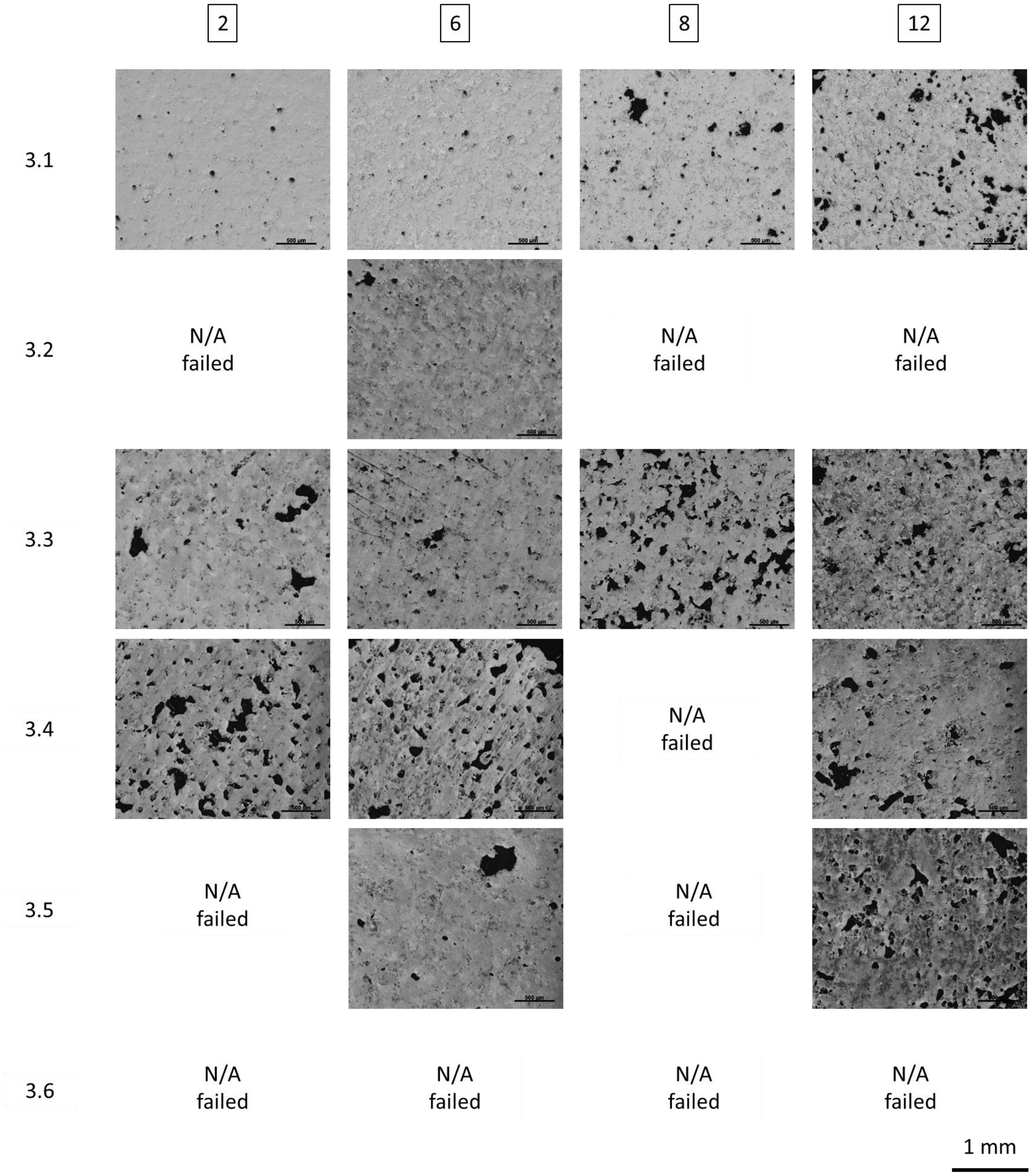

Figure III.19. A1 Microstructure of samples no. 2, 6, 8 and 12 fabricated with Parameters no. 3 and scanning strategies 3.1.-3.6.

Parameters no. 4

Based on obtained results for Parameters no. 3 we have selected new set of Parameters 4 which aim to further decrease of samples porosity. Followed modification compared to Parameters no. 3 was implemented:

- Hatch distance was decreased
- Laser power was decreased and increased

Moreover, two different parameters of remelting, R_a and R_b, was applied (Table III.11).

Firstly, single melting was performed (4.1) for 24 samples fabricated with parameters presented in Table III.10. Secondly, remelting with parameters R_a and R_b, was performed one, two and three times for scanning strategies 4.2-4.7.

As previously, no rotation (between first and following scanning) was applied for any of scanning strategy. The rotation of 45° scanning vector between successive layers was applied (Figure III.1 in the manuscript).

List of the variations (scanning strategies) for the Parameters no. 4 (no rotation applied):

3.1.Single melting

3.2.Single melting and remelting R_a

3.3.Single melting and 2x remelting R_a

3.4.Single melting and 3x remelting R_a

3.5.Single melting + remelting R_b

3.6.Single melting + 2x remelting R_b

3.7.Single melting + 3x remelting R_b

Table III.10. A1Parameters no. 4 (scanning strategies 4.1-4.7).

No.	**t [mm]**	**h [µm]**	**pd [µm]**	**ext [µs]**	**v [mm/s]**	**P [W]**	**E [J/mm^3]**
1	25	30	10	20	500	30	80
2	25	30	15	20	750	30	53
3	25	30	20	20	1000	30	40
4	25	30	10	20	500	27.5	73
5	25	30	15	20	750	27.5	49
6	25	30	20	20	1000	27.5	37

7	25	30	10	20	500	25	67
8	25	30	15	20	750	25	44
9	25	30	20	20	1000	25	33
10	25	70	10	20	500	30	34
11	25	70	15	20	750	30	23
12	25	70	20	20	1000	30	17
13	25	70	10	20	500	27.5	31
14	25	70	15	20	750	27.5	21
15	25	70	20	20	1000	27.5	16
16	25	70	10	20	500	25	29
17	25	70	15	20	750	25	19
18	25	70	20	20	1000	25	14
19	25	100	10	20	500	42.5	34
20	25	100	15	20	750	42.5	23
21	25	100	20	20	1000	42.5	17
22	25	100	10	20	500	47.5	38
23	25	100	15	20	750	47.5	25
24	25	100	20	20	1000	47.5	19

Table III.11. A1 Additional melting applied to Parameters no. 4 (scanning strategies 4.2-4.7).

No.	**t [mm]**	**h [µm]**	**pd [µm]**	**ext [µs]**	**v [mm/s]**	**P [W]**	**E [J/mm^3]**
R_a	25	150	20	20	1000	25	6.7
R_b	25	150	20	20	1000	75	20.0

Fabricated samples on the platforms along with platforms numbers and the marking of samples on the platforms are presented in Figure III.20:

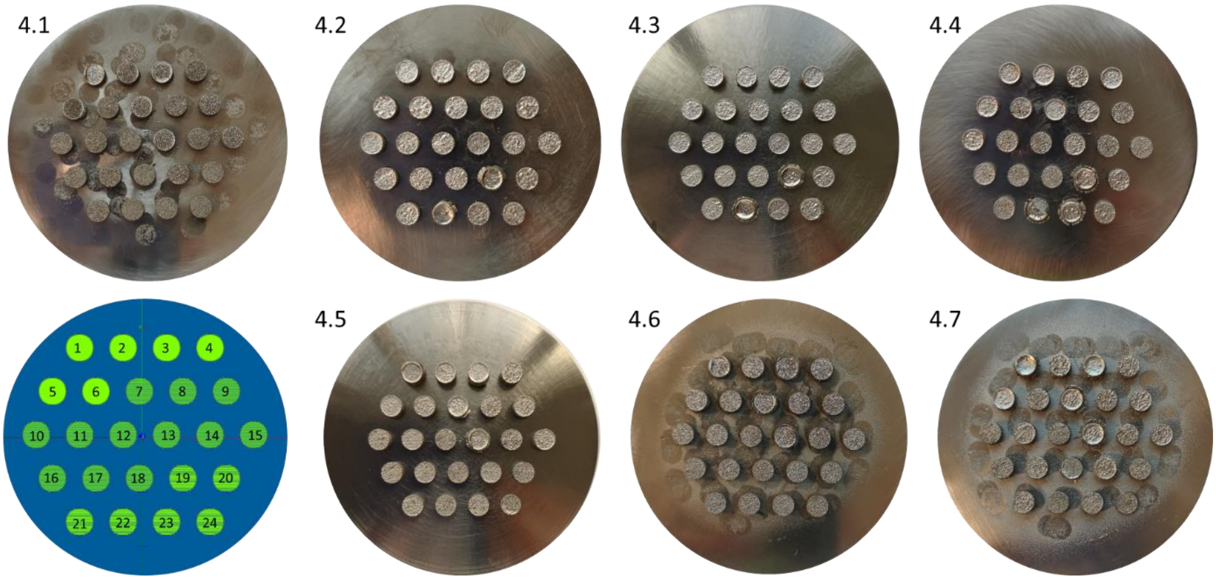

Figure III.20. A1 The Realizer SLM50 building platforms with NiTi samples made with set of Parameters no.3 with scanning strategies 4.1-4.7.

Metallographic observations of polished samples were performed (Figure III.21). Nevertheless, due to the high porosity and delamination some of the samples could not be removed from the platform in a form that allows the preparation of metallographic samples (have been damaged, when removed from the building platform). The samples that could not be successfully removed from the platform were completely eliminated from further analysis. Moreover, the samples that failed in early stage of fabrication (after few layers) was not analysed.

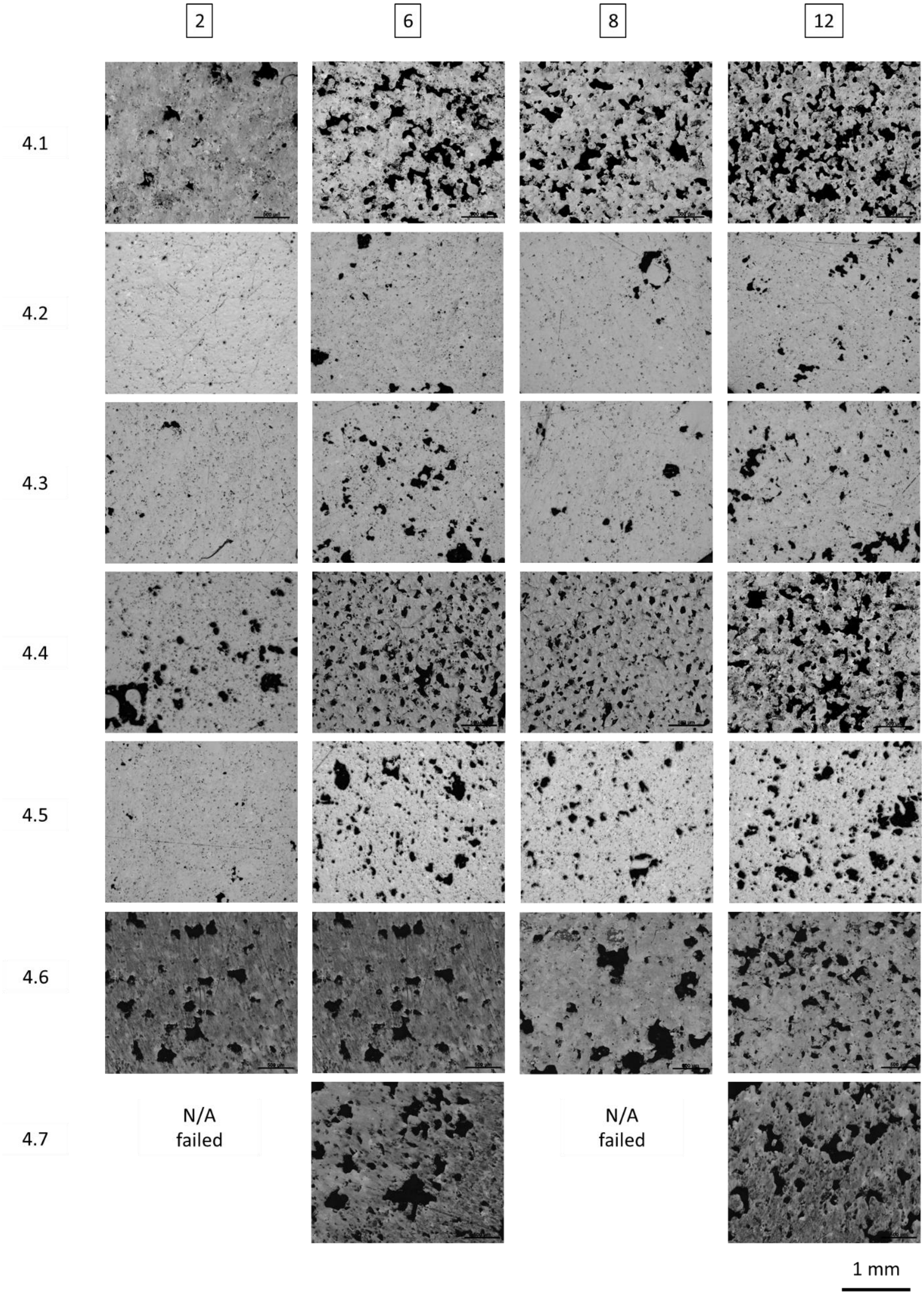

Figure III.21. A1 Microstructure of samples no. 2, 6, 8 and 12 fabricated with Parameters no. 4 and scanning strategies 4.1.-4.7.

Parameters no. 5

Based on obtained results for Parameters no. 4 we have selected new set of parameters. Followed modification compared to Parameters no. 4 was implemented:

- Hatch of 50 µm was added and 100 µm was delete

Firstly, single melting was performed (5.1) for 27 samples fabricated with parameters presented in Table III.12. Secondly, remelting with parameters R_1 and R_2, was performed one and two times for scanning strategies 5.2-5.5. Triple remelting with R1 parameters was not successful and samples failed in the early stage of the fabrication process (5.6). The results showed that after producing only a few layers (~20-30 layers, that was about 0.5-0.75 mm), the side cracks caused them to wrap and detach for the substrate and further production was not possible. The results were not presented within the manuscript. Double remelting with R2 parameters caused excessive melting (overheating) of some of the samples and defects increase, thus, triple remelting was not applied.

As previously, no rotation (between first and following scanning) was applied for any of scanning strategy. The rotation of 45° scanning vector between successive layers was applied (Figure III.1 in the manuscript).

List of the variations (scanning strategies) for the Parameters no. 5:

4.1. Single melting

4.2. Single melting + remelting R1

4.3. Single melting + 2x remelting R1

4.4. Single melting + remelting R2

4.5. Single melting + 2x remelting R2

4.6. Single melting + 3x remelting R1

Table III.12. A1 Parameters no. 5 (scanning strategies 5.1-5.6).

No.	t [mm]	h [µm]	pd [µm]	ext [µs]	v [mm/s]	P [W]	E [J/mm^3]
1	25	30	10	20	500	30	80
2	25	30	15	20	750	30	53
3	25	30	20	20	1000	30	40
4	25	30	10	20	500	27.5	73
5	25	30	15	20	750	27.5	49
6	25	30	20	20	1000	27.5	37
7	25	30	10	20	500	25	67
8	25	30	15	20	750	25	44
9	25	30	20	20	1000	25	33
10	25	50	10	20	500	30	48
11	25	50	15	20	750	30	32
12	25	50	20	20	1000	30	24
13	25	50	10	20	500	27.5	44
14	25	50	15	20	750	27.5	29
15	25	50	20	20	1000	27.5	22
16	25	50	10	20	500	25	40
17	25	50	15	20	750	25	27
18	25	50	20	20	1000	25	20
19	25	70	10	20	500	30	34
20	25	70	15	20	750	30	23
21	25	70	20	20	1000	30	17
22	25	70	10	20	500	27.5	31
23	25	70	15	20	750	27.5	21
24	25	70	20	20	1000	27.5	16
25	25	70	10	20	500	25	29
26	25	70	15	20	750	25	19
27	25	70	20	20	1000	25	14

Table III.13. A1Additional melting applied to Parameters no. 5 (scanning strategies 5.2-5.6).

No.	t [mm]	h [µm]	pd [µm]	ext [µs]	v [mm/s]	lp [W]	E [J/mm^3]
R1	25	30	20	20	1000	25	33.3
R2	25	30	60	20	3000	75	33.3

Fabricated samples on the platforms along with platforms numbers and the marking of samples on the platforms are presented in Figure III.22:

Figure III.22. A1 The Realizer SLM50 building platforms with NiTi samples made with set of Parameters no.5 with scanning strategies 5.1-5.6.

The results obtained within Parameters no. 5 and scanning strategies 5.1-5.5 were satisfying and allowed to fabricate high quality samples with high density (above 99%). It was observed that remelting improves the quality of fabricated coupons (decrease porosity and number cracks) and the parameters of remelting highly influence the results (differences were observed for R1 and R2 remelting parameters). Since scanning strategy 5.6 did not allowed for fabrication of any sample (excessive overheating and detaching samples from the platform) it was excluded from further analysis. The variations observed for using different scanning strategies 5.1-5.5 encouraged us to perform a more detailed analysis of the fabricated samples. The analysis was presented within the manuscript.

Appendix 2

Table III.14. A2 Relationship between relative density and energy density for NiTi manufactured with elementally blended powders (values for Figure III.6 in the Manuscript).

Energy density [J/mm^3]	**Material density [%]**				
	Single melting (SM)	**SM + single remelting R1**	**SM + double remelting R1**	**SM + single remelting R2**	**SM + double remelting R2**
80	94.90	96.00	97.56	97.55	97.35
73	92.84	N/A	N/A	97.44	97.40
67	91.10	94.90	94.15	98.19	98.34
53	92.45	94.00	94.46	97.19	96.89
49	93.19	93.27	93.36	96.10	96.54
48	94.84	94.11	93.92	96.31	97.01
44	83.44	88.98	90.68	94.08	94.32
44	85.11	95.58	95.89	95.31	96.44
40	79.74	87.19	85.88	94.08	91.32
40	94.39	96.77	95.46	96.60	97.50
37	81.34	92.80	92.95	95.89	95.30
34	93.82	96.16	92.58	93.17	96.65
33	76.87	N/A	N/A	92.34	92.74
32	89.62	94.51	89.49	94.64	94.12
31	94.85	97.63	N/A	94.58	96.93
29	78.94	N/A	N/A	90.44	N/A
29	92.88	95.24	N/A	92.04	93.63
27	85.97	97.34	92.22	88.75	88.65
24	71.61	93.28	N/A	90.22	82.39
23	81.18	93.43	N/A	88.52	88.40
22	68.12	81.50	89.92	81.66	83.32
21	78.41	96.71	N/A	92.89	85.73
20	57.29	93.52	92.56	85.22	91.92
19	76.36	94.84	N/A	85.25	89.96
17	67.47	96.00	N/A	81.15	80.78
16	72.50	90.82	N/A	84.69	89.01
14	65.02	93.85	N/A	80.93	80.50

**N/A- sample failed during fabrication*

Chapter IV

In situ alloying of NiTi: Influence of Laser Powder Bed Fusion (LBPF) scanning strategy on chemical composition.

Agnieszka Chmielewska, Bartłomiej Wysocki, Joseph Buhagiar, Bartosz Michalski, Bogusława Adamczyk-Cieślak, Michał Gloc, Wojciech Święszkowski

Published in: Materials Today Communications

DOI: 10.1016/j.mtcomm.2021.103007

Abstract

NiTi alloys are widely used in different industrial and medical applications. Due to the inherent difficulty in the machining of these alloys, the use of Additive Manufacturing (AM) methods has become a popular method for their production. When working with NiTi alloys, there is a requirement on the precise control of their chemical composition, as this determines the phase transition temperatures which are responsible for their shape memory or superelastic behaviour. The high energies used in AM to melt the NiTi alloy leads to nickel evaporation, resulting in a chemical change between the batch powder and the additively manufactured part. Therefore, in AM techniques applied to different NiTi alloys, understanding the relationship between the melting strategy and nickel evaporation is crucial during the developing the desired chemical composition of the final-fabricated material. In this study, three NiTi alloys were fabricated using laser powder bed fusion (LPBF) starting from elementally blended Ni and Ti powders. Different melting strategies, including single and multiple melting, were studied in this work. Remelting improved the density and reduced cracking of the AM part. Microscopic observations, using a Scanning Electron Microscope (SEM) with a Backscattered Electron (BSE) detector, showed that the chemical homogeneity of the materials was enhanced by multiple remelting. Pure Ni and Ti were not found in any of the samples, proving that the applied melting strategies ensured good alloying of both powders. Regardless of the number of melting runs, X-ray diffraction (XRD) analysis showed the presence of NiTi (B2) and (B19’) phases, as well as $NiTi_2$, Ni_4Ti_3 and Ni_3Ti precipitates in all samples. The research demonstrated that, during the AM process, and depending on the melting strategy, 1.6 to 3.0 wt.% of nickel evaporates from the material. It was demonstrated that the amount of evaporated nickel increased with the increasing number of melt cycles.

Graphical abstract

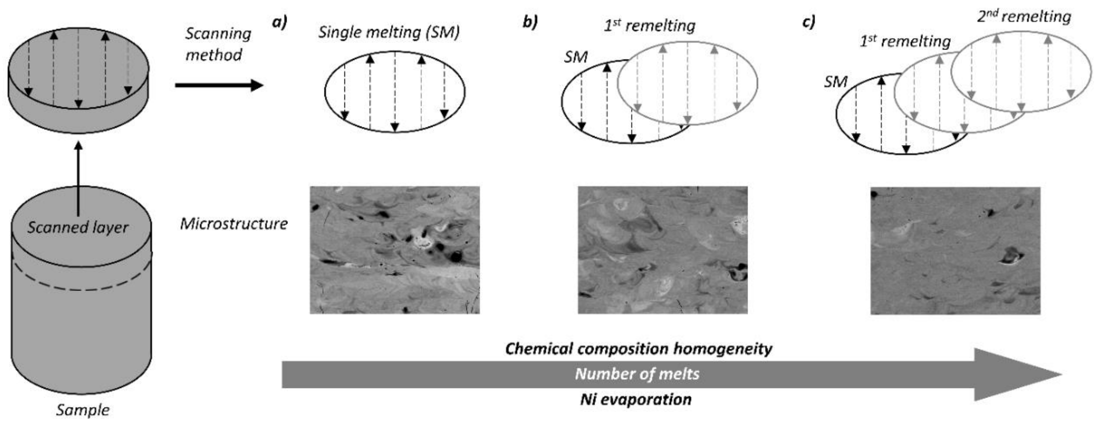

4.1. Introduction

Additive Manufacturing (AM) technologies provide many benefits and hence components built using this method are being frequently used in all the areas of our lives. Despite their successful development, there is still a strong need to understand and control the phenomenon associated with AM; as this would, in turn, allow a wider use of this technology. Among existing metal AM technologies, laser powder-bed fusion processes (LPBF) are among the most frequently investigated techniques. This is due to the flexibility of the process in the ability to change a large number of process variables and parameters; enabling the successful fabrication of fully dense metal parts with controlled properties [169,170].

NiTi alloys are widely used for many engineering and medical applications owing to their unique shape memory and superelasticity characteristics. However, the specific mechanical properties of NiTi alloys make their machining a challenging task. This significantly reduces their application use and limits the potential of these alloys. According to the previously mentioned difficulties and limitations, the additive manufacturing of NiTi alloys started gaining significant attention because this technology eliminates many of the challenges associated with the conventional methods [150,151]. Plenty of publications show studies on the fabrication of NiTi alloys using many different AM techniques, such as: the metal injection processes including laser direct energy deposition (LDED) [152], laser direct metal deposition (DMD) [153,154] and laser engineered net shaping (LENS) [155]; and the laser powder-bed fusion (LPBF) processes amongst which selective laser melting (SLM) [85,156–158,213] and electron beam melting (EBM) [51,159]. The majority of the research focuses on AM fabrication using pre-alloyed NiTi powders, however, some of the studies implement *in situ* alloying using Ni and Ti elemental powders [36,51,164–166]. *In situ* alloying is an approach that allows for the synthesis of an alloy from its elemental composition during the manufacturing process. *In situ* alloying, via AM from elemental powders, is a promising and a cost-effective alternative which offers the flexibility to tailor the composition of the AM part produced. Hence, this method is an easy way to control the material properties or create novel alloys. This route is particularly true and important for producing parts or alloys made of NiTi since their phase transition temperature is highly sensitive to the alloy's composition [36,37,51,102].

Current research into the AM of NiTi alloys, starting from elemental powders, has been associated with challenges related to the heterogeneity of chemical and phase composition of the fabricated materials. This can be induced by Ni evaporation during the melting process due to its relatively low temperature of evaporation (2732°C) as compared to that of titanium (3287°C) [163]. Precise control of the chemical composition of NiTi alloys is extremely important, since the smallest change in the relative Ni or Ti content has a large effect on the transition temperatures; which determine shape memory and superelasticity behaviour [102]. Below the martensite finish temperature (M_f), while above the A_f temperature, NiTi alloys will exhibit superelasticity. The M_s temperature changes by approximately 80°C for every atomic percent change in Ni content and therefore a great control of the alloying content is required during the manufacturing process [104]. Due to the nature of AM techniques of using high laser energies to consolidate the material, the manufacturing process can lead to evaporation of some alloying elements [214–218]. It is hypothesized that, finding a correlation between the amount of evaporated nickel, as a function of the initial powder composition and manufacturing conditions, would allow for predicting the final chemical composition of the manufactured material. Moreover, it was reported that the homogeneity of the materials fabricated from elemental powders can be improved by remelting each layer [167]. It is important to note that any additional energy input to the material caused by remelting can lead to an increased loss of Ni by evaporation. For this reason, to improve pre-alloying, the influence of manufacturing parameters on the amount of Ni lost by evaporation from the material which are fabricated from elementally blended Ni and Ti powders should be investigated.

This study investigates the level of Ni evaporation in three different NiTi elemental powder blends with the chemical compositions of $Ni_{53}Ti_{47}$ and $Ni_{57}Ti_{43}$ representing the limit values of industrially used NiTi shape memory alloys [219], and $Ni_{55.7}Ti_{43.7}$, which corresponds to pre-alloyed NiTi, used in our previous studies [220]. Moreover, a remelting scanning strategy was applied to increase the homogeneity of the fabricated material. To the best of the auhors' knowledge and in relation to the use of LPBF technology in conjunction with elementally blended Ni and Ti powders, the influence of remelting on the chemical composition (Ni:Ti ratio) has not been studied so far. Designing the alloys, and fabricating them from elemental powders, seems to be the promising approach to overcome the difficulties associated with chemical composition changes, and thus, the properties of additively manufactured NiTi alloys. This research will give new insights into new materials that could be developed immediately, and thus eliminating the necessity of the time-consuming and expensive manufacturing of powders. This work would therefore contribute to the faster development of the whole AM industry.

4.2. Materials and methods

Gas-atomised pure Ni (99.9% in purity, TLS Technik, Germany) and Ti (99.7% in purity, TLS Technik, Germany) powders, having a spherical shape with size below 45 μm were mixed in a tumbling mixer (Turbula, USA) for 2h and used as powder feedstock. Three different chemical compositions of powder blends were used: $Ni_{53}Ti_{47}$, $Ni_{55.7}Ti_{43.7}$, and $Ni_{57}Ti_{43}$ (wt.%). Samples were fabricated with laser powder bed fusion technique (LPBF) using Realizer SLM50 (DMG MORI Additive GmbH, Borchen, Germany) machine equipped with a pulsed-wave ytterbium fibre laser having a maximum power of 120 W. Experiments were conducted in an argon atmosphere and with an oxygen content below 0.3 vol.%. The NiTi substrate was preheated to 200°C to decrease the temperature gradient and facilitate the adhesion of the build to it. Samples were fabricated with three different melting strategies and are presented in Figure IV.1. The single melting (SM) (Figure IV.1a), or first melting, was performed with 30 W of laser power, 500 mm/s of scanning speed, and 30 μm of hatch distance. The remelting, which was done once (Figure IV.1b) or twice (Figure IV.1c) after single melting, was performed with 25 W of laser power, 1000 mm/s of scanning speed, and 30 μm of hatch distance. A layer thickness of 25 μm was used, and to reduce the influence of thermal stresses on samples, scanning rotations of 45° between adjacent layers were applied during fabrication.

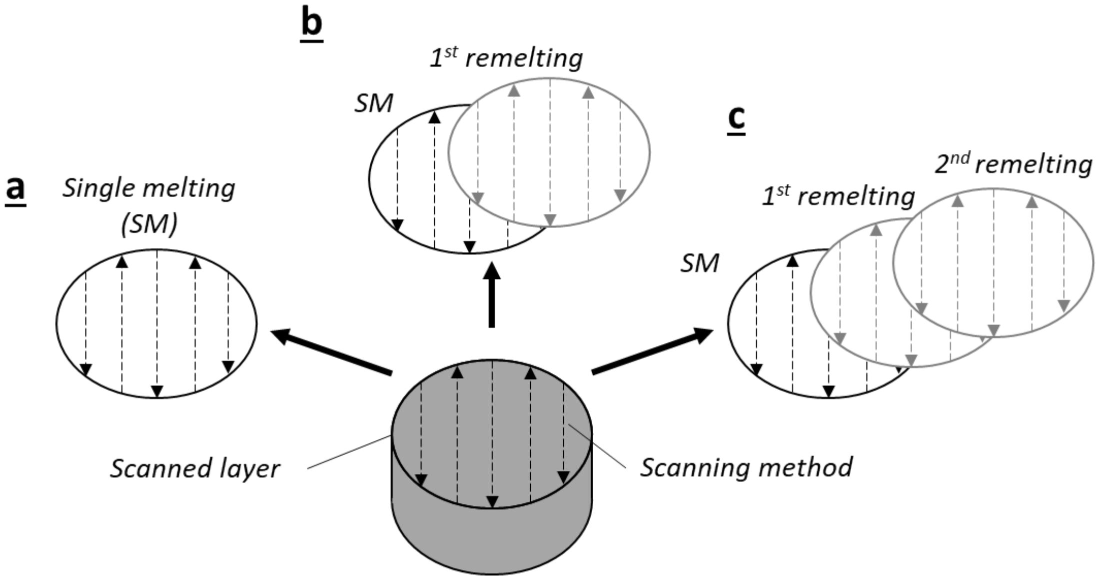

Figure IV.1 Schematic illustration of melting strategies: a) laser scanning strategy no. 1: single melting; b) laser scanning strategy no. 2: melting and single remelting; c) laser scanning strategy no. 3: melting and double remelting

The Archimedes standard method was applied to determine the relative density of the fabricated materials. Mass of each sample was measured independently 3 times in air and water using an electronic balance with ± 1 mg of accuracy. The relative density was calculated according to Eq. 1:

$$\rho = \frac{\rho_l}{m_a - m_l} \quad (1)$$

where ρ is relative density, ρ_l is the density of the liquid (water), m_a is the mass of the sample in air and m_l is the mass of the sample in the liquid.

Samples were hot mounted in resin and mechanically polished to be examined under a Zeiss Axio Scope Light Microscope (Germany). The presence of defects, such as porosity and cracks in the samples was assessed. Samples were also examined under a Hitachi SU-8000 (Japan) Scanning Electron Microscope (SEM) in Backscattered Electron (BSE) mode to determine the distribution of Ni and Ti elements.

Phase identification of the manufactured samples was conducted using a Bruker D8 Advance X-ray diffractometer (Bruker, USA) having filtered Cu Kα (λ = 0.154056 nm) radiation and operated at 40 kV and 40 mA. Bruker EVA software and a PDF-2 database (from the International Centre for Diffraction Data) were used to analyse the X-Ray Diffraction (XRD) patterns.

The chemical composition of the fabricated samples was analysed by using a PerkinElmer Optima 8300 (USA) inductively coupled plasma – optical emission spectrometry (ICP-OES). The samples were mineralised in a closed microwave system having an oxidising environment. The prepared samples were analysed by ICP-OES to determine the content of Ni and Ti elements.

Thermal analysis was carried using a DSC 8000 analyser (Perkin-Elmer, USA) which is capable of performing Differential Scanning Calorimetry (DSC) tests. Specimens were tested under an atmosphere of argon gas in the temperature range of 20 to 120°C. The heating and cooling rates were of 10°C/min.

4.3. Results

4.3.1. Macroscopic and microscopic observation

Macroscopic observations of each alloy, with an initial powder blend weight ratio of: $Ni_{53}Ti_{47}$, $Ni_{55.7}Ti_{43.7}$, and $Ni_{57}Ti_{43}$, showed that using the same manufacturing parameters ensures good printability. Delamination or macrocracks were not observed for any composition or manufacturing parameters used in this work. The samples were mechanically polished along the Z build direction to assess the presence of micro defects, such as microcracks and pores. As it can be seen in Figure IV.2, microcracks along the Z-axis were present in all samples. Other research [221] concluded that this kind of cracks are referred to as 'hot cracks' and will be described in detail in the discussion section of this work. The cross-sections show the presence of spherical and irregular pores. Spherical pores, also referred to as keyhole pores, are created by metal evaporation due to the excess heat input [196,198]. Irregular pores are formed as a result of an insufficient fusion of the subsequent layer of material. As the number of melt runs increases, the number of pores decreases; as does the presence of cracks. The effect is most noticeable for the first remelting when the number of pores and microcracks is significantly reduced. In contrast, after the second remelting run the reduction of pores or cracks number is not that distinct.

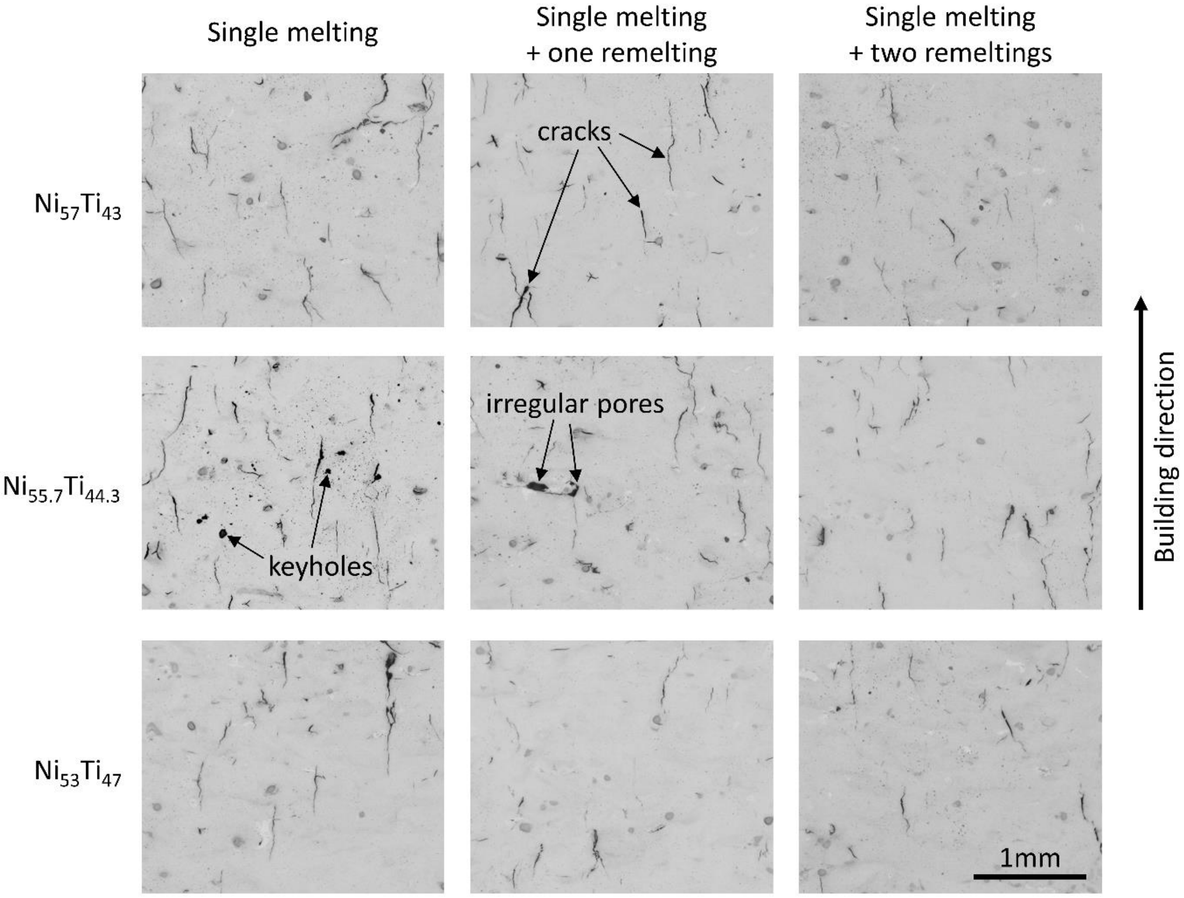

Figure IV.2 Light microscopy micrographs of samples manufactured from powders with different initial powder compositions and subjected to different numbers of melt runs. Arrows indicate cracks, irregular pores, and keyholes.

4.3.2. Density measurement

The alloys' densities expressed in g/cm^3 are shown in Figure IV.3. The Archimedes density of each sample was measured non-consecutively three times. The results showed that the samples with the highest nickel content (Ni 57%) exhibit the highest density, and the alloy with the lowest initial nickel content had the lowest density (Figure IV.3). The density of the fabricated samples increases as the number of melts increases. This confirms earlier assumptions from microscopic observations (Figure IV.2) that remelting reduces the closed porosity and cracks that affect the density measurement of the sample by the Archimedes method. There is no clear relationship between the chemical composition of the material or the number of melts and samples density; since the density varies differently for different compositions and numbers of melts. The greatest increase in density occurs after the second melting; the third melting does not significantly affect the density. This also confirms microscopic observations that the number of pores decreases most after the second melting and slightly after the third melting.

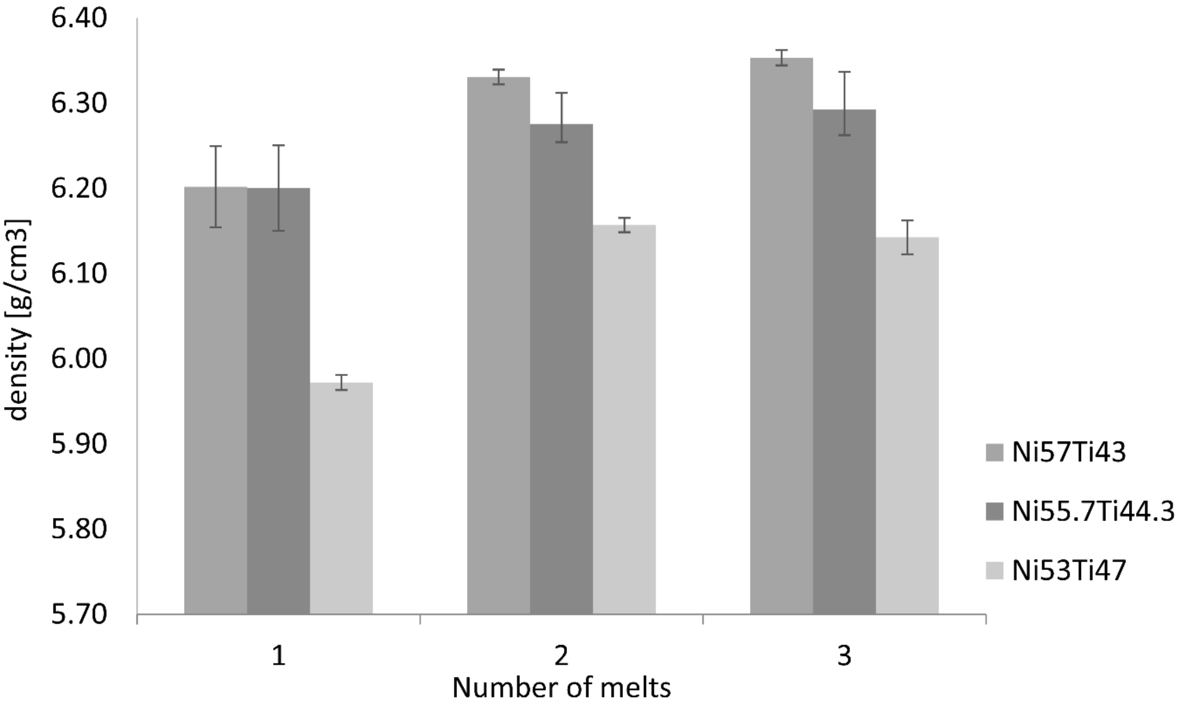

Figure IV.3 Relationship between relative density and number of melt runs for NiTi manufactured with elementally blended powders with different chemical compositions. Results represent the mean value of 3 measurements. Error bars present maximum and minimum value of measurements.

4.3.3. Scanning Electron Microscopy - Backscattering Electrons

Fusion zones, in the manufactured samples, were observed in the BSE SEM images (Figure IV.4). The bright areas are undiffused Ni-rich phases, while the dark shaded are Ti-rich regions. It can be noted that remelted samples have a more homogenous microstructure in terms of Ni and Ti distribution; with the homogeneity increasing with an increase in the number of melt runs. Higher homogeneity is indicated by the lower phase contrast in the BSE SEM images.

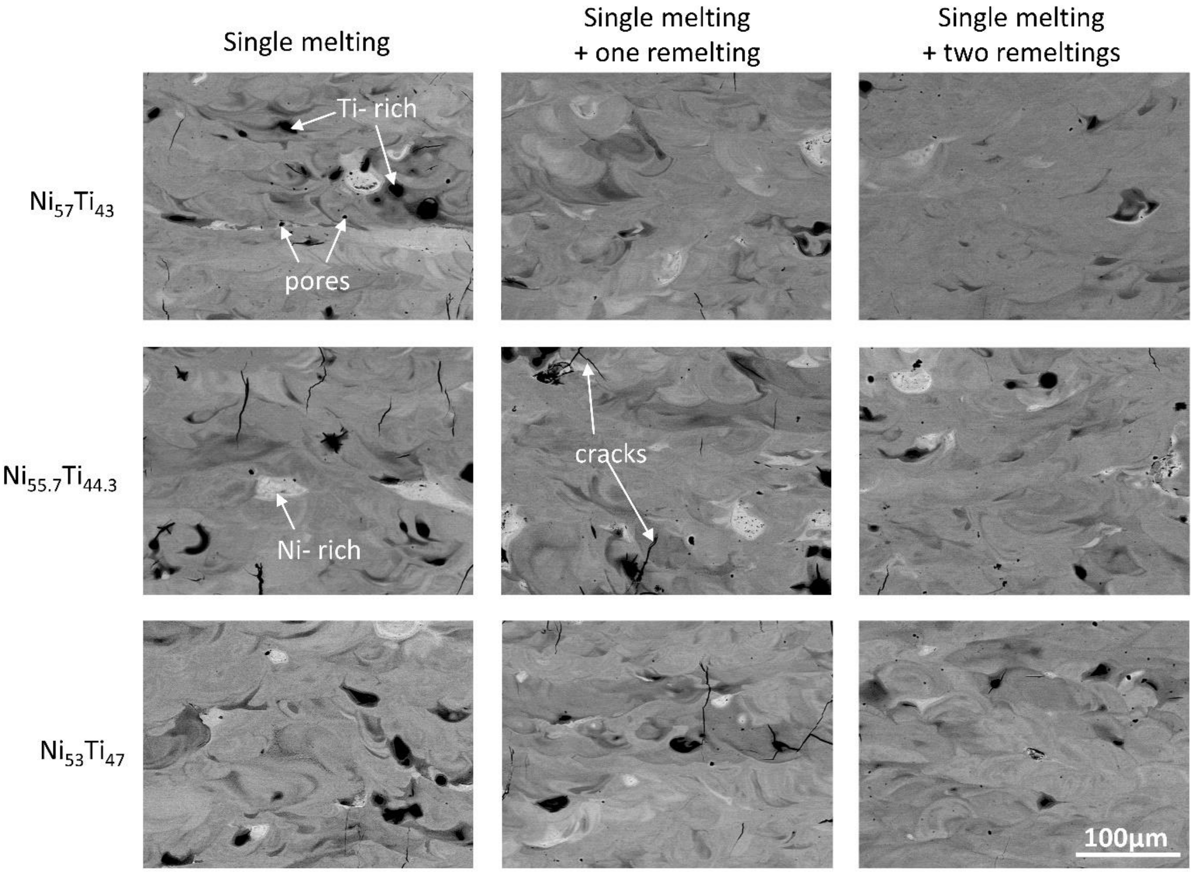

Figure IV.4 BSE SEM micrographs of samples manufactured from powders with different initial powders compositions and subjected to different numbers of meltings. Dark and light shaded areas are titanium- and nickel-rich, phases respectively. Arrows indicate cracks, pores and Ti- and Ni-rich areas.

4.3.4. X-ray Diffraction

The phase composition of the manufactured alloy was determined by XRD analysis and Figure IV.5 presents the patterns of all manufactured samples. The results indicate the presence of NiTi (B2) austenite phase, having a cubic structure, and (B19') martensite phase, having monoclinic structure. $NiTi_2$, Ni_4Ti_3 and Ni_3Ti phases were identified in all samples. There is no evidence of free nickel and titanium peaks; proving that both elements have been thoroughly alloyed. Variation in the $NiTi_2$ and NiTi B19' peaks intensities, which overlap each other, was found. The intensities of the $NiTi_2$ and NiTi B19' peaks are shown to increase with a decrease in the nickel content of the pre-printed powder composition.

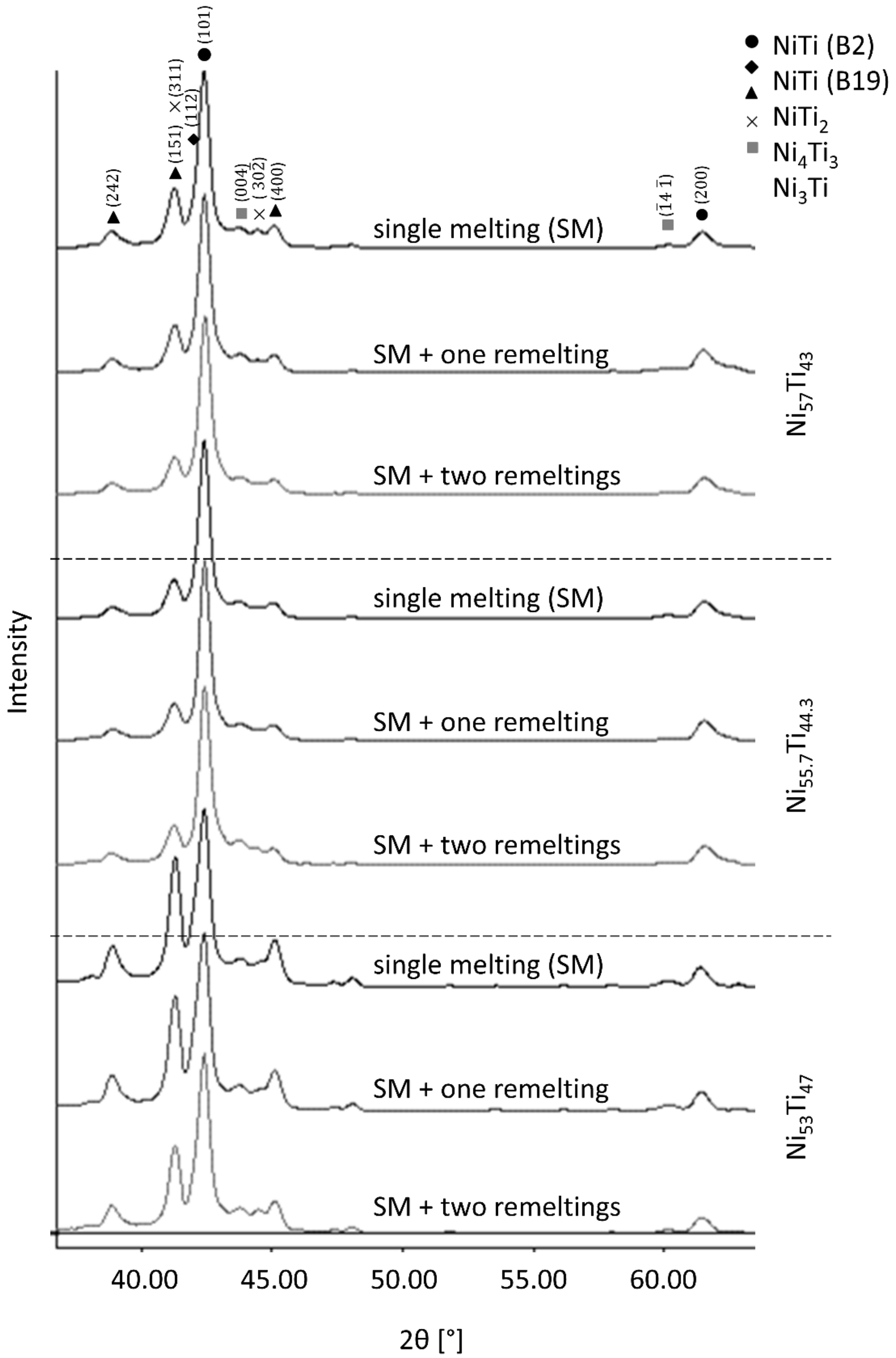

Figure IV.5 The XRD diffractograms of samples fabricated from powders with different initial powders compositions and subjected to different number of melt runs.

4.3.5. Inductively coupled plasma optical emission spectroscopy (ICP OES)

For each sample, the chemical composition was analysed using inductively coupled plasma-optical emission spectrometry (ICP-OES). The analysis was performed to determine changes in the chemical composition (nickel evaporation) depending on the chemical composition of the initial powder blend, as well as the number of melts. The ICP-OES data showed that the amount of nickel in the material decreases with an increasing number of melt runs (Figure IV.6). However, the decrease in nickel content with the number of melt runs was not uniform for each of the blends.

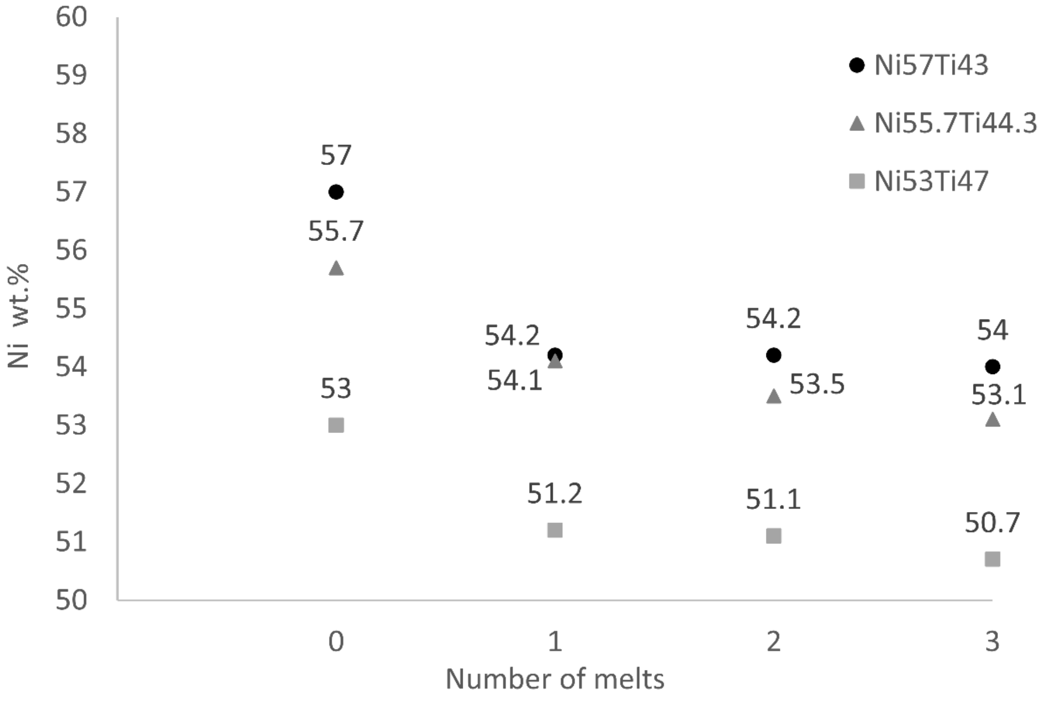

Figure IV.6 Results of ICP OES analysis of samples fabricated from powders with different initial powders compositions and subjected to different numbers of melt runs; 0 refers to pre-printed powder; 1- single melting run; 2- single melting run and one remelting run; 3- single melting run and two remelting runs; the measurement error was ±0.1 wt.%.

4.3.6. Differential Scanning Calorimetry (DSC)

Figure IV.7 presents the DSC curves of samples manufactured with different compositions and melting strategies. Due to the heterogeneous microstructure of the materials the DSC peaks are very wide, and it is difficult to determine the exact temperature of the start and end of both the austenitic and martensitic transition. However, it can be found that the martensitic transition temperatures decrease to about 5-8°C with the decreasing content of Ni for different blends. However, for the blends with the same initial powder composition and produced using different melting strategies (number of melts), the differences in transition temperatures are barely noticeable and have a range of about 1-2°C.

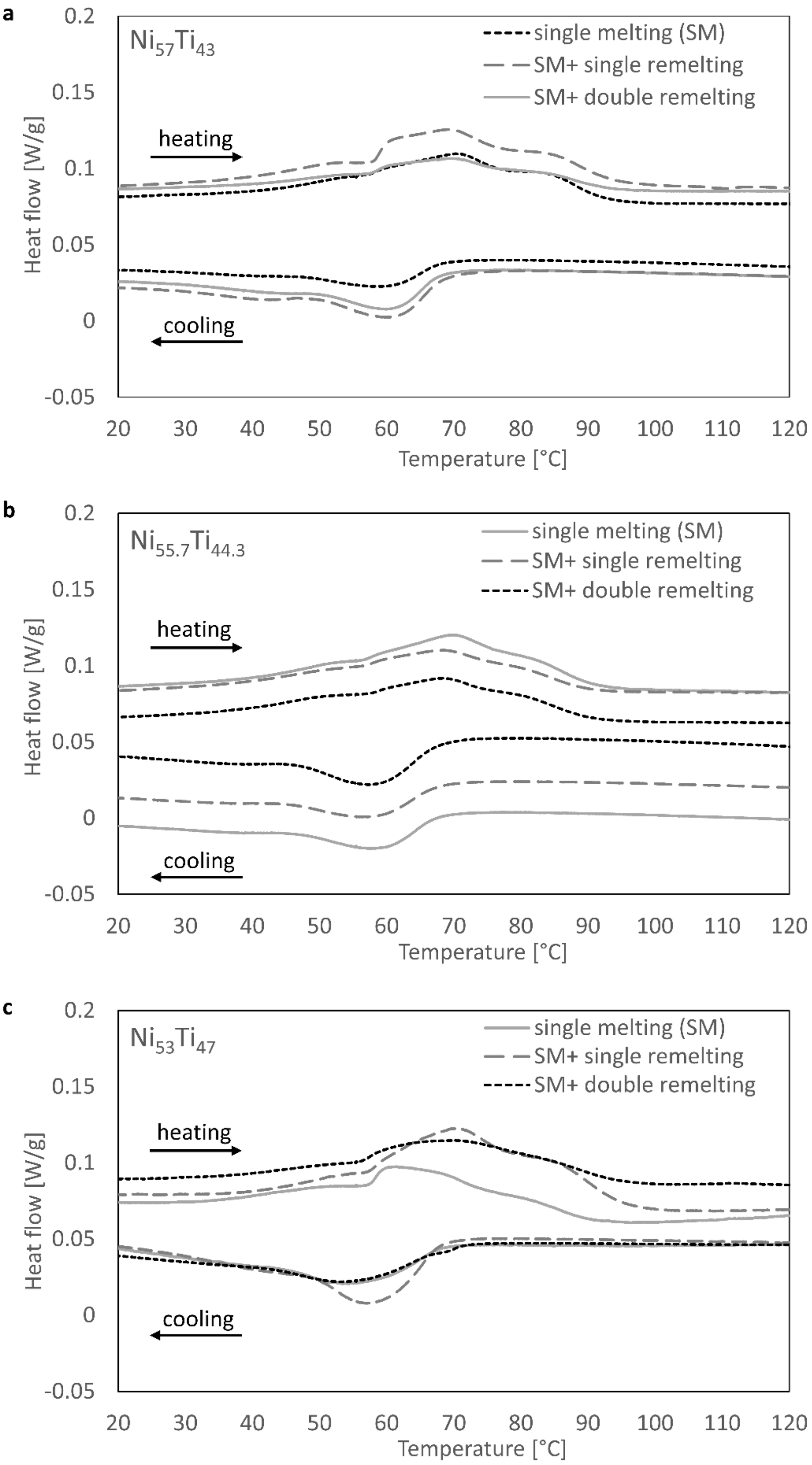

Figure IV.7 The DSC curves of samples manufactured with different composition and melting strategies: a) Ni53Ti47; b) Ni55.7Ti43.7 and c) Ni57Ti43.

4.4. Discussion

The research focused on determining the value of nickel evaporation from three NiTi powder mixtures with different chemical compositions: $Ni_{53}Ti_{47}$, $Ni_{55.7}Ti_{43.7}$, and $Ni_{57}Ti_{43}$ (wt.%) fabricated by LPBF with three different melting strategies. Moreover, the influence of multiple melting on the alloy microstructure was shown. Microscopic observation has revealed the presence of microcracks along the building direction (Figure IV.2). The high thermal gradients associated with the LPBF process contribute to the formation of residual stresses, and in turn, induce large susceptibility to hot cracking [221–223]. Two mechanisms of hot cracking can be distinguished: solidification cracking and liquidation cracking. Solidification cracking occurs in the fusion zone when the material is in a semi-solid state during laser melting, which means that it consists of a partially solidified material with a non-solidified liquid entrapped in between. Solidification of the entrapped liquid induces tensile residual stresses, which in turn initiates cracking. This phenomenon was observed for materials in which some phases had a much lower melting point than other components [224]. This problem applies to the Ni and Ti powder blends since titanium has a much higher melting point than nickel; which are 1670°C and 1455°C, respectively. Furthermore, the results of BSE images (Figure IV.4) and XRD (Figure IV.5) revealed the existence of various phases in the manufactured samples, including the NiTi phase, with a melting point of 1310°C, and a $NiTi_2$ phase with a much lower melting point of 984°C. Thus, due to the presence of various phases with different melting temperatures within the material, solidification cracking may occur. Liquation cracking occurs in the heat-affected zone where phases with low melting points are presented, such as eutectics and zones with chemical segregation. When the material is heated, a thin film of liquid material forms in the heat-affected zone, which eventually shrinks as it solidifies and promotes crack formation [82,221,225,226].

The number of cracks in samples subjected to additional melting (remelted) is reduced, which may be the result of filling cracks with liquid metal during remelting [221]. Significant differences in the reduction of microcracks are observed after the second melting, while the number of microcracks does not change distinctly after the third melting. This phenomenon may be evidenced by the fact that some of the microcracks were filled with liquid metal but some of them remained. This is due to the high internal stresses in the material generated by multiple remelting. The reduction in the number of cracks and pores also resulted in a density increase (Figure IV.3).

Although both components were not thoroughly blended (Figure IV.4), no peaks of free nickel and titanium were observed in the XRD traces (Figure IV.5). A recent study [155] demonstrated that martensitic (B19’) and austenitic (B2) phases coexist in additively manufactured NiTi. The B2 phase is known to be stable at higher temperatures, while the B19′ phase exists at lower temperatures. However, their transition temperatures depend on the chemical composition of the alloy. The lower the Ni content, the lower the transition temperature. This means, that at the same temperature the nickel-rich B2 phase can coexist simultaneously with the titanium-rich B19’ phase within one material with areas having different Ni/Ti contents. In this study, BSE SEM observations showed heterogeneity in the alloying of both elements, and therefore, Ni and Ti-rich areas are observed within the microstructure. Furthermore, the increase in $NiTi_2$/NiTi (B19’) peak intensity was observed for samples with the lowest Ni content in the initial powder blend. Since peaks corresponding to NiTi (B19’) and $NiTi_2$ overlap each other, it is not possible to unequivocally determine which of those phases has a greater impact on the increase of that specific peak intensity. Moreover, it is possible, that both phases contribute to the peak growth due to the presence of two different phenomena. Firstly, as the Ni content decreases, the likelihood of $NiTi_2$ phase formation increases due to the lack of sufficient nickel atoms to form the NiTi phase. Secondly, a decrease in Ni content also causes a decrease in the martensitic transition temperature. Accordingly, the probability of the formation of more martensite than austenite in the material increases. The nickel content in samples $Ni_{57}Ti_{43}$ and $Ni_{55.7}Ti_{43.7}$ is more similar to each other; 57 and 55.7% of Ni respectively. Thus, the differences between their peaks are lower, than that of the $Ni_{53}Ti_{47}$ samples,, with a nickel content of 53% [160]. The intensity of $NiTi_2$ and NiTi (B19’) diffraction peaks is the highest for 7-9 samples, which have significantly lower amounts of nickel.

The ICP OES results showed changes in Ni content in samples of different compositions subjected to a different number of melts (Figure IV.6). In all samples there was a decrease in the amount of nickel from the initial powder blend composition. Depending on the initial powder blend composition and melting strategy, the amount of evaporated Ni ranges from 1.6 to 3 wt.%. The content of Ni decreases with the increasing number of melts. During the subsequent laser melting with a high-power laser. the material is reheated and melted multiple times, hence, there is a higher probability for Ni evaporation. Consequently, the more times the material is remelted, the more Ni would evaporate. It would be beneficial to predict the amount of evaporated nickel during LPBF manufacturing depending on the composition of the batch powder and the scanning and melting strategy used during the manufacturing process. Thus, to obtain a desired final alloy composition, the initial powder composition and manufacturing strategy must be developed separately.

DSC plots, shown in Figure IV.7, are not uniform, and multiple small peaks are observed. In general, the existence of an additional peak before the austenitic and martensitic transition is related to the presence of the R phase, which is the intermediate phase between martensite and austenite [92]. Nevertheless, in the presented DSC results, multiple small additional peaks are observed along the entire length of the transition peak. Therefore, it can be concluded that these peaks are not related to the presence of R phase and might be generated by heterogeneity in Ni and Ti distribution in the NiTi phase. It can also be seen that the peaks of austenitic and martensitic transition are wide, and it is difficult to precisely determine the start and finish transition temperatures. Li *et al.* [82] have reported that the peak width is related to the inhomogeneity of the B19' phase. It is possible, that the range of the transition temperatures extends over a wider area, while B19'/B2 phases show chemical inhomogeneities in the Ti/Ni content; since the NiTi phase can be composed of 53-57 wt.% of Ni. Nevertheless, a slight shift of the value of the transition temperatures is observed in the samples with different initial powder blend compositions and this is due to the reduction in nickel content. It was found that with the decrease in Ni content in various blends, the transition temperature decreased by about 5-8°C, while for the blends with the same initial powder composition and produced using different melting strategies (number of melts), the transition temperature decreases by only about 1-2°C. It is well known that a 1 at.% change in nickel content changes the transition temperature by about 80°C [104]; however, such a large change in transition temperature was not noticeable in the studied AM produced samples of this work. This is because the microstructure is very heterogeneous, resulting in a wide DSC peak and the inability to accurately determine the start and end transition temperatures. Therefore, it would be necessary to homogenise the microstructure by a post-additive manufacturing heat treatment in order to be able to more accurately define the start and finish martensitic and austenitic transition temperatures.

4.5. Conclusions

Three NiTi powder blends with chemical compositions of $Ni_{53}Ti_{47}$, $Ni_{55.7}Ti_{43.7}$, and $Ni_{57}Ti_{43}$ (wt.%) were melted by LPBF using three different melting strategies. The same manufacturing parameters applied to all powder blends allowed each sample to be successfully fabricated. Ni evaporation from the manufactured samples was studied, and the amount of nickel that evaporates during the production process ranges from 1.6 to 3.0 wt. %. This depends on the initial powder's chemical composition and the number of melts. It was demonstrated that the amount of evaporated nickel increases with increasing number of melt cycles. Furthermore, an increase in the number of melt cycles reduces the number of cracks and pores and increases the chemical homogeneity of the alloy. Nevertheless, multiple meltings can still generate high residual stresses and result in crack formation. Thus, the number of remelting cycles must be precisely defined to increase the chemical homogeneity and density of the material and prevent cracking. Due to the large heterogeneity of the chemical composition of the manufactured materials, it was difficult to accurately determine the start and final transition temperatures of martensite and austenite. Therefore, homogenisation of the chemical composition would be necessary to precisely define the influence of different melting strategies on the transition temperatures, and hence, thermomechanical properties of the material. Since remelting does not eliminate the problem of heterogeneity an additional heat treatment would be required and further investigated. The presented results are very promising for *in situ* alloying in additive manufacturing and could provide valuable information for designing the batch material's chemical composition to obtain the desired chemical composition of the fabricated alloy.

Chapter V

Heat Treatment of NiTi alloys fabricated using Laser Powder Bed Fusion (LPBF) from elementally blended powders

Agnieszka Chmielewska, Bartłomiej Wysocki, Piotr Kwaśniak, Mirosław Jakub Kruszewski, Bartosz Michalski, Aleksandra Zielińska, Bogusława Adamczyk-Cieślak, Agnieszka Krawczyńska, Joseph Buhagiar, Wojciech Święszkowski

Under review in: Materials

Abstract

The use of elemental metallic powders and *in situ* alloying in additive manufacturing (AM) is of industrial relevance as it offers the required flexibility to tailor the batch powder composition. This solution has been applied to the AM manufacturing of Nickel Titanium (NiTi) shape memory alloy components. In this work, it has been shown that laser powder bed fusion (LPBF) can be used to create a $Ni_{55.7}Ti_{44.3}$ alloyed component, but the chemical composition of the build had a large heterogeneity. To solve this problem three different annealing heat treatments were designed, and the resulting porosity, microstructural homogeneity, and phase formation was investigated. The heat treatments were found to improve alloy's chemical and phase homogeneity, but the brittle $NiTi_2$ phase was found to be stabilized by the 0.54 wt. % of oxygen present in all fabricated samples. As a consequence, Ni_2Ti_4O phase was formed and was confirmed by transmission electron microscopy (TEM) observation. The study showed that pore formation in *in situ* alloyed NiTi can be controlled via heat treatment. Moreover, we have shown that the two-step heat treatment is a promising method to homogenise the chemical and phase composition of *in situ* alloyed NiTi powder fabricated by LPBF.

5.1. Introduction

Shape memory alloys (SMA) have generated great interest in a diverse number of engineering applications. Nickel-titanium (NiTi), also referred to as Nitinol, is the most frequently used SMA which demonstrates stable shape memory effect and superelastic behaviour which allows for large recoverable strains of up to 8% [151,174]. Furthermore, it has good biocompatibility, damping characteristics, corrosion resistance, and low Young's Modulus (50–80 GPa) compared to other alloys commonly used in biomedical applications [227,228]. The specific mechanical properties of NiTi alloys render their machining a challenging task. One of the challenges of NiTi alloys is their extremely poor machinability resulting in rapid and uncontrollable tool wear and poor surface quality. This is due to the high ductility, superelasticity, low elastic modulus, and work hardening of the NiTi alloy the machined part is made of [134,135]. Demanding machining generates a high cost of the fabricated parts and limits the applicability and commercial usage of NiTi alloys. For this reason, an extremely important issue is to reduce material cost by eliminating machining, which would result in a lower cost of the fabricated elements. Thanks to additive manufacturing (AM) techniques that eliminate the need for machining, complex shapes of NiTi alloys have been produced in recent years [172,173,229]. Laser powder bed fusion (LPBF) is one of the powder-based AM methods allowing the fabrication of a wide variety of functional complex three-dimensional shaped parts. In this technique the model is built directly from CAD data by melting successive layers of metal powder on top of the previous one, using thermal energy supplied by a focused and computer-controlled laser beam. It offers the opportunity to produce parts with complex geometries without resorting to cutting, pressing, grinding tools or fixtures. Since AM is a fast-growing industrial sector there is a strong need for new material development to satisfy the various engineering and medical application requirements. Despite its promise to overcome these challenges, AM of NiTi has rarely been considered or explored to produce NiTi devices. Current research into the AM of NiTi parts from pre-alloyed powders has been associated with difficulties concerning chemical homogeneity and chemical composition control caused by Ni evaporation during the melting process [156,157,230]. Since phase transition temperatures of NiTi alloys, which determine their unique properties, are highly sensitive to the alloy composition, any changes in the Ni/Ti ratio are undesirable [102,151]. One of the possible alternatives to solve the difficulties and reduce the costs of the production of a few different chemical compositions of NiTi powders (Ni/Ti ratio) is exploring the possibility of alloying Ni and Ti elemental powders *in situ* during the LPBF processes [51,163–166]. *In situ* alloying offers the flexibility to tailor the batch powder composition, by mixing the proper amount of pure metal powders [36,37]. The effect of *in situ* alloying during the LPBF process is the fabrication of the new object from a predesigned alloy composed of elemental powders [36,37]. For NiTi *in situ* fabrication, by knowing the amount of nickel evaporated during fabrication [151,173], the proper mixing ratio can be estimated in order to design the chemical composition of the final material [51]. Moreover, the use of nickel and titanium elemental powders is nearly three times cheaper than pre-alloyed NiTi powders currently available on the market. Thus, using elementally blended Ni and Ti powders would reduce the price of final objects.

It was reported that for NiTi AM-built objects using both elementally blended and pre-alloyed powders, a heat treatment is essential to improve the homogeneity, mechanical properties, and thermomechanical response [82,172]. As reported by Li *et al.* [82] and Lee *et al.* [231], the formation of $NiTi_2$ phase was observed in a NiTi alloy fabricated from pre-alloyed powder. In research work, where NiTi parts were AM-built from elementally blended powders, it was observed that the NiTi martensitic or austenitic, as well as $NiTi_2$ phases were present [51,162–166,172,205,232,233]. Moreover, the presence of secondary phases such as Ni_3Ti and

Ni_4Ti_3 were found in as-built specimens by Wang *et al.* [51] and Halani *et al.* [163], respectively. Hence, they investigated the influence of the heat treatment on the microstructure and phase composition of fabricated specimens. Based on the Ni-Ti phase diagram (Figure V.1), the melting point of $NiTi_2$ is 984°, thus, Wang *et al.* and Halani *et al.* subjected the as-built samples made from elementally blended NiTi powders to a solution heat treatment at 1000°C for 6h and 1050° for 10h, respectively. Nevertheless, they found that unwanted secondary Ni_3Ti and $NiTi_2$ phases were formed instead of being eliminated in the material after heat treatment.

In this study, a NiTi alloy was fabricated from elementally blended Ni and Ti powders using LPBF technique and heat-treated to improve microstructure homogeneity. The influence of the different heat treatments on the microstructure and phase composition of the LPBF fabricated specimens was investigated. Moreover, the aim of this study was to design a heat treatment that homogenizes the microstructure and prevents porosity increase. Three heat treatments were proposed to achieve our research goals: (1) A one step heat treatment at a temperature of 1100°C; (2) A one step heat treatment at a temperature of 900°C; and (3) a two-step heat treatment, with the first step at a temperature of 900°C and a second one at 1150°C. Moreover, for the first time the oxygen stabilization of the Ni_2Ti phase that resulted in formation of thermodynamically stable Ni_2Ti_4O phase was revealed in the *in situ* alloyed NiTi.

5.2. Materials and Methods

Powder of nickel (purity 99.9%, TLS Technik, Germany) and titanium (grade 1 purity 99.7%, TLS Technik, Germany) were mixed in a tumbling mixer for 2h, without any additives, to achieve a homogenous mixture of the NiTi alloy having a composition of $Ni_{55.7}Ti_{44.3}$ which corresponds to pre-alloyed NiTi, used in our previous study [220]. For both powders a particles size of <45µm was used. A Realizer SLM 50 (Realizer GmbH, Borchen, Germany) was employed for the laser powder bed fusion (LPBF) fabrication of cylindrical samples with a diameter of 6 mm and a height of 10 mm. Argon gas was used as a protective gas and the oxygen level was kept below 0.3 vol.%. Samples were fabricated on a NiTi substrate which was maintained at 200°C. An alternating scanning strategy including additional remelting after the first laser scanning was employed, thus each solidified layer was exposed to the laser beam two times. A laser power of 30 W and a scanning speed of 500 mm/s were used for first melting, while a slightly decreased laser power of 25 W and a scanning speed of 1000 mm/s were used for remelting. The layer thickness was set to 25 µm. The manufacturing procedure has been previously described in detail [230].

Annealing heat treatment (HT) was performed using an Elmor-1100 furnace (Falodlew, Poland). This was carried out in a vacuum, using sealed quartz tubes using the parameters described in Table V.1. The heating rate for each HT was fixed at 10°C/min. After annealing, all samples were water quenched.

The samples were exposed to three different heat treatments denoted as HT1-HT3. The parameters of the HT1 heat treatment were chosen based on the literature [51,82,163] while HT2 and HT3 were chosen directly based on the Ni-Ti phase diagram (Figure V.1) to avoid liquid phase formation. The liquid metal has a bigger volume than its solid state, thus, the melt pool shrinking during solidification results in the formation of voids (pores). This phenomenon was observed for HT1 heat treatment and is discussed extensively in this article in the discussion section. Therefore, the aim behind the HT2 and HT3 heat treatments was to minimize liquid phase formation during annealing to prevent further void formation. The proposed HT1 and HT2 are single step annealing heat treatments at 1100 and 900°C respectively, followed by immediate water quenching. The HT3 is a two-step heat treatment: firstly, samples were heated up to 900°C and held for 24h, then the temperature was increased to 1150°C (based on the DTA results) and held for another 24h. Annealing time for HT2 and HT3 was increased to 24h based on the literature to extend the diffusion time of alloying elements according to Fick's second law [234–236]. Samples were water quenched immediately after the second step of annealing. Water quenching was performed to retain NiTi phase and prevent the formation of brittle intermetallic phases i.e. $NiTi_2$, Ni_3Ti, Ni_4Ti_3 [188–190].

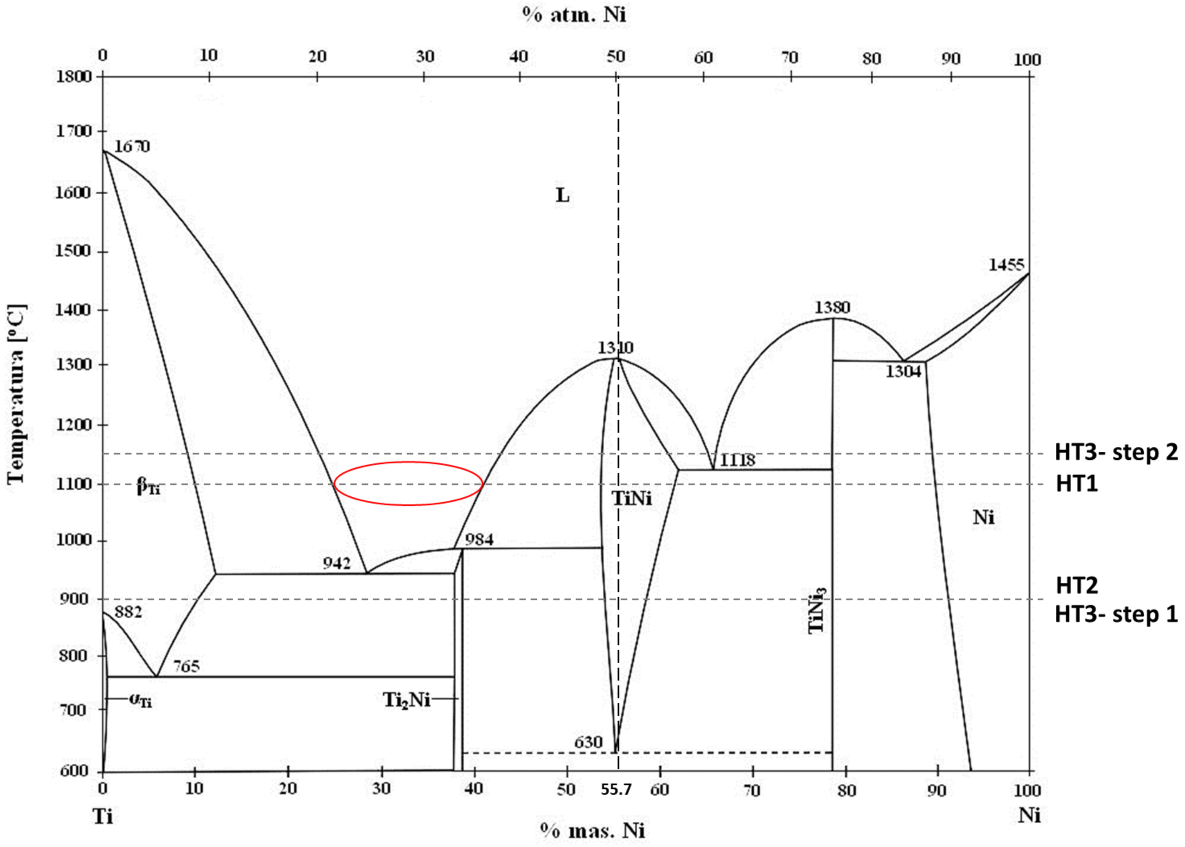

Figure V.1 Phase diagram of the Ni-Ti system [95]. *The horizontal dashed lines represent the temperatures of the HT1-HT3 heat treatments; The vertical dashed line represents the composition of the initial Ni-Ti powder blend studied in this work; the red circle indicates the local concentrations for which there is a liquid phase at 1100 °C.*

Table V.1 Parameters of the heat treatments of in situ alloyed NiTi fabricated by LPBF

Name	Number of steps	Temperature [°C]	Time [h]
HT1	1	1100	10
HT2	1	900	24
HT3	2	900+1150	24+24

After the heat treatment samples were mounted in epoxy and mechanically polished on a Saphire 550 grinding and polishing machine (ATM Qness GmbH, Germany) using SiC grinding papers (from #600 to #2000), and subsequently polished using 0.1 μm alumina oxide suspensions. Light microscopy (LM) was performed on Axio Scope Microscope (Zeiss, Germany). Porosity was determined by the Archimedes' principle. Each sample was weighed three times, non-consecutively, in air and water using an electronic balance with ± 1 mg of accuracy. Scanning electron microscopy (SEM) observations using backscattered electron (BSE) detector (SU-8000, Hitachi, Japan) at 5kV and energy dispersion spectroscopy (EDS) analysis at 10 kV were used to reveal the chemical composition. To determine the phases present, in the as-built NiTi alloy and after different heat treatments, X-ray diffraction (XRD) was performed at room temperature using a Bruker D8 Advance diffractometer (Bruker, Germany) with filtered Cu Kα ($\lambda = 0.154056$ nm) radiation. The XRD machine parameters were as follows: voltage 40 kV, current 40 mA, angular range 2Θ from 20° to 55°, step $\Delta 2\Theta$ 0.05° and dwell time 3 s. The XRD patterns were analysed using Bruker EVA software and a PDF-2 database (from the International Centre for Diffraction Data). A Labsys DTA/DSC (Setaram, France) differential thermal analysis (DTA) machine, with heating/cooling varying between room temperature to 1500°C at a rate of 40°/min, was used to determine the $NiTi_2$ transformation temperature. In order to identify phases present in the HT3 sample, a cross-sectional membrane (thin foil) of the selected region was prepared by a focused ion beam (FIB) system (NB5000, Hitachi, Japan). Subsequently, their microstructure was studied using a transmission electron microscope (TEM) JEOL JEM 1200 (JEOL, Japan) operated at 120 kV.

A TCH 600 Nitrogen/ Oxygen/ Hydrogen determinator (LECO, USA) was used to determine the content of oxygen in all fabricated samples. The elements are converted to their oxidized form by utilizing the gas fusion method and the infrared absorption (IR) is used to measure combustion gases within a metallic sample.

5.3. Results

5.3.1. Microscopic observation and phase analysis

The as-built and heat-treated samples were subjected to light microscopic observations. Microstructures of all samples are shown in Figure V.2. Pores are evident in each sample and show a spherical morphology. The porosity of the samples was determined by the Archimedes principle. For HT1 heat treatment, the phenomenon of the formation of the liquid phase, described in the discussion section, appeared in the sample. This caused the material porosity to increase remarkably. The porosity of HT1 sample is almost seven times greater than that of the as-built sample. However, the porosity measurement results of the as-built sample, as well as HT2 and HT3 samples are similar. No significant influence of heat treatment on the porosity of the sample was noticed and the slight differences in porosity are within the measurement error (Figure V.2). In addition, no increase in the number of cracks was observed in any of the heat-treated samples.

	as-built	HT1 1100°C / 10h	HT2 900°C / 24h	HT3 900°C / 24h + 1150°C / 24h
porosity	1.30 % (± 0.15 %)	8.97 % (± 0.38 %)	1.37 % (± 0.25 %)	1.41 % (± 0.32 %)

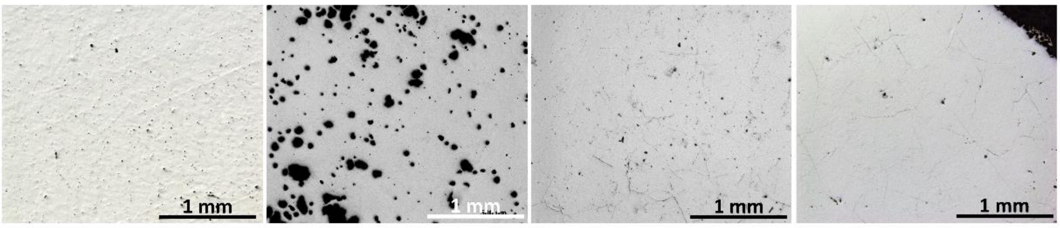

Figure V.2 Light microscopic observation and porosity results of as-built sample; HT1 (1000°C/10h), HT2 (900°C/24h), and HT3 (900°C/24h + 1150°C/24h) heat-treated samples.

The XRD results of the as-built and heat-treated samples are shown in Figure V.3. The XRD patterns of the as-built sample showed the presence of multiple phases, including NiTi (B2) [237] and (B19')[238], $NiTi_2$[239], Ni_2Ti_4O [239], Ni_3Ti [240]and Ni_4Ti_3 [241]. A distinct change in the phases was observed in the heat-treated samples. After each heat treatment only NiTi (B19'), (B2), $NiTi_2$ and Ni_2Ti_4O phases were identified. Since NiTi (B19'), $NiTi_2$ and Ni_2Ti_4O peaks overlap each other, it is not possible to distinguish them on XRD.

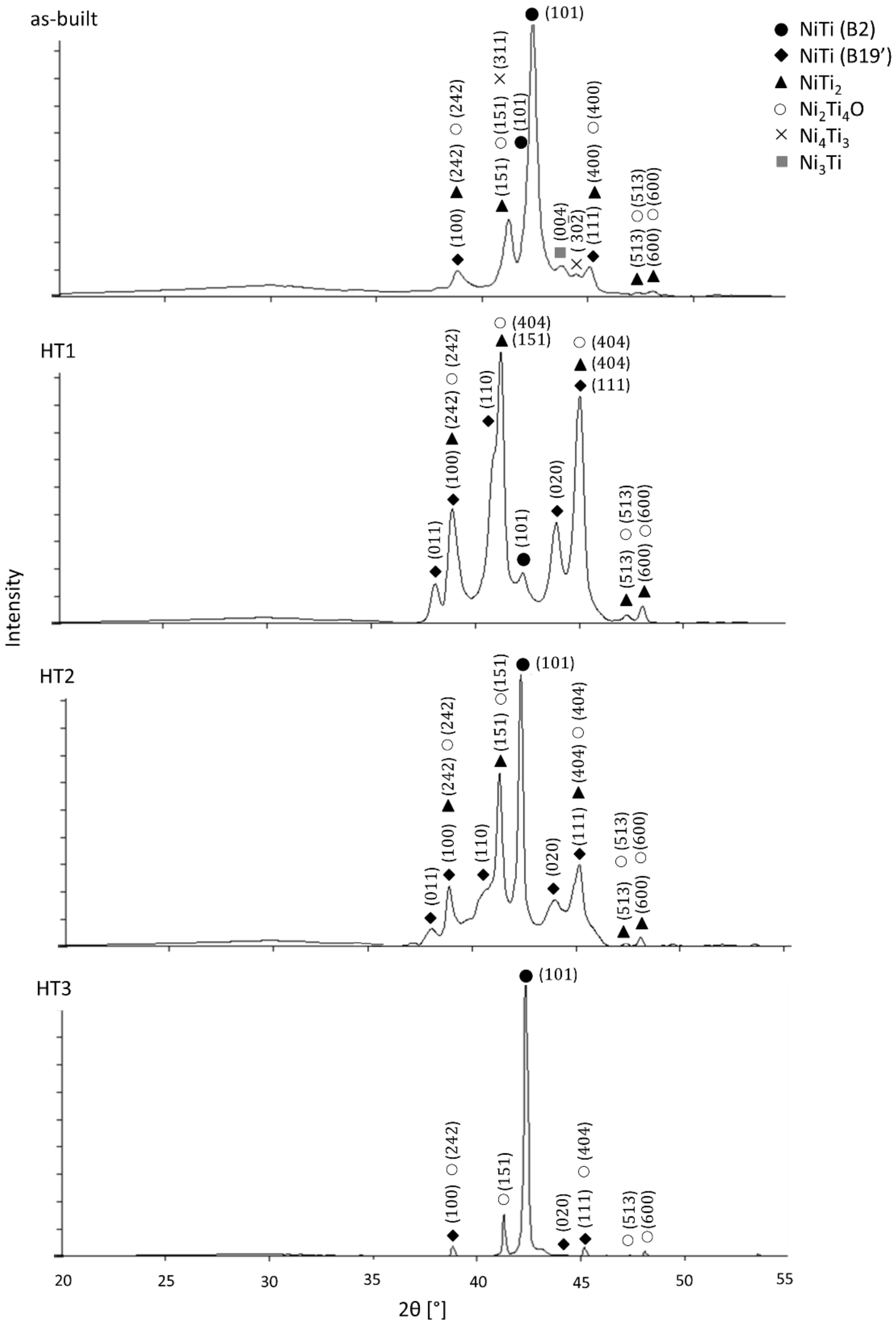

Figure V.3 XRD diffractograms of as-built and HT1 (1000°C/10h), HT2 (900°C/24h), and HT3 (900°C/24h + 1150°C/24h) heat-treated samples.

The phase composition homogeneity of the samples and the microstructures were captured by SEM BSE observations, as illustrated in Figure V.4. The SEM BSE images of the as-built sample indicated a large heterogeneity of the chemical composition. EDS analysis (Figure V.5) was performed to determine the Ni and Ti distribution in the as-built material.

Distinct differences in contrast indicate the presence of titanium-rich (dark) and nickel-rich (bright) areas. In the case of heat-treated samples, only two different phases can be distinguished in the images, the dark-shaded titanium-rich phase, and the bright-shaded nickel-rich phase. EDS point analysis showed the presence of the oxygen in some regions of a dark-shaded phase in samples HT1-HT3; however, the presence of the oxygen was not detected in all regions of the phase in HT1 and HT2 samples. Therefore, the dark-shaded areas consist of $NiTi_2$ and/or Ni_2Ti_4O phases. More detailed analysis of the phase composition of dark-shaded phase in each sample is discussed in paragraph 4. Based on the SEM BSE images, the percentage amount of the dark-shaded Ti-rich phases in each of the tested samples was calculated in the Micrometer software (Micrometer, Poland) using the method described by Wejrzanowski et al. [15], [16] (Table V.2). The greatest amount of dark-shaded phase is found in the HT2 sample (26 ± 4%), while the least amount was found in the HT3 sample (12.5 ± 0.5%). The amount of dark-shaded phase in HT1 sample was 18 ± 2%. It was found that the dark-shaded phase in HT1 and HT2 samples is finer and has a more irregular shape than the phase in the HT3 sample, which is larger and has a nearly spherical shape. The presence of C, Si and W elements detected by EDS (Figure V.5) is a result of surface contamination that remains from materials used for surface polishing and preparation for TEM observations.

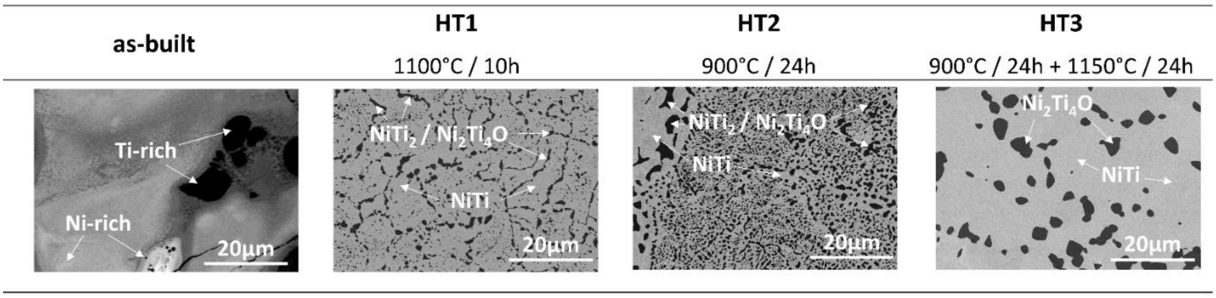

Figure V.4 BSE SEM observation of the as-built sample; HT1 (1000°C/10h), HT2 (900°C/24h), and HT3 (900°C/24h + 1150°C/24h) heat-treated samples.

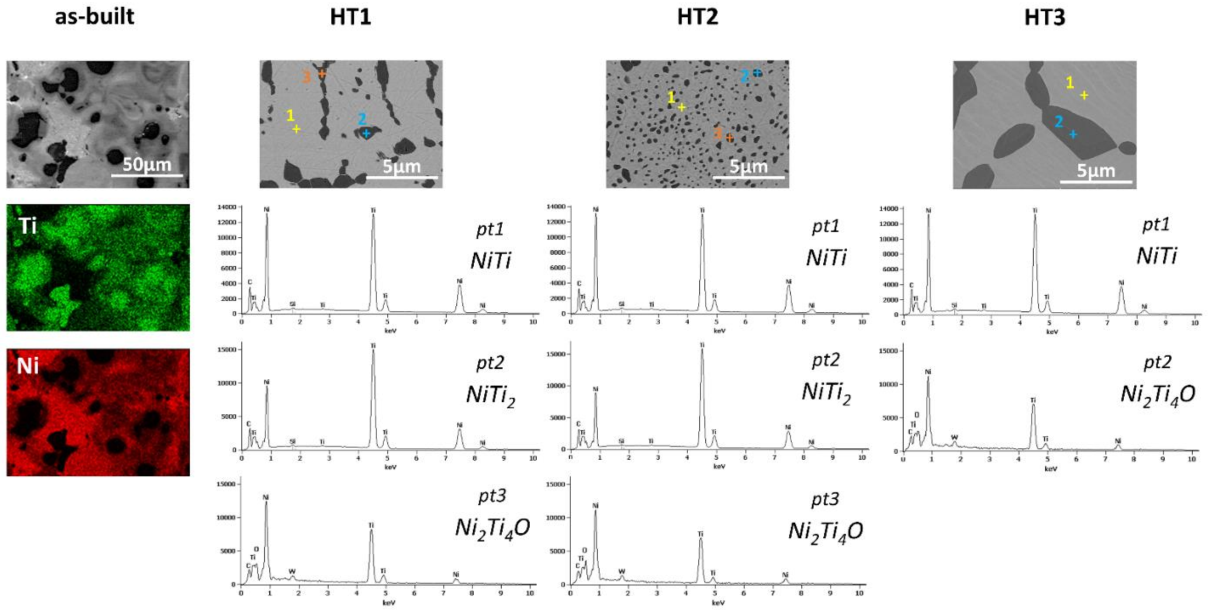

Figure V.5 EDS mapping of the as-built sample indicates that the dark shaded areas are titanium-rich and bright shaded areas are nickel-rich; EDS point analysis revealed the presence of Ni, Ti and O elements

Table V.2 The volume fraction of $NiTi_2$ / Ni_2Ti_4O *phases in HT1-HT3 samples.*

	HT1	**HT2**	**HT3**
$NiTi_2$ / Ni_2Ti_4O volume fraction (%)	18 ± 2	26 ± 4	12.5 ± 0.5

5.3.2. Differential Thermal Analysis

The Differential Thermal Analysis (DTA) test was performed on the HT2 sample to determine the $NiTi_2$ phase transformation behaviour and indicate its melting temperature (Figure V.6). The results indicated that the $NiTi_2$ melts at about 1128°C.

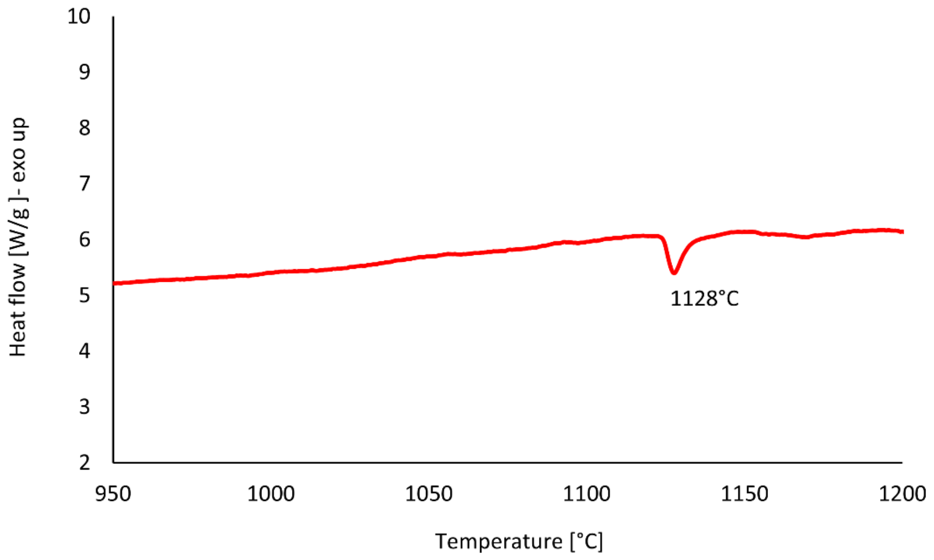

Figure V.6 DTA trace of HT2 (900°C/24h) sample shows that $NiTi_2$ melts at about 1128°C and solidifies during cooling at about 1113°C.

5.3.3. Transmission Electron Microscopy

For a more detailed examination of the dark-shaded phase in HT3 sample (Figure V.4), (that was not removed after HT3, as expected) Transmission Electron Microscopy (TEM) was performed. Figure V.7 shows a bright-field image of NiTi matrix and a corresponding SAED pattern. The matrix consists of B2 cubic austenite and B19' monoclinic martensite phases as presented by Dutkiewicz *et al.* [242]. The crystallographic relationship (001) B2 II (011) B19'and [100] B2II [100] B19' results from SAED pattern. Figure V.8 shows particles present in NiTi matrix with a corresponding selected area electron diffraction (SAED) from a single particle. One can expect to find $NiTi_2$ or Ni_2Ti_4O (Figure V.8) which are in the same crystal system and possess approximately the same lattice parameter. However, the differences between intensities of diffraction spots from {311} and {331} planes on the diffraction pattern enabled the identification of the Ni_2Ti_4O phase; a phase having XRD peaks overlapping $NiTi_2$. Moreover, in the case of $NiTi_2$ phase the intensity from the diffraction spot from {311} planes would be negligible contrary to Ni_2Ti_4O phase.

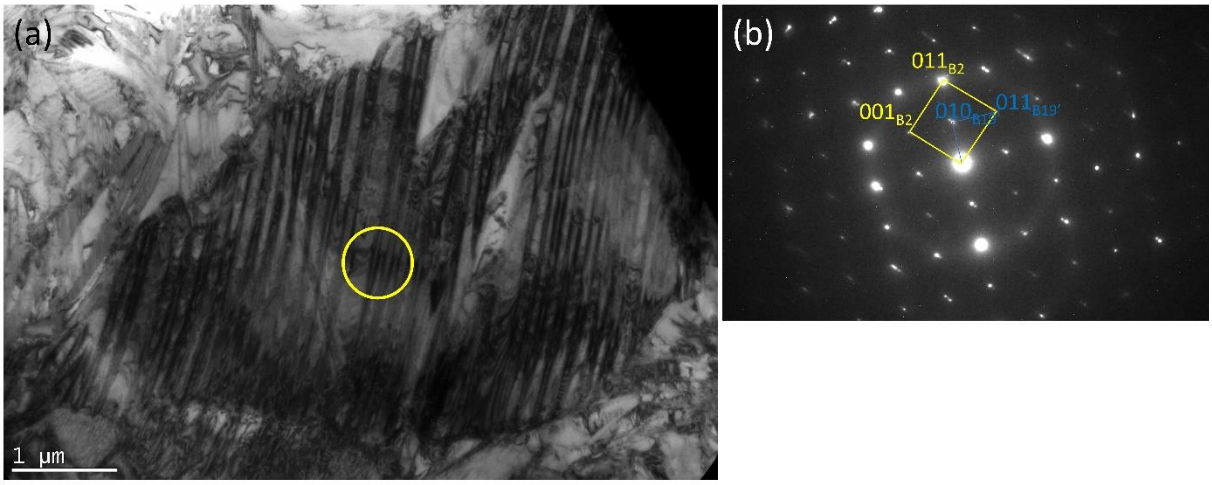

Figure V.7 (a) A bright-field image of the NiTi matrix; (b) with a corresponding SAED pattern from an area marked by a yellow circle).

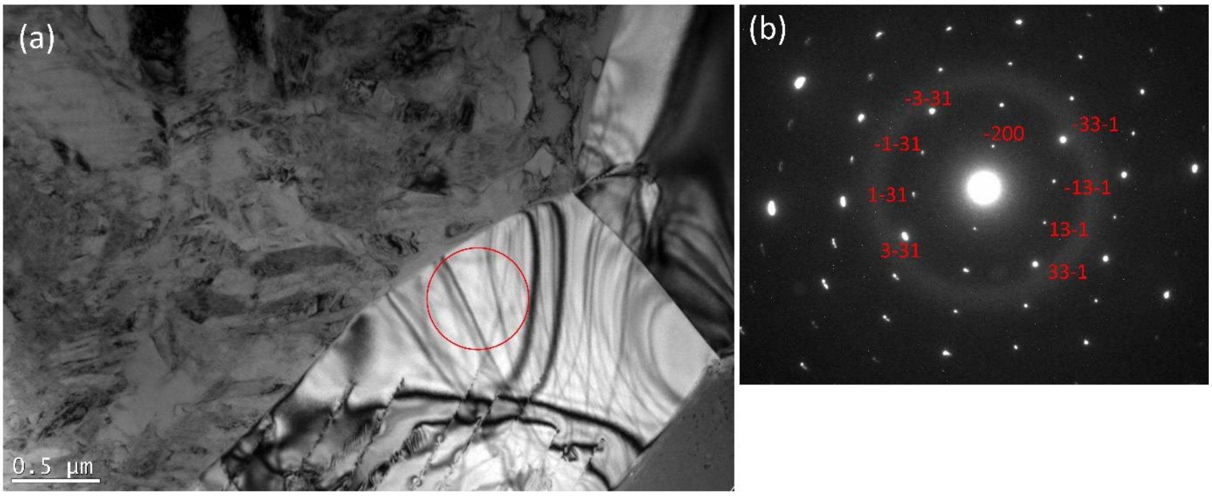

Figure V.8 (a) TEM image of NiTi matrix with Ni_2Ti_4O particles; (b) SAED of Ni_2Ti_4O in the orientation [013].

5.3.4. *Oxygen content*

The oxygen content in all samples was analysed to check whether the oxygen, that caused the formation of the Ni_2Ti_4O phase, could have dissolved in the sample during the LPBF fabrication or the heat treatment. The presence of 0.52 to 0.54 wt.% of the oxygen is observed in all samples. There are no significant differences in the oxygen content between the as-built and heat-treated samples. Thereby, it can be assumed that oxygen was dissolved in the sample during the LPBF fabrication, and this stabilized the Ni_2Ti_4O phase.

Table V.3 Oxygen content in as-built and HT1-HT3 samples.

	as-built	**HT1**	**HT2**	**HT3**
oxygen content (wt.%)	0.52 ± 0.1	0.53 ± 0.1	0.54 ± 0.2	0.52 ± 0.1

5.4. Discussion

The $Ni_{55.7}Ti_{44.3}$ alloy was fabricated by laser powder bed fusion (LPBF) from elementally blended nickel and titanium powders and the high chemical and phase composition heterogeneity suggested that heat treatment is necessary to improve homogeneity. Therefore, three heat treatments were applied to solve this technical problem.

As-built sample

Microscopic observation of as-built samples is presented in Figure V.2. It shows that the sample is free of cracks or delamination and has a porosity of 1.30 %. SEM observations in BSE mode showed the heterogeneity of the chemical composition of the sample (Figure V.4). The Ti-rich and Ni-rich areas were revealed by EDS (Figure V.5), meaning that components were not fully alloyed during laser melting. XRD phase analysis (Figure V.3) indicated the presence of NiTi (B2) and NiTi (B19'), $NiTi_2$, Ni_2Ti_4O, Ni_3Ti, and Ni_4Ti_3 phases. Therefore, heat treatment of the manufactured alloy is necessary to homogenise its chemical and phase composition.

First heat treatment- HT1

In the first heat treatment, HT1, the temperature and time were determined based on the literature. Wang *et al.* [51] employed LPBF to manufacture a NiTi alloy from elementally blended Ni and Ti powders and subjected the fabricated samples to a solution heat treatment at 1000°C for 6h, and subsequently quenched in water. Halani and Shin [163] fabricated NiTi coupons using elementally blended powders by the flow-based direct energy deposition (DED) method and heat-treated them at 1050°C for 10h, with the subsequent quenching in water. In the work presented by Li *et al.* [82] a additively manufactured NiTi alloy was heat-treated at temperatures that were determined based on DSC tests. It was concluded that $NiTi_2$ in the alloy studied by Li *et al.* [82] has a melting temperature of 1010°C. Thus, they performed heat treatment at a temperature close to the determined $NiTi_2$ melting point (1010°C). When analysing the Ni-Ti phase diagram (Figure V.1), it can be seen, that the widest range of NiTi phase presence (49-57 at. % of Ni) occurs at 1118°C. The temperature of HT1 was determined based on the literature review and the Ni-Ti phase diagram analysis. Therefore, HT1 was performed at 1100°C for 10h. Microscopic observation of HT1 sample was shown in Figure V.2 and the presence of large spherical pores was revealed. The porosity of the sample was 8.97 %. EDS analysis showed the presence of the oxygen in some regions of a dark-shaded phase (Figure V.5), however, the presence of the oxygen was not detected in all regions of the phase. SEM BSE observations (Figure V.4), EDS analysis (Figure V.5) and corresponding XRD analysis (Figure V.3) determined the presence of NiTi (B2), NiTi (B19'), $NiTi_2$ and Ni_2Ti_4O phases. The Ni_3Ti and Ni_4Ti_3 phases on the other hand were eliminated. The amount of dark-shaded $NiTi_2$ and Ni_2Ti_4O phases in HT1 sample was 18 ± 2%. Although the microstructure was significantly homogenized, the porosity of the sample increased almost seven times.

Morris and Morris [243] examined different techniques for the sintering of Ni and Ti elemental powders. They found that when samples are sintered at high temperatures, where melting of a phase occurs, high porosity is generated in the material. Moreover, they noticed a large heterogeneity in the microstructure of sintered samples. They concluded that homogeneity of the material can be increased due to solid-state interfusion, occurring at temperatures below 900°C, when no liquid phase appears in the material. In our study, the occurrence of Ti and Ni-rich regions were presented in the as-built sample (Figure V.4). According to the Ni-Ti phase diagram (Figure V.1), the liquid phase occurs at the temperature of 1100°C in a wide range of compositions; especially 27 to 38 wt. % of Ni. The liquid phase of a material has a larger volume than its solid counterpart, therefore, during cooling, the material will shrink, resulting in voids. These voids induced porosity that is observed in Figure V.2.

Second heat treatment- HT2

The second heat treatment, HT2, was aimed at homogenizing the microstructure and composition at a temperature that does not allow any phase to liquify, since this could generate high porosity. Various conditions of material fabrication and, inter alia, the presence of internal stresses can influence the melting temperature (increase or decrease it) of materials [244]. To this effect, HT2 was performed at 900°C, i.e., well below the lowest transition temperature of titanium-rich phases to the liquid state (942°C). The HT2 time was extended to 24h to increase the diffusion time according to Fick's second law [234–236]. Microscopic observations and porosity measurement results (Figure V.2) showed that the porosity has not increased and is well below to that found in HT1 sample. Thus, the reduction of the heat treatment temperature avoided pores formation caused by the melting of the Ti-rich phases. SEM BSE images (Figure

V.4) revealed the presence of two phases. The presence of oxygen was revealed by EDS in some areas of dark-shaded phase in HT2 sample (Figure V.5). XRD analysis (Figure V.3) confirmed that the samples consisted of B2, B19', $NiTi_2$ and Ni_2Ti_4O phases. It has been observed that both HT2 and HT1 reduced the number of phases when compared to the as-built samples. The amount of dark-shaded phases in HT2 sample was 26 ± 4% (Table V.2). Due to the fact that HT1 was conducted at a temperature 1100°C that is close to the solubility of the $NiTi_2$ phase in the fabricated material (1123°C), more of it diffused into the surrounding phase, than it was for HT2, which was carried out at a lower temperature (900°C). Thus, the highest amount of dark-shaded $NiTi_2$ and Ni_2Ti_4O phases remained in the HT2 sample.

Since $NiTi_2$ is a brittle phase, it favours cracks formation and decreases the ductility [245] and it would be therefore beneficial to eliminate the presence of this phase. DTA analysis, shown in Figure V.6, was performed to determine the melting temperature of $NiTi_2$ phase formed in HT2 heat-treated sample. The melting temperature of the $NiTi_2$ phase in the studied alloy was at 1128°C. Based on this result, it was expected that the annealing heat treatment at a temperature slightly above the melting point of the $NiTi_2$ phase will allow the diffusion of the elements and the elimination of the phase from the alloy. According to the Ni-Ti phase diagram (Figure V.1), the liquid phase is present for a wide range of Ti concentrations (~75 to 60 wt. %) at 1100°C. Direct annealing conducted above this temperature leads to pronounced, local melting of the material resulting in voids formation after the heat treatment routine. Initial annealing at temperatures where only solid phases exist activates diffusional homogenization and accelerates the formation of the ordered structures which are thermodynamically favoured over solid solutions due to low enthalpies of formation [246]. In such scenario, the temperature of a second annealing step can be adjusted to eliminate the unwanted phase by heating the material slightly above the thermal stability of the selected, ordered structure. In this case, the amount of the liquid phase is minimal, and melted elements will diffuse to neighbouring phases and/or form other, intermetallic compounds stable at given thermodynamic conditions. To conclude, the HT2 heat treatment improved the homogenization of the chemical composition, however, the $NiTi_2$ and Ni_2Ti_4O phases remained within the alloy. Therefore, the HT3 heat treatment has been designed and performed to eliminate the $NiTi_2$ and Ni_2Ti_4O phases.

Third heat treatment- HT3

Based on the observations made and discussed above, the third heat treatment, HT3, was designed to eliminate from the alloy the $NiTi_2$ phase through a two-step annealing treatment. Firstly, the samples were heated to 900°C for 24 hours to diffuse the elements and homogenise the chemical composition. Secondly, the samples were immediately heated to 1150°C (no cooling between steps) and annealed for 24 hours. After the second step was completed, samples were immediately water quenched. Since DTA analysis (Figure V.6) showed that the $NiTi_2$ phase melts at 1128°C, it was expected that annealing just above the melting point, thus at 1150°C, should allow the elements to diffuse into the NiTi phase and 1150°C temperature was chosen for our study. The motivation behind the selection of the two annealing temperatures arises from the thermal stability of intermetallic compounds occurring in Ni-Ti mixtures. It is expected that laser melting of commercially pure Ti and Ni elemental powders can lead to local Ti-rich or Ni-rich regions, which favour crystallisation of $NiTi_2$, Ni_4Ti_3, or Ni_3Ti phases. The main goal behind the adopted annealing treatments is chemical homogenisation of the fabricated material, however, due to possible local inhomogeneity, the maximum temperature of heat treatment (1150°C) was chosen slightly above the stability of $NiTi_2$ (1128°C) to minimize the risk of formation of a large amount of liquid phase inside the samples. Microscopic observations of HT3 sample and porosity measurement results (Figure V.2) showed, that the porosity did not significantly increase compared to the as-built sample. SEM BSE observation (Figure V.4) and the calculation of the dark-shaded phase volume fraction content (Table V.2) revealed that when compared to HT1 (18 ± 2%) and HT2 (26 ± 4%) samples there was a reduction of dark-shaded phase and its amount in HT3 sample was 12.5 ± 0.5%. It should be noted that the phase was not completely eliminated. Moreover, EDS analysis revealed the presence of oxygen in all regions of the dark-shaded phase (Figure V.5). Recent studies on NiTi alloys have suggested that $NiTi_2$ phase can be stabilized by oxygen. The presence of Ni_2Ti_4O phase in NiTi alloy was reported by Kai *et. al.* [125] and Frenzel *et al.* [102]. $NiTi_2$ can absorb oxygen up to 14 at. % without changing its FCC crystal structure [247]. Oxygen can dissolve in the $NiTi_2$ structure, and cause it to transform into a thermodynamically stable oxygen-rich Ni_2Ti_4O oxide phase [125]. Both $NiTi_2$ and Ni_2Ti_4O are crystallographically very similar to each other, both possess FCC structure, thus, it is impossible to distinguish them apart using the XRD technique [248]. Hiroyuki *et al.* [247] stated that the Ni_2Ti_4O phase in NiTi alloys cannot be eliminated even after two annealing heat treatments at 900°C. In the HT3 sample NiTi (B2), NiTi (B19’), and $NiTi_2$ / Ni_2Ti_4O phases were identified by XRD (Figure

V.3). The XRD phase analysis has not indicated the presence of TiO_2. However, it was shown in our previous study that the thin layer of TiO_2 was found on the material's surface by X-ray photoelectron spectroscopy (XPS) [249]. Since the peaks corresponding to NiTi (B19'), $NiTi_2$ and Ni_2Ti_4O overlap each other the XRD technique cannot be used alone to determine which phase is present in the studied alloy. To this effect, TEM was performed to confirm whether the analysed dark phase, shown in Figure V.4, was $NiTi_2$ or Ni_2Ti_4O. TEM analysis of the matrix revealed the presence of both B2 and B19' phases (Figure V.7). Furthermore, the differences between intensities of diffraction spots on the diffraction pattern enabled the identification of the dark phase as Ni_2Ti_4O (Figure V.8). Based on this, the oxygen content in the chemical composition of the studied samples was determined and was found in all samples to be 0.52 to 0.54 % (Table V.3). Since the amount of oxygen in the as-built sample is comparable to all the heat-treated samples, it can be concluded that oxygen was introduced into the samples during the LPBF fabrication and not during heat treatment. The Realizer SLM50 machine used for samples fabrication does not provide a 100 % pure oxygen-free atmosphere since the oxygen level in the building chamber during the fabrication process was about 0.3 vol. %. The oxygen residuals in the machine chamber caused oxygen pickup by the NiTi during the LPBF process, in a similar way to oxygen pickup by other materials reported in recent studies [206,220]. As was shown in this study, it is subsequently difficult to remove unwanted secondary phases from the material applying heat treatments. The negative effect of oxygen residuals and other side effects of powders processing in an inert atmosphere can be eliminated during additive manufacturing processes by using a vacuum [250,251]. Vacuum LPBF processing, which is a relatively new technique for AM processes, could avoid the stabilization of the unwanted secondary phases, such as the $NiTi_2$ phase. Therefore, further research should focus on the elimination of oxygen from the building chamber. Moreover, the issue of the as-built material heterogeneity can be eliminated during AM processes using machines that give the possibility to fabricate materials at elevated temperatures. For this reason, the fabrication at elevated temperatures (above 500°C) would be implemented to perform *in situ* heat treatment during the LPBF process. Consequently, the transformation temperatures of the fabricated materials would be further investigated using differential scanning calorimetry, as described by Martins et. al [252].

5.5. Conclusions

Laser powder bed fusion (LBPF), using a remelting scanning strategy and elementally blended Ni and Ti powders, was used to additively manufacture NiTi alloys. Since the as-built components possessed a heterogeneous chemical and phase composition, three different annealing heat treatments were designed and applied. The study led to the following main conclusions:

- The selected two-step HT3 heat treatment condition (900°C/24h + 1150°C/24h) allows for the significant homogenization of the chemical and phase composition of the LPBF *in situ* alloyed NiTi components;
- The Ti-rich phases in the as-built material melt during the chosen HT1 temperature (1100°C) and upon solidification shrinkage occurs resulting in pore formation;
- Oxygen pickup during the LBPF manufacturing process promoted the formation of a thermodynamically stable oxygen-rich Ni_2Ti_4O phase that is observed even after an annealing heat treatment;
- LPBF combined with post annealing is a promising way of fabricating NiTi alloys using elemental powder blends. Elimination of the oxygen pickup during the process and decrease of the possibility for formation of the oxides like Ni_2Ti_4O could be reached by providing process in vacuum conditions, however further study proving this hypothesis should be performed.

Chapter VI

Chemical Polishing of Additively Manufactured, Porous Nickel-Titanium Skeletal Fixation Plates

Agnieszka Chmielewska, Ahmadreza Jahadakabar, Bartłomiej Wysocki,
Mohammad Elahinia, Wojciech Święszkowski, David Dean

Published in: 3D Printing and Additive Manufacturing,

DOI: 10.1089/3dp.2020.0209

Abstract

Nickel-titanium (NiTi) alloys have been shown promise for a variety of biomedical applications because of their unique properties of shape memory, superelasticity, and low modulus of elasticity (Young's modulus). Nevertheless, NiTi bulk components cannot be easily machined (e.g., CNC, rolling, grinding, casting, or press molding) due to their thermomechanical sensitivity as well as inherent superelasticity and shape memory. Thus, powder bed fusion (PBF) additive manufacturing, has been used to successfully fabricate NiTi medical devices that match the geometric and mechanical needs of a particular patient's condition. However, NiTi PBF fabrication leaves unmelted particles from the source powder adhered to external surfaces, which cause minor dimensional inaccuracy, increase the risk of mechanical failure, and once loose may irritate or inflame surrounding tissues. Therefore, there is a need to develop a chemical polishing (cleaning) technique to remove unmelted powder from the surfaces of PBF-fabricated implants, especially from inner surfaces that are difficult to access with mechanical polishing tools. This technique is especially useful for highly porous devices printed at high resolution. In this study, a chemical polishing method utilizing HF/HNO_3 solution was used to remove loosely attached (i.e., unmelted) powder particles from surfaces of porous, skeletal fixation plates manufactured by PBF AM. It was observed that 7 min of polishing in an HF/HNO_3 solution comprising 7.5 HF: 50 HNO_3: 42.5 H_2O enabled successful removal of all relatively loose and unmelted powder particles. A microcomputed tomography study examination found that the volumetric accuracy of the polished skeletal fixation plates was ±10% compared with the computer-aided design (CAD) model from which it was rendered. This postprocessing chemical polishing protocol is also likely to be useful for removing loose powder while maintaining CAD model accuracy and mechanical stability for other complexly shaped, porous, three-dimensional (3D), printed NiTi devices.

6.1. Introduction

Nickel-titanium (also known as nitinol, NiTi alloy) is a shape memory alloy that is widely used in aerospace, civil, and biomedical applications [8,94,175,253–256]. NiTi alloys have tunable superelasticity and shape memory properties. These two unique properties are mainly due to the fact that NiTi alloys are able to undergo a reversible solid-state phase transformation in response to stress or a change of the temperature between the austenite and martensite phases[10,103]. Moreover, this material exhibits high corrosion resistance and is biocompatible when properly alloyed[256]. However, shape memory and superelasticity properties, as well as its high reactivity and ductility [135], make machining and processing of NiTi a challenging task. Therefore, the use of conventional manufacturing methods to render complex geometries are imprecise, expensive, time-consuming, and in some situations impossible [11,151,257]. However, additive manufacturing (AM) methods are relatively new, attractive alternatives for the fabrication of complex geometries from a wide range of materials including NiTi[113,151], titanium [258,259], nickel [260,261], and other alloys [28,262] directly from a computer-aided design (CAD) file. Thanks to AM techniques for these metals, complexly shaped lattice or pore structures can be achieved that enable the manufacture of lightweight devices with engineered mechanical properties[263].

In recent years, these methods have been adapted for fabricating patient-specific implants and medical devices [85,103,150,263,264]. Due to the high difference in Young's modulus between bone and conventional implants, primarily fabricated from Ti-6Al-4V, stress shielding, and subsequent bone resorption may occur. Stress shielding may lead to bone resorption if medical device leads to insufficient loading of the reconstructed bone [70,75]. Among other metallic medical materials, NiTi alloy has a relatively Young's modulus and thus low stiffness. NiTi's Young's modulus ranges between 55 and 80 GPa, which is closer to compact bone (12-17 GPa) than for most commonly used titanium alloys ~110 GPa, stainless steel ~190 GPa, and cobalt-based alloys ~210 GPa [227]. Implant stiffness, which depends on its geometry and Young's modulus, can be reduced by introducing porosity through conventional methods [265,266] or by the use of multiple materials [267]. Nevertheless, conventional manufacturing methods may not provide sufficient control over strut and pore geometry and thus the mechanical properties, especially the attempt to surgically reconstruct normal stress-strain trajectories, may fail. Therefore, to solve these problems, AM technologies have recently been extensively explored to produce structures called scaffolds with engineered porosity and mechanical properties from biocompatible metal materials [83,256,268,269], polymers [61,83,270], ceramics and composites [271,272] .

Among metal AM techniques, we can distinguish powder bed fusion (PBF) (e.g., selective laser melting [SLM] and electron beam melting), and flow-based solutions (e.g., laser engineering net shaping or direct meal deposition) [273]. The SLM PBF has, to date, attracted the most attention and use for the creation of complexly shaped NiTi-based parts [11,157,257]. Current SLM PBF devices achieve rendering accuracy up to 20 μm [14,106]. This high accuracy allows parts to be built with confidence. However, setup parameters must be optimized allow achieving the necessary or, if needed, full accuracy.

One of the challenges is that PBF-fabricated metal parts have loose, unmelted powder particles fused to all external surfaces. This phenomenon is explained by the nature of the melt pool in PBF fabrication. The high-energy laser produces sufficient heat to create the melt pool at the surface of the powder bed [274]. The temperature surrounding the melt pool is immediately increased by heat conduction. However, by design, particles in this zone do not melt but may become lightly sintered to the surface of the part [275–277]. These loosely adhered particles may be released into adjacent tissue and can cause minor differences between the intended dimensions of the CAD model and the dimensions after the fabrication process and can lead to undesirable and unexpected mismatch with the modeled mechanical properties, especially in parts with small features [259,263,278]. Rough surfaces created by partially melted powder particles also increase stress concentrations and can cause early fatigue failure of the components. Thus, for these reasons, the loose powder particles sintered to the surfaces in PBF fabrication are undesirable and postprocessing is necessary to remove them.

Traditional surface treatments for biomaterials include mechanical polishing, sandblasting, and shot peening [176,279,280]; however, in areas where minute porous spaces do not allow for the application of mechanical cleaning devices, these methods are not feasible. In these instances, it may be possible to adequately remove loose powder particles through chemical and/or electrochemical polishing methods. During chemical polishing processes, the part’s material and the applied etchant undergo a chemical reaction that leads to removal of loose powder particles. The success of chemical polishing depends on the extent of this reaction, which in turn depends on the applied etchant, the temperature of etching, duration of etching, and applied agitation. For titanium and its alloys, chemical polishing in HF/HNO_3 (hydrofluoric acid/nitric acid) solution is well documented and has been extensively utilized [199,209,258,281]. Usually, this method involves the fabricated part being immersed in the cleaning solution to dissolve the area where powder particles are loosely sintered to the surface of the part. The goal of this activity is to remove loose powder, obtain the dimensions seen in the CAD file, and achieve the predicted short- and long-term mechanical properties (Figure VI.1)[199]. Additionally, if needed, the particle removal process can be enhanced with an ultrasonic bath device [281]. The proper composition of the solution, which allows effective removal of powder particles, and the appropriate polishing time must be determined experimentally. In addition, when the printed parts contain very fine features, the composition of the etchant and the duration of the procedure are critical parameters because excessive polishing will lead to removal of small features. Therefore, the outcome of the chemical polishing procedure must be carefully evaluated to make sure that critical features are not removed during polishing.

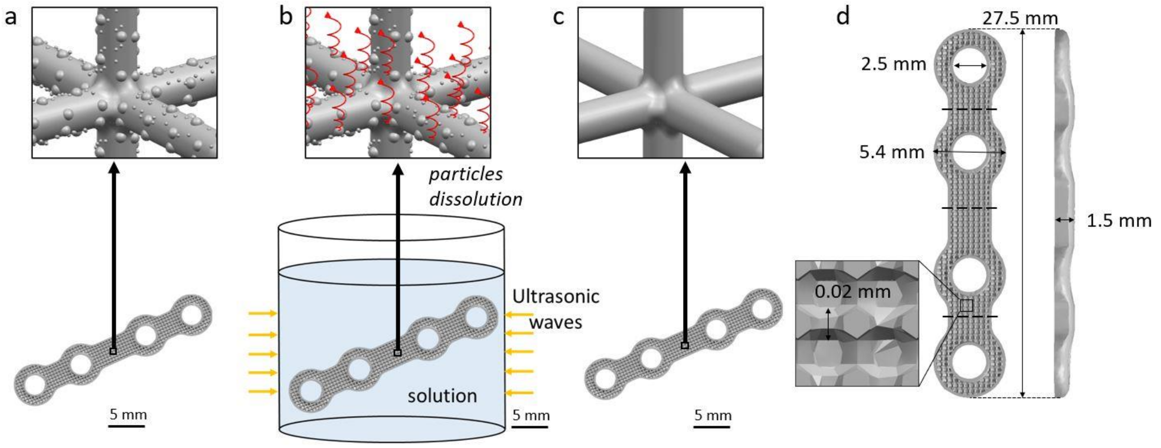

Figure VI.1 Chemical polishing postprocessing for removal of (a) unmelted powder particles sintered to the surface of a 3D printed skeletal fixation plate. (b) Powder particle dissolution in an appropriate cleaning solution is enhanced by the addition of ultrasonic wave energy. (c) Smooth part surface free of unmelted sintered particles. (d) Visualization and dimensions of the studied skeletal fixation plate CAD model with the scheme of functional components. 3D, three-dimensional; CAD, computer-aided design.

Chemical etching is commonly utilized to process NiTi and metallic parts. In the case of NiTi, it serves to remove surface contaminants, defects, and heavy deformation zones after cold drawing [282]. Moreover, previous studies have shown that chemical processing of NiTi is known to be efficient for elimination of defective surface layers and surface oxidizing [283,284] as well as surface structuring [176]. Additionally, chemical surface modification of NiTi elements for biomedical applications are performed to reduce cytotoxic nickel ion release from the surface. Furthermore, chemical polishing can roughen a smooth surface. It should be noted that two different types of roughness are observed on SLM-fabricated parts. The first type of roughness is created by partially melted powder particles adhering to the external surfaces. As previously noted, this is undesirable because the loose powder fused to the surface of medical devices may be released into adjacent tissues and lead to toxicity, infection, and allergic or foreign body reactions. The second type of roughness is generated by mechanical [285] and chemical methods[209,268] or by providing coatings [286]. This may enhance cell adhesion and proliferation and overall biointegration, which is desirable for some medical applications [282,287]. Chu *et al.* [288] used chemical etching of NiTi in HCl-HNO_3 pickling solution to remove struts created during a laser cutting process. Indeed, chemical polishing of NiTi has been mainly used for conventionally manufactured components. Chemical treatment of NiTi elements made by AM methods to remove unmelted powder particles from the surface and, more importantly, to verify the CAD dimensions and predicted mechanical function of a three-dimensional (3D) printed NiTi part using microcomputed tomography (μCT) scanning, to our knowledge, has not been previously done. Thus, the aim of this study was to develop a chemical polishing procedure to remove loosely sintered, unmelted powder particles from the surfaces of NiTi parts fabricated through an SLM PBF process. This protocol was tested to evaluate the possibility of ensuring CAD model dimensions and obtain mechanically reliable and biomedically safe skeletal fixation device surface.

6.2. Materials and methods

6.2.1. Fabrication procedure

Skeletal fixation plates with mechanical properties desirable for mandibular graft fixation were achieved, in part, by including custom-designed porosity. A SLM machine (3D Systems PXM, Rock Hill, SC), equipped with a 300 W ytterbium fiber laser, was used to produce Ni-rich NiTi skeletal fixation plates. A slightly Ni-rich Ni50.8Ti49.2 (at%) ingot was subjected to electrode induction melting gas atomization by TLS Technik GmbH (Bitterfeld, Germany) to produce the NiTi powder. To ensure adequate layer resolution and powder flow, particle size ranging from 25 to 75 μm was used. To minimize the level of impurity content within the resultant part, the oxygen level was decreased to 500 ppm before fabrication. Process parameters used in the fabrication are shown in the Table VI.1 (energy input is defined as $E=p/(v.h.t)$) [83,269,289]. The shape and dimensions of the fixation plate studied are shown in Figure VI.1d.

Table VI.1 Selective Laser Melting process parameters for fabrication of skeletal fixation plates

Laser power (p) [W]	**Scanning speed (v) [mm/s]**	**Hatch spacing (h) [µm]**	**Layer thickness (t) [µm]**	**Energy input (E) [J/mm^3]**
250	1250	80	30	83.33

6.2.2. Polishing procedure

The NiTi fixation plates were ultrasonically cleaned in deionized water before immersion in a beaker with HF/HNO_3 acid solutions. The HF/HNO_3 solutions used to remove attached (i.e., unmelted and sintered) powder particles, were as follows: solution 1: 10 HF: 40 HNO_3: 50 H_2O (S1); solution 2: 3.3 HF: 13.9 HNO_3: 82.8 H_2O (S2); and solution 3: 7.5 HF: 50 HNO_3: 42.5 H_2O (S3). The compositions of solutions S1 and S2 compositions were selected on the basis of the literature *[268,288,290]*, while the S3 composition was based on characterization of the fixation plates polished in Solutions S1 and S2. The assessment of Solutions S1 and S2 was done with partial plate sections (Figure VI.1d), while full size skeletal fixation plates were used for the analysis of polishing via Solution S3. Solution ratios, polishing times, and reagent concentrations are presented in Table VI.2. Moreover, additional polishing in Solution S3, referred to as “re-polishing”, was applied to samples that were also studied by µCT scanning (Table VI.3). The re-polishing was done to achieve a total polishing time of 7 min. This experiment allowed us to determine whether re-polishing could be used successfully with NiTi plates when the process of polishing is interrupted, an insufficient amount of powder would be removed. All of the polishing and re-polishing experiments were carried out in an ultrasonic bath at room temperature. After all chemical polishing procedures, polished samples were rinsed with DI water and cleaned in an ultrasonic bath of DI water. Each sample was ultrasonically cleaned 3 times for 10 minutes to remove all remaining acid [291]. The DI water was replaced after each iteration of ultrasonic cleaning.

The polishing times were adapted according to the observations of polishing speed, as determined by the intensity of gas released from the plate’s surface during the immersion.

Table VI.2 Chemical composition of test solutions and polishing time

Solution	**Component volume [ml]**			**Polishing time [min]**
	HF (40%)	HNO_3(60%)	H_2O	
S1	10	40	50	3, 4, 5, 6, 7
S2	3.3	13.9	82.8	3, 6, 12
S3	7.5	50	42.5	3, 4, 5, 6, 7, 8, 9, 10

Table VI.3 Volume measurement of samples before and after polishing in solution S3.

As-made		**Polishing**			**Re-polishing (polishing+ additional polishing)**		
sample No.	**Volume [mm3]**	**Etching time [min]**	**Volume [mm3]**	**Volume loss [%]**	**Etching time [min]**	**Volume [mm3]**	**CAD accuracy [%]**
CAD model	60.2						
1	93.8	3	77.6	17.3	7 (3+4)	65.7	109.1
2	93.4	4	66.9	28.4	7 (4+3)	54.2	90.1
3	94.8	5	64.7	31.8	7 (5+2)	63.4	105.3
4	94.4	6	64.2	32.1	7 (6+1)	61.2	101.7
5	93.3	7	58.3	37.5	7	58.3	96.9
6	98.5	8	23.6	76.1			
7	93.7	9	23.5	74.9			

6.2.3. Characterization methods

The mass loss owing to chemical polishing was determined by taking each specimen’s weight before and after the chemical polishing procedure. More specifically, each fixation plate’s mass was nonconsecutively measured three times before and after the chemical polishing. The samples’ surfaces were observed using scanning electron microscopy (SEM) on an Apreo LoVac HR scanning electron microscope (Thermo Fisher, Waltham, MA). µCT scans were performed on a HeliScan (Thermo Fisher Scientific, Waltham, MA) µCT scanner with a voxel size of 7.6450 µm, before and after chemical polishing, to verify the difference in sample volume before and after subsequent stages of chemical treatment in the final solution. Source voltage and source current were set to 100kV and 45µA respectively. A 2-mm aluminum filter material was chosen. The scanning procedure was carried out by performing a rotation of an emitted X-ray by 180°, 1800 projections per resolution, and an exposure time of 0.25 s per projection. The accuracy of the rendered CAD model was evaluated based on a comparison of the standard tessellation language (STL) model volume with the original (used for SLM PBF fabrication) CAD model volume.

6.3. Results

6.3.1. Mass loss measurement

Polishing of fixation plate sections was performed in solutions S1 and S2, while full skeletal fixation plates were polished in solution S3. Mass measurements indicated that, for all tested solutions, mass loss increased in relation to increasing chemical polishing time. Chemical polishing in solution S1 caused the greatest mass loss, while mass lose due to polishing in solution S2 was significantly less, including after a much longer soak time. The weight of samples polished in solution S3 decreased slightly faster than for samples polished in solution S2 and much more slowly than for solution S1 (Figure VI.2). Complete dissolution of the plate was observed after 7 min of polishing in solution S1 and after 10 min of polishing in solution S3.

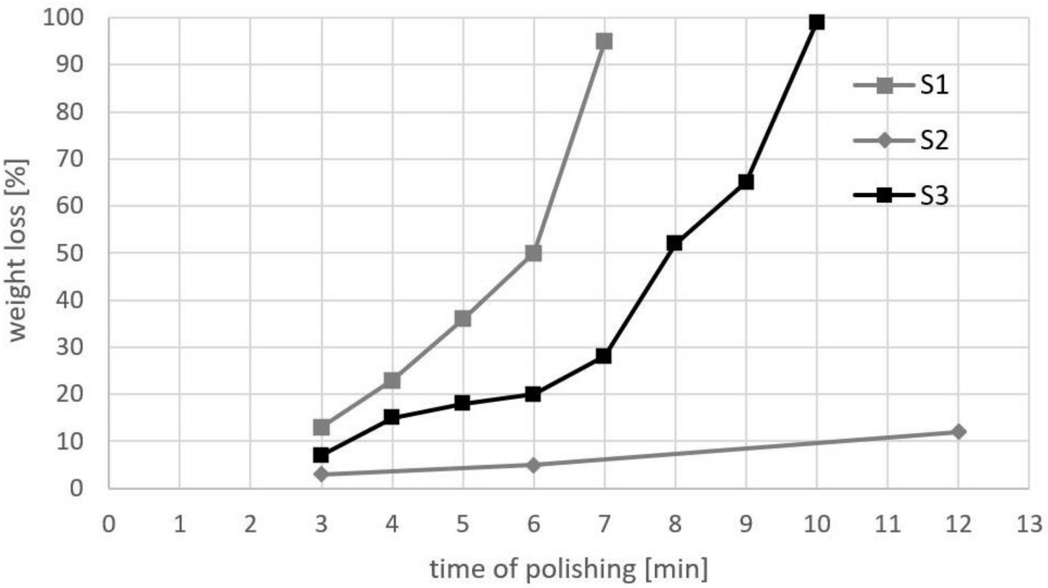

Figure VI.2 Percentage weight loss results during polishing in three different solutions: S1, S2, and S3.

6.3.2. SEM observations

SEM pictures of unpolished and polished fixation plates are shown in Figure VI.3. Each HF-HNO_3 solution used for the polishing experiments acted in a different way on the loosely sintered powder particles on the NiTi plate surfaces. It was observed that solution S1 caused rapid dissolution of loosely sintered powder particles; nevertheless, linear edges (Figure VI.3) were not eliminated. The acid concentration in solution S2 was too low to remove all loosely sintered particles from the surface, even after relatively long polishing times. Solution S3 removed all loosely sintered particles from the surface and left it smooth after 7 min, without causing excessive dissolution of the processed material.

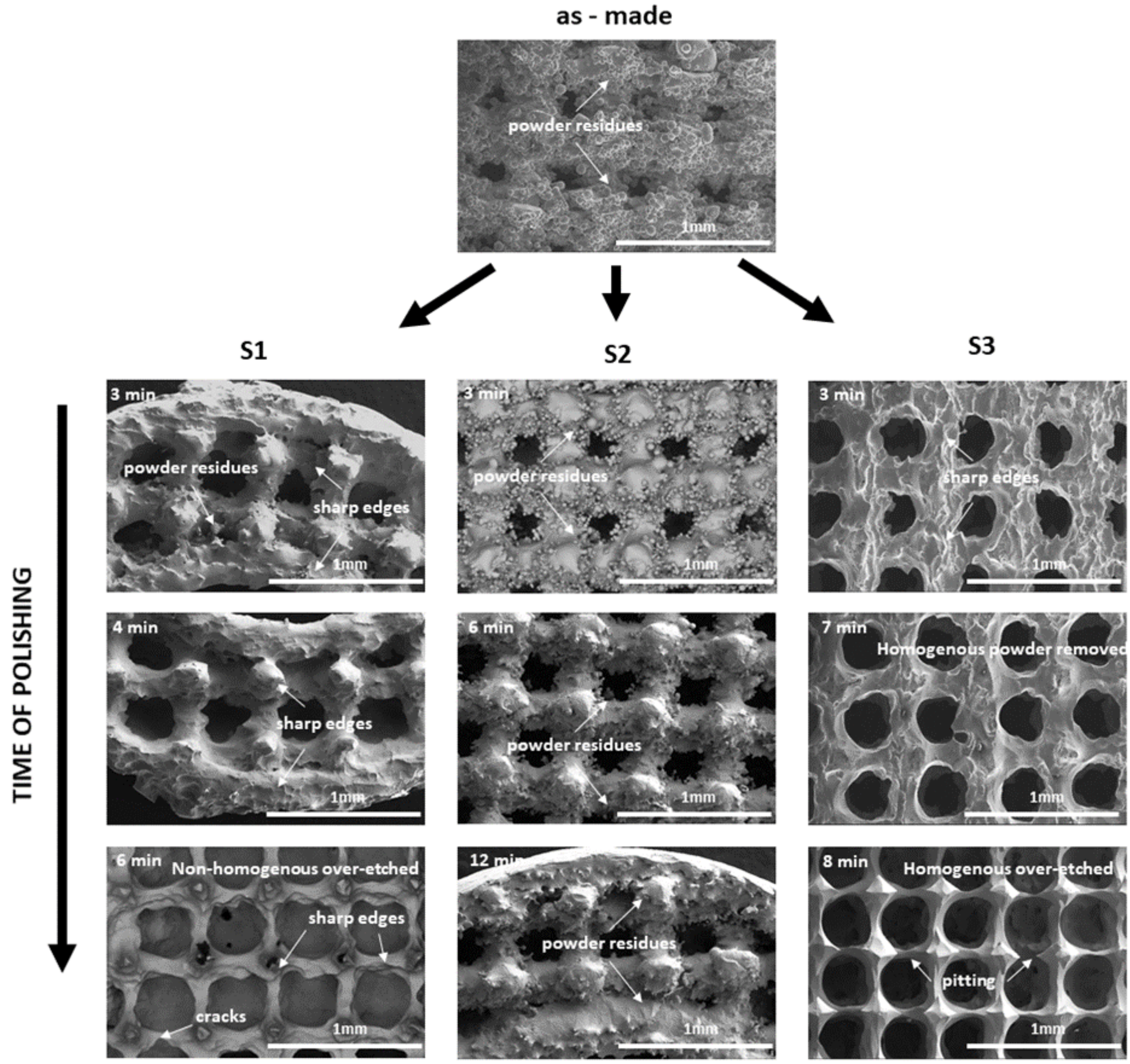

Figure VI.3 SEM images of the as-made sample and samples polished in solutions S1, S2, and S3 for a specified time. SEM, scanning electron microscopy.

6.4. µCT validation

µCT scans and volume reconstructions were performed for the plates before and after the chemical polishing process. Volume loss measurements are summarized in Table VI.3 and presented in Figure VI.4. Three dimensional reconstructed models were created as STL files from the original µCT slice data. By comparing the STL files of samples before and after polishing, the influence of the polishing time on volume was determined. The unpolished mCT-derived surface image files were overlaid on the relevant original CAD files initially to study the rendering accuracy, especially of the most detailed and fine features for each skeletal fixation plate. The CAD file and three of µCT scans of polished plates are shown in Figure VI.5.

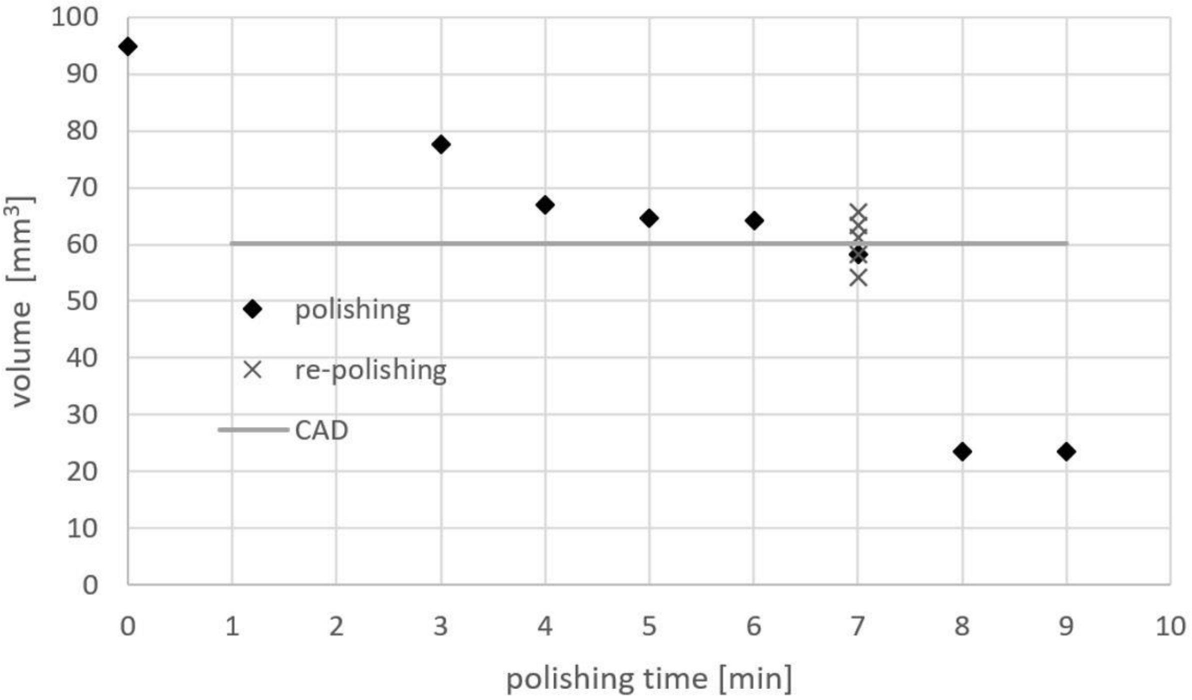

Figure VI.4 Volume change during polishing in solution S3.

Table VI.4 Surface area values for samples polishes in solution S3

Polishing time	3 min	4 min	5 min	6 min	7 min	8 min	9 min
				Surface area [mm^2]			
As-made	597	577	575	587	588	563	574
polished	574	566	581	598	622	392	416

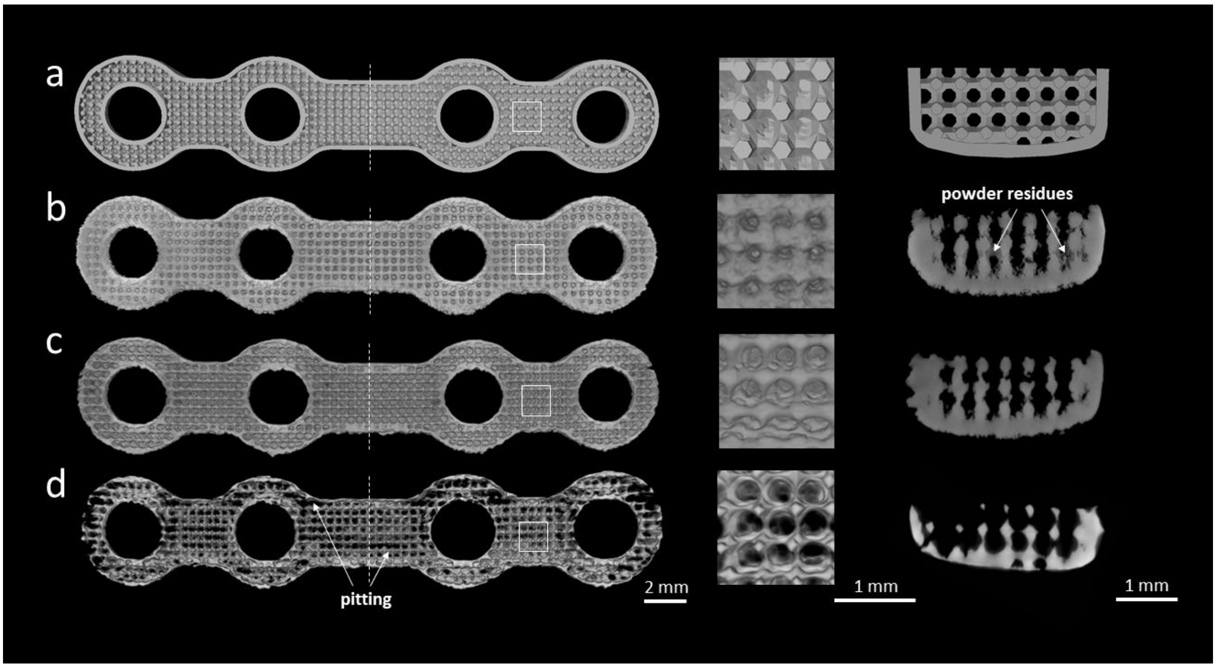

Figure VI.5 (a) CAD model of the sample and µCT visualization of (b) the as-made sample. (c) Sample polished for 7 min in solution S3. (d) Overetched sample polished for 9 min in solution S3. µCT, microcomputed tomography.

6.5. Discussion

6.5.1. Mass loss measurement

During the polishing in solution S1, intense gas release was observed at the surface of each sample throughout the full range of applied immersion times. After 7 min of polishing in solution S1, the sample was damaged and almost completely dissolved and its mass loss was above 95%. Alternatively, there was almost no gas release from the sample surface during polishing in solution S2, even for 12 min of immersion, and there were no changes visible to the unaided eye in the sample appearance during the immersion. Mass measurement following soaking in solution S2 showed minimal to modest weight loss, which was never greater than 12%, throughout the study. Polishing in solution S3 did not cause intense gas release and slow and uniform change in volume was observed through the first 7 min of immersion. However, rapid mass loss was observed after 7 min of polishing in solution S3. Furthermore, polishing times longer than 9 min resulted in complete dissolution of the parts in solution S3. Likewise, 6 min of polishing in solution S1 resulted in a 50% weight loss and after 7 min, the sample was almost completely dissolved. This may indicate that for both the S3 and S1 solutions, at the initial stage of polishing, the connection sites of loose and unmelted particles dissolve and this results in an almost constant weight loss. After the particles have been completely removed from the solution, the solid part itself begins to dissolve, which results in rapid weight loss, something that did not occur with the specimens soaked in solution S2. The results of the weight loss measurements show that the weight of samples polished in solution S3 decreased much slower than for samples polished in solution S1 (Figure VI.2). Furthermore, it was observed that the surface of the polished samples became shinier as soak time increased for all three solutions studied.

6.5.2. SEM observations

SEM observations of samples polished in solutions S1 and S3 showed that polishing times less than 6 and 7 min, respectively, did not provide removal of all powder particles and sharp edges from the surface. On the other hand, for both solution S1 and solution S3, longer soak times eventually led to strut damage and dissolution. Although much loose powder adhered to all parts after SLM PBF printing, all loosely annealed powder particles were removed after 4 and 7 min of polishing in solution S1 and solution S3, respectively. We also observed that in both solution S1 and solution S3, larger plate surfaces became rough and sharp edges also became visible. The sharp edges are not desirable features and do not meet the requirements of the postprocessed fixation device because they can irritate adjacent tissues and their appear with other negative features (pitting pores and the remaining unmelted powder particles). These sharp edges can lead to stress concentrations that propagate cracks, especially because they occur in solutions with intense hydrogen generation. Due to that risk, it is recommended that sharp edges be removed from the surface of the part. Polishing in solution S1 was severe and too aggressive for small struts. It caused strut cracking and splitting, which was also observed for solution S3 after 8 min of polishing. It can be observed that 7 min of polishing in solution S3 ensure full powder particle removal, while maintaining adequate surface smoothness, and longer polishing times left the part over-etched. Polishing in solution S2 for 12 min did not completely remove loose particles from the plate's surface. Therefore, acid concentration in solution S2 was too deemed to be too low for the devices that were tested.

It has been reported that the HF/HNO_3 ratio has the greatest influence on homogenous removal of unmelted powder particles from pure titanium scaffolds made with the SLM PBF process [291]. This phenomenon might be explained by different changes in the surface chemical composition after soaking in HF and HNO_3 acids. It has also been reported that HF works as a dissolvent, while HNO_3 mostly passivates the surface of the processed material [209,292]. Properly selected proportions of both acids provide a balance between etching and passivation of the material so that uniform dissolution is observed over the entire surface, which is then smooth and free of rough patches or sharp edges. The HF/HNO_3 ratio in solutions S1 and S2 was similar, close to 0.25. However, the dissolution of the material in both solutions varied due to the different HF and HNO_3 concentrations. Our analysis showed that the concentration of HF and HNO_3 acids in solution S2 was too low to fully remove loose particles from the surface in a relatively short time, while the concentration of acids in solution S1 was too high and it was difficult to avoid surface damage. The ratio of HF/HNO_3 in solution S3 was decreased to 0.12. The SEM analysis revealed that solution S3 successfully removed the unmelted powder particles from part surfaces. A smooth and powder-free surface was generated after 7 min of polishing. Polishing in solution S3 resulted in slower material dissolution than in solution S1, thereby improving surface smoothness. Based on the results obtained from the experiments reported here, solution S3 was selected to be studied in the next step of the polishing evaluation by μCT.

6.5.3. μCT validation

The μCT reconstruction and volume measurements showed that the volume of as-made samples increased by more than half on average compared with the CAD model. That is unacceptable for elements with predesigned mechanical properties and likely poses a risk for the release of large amounts of loosely sintered powder particles into surrounding tissue. The results of volume measurements for polished samples showed that sample volume gradually decreased as the polishing time increased (Figure VI.4). During 4-6 min of polishing, the volume of the elements changed very little and was close to the CAD model volume. However, by comparing these results with SEM observations, it is observed that the surface smoothness is not acceptable for biomedical applications that require a reliable feature shape for immediate biomechanical function, long-term fatigue strength, and no possibility of loose powder invading adjacent tissues. After 7 min of solution S3 polishing, the volume reduces and becomes closest (96.9%) to the volume of the CAD model. At the same time, comparing the results with SEM images, we can see that the surface smoothness has significantly improved, and this amount of time is optimal for PBF fabricated plates. Further, polishing longer than 7 min caused a significant and detrimental dissolution of the plate material with either solution S1 or solution S3, resulting in unacceptable volume loss of more than 60%, (Figure VI.4) as well as gaps in some of the struts and formation of excessive surface pitting (Figure VI.5). During first 4 min of polishing, a slight decrease of the plate surface area was observed. After this time, surface area starts to increase and after 7 min is almost 6% larger than for as-made sample (Table VI.4). The rapid volume loss after 7 min of polishing may be due to the increased surface area of the bulk sample surrounded by the chemical solution after removing all unmelted powder particles from its surface. We consider it most likely that after 7 min of polishing in S3, the loose powder particles were completely dissolved from the plate inner and outer surfaces (Figure VI.5c), and when they had completely disappeared, the solution acted directly on the bulk plate, causing significant dissolution and volume decrease. These results are also confirmed by the SEM observations.

It is important to note that samples polished in the range of 1-6 min in solution S3 were additionally polished to achieve a total polishing time of 7 min. We refer to this sequential operation as repolishing. As previously noted, this two-part procedure was done to check whether the polishing procedure can be stopped and restarted with the same final result. The repolishing was done to achieve a total polishing time of 7 min, because 7 min of polishing resulted, cumulatively, in the optimal loose powder removal and best fixation plate accuracy when compared with the CAD model. With solution S3, it was observed that after 7 min, the accuracy of volume, compared with the CAD model, was ±10% (Table VI.3). Thus, our study confirmed that using this protocol, the surface of our 3D printed NiTi skeletal fixation plates can be safely and usefully made free of unmelted powder particles (Figure VI.5c). Solution S3 polishing times longer than 7min induced pitting formation and intense dissolution of the material (Figure VI.5d).

6.6. Conclusions

Chemical polishing in the HF/HNO_3 solution was found to be an effective method to remove unmelted particles from the outer and inner surfaces of skeletal fixation plates (3D) printed from NiTi powder through SLM PBF. The proper ratio of hydrofluoric acid, nitric acid, and water components of the polishing solution, as well as time of polishing, was determined in order to obtain high-quality surfaces that are free of loosely sintered powder particles. Since the degree of chemical polishing is determined by the time of polishing and the type of solution, reducing the amount of HF, responsible for dissolution, and increasing the amount of HNO_3, responsible for passivation, were found to be the best method to optimize the polishing process kinetics for these fixation plates. The volume and weight of the samples gradually decreased as polishing time increased and the intensity of this phenomena depended on the solution used. We found that solution S3 was the most appropriate for removing loosely sintered powder particles from the surface of these 3D printed NiTi skeletal fixation plates. The weight and volume decrease during the first 6 min of polishing with solution 3 was not significant and increased rapidly after this time. Likewise, SEM observations showed that the best surface quality or smoothness of surfaces was obtained at 7 min of polishing in solution S3. Exceeding this time caused critical features to dissolve. This fact was confirmed by both SEM and μCT analysis. The reason for this may be that at the initial stage of polishing, the connections of the unmelted powder particles to the surface of the skeletal fixation plate dissolve, and after the removal of a significant portion of these powder particles, the surface of the skeletal fixation plate itself is more exposed and undergoes more significant dissolution. In addition, it was observed that additional periods of polishing (i.e., repolishing fixation plates that have previously been polished) for a shorter time can be effectively used. Other studies are being conducted to confirm that finite element method modeled mechanical properties of the polished parts are accurate and that after polishing, potentially dangerous (cytotoxic) Ni ion release has been minimized

Chapter VII

Biological and Corrosion Evaluation of *In Situ* Alloyed NiTi Fabricated through Laser Powder Bed Fusion (LPBF)

Agnieszka Chmielewska, Anna Dobkowska, Ewa Kijeńska-Gawrońska, Michał Jakubczak, Agnieszka Krawczyńska, Emilia Choińska, Agnieszka Jastrzębska, David Dean, Bartłomiej Wysocki, Wojciech Święszkowski

Published in: International Journal of Molecular Science

DOI: 10.3390/ijms222413209

Abstract

In this work, NiTi alloy parts were fabricated using laser powder bed fusion (LBPF) from pre-alloyed NiTi powder and *in situ* alloyed pure Ni and Ti powders. Comparative research on the corrosive and biological properties of both studied materials was performed. Electrochemical corrosion tests were carried out in phosphate buffered saline at 37 °C, and the degradation rate of the materials was described based on Ni ion release measurements. Cytotoxicity, bacterial growth, and adhesion to the surface of the fabricated coupons were evaluated using L929 cells and spherical *Escherichia coli* (*E. coli*) bacteria, respectively. The *in situ* alloyed NiTi parts exhibit slightly lower corrosion resistance in phosphate buffered saline solution than pre-alloyed NiTi. Moreover, the passive layer formed on *in situ* alloyed NiTi is weaker than the one formed on the NiTi fabricated from pre-alloyed NiTi powder. Furthermore, *in situ* alloyed NiTi and NiTi made from pre-alloyed powders have comparable cytotoxicity and biological properties. Overall, the research has shown that nitinol sintered using *in situ* alloyed pure Ni and Ti is potentially useful for biomedical applications.

7.1. Introduction

Personalised implants and medical instrumentation that can be adapted to the anatomy and needs of a particular patient, may bring many benefits to the healing process and improved quality of life. Additive manufacturing (AM) allows the production of personalised, complexly-shaped implants (e.g., highly curving surfaces or lattice structures), and pre-defined mechanical properties that are not possible to form using traditional manufacturing strategies [1–3]. Therefore, the use of AM has recently received a lot of attention from the medical industry [4]. Simultaneously, many biocompatible materials, which previously could not be used or were useful only in limited applications, have now been operationalised for AM. Besides biocompatibility, the critical issue of medical devices for skeletal reconstruction is to adjust their mechanical properties in relation to their attachment to the surrounding bone [4–6]. The currently predominant alloy for these devices, Ti-6Al-4V, often presents a mismatch between bone and device mechanical properties. This may lead surgically reconstructed bone to fail due to stress shielding and/or device failure due to stress concentration [7–9]. In the latter case, unexpected device failure is likely to require emergency revision surgery. In terms of skeletal replacement devices or fracture fixation, currently available Ti-6Al-4V hardware is associated with problems due to its high stiffness, relative to bone. NiTi alloys have been recently shown to be promising materials for reducing the risk of stress shielding and hardware failure due to their low stiffness provided by superelasticity and shape memory behaviour [10–12]. Moreover, the unique combination of shape memory and superelastic properties, coupled with good biocompatibility, has elevated exploration of NiTi as a candidate for medical devices. On the surface of NiTi parts, Ti ions interact with dissolved oxygen to form a passive layer of titanium dioxide (TiO_2). That layer is extraordinarily tenacious and passive, thereby giving NiTis excellent corrosion resistance and biocompatibility. Recent studies of self-disinfecting TiO_2 coatings have shown a high level of protection against pathogenic microbes such as *E. coli* bacteria [13–15]. Such surfaces eliminate microorganisms *in situ* and prevent the development of bacterial biofilms, which can cause degradation of NiTi 3D printed parts [16–18]. The TiO_2 layer also protects NiTi materials from the external environment and limits Ni ion release, which could be hazardous for health in high local concentrations. Other researchers have reported that, although NiTi alloys have a high percentage of Ni, the quantity of Ni ions released from those alloys is minor compared with the release of toxic components from typical biocompatible materials such as stainless steel when it is used for medical application [19–21].

One obstacle to successful NiTi AM is the loss of Ni due to the evaporation during the laser-induced melting process. Since the evaporation temperature of Ni is lower than Ti, 2913 °C and 3287 °C, respectively, the Ni/Ti ratio shifts toward higher Ti content. The decrease of Ni/Ti ratio may increase the martensitic transformation temperature, O_2 absorption, and formation of Ni_4Ti_3 precipitates [22–24]. For example, it was reported that each 1 at. % change in the amount of Ni results in an 80 °C shift in the transformation temperature of the alloy [25]. In addition, the Ni/Ti ratio is crucial for the medical applications of NiTi since it determines the shape memory (thermal memory) and superelastic properties of the alloy. The thermal memory properties of NiTi medical devices can be tuned to be sensitive at body temperature, which is higher than common room temperature and much higher than common refrigeration or freezing temperatures. Thus, to ensure these effects, their chemical composition must be accurately controlled. Manufacturing NiTi alloys directly from elemental powders, known as *in situ* alloying, if successful, would allow immediate changes in the chemical composition of the batch powder by mixing the desired amount of both alloys' elements. Considering Ni evaporation during the fabrication process, the predetermined amount of Ni in the batch powder would likely need to be increased to obtain the desired chemical composition of the final alloy that results from laser powder-bed fusion (LPBF) part fabrication.

To date, studies on *in situ* alloying of NiTi have focused on the characterisation of mechanical and thermomechanical properties. To the best of the authors' knowledge, *in situ* alloyed NiTi fabricated via LPBF has not been investigated in terms of corrosion resistance and biocompatibility. Hence, to the authors' knowledge, this is the first study to characterises the microstructure, corrosion, and biocompatibility of LPBF, *in situ* alloyed NiTi from an elementally blended mixture of pure Ni and pure Ti powders. In this novel study, pre-alloyed NiTi powder, that has already been qualified for LPBF, was used as a control. The favourable results of this study widen the possibilities of NiTi alloy production and would have use in the validation whether NiTi alloys' manufacturing using powders other than pre-alloyed NiTi will meet the requirements for specific biomedical applications.

7.2. Results

7.2.1. Microstructure Characterisation

SEM and XRD microstructure analysis of both the NiTi (i.e., alloyed prior to 3D printing) and Ni+Ti (i.e., not alloyed prior to 3D printing) coupons began with Figure VII.1a, where the XRD pattern depicted in Figure VII.1c, confirms the presence of a martensitic NiTi (B19′) phase in the pre-alloyed NiTi coupons. Despite NiTi (B19′), peaks coming from the NiTi (B2) austenite phase exist in the Ni+Ti coupons (Figure VII.1d). Some dark irregularly shaped phases formed in the Ni+Ti coupons (Figure VII.1c). As shown in Figure VII.1d, those phases can be identified in terms of $NiTi_2$. Summing up, the microstructure of the coupon prepared from pre-alloyed NiTi powder consists of NiTi (B19′). In contrast, the microstructure of the coupon produced from the blended mixture of pure Ni and pure Ti is composed of NiTi (B19′), NiTi (B2), and $NiTi_2$.

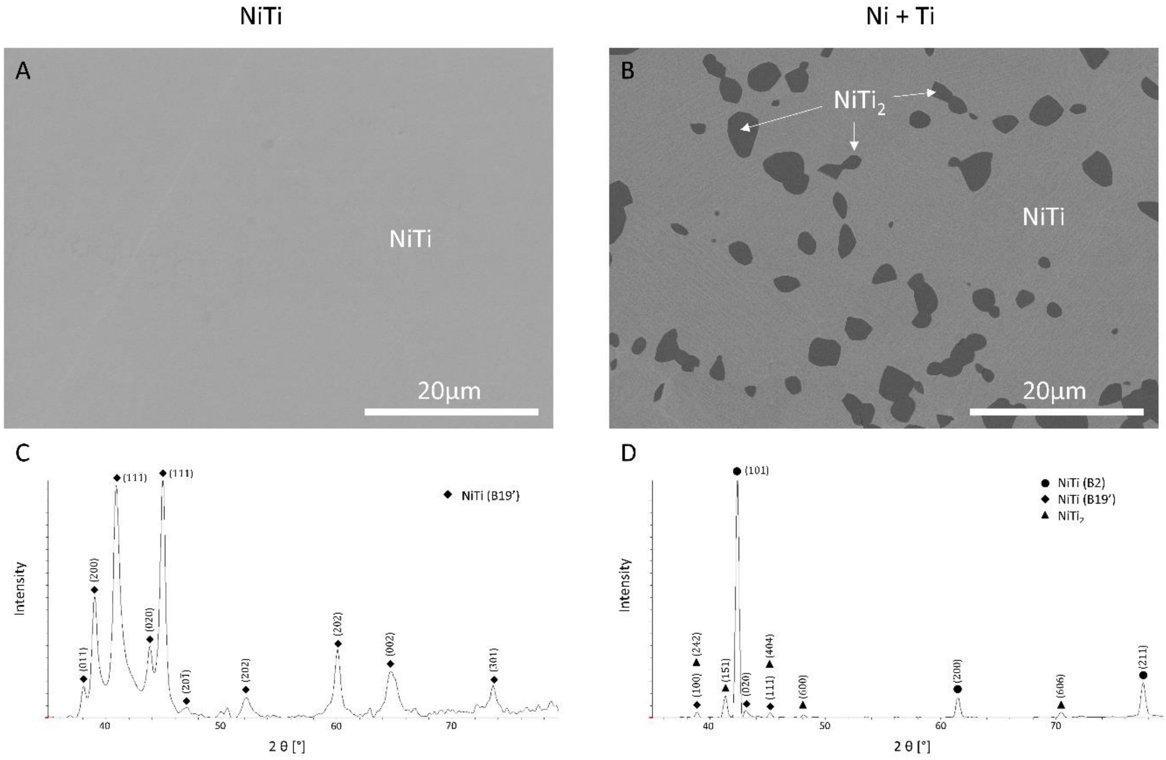

Figure VII.1 The microstructure of (A) NiTi and (B) Ni+Ti coupons under SEM BSE; XRD patterns of (C) NiTi and (D) Ni+Ti coupons.

7.2.2. Surface Characterisation

Figure VII.2a shows the phase chemical state of the top layer of NiTi and Ni+Ti coupons. The XPS spectra corresponding to NiTi and Ni+Ti coupons are presented in Figure VII.2b and Figure VII.2a, respectively. The dominant oxide on the surface of both coupons is TiO_2. Nevertheless, a fraction of TiO and TiO_3 titanium oxides, as well as Ti in pure a metallic state, were observed. Moreover, 1% and 0.6% of NiO was detected on the surface of the NiTi and Ni+Ti coupons, respectively, as was the presence of 4.5 and 4.8% of a pure Ni metallic state, respectively.

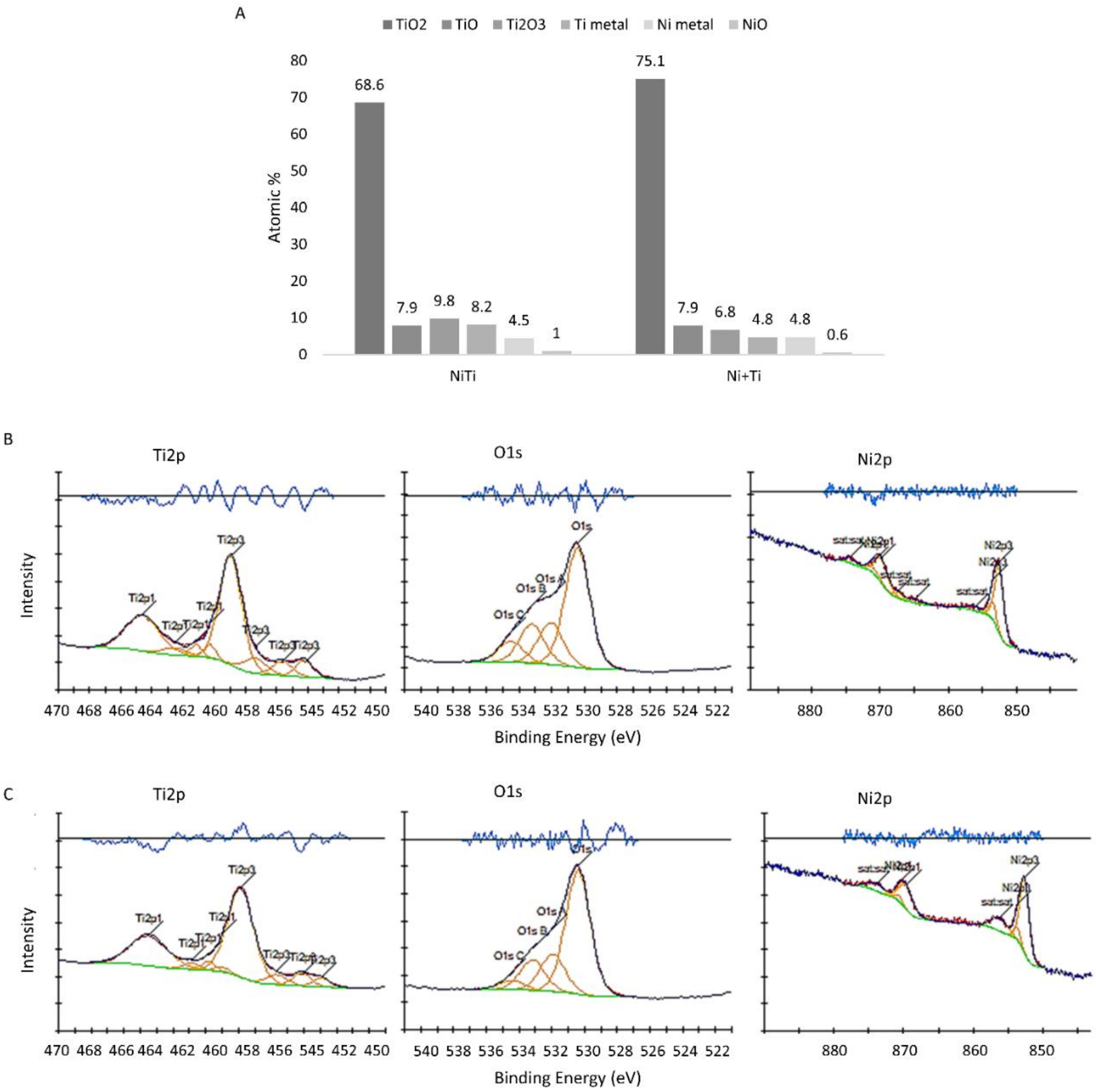

*Figure VII.2 XPS results: (**A**) surface chemical state measured with XPS, (**B**) high resolution spectra of Ti 2p, O 1s and Ni 2p acquired from the NiTi coupon surface, (**C**) high resolution spectra of Ti 2p, O 1s and Ni 2p acquired from the Ni+Ti coupon surface.*

7.2.3. Corrosion Behaviour

Figure VII.3a depicts the evolution of the E_{corr} with time acquired from the NiTi and Ni+Ti coupons suspended in PBS solution. Values of E_{corr} obtained for Ni+Ti are more negative than those observed for the NiTi coupon, suggesting more corrosion of the Ni+Ti alloy occurred in this corrosive medium [26]. A rapid rise of the E_{corr} value is observed for the NiTi coupons, starting from −0.32 V/Ref approaching O V/Ref. The E_{corr} value observed for Ni+Ti decreased abruptly at the beginning of immersion from −0.23 V/Ref to -0.30 V/Ref. Afterward, it has started to increase approaching −0.20 V/Ref at the end of immersion time.

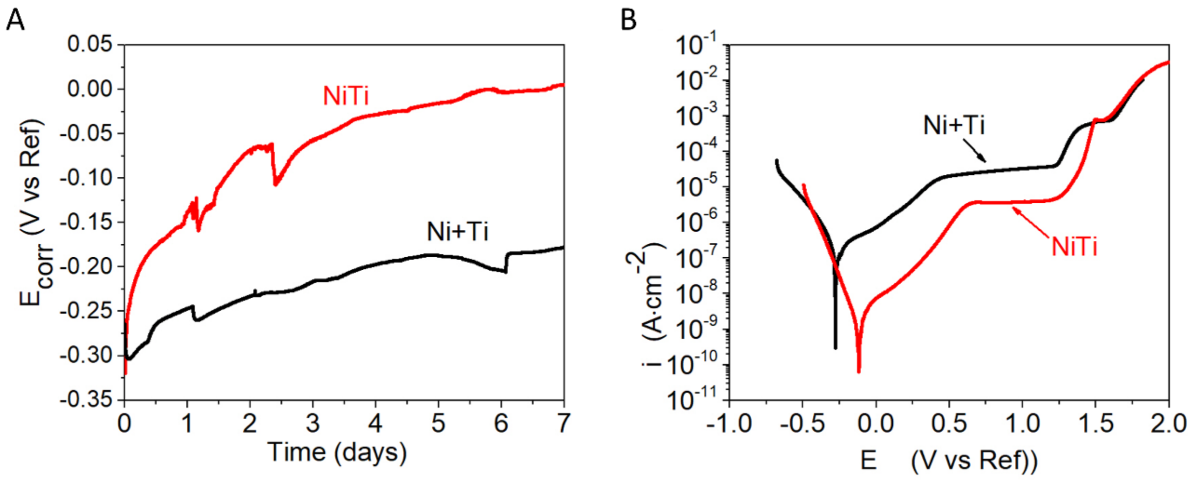

Figure VII.3 The results delivered from the electrochemical measurements performed in PBS: (A) Ecorr evaluation, (B) potentiodynamic polarisation curves.

Potentiodynamic polarisation curves observed for both coupons are shown in Figure VII.3b. The characteristics for potentiodynamic measurements parameters are given in Table VII.1. The higher corrosion current density (i_{corr} = 130 nA·cm^{-2}) and more positive values of corrosion potential (E_{corr} = −0.13 V/Ref) were calculated and are shown for coupons made from pre-alloyed NiTi powder. Lower values of E_{corr} and higher i_{corr} were observed for the Ni+Ti material. Both curves exhibit primarily two regions in their anodic branches, namely an active region at lower anodic potentials and a passive region at higher anodic potentials (indicated by the current plateau). The maximum current density at the active region is higher for the Ni+Ti coupon than for the NiTi coupon. This can be attributed to variation in the rate of the metal oxidation [27,28]. Next, the protective oxide layer was formed over the surface of both alloys, and a sudden increase of current density is observed due to its breakdown (pitting potential, E_{pit}, for both is similar and it is found to be −1.28 V/Ref for NiTi and −1.24 V/Ref for Ni+Ti, Table VII.1).

Table VII.1 Electrochemical Parameters. The electrochemical parameters were calculated from Tafel extrapolation based on results from potentiodynamic polarisation tests recorded in phosphate buffered saline (PBS).

Materials	**E_{corr} (V/Ref)**	**i_{corr} (nA·cm^{-2})**	**E_b (V/Ref)**
NiTi	−0.13	130	−1.28
Ni+Ti	−0.27	201	−1.24

EIS (Electrochemical Impedance Spectroscopy) data for NiTi and Ni+Ti taken after 7 days of immersion in PBS are presented in Figure VII.4. Although the shape of the Nyquist plots is similar, there are distinguishable differences between the diameters of the semicircles. The semicircle observed for the pre-alloyed NiTi coupon is wider, indicating enhancement of polarization resistance. As shown in Figure VII.4b, one time constant can be recognized for NiTi, whilst the Bode plot observed for the Ni+Ti presents two different time constants. Therefore, two various equivalent circuits have been chosen to fit the EIS data (Figure VII.4c, d). For the NiTi coupons, a simple Randles cell was used to fit the data [29]. In this circuit, R_s is an electrolyte resistance, R_{film} is the resistance of the oxide film. To account for the nonideal capacitive behaviour of the oxide, constant-phase element CPE_{film} was chosen [30–32]. The EIS data obtained for the Ni+Ti coupons can be fitted employing the equivalent circuit model, as shown in Figure VII.4d, with two time constants indicating the presence of the oxide film. The oxide film is composed of two layers: the porous oxide layer, that can be penetrated by the electrolyte, and a second layer closer to the unoxidised metal. In this model, R_S is also solution resistance, CPE_{film} is the constant phase element of the passive film layer, and CPE_{dl} is the double-layer capacitance. The passive film resistance, as described by R_{film}, and R_{ct}, represents charge transfer resistance [33–35].

The diameter of the capacitive loop in the Nyquist plots shows that both materials exhibit good corrosion resistance (Figure VII.4a) [34]. The high absolute value of the impedance at low frequency, and a phase angle close to 90°, are typical capacitive behaviour for nitinol immersed in PBS (Figure VII.4b) [36,37]. The fitting parameters are given in Table VII.2. The material produced from pre-alloyed NiTi powder exhibits the highest total resistance value. This indicates that the corrosion resistance of this alloy is higher than the corrosion resistance of Ni+Ti. Additionally, the greater the value of R_{film}, better corrosion resistance of the film. According to that observation, the oxide film formed on the NiTi coupon is more resistant to corrosion than the film formed on the Ni+Ti coupon. The R_{film} for the NiTi coupon is about 20 MΩ cm^2, whereas R_{film} for Ni+Ti is only 7 kΩ cm^2.

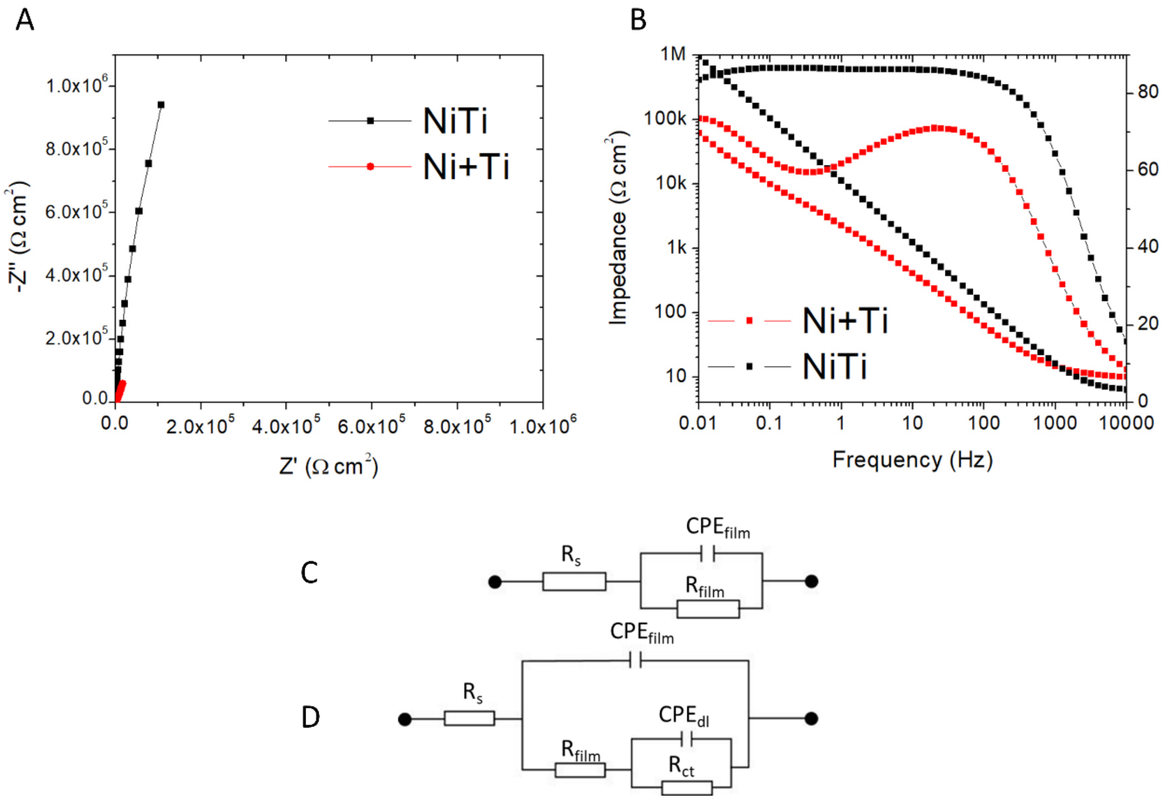

Figure VII.4 EIS data recorded for the analysed coupons presented in the form of (A) Nyquist plots and (B) Bode plots; (C) equivalent circuit used for fitting the EIS results obtained for NiTi, and (D) equivalent circuit used for fitting the Electrochemical Impedance Spectroscopy (EIS) results obtained for Ni+Ti.

Table VII.2 Equivalent circuit parameters obtained from Electrochemical Impedance Spectroscopy (EIS) data.

	R_s (Ω cm²)	**R_{film}** (Ω cm²)	**CPE_{film}** (µF cm⁻²)	**n_1**	**R_{ct}** (Ω cm²)	**CPE_{dl}** (µF·cm⁻²)	**n_2**
NiTi	6	20×10^6	15	0.96	-	-	-
Ni+Ti	8	7×10^3	79	0.83	9×10^6	90	0.82

SEM observations before and after immersion in PBS were performed to have additional data on the corrosion behaviour of the analysed materials (Figure VII.5). The NiTi surface is observed to be uniformly covered with an oxide film and needle-like shapes (Figure VII.5a). The EDX point analysis indicates that those shapes may be identified with NaCl crystals (Figure VII.5c) [38]. The Ni+Ti coupon was also covered with oxide film as well as globular nodules that are distributed non-uniformly across the entire surface after immersion (Figure VII.5b). The EDX chemical analyses did not reveal any Ca or P. This suggests that after 7 days of immersion in PBS, hydroxyapatite growth does not occur on either type of coupons (Figure VII.5c).

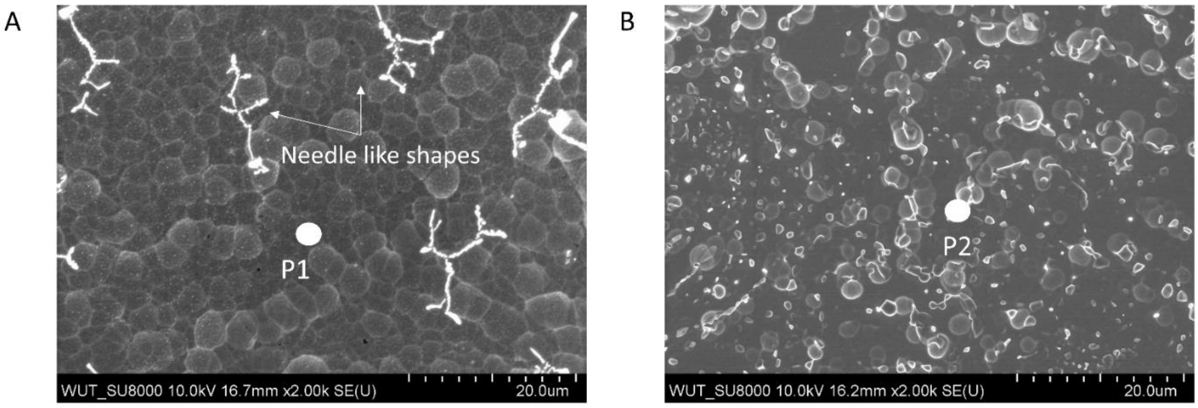

C

	C (at.%)	O (at.%)	Ti (at.%)	Ni (at.%)	Na(at.%)	Cl (at.%)
NiTi (P1)	0.9	2.2	47.3	49.6	-	-
Ni+Ti (P2)	2.8	2.6	49.0	45.6	-	-
Needle like shapes	3.1	1.3	45.0	41.5	6.9	2.2

Figure VII.5 Surface morphology of the coupons after 7 days of immersion in PBS under open-circuit conditions: (A) NiTi, (B) Ni+Ti, (C) EDX point analysis made in P1 and P2.

Ni ion release during immersion in PBS was measured to describe the corrosion behaviour of both coupons more thoroughly as well as potential biocompatibility issues. Cumulative amounts of Ni ion release in PBS must be studied as a function of immersion time as presented in Figure VII.6. In the case of both materials, the largest amount of nickel ion release occurs during the first 7 days. Thereafter, the rate and amount of Ni ion release slows down. After 7 days of immersion of NiTi coupons, 0.0024 µg/mL of Ni was found in the solution versus 0.257 µg/mL of Ni was observed in solution following a 7 day immersion of Ni+Ti coupons. The observed difference may confirm the electrochemical results. The electrochemical results suggest that Ni+Ti is more corrosive (i.e., offers less resistance to corrosion) than NiTi in PBS. When the time of immersion was extended to 28 days, Ni+Ti coupons continued the trend of higher Ni ion release than NiTi; however, that that difference was no longer statistically significant. Note that the cumulative Ni ion release after the first 7 days of Ni+Ti coupon immersion was observed to be more than 100 times greater than the NiTi coupons. Thereafter, the difference between Ni ion release in the two types of coupons decreased. After 14 days, around 90 times more Ni ions were released from Ni+Ti coupons than from the NiTi coupons. After 28 days of immersion the difference also decreased, and cumulative Ni release was around 80 times higher for the Ni+Ti coupons than for the NiTi coupons.

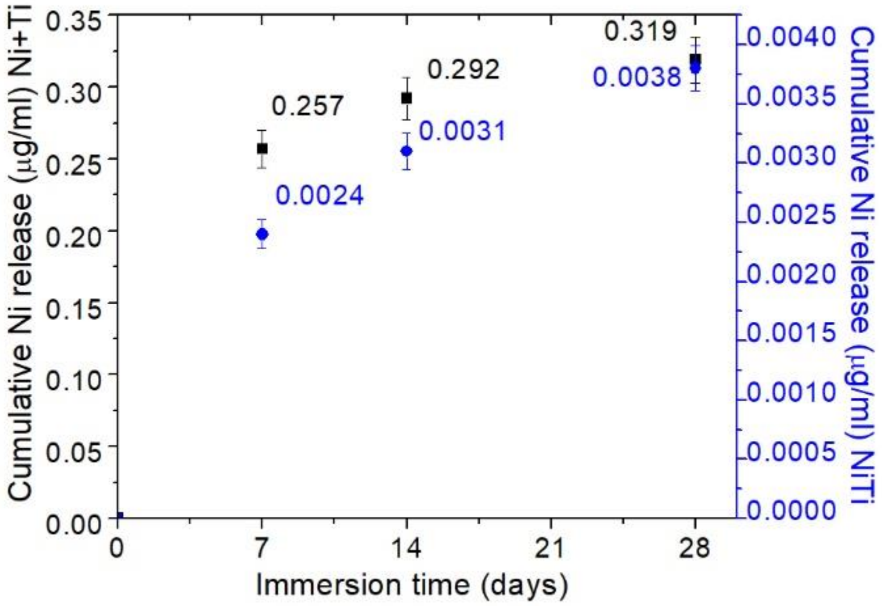

Figure VII.6 Ni ion release from NiTi (blue) and Ni+Ti (black) coupons as a function of immersion time.

7.2.4. Biological Properties

Figure VII.7 shows the viability of L929 cells treated with NiTi or Ni+Ti solute (i.e., recovered immersion media) for 24h. The viability of the cells cultured in non-diluted solute compared to control was 99.4% and 95.5% for NiTi and Ni+Ti, respectively. The cell viability results obtained for 2.5, 5, and 10x diluted media of both tested materials were close to those for non-diluted solute and were within the range of 95.5–102% (the differences are not significant).

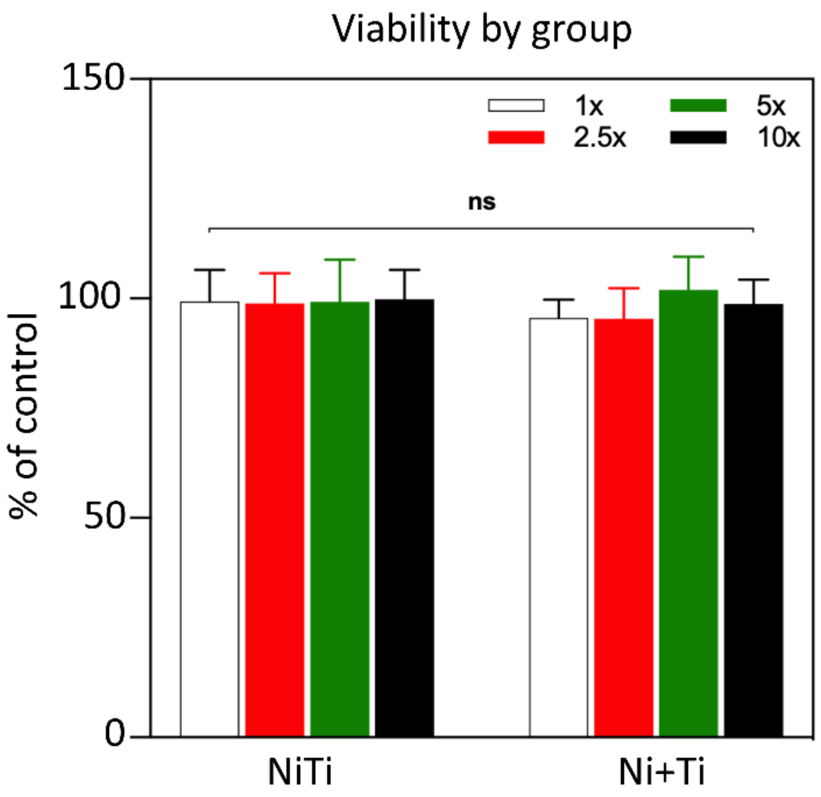

Figure VII.7 Cytotoxicity (% viability) of L929 fibroblast cell line treated with NiTi or Ni+Ti solute aliquots (1x [i.e., undiluted], 2.5x, 5x and 10x indicate dilution factor of the solutes).

The SEM images of *E. coli*-generated biofilm that developed on the NiTi and Ni+Ti coupons are presented in Figure VII.8a and Figure VII.8b, respectively. Figure VII.8c depicts the number of *E. coli* cells recovered after washing the NiTi, and Ni+Ti unalloyed coupons. The surfaces of investigated coupons are covered with a large number of bacterial cells, which is additionally confirmed by the results obtained from the pour plate method (Figure VII.8c). The results shown were observed uniformly across each coupon's surface, with no preferential sights of biofilm formation or cell death. The morphology of the cells on both types of coupons is similar and the cells retain their spherical (viable) form [39]. In addition, the spherical *E. coli* bacteria did not adhere firmly to the surface and were easily washed off the investigated coupons. As calculated, the surfaces of NiTi and Ni+Ti alloy coupons were well-coated, with $3.77 \pm 1.23 \times 10^8$ and $3.89 \pm 2.12 \times 10^8$ CFU cells per cm^2, respectively (Figure VII.8c).

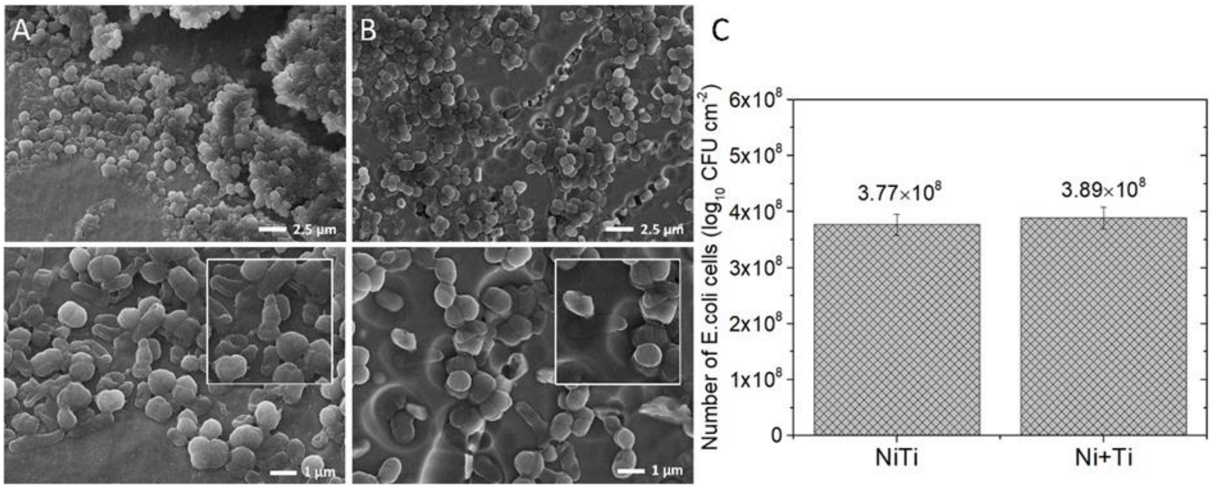

Figure VII.8 SEM images of E. coli adhesion to the surface of: (A) NiTi and (B) Ni+Ti coupons; (C) the number of bacteria cells washed out from the surface after biofilm formation.

7.3. Discussion

In this study, the corrosion and biological properties of NiTi pre-alloyed and Ni+Ti unalloyed powders used in LPBF manufacturing of test coupons with an Ni:Ti ratio of 55.7:44.3 (at. %) were studied. The form of batch powders used during LBPF determined the microstructure and phase composition of the alloys the LPBF-printed coupons. The parts fabricated from pre-alloyed NiTi powder presented the NiTi (B19′) martensitic phase. In contrast, assays of the parts prepared by LPBF from blended elementally pure (i.e., unalloyed) Ni and Ti powders presented NiTi (B19′), NiTi (B2), and $NiTi_2$.

Chemical polishing of both types of coupons in $HF:HNO_3$ removed particles that were sintered to the surface. Loosely sintered powder particles are expected following LPBF fabrication [40,41]. Moreover, it is known that the chemical processing of NiTi alloys is an efficient method, not only for the elimination of unmelted, loosely sintered particles and other small surface defects, but also as a way of improving biomedically desirable surface oxidation [42,43]. The qualitative chemical state of both coupons surface, characterised with XPS was observed to be identical; however, the quantitative results differed between the two types of coupons. Titanium oxide TiO_2 is a dominant phase, and the amount observed is 68.6 and 75.1% for the NiTi and Ni+Ti coupons, respectively. Moreover, the fraction of TiO and TiO_3 titanium oxides, as well as Ti in a pure metallic state, was determined. Ni in a pure metallic state and NiO oxide found on the surfaces may suppress the release of Ni ions.

The corrosion potential of NiTi produced from elementally blended pure Ni and Ti experienced a pronounced decline compared to coupons prepared from pre-alloyed NiTi powder, presented a reduction in the corrosion resistance of the Ni+Ti coupons. The fact that the Ni+Ti specimen is more corrosive in PBS is confirmed by the numerical values of corrosion current in the range of which the potentiodynamic polarisation curve for that coupon was observed. Both coupons exhibit a tendency for passivation. However, for Ni+Ti, passivity occurs in a slightly wider range of potentials, suggesting a lower tendency for localised corrosion versus the coupons prepared from pre-alloyed NiTi.

The more active behaviour of the material fabricated from a mixture of pure Ni and pure Ti in PBS is also confirmed by Ni ion release and EIS results. More Ni ions were released from the alloy prepared using the elementally blended powders than from the alloy produced from the pre-alloyed powder. The amount of released Ni ions is related to the stability and thickness of the oxide film formed on the surface, which was previously shown by Shabalovskaya et al. [44] and Nasakina et al. [45]. Three factors are expected to suppress the leaching of Ni ions from the coupons produced using a mixture of pure Ni and pure Ti during the immersion. First, the higher amount of metallic Ni found via XPS on the surface of the coupons prepared from elementally blended pure Ni and pure Ti, can effectively impede Ni ion release during the entire immersion time. Second, the amount of released Ni ions is dependent on the crystal structure of phases formed in the materials. As shown in this work, the NiTi phase in coupons prepared from pre-alloyed NiTi powder is present only in the form of monoclinic B19′, whereas both monoclinic B19′ and cubic B2 NiTi phases, as well as a $NiTi_2$ phase, exist in coupons fabricated from the elementally blended mixture of pure Ni and Ti. The surface energy values of dense surface configurations with a stoichiometric ratio for B2-NiTi (101) and B19’-NiTi (010) are 1.81 J/m^2 and 1.93 J/m^2, respectively [46], which can reduce Ni ion release. Third, corrosion processes are microstructure-dependent and the presence of $NiTi_2$ supports micro-galvanic corrosion between the matrix and secondary phases (NiTi behaves as cathode, whilst $NiTi_2$ is an anode) [34,47].

The cytotoxicity of both materials appears to be minor and similar. The materials were found to demonstrate more than 95.5% viability at all dilution factors, and the differences between the percentage of the viability of all tested dilutions of both groups of coupons are not significant. According to the ISO 10993-5 cytotoxicity testing standard, which states that any material reducing the cell number by equal to or more than 30% is toxic. Neither of the two groups of coupons tested have a cytotoxic effect on L929 cells. A similar situation is observed for bacterial growth and bacterial adhesion to the surface of both types of coupons. Similar cytotoxicity properties were observed for both with no significant differences between both types of coupons. TiO_2-coated surfaces may reduce bacterial adhesion due to the alternation of surface free energy [48]. It is assumed that bacterial adhesion occurs with the least intensity on low-energy surfaces because of weaker binding at the interface [49]. However, Zhang et al. [48] have shown that bacterial adhesion may be minimal at specific optimal surface energies, all of which are due to multiple factors. According to Derjaguin–Landau–Verwey–Overbeek's (DLVO) theory, bacteria adhere to the surface when the summary of all possible interactions gives a negative surface energy value. As all interactions are related to the distance of separation, bacterial cells adhere after they are in close contact with the surface. Thus, at close contact, *E. coli* bacteria encounter a deep-primary energy minima and, therefore, adhere [50,51]. As TiO_2 coating increases surface energy, the bacterial adhesion would be modulated (reduced) [13,52].

It must be noted that Ni ion release from both types of coupons studied is much lower than what is observed for the conventionally manufactured NiTi alloy investigated by Meng et al. [53]. Moreover, the NiTi coupons prepared from elementally blended pure Ni and Ti exhibited lower corrosion resistance than the coupons LPBF fabricated from pre-alloyed NiTi powder. Results presented in this work show opportunities for further investigation of elementally pure Ni and Ti powders as a substitute for pre-alloyed NiTi powder. This is confirmed by the similar cytotoxicity and similar biological behaviour of both the pre-alloyed NiTi and coupons prepared from elementally pure Ni+Ti. In future studies it may be possible to improve the corrosion properties of the coupon produced from a mixture of pure Ni and Ti elements. Further research is also needed, especially on heat treatments, that could result in a single phase microstructure of NiTi alloy coupons rendered from elementally pure Ni and pure Ti source materials.

7.4. Materials and Methods

7.4.1. Materials and Fabrication Procedure

Pre-alloyed $Ni_{55.7}Ti_{44.3}$ powder, referred to as NiTi, and elementally pure Ni and pure Ti powders, referred to as Ni+Ti, blended in the ratio Ni:Ti = 55.7:44.3 wt %, were used to fabricate materials using LPBF. All powders were provided by TLS Technik GmbH (Bitterfeld-

Wolfen, Germany) and had a spherical shape and particle size below 63 µm. The chemical compositions of powders (including impurities) are shown in Table VII.3. A Realizer SLM50 machine (Realizer GmbH, Borchen, Germany) was employed for LPBF fabrication of cylindrical coupons with a dimension of $\phi = 5$ mm. LPBF manufacturing was carried out under an Ar atmosphere with an O_2 concentration below 0.3%. A two-step melting-remelting process was applied. The first step, referred to as melting, was used to consolidate the powder. Various laser process parameters were applied to the second step, referred to as remelting, to improve final part density. The parameters of both the melting and the remelting steps used for manufacturing NiTi and Ni+Ti parts are given in Table VII.4. The manufacturing procedure has been previously described in detail [54]. To homogenise chemical and phase composition, Ni+Ti materials were subjected to a solution heat treatment composed of a two-step vacuum heat treatment performed at 900 °C for 24 h followed by solutionising at 1150 °C for another 24 h and subsequent immediate quenching in water. All parts were ultrasonically cleaned three times in deionised water for 15 min, and then chemically polished in a solution composed of 7.5 HF: 50 HNO_3: 42.5 H_2O to remove particles sintered to the surface. The chemical polishing procedure has been previously described in detail [40].

Table VII.3 The chemical composition of powders used (from the powder manufacturer).

Material	**Elements (wt.%)**						
	Ti	Ni	C	O	N	H	Fe
NiTi	bal.	55.7	0.005	0.046	0.007	0.0006	
Ti	bal.		0.01	0.13	0.1	0.001	0.11
Ni		99.9	0.017				<0.1

Table VII.4 LPBF manufacturing parameters (NiTi is pre-alloyed and Ni+Ti is in situ-alloyed material).

		Laser Power P [W]	**Scanning Speed v [mm/s]**	**Hatch Distance h [µm]**
NiTi	melting	108	100	120
	remelting	22	500	120
Ni+Ti	melting	30	500	30
	remelting	25	500	30

7.4.2. *Microstructural Characterisation*

The microstructure of the coupons was examined using a Hitachi (Tokyo, Japan) SU8000 scanning electron microscope (SEM) in backscattered electron mode (BSE To undertake this examination metallographic samples were prepared. Coupons were polished on Saphire 550 grinding and polishing machine (ATM Qness GmbH, Germany) using SiC papers (from #600 to #4000, 15 min each), and subsequently polished using 0.1 µm alumina oxide suspensions for 30 min. Concurrent rotation of grinder and head, equal to 120 min^{-1}, was used in each step. The single pressing force applied to the sample was 10N. Afterward, coupons were polished by an Ar beam using a Hitachi IM4000 (Tokyo, Japan) ion milling system. The phase composition was identified at room temperature using a Bruker (Billerica, MA, USA) X-ray diffraction (XRD) device. Filtered Cu Kα (λ = 0.154056 nm) radiation was used at operating values of 40 kV and 40 mA. The XRD data were collected over 2Θ angular range of 35–80°, with a step Δ2Θ–0.05° and count time of 3 s.

7.4.3. *Surface Chemical State Characterisation*

The surface chemical state of the coupons was characterised using a Thermo Electron Corporation (Waltham, MA) Microlab 350 XPS spectrometer. A monochromatised Al *Ka* radiation source with 300 W power and energy of 1486.6 eV was used. Measurements were carried out in the vacuum range of ~10^{-9} mbar. To determine the chemical states and concentrations of Ti 2p, O 1s, and Ni 2p, high-resolution spectra were acquired at a pass energy of 40 eV at a 0.1 eV/step. The C 1s peak was used to correct binding energy positions.

7.4.4. *Corrosion Behaviour*

7.4.4.1. *Electrochemical Procedure*

To determine corrosion behaviour of both alloys in the simulated body fluid solutions, electrochemical measurements were carried out in naturally aerated, quiescent PBS solution at 37 °C. The measurements were carried out using a FAS1 Gamry potentiostat equipped with three electrodes: platinum as the counter electrode, Ag/AgCl as the reference electrode, and the measured sample was the working electrode. The reference electrode was inserted into a Luggin capillary. The setup was placed in front of the working electrode. Phosphate buffered saline (PBS) solution (pH 7.4) was prepared by adding a Sigma Aldrich (St. Louis, MO, USA) certified tablet to 200 mL of distilled. The corrosion potential (E_{corr}) of the coupons was recorded for 7 days under open-circuit conditions. Then, the potentiodynamic polarisation tests were carried out after immersion in the range of 0.5 V below E_{OCP} to 2 V vs. E_{OCP} (a scan rate of 5 mV/s was used). The corrosion potential (E_{corr}) and current density (i_{corr}) were calculated by the Tafel extrapolation method [55]. At least three tests were conducted for each specimen. Electrochemical Impedance Spectroscopy (EIS) measurements were recorded just after immersion of the coupons in PBS solution. The EIS tests were performed in a frequency range from 0.01 to 10000 Hz with a sinusoidal signal amplitude of 10 mV. The polarisation curves were fitted using Gamry's (Philadelphia, PA, USA) Elchem software in Tafel mode. EIS data were also fitted using Gamry Elchem Software. SEM surface observations were made before and after immersion in PBS under open-circuit conditions to better understand the corrosion processes.

7.4.4.2. Ni ion Release

Ni ion release evaluation of the coupons was performed according to ASTM F3306 [56]. Each coupon was placed in a separate container filled with PBS that prepared according to the ASTM F2129 [57] protocol. A coupon surface area to PBS volume ratio of 0.1 $cm^{2}/^{mL}$ was used, as recommended by the US Food and Drug Administration (FDA) (Silver Spring, MD, USA). All containers were placed in a heating chamber at 37 ± 2 °C for 7, 14, and 21 days. At each time point, NiTi and Ni+Ti coupon were removed from the solution and the immersion solutes for Ni ion measurement were collected. NiTi and Ni+Ti coupons were immediately transferred into a new container filled with fresh PBS solution. The relative concentration of Ni ions was measured using inductively coupled plasma mass spectrometry (ICP-MS) on a Perkin Elmer (Waltham, MA, USA) PE Elan DRC-e machine.

7.4.5. Biological Behaviour

7.4.5.1. Cytotoxicity Study

The cytotoxicity of the coupons was evaluated as per the ISO 10993-5 standard [58–60]. The analysis began with the proliferation of American Type Culture Collection (ATCC) (Manassas, VA, USA) L929 murine fibroblast cells in a complete medium of Dulbecco's Modified Eagle Medium (DMEM) supplemented with heat-inactivated fetal bovine serum (FBS) and 1% penicillin-streptomycin in 5% CO_2. The cells were proliferated in an incubator at 37 °C for 2–3 days until sufficient confluence was obtained. Next, the cells were detached with 0.05% trypsin-EDTA and seeded in 96-well plates at a concentration of 10,000/well in

100 μL of media. Meanwhile, coupons were sterilised by dipping in 70% ethanol solution, followed by 1h exposure to UV, and three rinses with PBS. Solutes were obtained by soaking both types of coupons (*n* = 5) in a complete cell culture medium, including DMEM, 10% FBS, and 1% PS. The mass of the material in the volume of the extraction vehicle was adjusted to 200 mg/mL (according to ISO 10993-12 standard) [61]. These specimens were held in solution for 72 h in an incubator (37 °C, 5% CO_2). The 72 h solutes were utilised in four dilutions (1x, 2.5x, 5x, and 10x) and each dilution was prepared in triplicate. After removing cell culture media, 100 μL of each solute was added to a well where cells were then incubated for 24 h. Thereafter, release media were aspirated from each well, and replaced with 100 μL fresh DMEM supplemented with 1% penicillin and 20 μL MTS solution and incubated for 2 h at 37 °C (5% CO_2). After 2 h, aliquots were transferred to fresh 96-well plates and the absorbance was read at 490 nm using a microplate reader (FLUOstar Omega BMG Labtech, Offenburg, Germany). Cell viability in each the solutes was reported as the percentage of viable cells that grew in complete medium under the same conditions (i.e., the “negative control”).

7.4.5.2. Bacterial Growth and Adhesion to the Surface

Bacterial growth and adhesion to the surface of the coupons was evaluated using ATCC 10799 spherical *E. coli* bacteria [62–64]. Bacteria cells were cultivated on Merck (Readington Township, NJ, USA) nutrient agar for 24 h at 37 °C. Then, the cells were harvested from a solid medium and resuspended in PBS containing 10 g L^{-1} of glucose. The final density of bacterial suspension was adjusted to 1.09×10^9 CFU mL^{-1}. Further, NiTi and Ni+Ti disc-shaped coupons were placed in 24-well plates and topped with 2 mL of the bacterial suspension. The suspended coupons were incubated for 24 h at 37 °C. After incubation, the coupons were washed with 3 mL and transferred into 9 mL of PBS. The number of bacterial cells in the obtained suspension was determined using a pour plate method. The results were calculated in relation to the surface area of the coupons. Biofilm formed on the coupons was observed using a Hitachi SU8000 SEM. To approach this, NiTi and Ni+Ti coupons were immersed in 3 mL of glutaraldehyde (3% *v*/*v*) solution and kept overnight. Then, the NiTi and Ni+Ti coupons were washed with PBS and dehydrated using the increasing concentrations of ethanol. Prior to SEM imaging, the coupons were coated with a thin layer of gold using a BAL-TEC Corporation (Canonsburg, PA, USA) SCD 005 sputter coater.

7.5. Conclusions

This study evaluated the corrosion and biological performance of NiTi alloy fabricated by LPBF using two different source materials with the same initial chemical composition: pre-alloyed NiTi powder and elementally blended Ni and Ti powders. It was observed that:

- The corrosion resistance of LPBF-printed parts produced from elementally blended pure Ni and Ti is slightly lower when compared to parts which were LPBF-printed from pre-alloyed NiTi powder; however, both materials show similar biocompatibility in terms of cytotoxicity.
- The low cytotoxicity and high passivation suggest that elementally blended pure Ni and Ti powders merit further investigation for use in biomedical applications.
- Further research on the LPBF manufacturing and post-printing process parameters and microstructure-dependent corrosion of elementally pure Ni and pure Ti is merited given the potential cost savings and improvements in corrosion and biocompatibility behaviour.

Chapter VIII

Summary and future perspectives

8.1. Summary

Additive Manufacturing (AM) is the technique that allows the production of complexly shaped geometries, often made with lattice structures with pre-defined mechanical properties. Therefore, recently AM has been evolving rapidly and revolutionizing many areas of the industry. Simultaneously, many materials that were not used or their usage was significantly reduced can now be applied thanks to the possibilities given by AM. Recently *in situ* alloying has gained significant attention for fabricating alloys by employing pure elemental blends instead of pre-alloyed ones. Designing the alloys, and manufacturing them from elemental powders, seems to be the promising approach to overcome the difficulties associated with limited feedstock materials and provide flexibility in controlling the material properties or creating novel alloys. The precise control of chemical composition is essential for NiTi alloys, as their phase transformation temperature is susceptible to the alloy composition. The main limitation of NiTi research and commercial usage is the high cost and excessive difficulty in machining due to the inherent superelasticity or shape memory. For this reason, a crucial issue is to reduce material costs and eliminate machining, which would initiate lower costs of the fabricated elements. Thus, AM techniques have gained significant attention for processing NiTi since they eliminate many of the challenges associated with the conventional methods. *In situ* alloying is a promising, cost-effective alternative for tailoring the required chemical composition, i.e., nickel-titanium ratio.

In the presented dissertation, laser powder bed fusion (LPBF) AM technique was utilized to fabricate NiTi alloy from elementally blended pure nickel and titanium powders. For the first time, designed melting strategies (multiple melting/ remelting) were applied to *in situ* alloying of NiTi (Chapter III). The study showed that remelting significantly improved the blending of the Ni and Ti elements during LPBF and reduced porosity compared with single melt processes. However, multiple phases were observed regardless of the number of remelts; thus, remelting did not eliminate phase composition inhomogeneity entirely.

The next part of the work (Chapter VI) was devoted to investigating the level of Ni evaporation in three different NiTi elemental powder blends with the chemical compositions of $Ni_{53}Ti_{47}$ and $Ni_{57}Ti_{43}$, representing the limit values of industrially used NiTi shape memory alloys and $Ni_{55.7}Ti_{43.7}$, which corresponds to pre-alloyed NiTi, used in the presented research as a reference material. It was found that the same manufacturing parameters applied to all powder blends allowed for the successful fabrication of NiTi alloy from each of studied powder blend composition. The amount of nickel that evaporates during the production process ranged from 1.6 to 3.0 wt. % and depended on the initial powder's chemical composition and the scanning strategy (number of melts).

Further research (Chapter V) demonstrates the development of the solution heat treatment to improve chemical and phase homogeneity of the *in situ* alloyed NiTi fabricated by LPBF. The selected two-step HT3 heat treatment condition (900°C/24h + 1150°C/24h) allowed for the significant homogenization of the chemical and phase composition of the LPBF *in situ* alloyed NiTi components. It was found that oxygen pickup during the LBPF manufacturing process promoted the formation of a thermodynamically stable oxygen-rich Ni_2Ti_4O phase that is observed even after an annealing heat treatment.

In the following step (Chapter VI), the chemical polishing in the HF/HNO_3 solution was utilized to remove loosely attached (i.e., unmelted) powder particles from surfaces of porous NiTi parts. The proper ratio of hydrofluoric acid, nitric acid, and water components of the polishing solution and time of polishing was determined in order to obtain high-quality surfaces that are free of loosely sintered powder particles. Since the degree of chemical polishing is determined by the time of polishing and the type of solution, reducing the amount of HF responsible for dissolution, and increasing the amount of HNO_3 responsible for passivation, were found to be the best method to optimize the polishing process kinetics for the NiTi coupons.

The final step of this study evaluated the corrosion and biological performance of NiTi alloy fabricated by LPBF using two different source materials with the same initial chemical composition: pre-alloyed NiTi powder and elementally blended Ni and Ti powders (Chapter VII). It was observed that the corrosion resistance of parts produced from elementally blended pure Ni and Ti is slightly lower when compared to parts that were produced from pre-alloyed NiTi powder; however, both materials show similar biocompatibility in terms of cytotoxicity. Therefore, the low cytotoxicity and high passivation suggest that elementally blended pure Ni and Ti powders merit further investigation for use in biomedical applications.

In conclusion, the LPBF technique is a promising way of synthesizing NiTi alloy from elemental powders. Furthermore, the comparison of the results obtained for samples fabricated from the pre-mixed Ni and Ti powders with those obtained from pre-alloyed NiTi powder showed similar characteristics in terms of corrosion resistance and biological evaluation. The presented results highlight the capabilities of LPBF *in situ* alloying to fabricate NiTi alloy with a potential use for biomedical and industrial applications. Moreover, understanding the impact of the parameters of the LPBF technology fabrication process of the NiTi pre-mixed powders would enable a better understanding of the phenomena accompanying this method and the broadening of the possibility of using it to produce new metallic materials.

The research included in this thesis allowed me to prove my hypothesis and accomplish the utilitarian and scientific objectives.

8.2. Future perspectives

The presented results showed high potential for *in situ* alloying in additive manufacturing and could provide valuable information for designing the batch material's chemical composition to obtain the desired chemical composition of the fabricated alloy. This research will give new insights into new materials that could be developed immediately, thus eliminating the necessity of the time-consuming and expensive manufacturing of powders. Therefore, this work would contribute to the faster development of the whole AM industry.

However, the performed research revealed difficulties in homogenous alloying material components and the need for heat treatment postprocessing. Therefore, the combination of *in situ* heat treatment and *in situ* alloying by using LPBF machines with heated building platforms and chambers above 500°C will be the subject of further research. Furthermore, studies on shape memory and superelasticity behaviour of the *in situ* alloyed NiTi should be performed to prove commercial profit for using the material in industrial and medical applications. Another aspect worthy of attention is powder recycling, especially chemical composition control and investigation of alloy particles' formation from spatters. Nevertheless, the primary attention will be devoted to developing *in situ* alloying of other shape memory alloys and evolution into 4D printing by manufacturing 3D elements with adjustable properties, functionalities, and shapes.

References

1. Bourell, D.; Kruth, J.P.; Leu, M.; Levy, G.; Rosen, D.; Beese, A.M.; Clare, A. Materials for additive manufacturing. *CIRP Ann. - Manuf. Technol.* **2017**, *66*, 659–681, doi:10.1016/j.cirp.2017.05.009.

2. Simons, M. Additive manufacturing—a revolution in progress? Insights from a multiple case study. *Int. J. Adv. Manuf. Technol.* **2018**, *96*, 735–749, doi:10.1007/s00170-018-1601-1.

3. Lu, H.Z.; Yang, C.; Luo, X.; Ma, H.W.; Song, B.; Li, Y.Y.; Zhang, L.C. Ultrahigh-performance TiNi shape memory alloy by 4D printing. *Mater. Sci. Eng. A* **2019**, *763*, doi:10.1016/j.msea.2019.138166.

4. Ahmed, A.; Arya, S.; Gupta, V.; Furukawa, H.; Khosla, A. 4D printing: Fundamentals, materials, applications and challenges. *Polymer (Guildf).* **2021**, *228*, 123926, doi:10.1016/j.polymer.2021.123926.

5. Dhanasekaran, R.; S, S.R.; B, G.K.; Anirudh, A.S. Shape Memory Materials for Bio-medical and Aerospace Applications. *Mater. Today Proc.* **2018**, *5*, 21427–21435, doi:10.1016/j.matpr.2018.06.551.

6. Miyazaki, S.; Kim, H.Y.; Hosoda, H. Development and characterization of Ni-free Ti-base shape memory and superelastic alloys. **2006**, *440*, 18–24, doi:10.1016/j.msea.2006.02.054.

7. Arun, I.D.; Chakravarthy, P.; Arockiakumar, R.; Santhosh, B. *Shape Memory Materials*; 1st ed.; CRC Press Taylor & Francis Group: Boca Raton, 2018; ISBN 978-0-8153-5969-2.

8. Hartl, D.J.; Lagoudas, D.C. Aerospace applications of shape memory alloys. **2007**, *221*, 535–552, doi:10.1243/09544100JAERO211.

9. Humbeeck, J. Van Non-medical applications of shape memory alloys. *Mater. Sci. Eng. A* **1999**, *273–275*, 134–148.

10. Memry Corporation *Introduction to Nitinol*; 2017;

11. Ou, S.-F.; Peng, B.-Y.; Chen, Y.-C.; Tsai, M.-H. Manufacturing and Characterization of NiTi Alloy with Functional Properties by Selective Laser Melting. *Metals (Basel).* **2018**, *8,* 342, doi:10.3390/met8050342.

12. Di Prima, M. *Technical Considerations for Non- Clinical Assessment of Medical Devices containing Nitinol*; 2021;

13. ASTM International *F2792 − 12a Standard Terminology for Additive Manufacturing Technologies*; 2016;

14. Dadbakhsh, S.; Speirs, M.; Kruth, J.P.; Schrooten, J.; Luyten, J.; Van Humbeeck, J. Effect of SLM parameters on transformation temperatures of shape memory nickel titanium parts. *Adv. Eng. Mater.* **2014**, *16*, 1140–1146, doi:10.1002/adem.201300558.

15. Manjaiah, M.; Raghavendra, K.; Balashanmugam, N.; Davim, J.P. *Additive Manufacturing: A Tool for Industrial Revolution 4.0*; Woodhead Publishing, 2021; ISBN 978-0128220566.

16. Leary, M. *Design for Additive Manufacturin*; Elsevier Science, 2020; ISBN 9780128168875.

17. Sun, Z.; Tan, X.; Tor, S.B.; Yeong, W.Y. Selective laser melting of stainless steel 316L with low porosity and high build rates. *Mater. Des.* **2016**, *104*, 197–204, doi:10.1016/j.matdes.2016.05.035.

18. Tempelman, E.; Shercliff, H.; van Eyben, B.N. *Manufacturing and Design: Understanding the Principles of How Things Are Made*; 1st ed.; Butterworth-Heinemann, 2014; ISBN 978-0-08-099922-7.

19. Frazier, W.E. Metal additive manufacturing: A review. *J. Mater. Eng. Perform.* **2014**, *23*, 1917–1928, doi:10.1007/s11665-014-0958-z.

20. Lewandowski, J.J.; Seifi, M. Metal Additive Manufacturing: A Review of Mechanical Properties. *Annu. Rev. Mater. Res.* **2016**, *46*, 151–186, doi:10.1146/annurev-matsci-070115-032024.

21. Fredriksson, C. Sustainability of metal powder additive manufacturing. *Procedia Manuf.* **2019**, *33*, 139–144, doi:10.1016/j.promfg.2019.04.018.

22. Babuska, T.F.; Krick, B.A.; Susan, D.F.; Kustas, A.B. Comparison of powder bed fusion and directed energy deposition for tailoring mechanical properties of traditionally brittle alloys. *Manuf. Lett.* **2021**, *28*, 30–34, doi:10.1016/j.mfglet.2021.02.003.

23. Tofail, S.A.M.; Koumoulos, E.P.; Bandyopadhyay, A.; Bose, S.; O'Donoghue, L.; Charitidis, C. Additive manufacturing: scientific and technological challenges, market uptake and opportunities. *Mater. Today* **2018**, *21*, 22–37, doi:10.1016/j.mattod.2017.07.001.

24. Williams, S.; Martina, F.; Wood, D.; Garcia Colomo, A. A comparison framework to support the selection of the best additive manufacturing process for specific aerospace applications. *Int. J. Rapid Manuf.* **2020**, *9*, 1, doi:10.1504/ijrapidm.2020.10019230.

25. Brandt, M. *Laser Additive Manufacturing: Materials, Design, Technologies, and Applications*; Woodhead Publishing, 2017; ISBN 9780081004340.

26. Karami, K.; Blok, A.; Weber, L.; Ahmadi, S.M.; Petrov, R.; Nikolic, K.; Borisov, E. V.; Leeflang, S.; Ayas, C.; Zadpoor, A.A.; et al. Continuous and pulsed selective laser melting of Ti6Al4V lattice structures: Effect of post-processing on microstructural anisotropy and fatigue behaviour. *Addit. Manuf.* **2020**, *36*, 101433, doi:10.1016/j.addma.2020.101433.

27. Prashanth, K.G.; Scudino, S.; Maity, T.; Das, J.; Eckert, J. Is the energy density a reliable parameter for materials synthesis by selective laser melting? *Mater. Res. Lett.* **2017**, *5*, 386–390, doi:10.1080/21663831.2017.1299808.

28. Ni, J.; Ling, H.; Zhang, S.; Wang, Z.; Peng, Z.; Benyshek, C.; Zan, R.; Miri, A.K.; Li, Z.; Zhang, X.; et al. Three-dimensional printing of metals for biomedical applications. *Mater. Today Bio* **2019**, *3*, doi:10.1016/j.mtbio.2019.100024.

29. Gu, D.D.; Meiners, W.; Wissenbach, K.; Poprawe, R. Laser additive manufacturing of metallic components: Materials, processes and mechanisms. *Int. Mater. Rev.* **2012**, *57*, 133–164, doi:10.1179/1743280411Y.0000000014.

30. Jiang, J.; Xu, X.; Stringer, J. Support structures for additive manufacturing: A review. *J. Manuf. Mater. Process.* **2018**, *2*, doi:10.3390/jmmp2040064.

31. Pou, J. *Additive Manufacturing*; Antonio, J.P., Riveiro, A., Davim, J.P., Eds.; Elsevier, 2021; ISBN 0128184116.

32. Hamilton, R.F.; Palmer, T.A.; Bimber, B.A. Spatial characterization of the thermal-induced phase transformation throughout as-deposited additive manufactured NiTi bulk builds. *Scr. Mater.* **2015**, *101*, 56–59, doi:10.1016/j.scriptamat.2015.01.018.

33. Wang, H.; Luo, H.L.; Chen, J.Q.; Tang, J.C.; Yao, X.Y.; Zhou, Y.H.; Yan, M. Cost-affordable, biomedical Ti-5Fe alloy developed using elemental powders and laser in-situ alloying additive manufacturing. *Mater. Charact.* **2021**, *182*, 111526, doi:10.1016/j.matchar.2021.111526.

34. Zhang, D.; Li, Y.; Cong, W. In-situ synthesis of high-quality pseudoelastic NiTi alloys with intrinsic Ni4Ti3 phase precipitation using laser DED. *J. Manuf. Process.* **2022**, *74*, 308–318, doi:10.1016/j.jmapro.2021.12.029.

35. Wang, J.; Wang, Y.; Su, Y.; Shi, J. Evaluation of in-situ alloyed Inconel 625 from elemental powders by laser directed energy deposition. *Mater. Sci. Eng. A* **2022**, *830*, 142296, doi:10.1016/j.msea.2021.142296.

36. Mosallanejad, M.H.; Niroumand, B.; Aversa, A.; Saboori, A. In-situ alloying in laser-based additive manufacturing processes: A critical review. *J. Alloys Compd.* **2021**, *872*, 159567, doi:10.1016/j.jallcom.2021.159567.

37. Katz-Demyanetz, A.; Koptyug, A.; Popov, V. V. In-situ Alloying as a Novel Methodology in Additive Manufacturing. *Proc. 2020 IEEE 10th Int. Conf. "Nanomaterials Appl. Prop. N. 2020* **2020**, 26–29, doi:10.1109/NAP51477.2020.9309652.

38. Zhao, R.; Gao, J.; Liao, H.; Fenineche, N.; Coddet, C. Selective laser melting of elemental powder blends for fabrication of homogeneous bulk material of near-eutectic Ni–Sn composition. *Addit. Manuf.* **2020**, *34*, 101261, doi:10.1016/j.addma.2020.101261.

39. Simonelli, M.; Aboulkhair, N.T.; Cohen, P.; Murray, J.W.; Clare, A.T.; Tuck, C.; Hague, R.J.M. A comparison of Ti-6Al-4V in-situ alloying in Selective Laser Melting using simply-mixed and satellited powder blend feedstocks. *Mater. Charact.* **2018**, *143*, 118–126, doi:10.1016/j.matchar.2018.05.039.

40. Skelton, J.M.; Sullivan, E.J.; Fitz-Gerald, J.M.; Floro, J.A. Efficacy of elemental mixing of in situ alloyed Al-33wt%Cu during laser powder bed fusion. *J. Mater. Process. Technol.* **2022**, *299*, 117379, doi:10.1016/j.jmatprotec.2021.117379.

41. Fischer, M.; Joguet, D.; Robin, G.; Peltier, L.; Laheurte, P. In situ elaboration of a binary Ti-26Nb alloy by selective laser melting of elemental titanium and niobium mixed powders. *Mater. Sci. Eng. C* **2016**, *62*, 852–859, doi:10.1016/j.msec.2016.02.033.

42. Zhang, F.; Mei, M.; Al-Hamdani, K.; Tan, H.; Clare, A.T. Novel nucleation mechanisms through satelliting in direct metal deposition of Ti-15Mo. *Mater. Lett.* **2018**, *213*, 197–200, doi:10.1016/j.matlet.2017.11.036.

43. Zhang, D.; Qiu, D.; Gibson, M.A.; Zheng, Y.; Fraser, H.L.; StJohn, D.H.; Easton, M.A. Additive manufacturing of ultrafine-grained high-strength titanium alloys. *Nature* **2019**, *576*, 91–95, doi:10.1038/s41586-019-1783-1.

44. Yadroitsev, I.; Krakhmalev, P.; Yadroitsava, I. Titanium Alloys Manufactured by In Situ Alloying During Laser Powder Bed Fusion. *Jom* **2017**, *69*, 2725–2730, doi:10.1007/s11837-017-2600-7.

45. Guo, S.; Lu, Y.; Wu, S.; Liu, L.; He, M.; Xu, X.; Zhao, C.; Gan, Y.; Lin, J.; Luo, J.; et al. Preliminary study on the corrosion resistance, antibacterial activity and cytotoxicity of selective-laser-melted Ti6Al4V-xCu alloys. *Mater. Sci. Eng. C* **2017**, *72*, 631–640, doi:10.1016/j.msec.2016.11.126.

46. Vora, P.; Mumtaz, K.; Todd, I.; Hopkinson, N. AlSi12 in-situ alloy formation and residual stress reduction using anchorless selective laser melting. *Addit. Manuf.* **2015**, *7*, 12–19, doi:10.1016/j.addma.2015.06.003.

47. Qiu, C.; Fones, A.; Hamilton, H.G.C.; Adkins, N.J.E.; Attallah, M.M. A new approach to develop palladium-modified Ti-based alloys for biomedical applications. *Mater. Des.* **2016**, *109*, 98–111, doi:10.1016/j.matdes.2016.07.055.

48. Gu, D.; Wang, H.; Dai, D.; Yuan, P.; Meiners, W.; Poprawe, R. Rapid fabrication of Al-based bulk-form nanocomposites with novel reinforcement and enhanced performance by selective laser melting. *Scr. Mater.* **2015**, *96*, 25–28, doi:10.1016/j.scriptamat.2014.10.011.

49. Gu, D.; Hagedorn, Y.C.; Meiners, W.; Wissenbach, K.; Poprawe, R. Nanocrystalline TiC reinforced Ti matrix bulk-form nanocomposites by Selective Laser Melting (SLM): Densification, growth mechanism and wear behavior. *Compos. Sci. Technol.* **2011**, *71*, 1612–1620, doi:10.1016/j.compscitech.2011.07.010.

50. Gu, D.; Meng, G.; Li, C.; Meiners, W.; Poprawe, R. Selective laser melting of TiC/Ti bulk nanocomposites: Influence of nanoscale reinforcement. *Scr. Mater.* **2012**, *67*, 185–188, doi:10.1016/j.scriptamat.2012.04.013.

51. Wang, C.; Tan, X.P.; Du, Z.; Chandra, S.; Sun, Z.; Lim, C.W.J.; Tor, S.B.; Lim, C.S.; Wong, C.H. Additive manufacturing of NiTi shape memory alloys using pre-mixed powders. *J. Mater. Process. Technol.* **2019**, *271*, 152–161, doi:10.1016/j.jmatprotec.2019.03.025.

52. Attar, H.; Bönisch, M.; Calin, M.; Zhang, L.C.; Scudino, S.; Eckert, J. Selective laser melting of in situ titanium-titanium boride composites: Processing, microstructure and mechanical properties. *Acta Mater.* **2014**, *76*, 13–22, doi:10.1016/j.actamat.2014.05.022.

53. Bazaka, O.; Bazaka, K.; Kingshott, P.; Crawford, R.J.; Ivanova, E.P. The Chemistry of Inorganic Biomaterials. In; Spicer, C., Ed.; Royal Society of Chemistry, 2021; pp. 1–98 ISBN 9781788019828.

54. Kaur, M.; Singh, K. Review on titanium and titanium based alloys as biomaterials for orthopaedic applications. *Mater. Sci. Eng. C* **2019**, *102*, 844–862, doi:10.1016/j.msec.2019.04.064.

55. Wegener, K.; Spierings, A.; Staub, A. Bioinspired intelligent SLM cell. *Procedia CIRP* **2020**, *88*, 624–629, doi:10.1016/j.procir.2020.05.109.

56. Grand View Research *Orthopedic Surgery - Global Trends & Opportunities*; 2018;

57. Strier, K.B.; Chaves, P.B.; Mendes, S.L.; Fagundes, V.; Di Fiore, A. Molecular paternity analyses confirm inbreeding avoidance and low reproductive skew in the northern muriqui, Brachyteles hypoxanthus. *Am. J. Phys. Anthropol.* **2011**, *144*, 287.

58. Giannoudis, P. V.; Einhorn, T.A.; Marsh, D. Fracture healing: The diamond concept. *Injury* **2007**, *38*, 11–12, doi:10.1016/S0020-1383(08)70003-2.

59. Rho, J.Y.; Ashman, R.B.; Turner, C.H. Young's modulus of trabecular and cortical bone material: Ultrasonic and microtensile measurements. *J. Biomech.* **1993**, *26*, 111–119, doi:10.1016/0021-9290(93)90042-D.

60. Sola, A.; Bellucci, D.; Cannillo, V. Functionally graded materials for orthopedic applications – an update on design and manufacturing. *Biotechnol. Adv.* **2016**, *34*, 504–531, doi:10.1016/j.biotechadv.2015.12.013.

61. Andani, M.T.; Haberland, C.; Walker, J.M.; Karamooz, M.; Turabi, A.S.; Saedi, S.; Rahmanian, R.; Karaca, H.; Dean, D. Achieving biocompatible stiffness in NiTi through additive manufacturing. *J. ofIntelligent Mater. Syst. Struct.* **2016**, *27*, 2661–2671, doi:10.1177/1045389X16641199.

62. Uddin, M.S.; Chan, G.W.C. Reducing stress concentration on the cup rim of hip implants under edge loading. *Int. j. numer. method. biomed. eng.* **2019**, *35*, 1–11, doi:10.1002/cnm.3149.

63. Lin, C.; Hu, H.; Zhu, J.; Wu, Y.; Rong, Q.; Tang, Z. Influence of sagittal root positions on the stress distribution around custom-made root-analogue implants: a three-dimensional finite element analysis. *BMC Oral Health* **2021**, *21*, 1–11, doi:10.1186/s12903-021-01809-4.

64. Yao, Z.; Lin, T.H.; Pajarinen, J.; Sato, T.; Goodman, S. Host Response to Orthopedic Implants (Metals and Plastics). In *Host Response to Biomaterials*; Elsevier Inc., 2015; pp. 315–373 ISBN 9780128005002.

65. Hench, L.L. Repair of skeletal tissues. In *Biomaterials, artificial organs and tissue engineering*; Woodhead Publishing: Cambridge, England, 2005; pp. 119–128.

66. Fuchss, R.K.; Wardenc, J.; Turner, H. Bone anatomy, physiology and adaptation to mechanical loading. In *Bone Repair Biomaterials*; Woodhead Publishing: Cambridge, England, 2009; pp. 25–68.

67. Burke, M.; Goodman, S. Failure mechanisms in joint replacement. In *Joint Replacement Technology*; Woodhead Publishing Limited, 2008; pp. 264–285 ISBN 9781845692452.

68. Goharian, A. Conception of Osseointegration in Development of Orthopedic Implant

Industry. In *Osseointegration of Orthopaedic Implants*; Academic Press, 2019; pp. 163–183 ISBN 978-0-12-813384-2.

69. Andani, M.T.; Shayesteh Moghaddam, N.; Haberland, C.; Dean, D.; Miller, M.J.; Elahinia, M. Metals for bone implants. Part 1. Powder metallurgy and implant rendering. *Acta Biomater.* **2014**, *10*, 4058–4070, doi:10.1016/j.actbio.2014.06.025.

70. Zhang, Q.H.; Cossey, A.; Tong, J. Stress shielding in periprosthetic bone following a total knee replacement: Effects of implant material, design and alignment. *Med. Eng. Phys.* **2016**, *38*, 1481–1488, doi:10.1016/j.medengphy.2016.09.018.

71. Rahimizadeh, A.; Nourmohammadi, Z.; Arabnejad, S.; Tanzer, M.; Pasini, D. Porous architected biomaterial for a tibial-knee implant with minimum bone resorption and bone-implant interface micromotion. *J. Mech. Behav. Biomed. Mater.* **2018**, *78*, 465–479, doi:10.1016/j.jmbbm.2017.11.041.

72. Martin, J.R.; Watts, C.D.; Levy, D.L.; Kim, R.H. Medial Tibial Stress Shielding: A Limitation of Cobalt Chromium Tibial Baseplates. *J. Arthroplasty* **2017**, *32*, 558–562, doi:10.1016/j.arth.2016.07.027.

73. Nagels, J.; Stokdijk, M.; Rozing, P.M. Stress shielding and bone resorption in shoulder arthroplasty. *J. Shoulder Elb. Surg.* **2003**, *12*, 35–39, doi:10.1067/mse.2003.22.

74. McAFEE, P.C.; Farey, I.; Sutterlin, C.E.; Gurr, K.R.; Warden, K.E.; Cunningham, B.W. The Effect of Spinal Implant Rigidity on Vertebral. *Spine (Phila. Pa. 1976).* **1991**, *16*, 190–197.

75. Sumner, D.R. Long-term implant fixation and stress-shielding in total hip replacement. *J. Biomech.* **2015**, *48*, 797–800, doi:10.1016/j.jbiomech.2014.12.021.

76. Acklin, Y.P.; Bircher, A.; Morgenstern, M.; Richards, R.G.; Sommer, C. Benefits of hardware removal after plating. *Injury* **2018**, *49*, S91–S95, doi:10.1016/S0020-1383(18)30311-5.

77. Morris, A.P.; Anderson, A.A.; Barnes, D.M.; Bright, S.R.; Knudsen, C.S.; Lewis, D.D.; Pozzi, A.; Langley-Hobbs, S.J. Plate failure by bending following tibial fracture stabilisation in 10 cats. *J. Small Anim. Pract.* **2016**, *57*, 472–478,

doi:10.1111/jsap.12532.

78. Suganuma, S.; Tada, K.; Yamamoto, N.; Shirai, T.; Hayashi, K.; Takeuchi, A.; Tsuchiya, H. Reconstruction Using a Free Vascularized Fibular Graft after Frozen Autograft Reconstruction for Osteosarcoma of the Distal Tibia: A Case Report. *Mod. Plast. Surg.* **2013**, *03*, 47–50, doi:10.4236/mps.2013.31009.

79. Vrancken, B.; Thijs, L.; Kruth, J.P.; Van Humbeeck, J. Microstructure and mechanical properties of a novel β titanium metallic composite by selective laser melting. *Acta Mater.* **2014**, *68*, 150–158, doi:10.1016/j.actamat.2014.01.018.

80. Chenlin, J.-H.; Chien-Ping, J.; Ho, J.-F. Biocompatible low modulus titanium alloy for medical implant 2002.

81. Lin, D.J.; Chuang, C.C.; Chern Lin, J.H.; Lee, J.W.; Ju, C.P.; Yin, H.S. Bone formation at the surface of low modulus Ti-7.5Mo implants in rabbit femur. *Biomaterials* **2007**, *28*, 2582–2589, doi:10.1016/j.biomaterials.2007.02.005.

82. Li, S.; Hassanin, H.; Attallah, M.M.; Adkins, N.J.E.; Essa, K. The development of TiNi-based negative Poisson's ratio structure using selective laser melting. *Acta Mater.* **2016**, *105*, 75–83, doi:10.1016/j.actamat.2015.12.017.

83. Jahadakbar, A.; Moghaddam, N.S.; Amerinatanzi, A.; Dean, D.; Karaca, H.E.; Elahinia, M. Finite element simulation and additive manufacturing of stiffness-matched NiTi fixation hardware for mandibular reconstruction surgery. *Bioengineering* **2016**, *3*, 1–20, doi:10.3390/bioengineering3040036.

84. Vance, A.; Bari, K.; Arjunan, A. Compressive performance of an arbitrary stiffness matched anatomical Ti64 implant manufactured using Direct Metal Laser Sintering. *Mater. Des.* **2018**, *160*, 1281–1294, doi:10.1016/j.matdes.2018.11.005.

85. Jahadakbar, A.; Shayesteh Moghaddam, N.; Amerinatanzi, A.; Dean, D.; Elahinia, M. Mechanical evaluation of the SLM fabricated, stiffness-matched, mandibular bone fixation plates. *Proc. SPIE* **2018**, *1059610*, 31, doi:10.1117/12.2300740.

86. Enami, K.; Yamauchi, K.; Seto, T.; Takahata, O. Influence of W addition on the martensitic transformation of the TiPd alloy. *Ecomaterials* **1994**, 1021–1024,

doi:10.1016/b978-1-4832-8381-4.50238-9.

87. Yamabe-Mitarai, Y.; Arockiakumar, R.; Wadood, A.; Suresh, K.S.; Kitashima, T.; Hara, T.; Shimojo, M.; Tasaki, W.; Takahashi, M.; Takahashi, S.; et al. Ti(Pt, Pd, Au) based high temperature shape memory alloys. *Mater. Today Proc.* **2015**, *2*, S517–S522, doi:10.1016/j.matpr.2015.07.338.

88. Kawakita, M.; Takahashi, M.; Takahashi, S.; Yamabe-Mitarai, Y. Effect of Zr on phase transformation and high-temperature shape memory effect in TiPd alloys. *Mater. Lett.* **2012**, *89*, 336–338, doi:10.1016/j.matlet.2012.07.104.

89. Roca, P. La; Isola, L.; Vermaut, P.; Malarría, J. Relationship between grain size and thermal hysteresis of martensitic transformations in Cu-based shape memory alloys. *Scr. Mater.* **2017**, *135*, 5–9, doi:10.1016/j.scriptamat.2017.03.016.

90. Buenconsejo, P.J.S.; Ludwig, A. New Au-Cu-Al thin film shape memory alloys with tunable functional properties and high thermal stability. *Acta Mater.* **2015**, *85*, 378–386, doi:10.1016/j.actamat.2014.11.035.

91. Yamabe-Mitarai, Y. TiPd-and TiPt-based high-temperature shape memory alloys: A review on recent advances. *Metals (Basel).* **2020**, *10*, 1–21, doi:10.3390/met10111531.

92. Lagoudas, D.C. *Shape Memory Alloys- Modeling and Engineering Applications*; Lagoudas, D.C., Ed.; Springer, 2008; ISBN 9780387476841.

93. Yahia, L. *Shape Memory Implants*; Yahia, L., Ed.; 1st ed.; Springer, 2000; ISBN 9783642641183.

94. Duerig, T.; Pelton, A.; Sto, D. An overview of nitinol medical applications. *Mater. Sci. Eng. A* **1999**, *275*, 149–160, doi:10.1016/S0921-5093(99)00294-4.

95. Batalu, D.; Guoqiu, H.; Aloman, A.; Coşmeleaţă, G. A review on TiNi shape memory alloys (SMA) used for medical applications . Recycling aspects. **2014**, 1–10.

96. ASTM International *F2005 Standard Terminology for Nickel-Titanium Shape Memory Alloys*; 2015;

97. Wang, X.B.; Verlinden, B.; Van Humbeeck, J. R-phase transformation in NiTi alloys.

Mater. Sci. Technol. (United Kingdom) **2014**, *30*, 1517–1529, doi:10.1179/1743284714Y.0000000590.

98. Wang, X.B.; Verlinden, B.; Humbeeck, J. Van R-phase transformation in NiTi alloys. *Mater. Sci. Technol.*

99. Šittner, P.; Landa, M.; Lukáš, P.; Novák, V. R-phase transformation phenomena in thermomechanically loaded NiTi polycrystals. *Mech. Mater.* **2006**, *38*, 475–492, doi:10.1016/j.mechmat.2005.05.025.

100. Duerig, T.W.; Bhattacharya, K. The Influence of the R-Phase on the Superelastic Behavior of NiTi. *Shape Mem. Superelasticity* **2015**, *1*, 153–161, doi:10.1007/s40830-015-0013-4.

101. HOLEC, D. On the precipitation in NiTi based shape memory alloys, Masaryk University, 2005.

102. Frenzel, J.; George, E.P.; Dlouhy, A.; Somsen, C.; Wagner, M.F.X.; Eggeler, G. Influence of Ni on martensitic phase transformations in NiTi shape memory alloys. *Acta Mater.* **2010**, *58*, 3444–3458, doi:10.1016/j.actamat.2010.02.019.

103. Elahinia, M.H.; Hashemi, M.; Tabesh, M.; Bhaduri, S.B. Manufacturing and processing of NiTi implants: A review. *Prog. Mater. Sci.* **2012**, *57*, 911–946, doi:10.1016/j.pmatsci.2011.11.001.

104. Mouis, M.; Chávez-Ángel, E.; Sotomayor-Torres, C.; Alzina, F.; Costache, M. V.; Nassiopoulou, A.G.; Valalaki, K.; Hourdakis, E.; Valenzuela, S.O.; Viala, B.; et al. Thermal Energy Harvesting System. In *Beyond CMOS Nanodevices 1*; Balestra, F., Ed.; ISTE Ltd and John Wiley & Sons, Inc., 2014; p. 194 ISBN 978-1-118-98485-7.

105. Chluba, C.; Ge, W.; Dankwort, T.; Bechtold, C.; De Miranda, R.L.; Kienle, L.; Wuttig, M.; Quandt, E. Effect of crystallographic compatibility and grain size on the functional fatigue of sputtered TiNiCuCo thin films. *Philos. Trans. R. Soc. A Math. Phys. Eng. Sci.* **2016**, *374*, doi:10.1098/rsta.2015.0311.

106. Saedi, S.; Turabi, A.S.; Andani, M.T.; Moghaddam, N.S.; Elahinia, M.; Karaca, H.E. Texture, aging, and superelasticity of selective laser melting fabricated Ni-rich NiTi

alloys. *Mater. Sci. Eng. A* **2017**, *686*, 1–10, doi:10.1016/j.msea.2017.01.008.

107. Gil, F.J.; Manero, J.M.; Planell, J.A. Effect of grain size on the martensitic transformation in NiTi alloy. *J. Mater. Sci.* **1995**, *30*, 2526–2530, doi:10.1007/BF00362129.

108. Hamilton, R.F.; Bimber, B.A.; Palmer, T.A. Correlating microstructure and superelasticity of directed energy deposition additive manufactured Ni-rich NiTi alloys. *J. Alloys Compd.* **2018**, *739*, 712–722, doi:10.1016/j.jallcom.2017.12.270.

109. Miller, D.A.; Lagoudas, D.C. Thermomechanical characterization of NiTiCu and NiTi SMA actuators: Influence of plastic strains. *Smart Mater. Struct.* **2000**, *9*, 640–652, doi:10.1088/0964-1726/9/5/308.

110. Kurzawa, M.; Stachowiak, D. Investigation on thermo-mechanical behavior of shape memory alloy actuator. *Arch. Electr. Eng.* **2017**, *66*, 751–760, doi:10.1515/aee-2017-0057.

111. Fu, C.H.; Sealy, M.P.; Guo, Y.B.; Wei, X.T. Austenite-martensite phase transformation of biomedical Nitinol by ball burnishing. *J. Mater. Process. Technol.* **2014**, *214*, 3122–3130, doi:10.1016/j.jmatprotec.2014.07.019.

112. Guo, Y.; Klink, A.; Fu, C.; Snyder, J. Machinability and surface integrity of Nitinol shape memory alloy. *CIRP Ann. - Manuf. Technol.* **2013**, *62*, 83–86, doi:10.1016/j.cirp.2013.03.004.

113. Habijan, T.; Haberland, C.; Meier, H.; Frenzel, J.; Wittsiepe, J.; Wuwer, C.; Greulich, C.; Schildhauer, T.A.; Köller, M. The biocompatibility of dense and porous Nickel-Titanium produced by selective laser melting. *Mater. Sci. Eng. C* **2013**, *33*, 419–426, doi:10.1016/j.msec.2012.09.008.

114. Šittner, P.; Heller, L.; Pilch, J.; Curfs, C.; Alonso, T.; Favier, D. Young's modulus of austenite and martensite phases in superelastic NiTi wires. *J. Mater. Eng. Perform.* **2014**, *23*, 2303–2314, doi:10.1007/s11665-014-0976-x.

115. Cirstea, C.D.; Karadeniz-Povoden, E.; Kozeschnik, E.; Lungu, M.; Lang, P.; Balagurov, A.; Cirstea, V. Thermokinetic Simulation of Precipitation in NiTi Shape Memory Alloys.

IOP Conf. Ser. Mater. Sci. Eng. **2017**, *209*, doi:10.1088/1757-899X/209/1/012057.

116. Fan, Q.C.; Zhang, Y.H.; Wang, Y.Y.; Sun, M.Y.; Meng, Y.T.; Huang, S.K.; Wen, Y.H. Influences of transformation behavior and precipitates on the deformation behavior of Ni-rich NiTi alloys. *Mater. Sci. Eng. A* **2017**, *700*, 269–280, doi:10.1016/j.msea.2017.05.107.

117. Yu, H.; Qiu, Y.; Young, M.L. Influence of Ni4Ti3 precipitate on pseudoelasticity of austenitic NiTi shape memory alloys deformed at high strain rate. *Mater. Sci. Eng. A* **2021**, *804*, 140753, doi:10.1016/j.msea.2021.140753.

118. Jiang, S.Y.; Zhang, Y.Q.; Zhao, Y.N.; Liu, S.W.; Hu, L.; Zhao, C.Z. Influence of Ni4Ti3 precipitates on phase transformation of NiTi shape memory alloy. *Trans. Nonferrous Met. Soc. China (English Ed.* **2015**, *25*, 4063–4071, doi:10.1016/S1003-6326(15)64056-0.

119. Khalil-Allafi, J.; Dlouhy, A.; Eggeler, G. Ni4Ti3-precipitation during aging of NiTi shape memory alloys and its influence on martensitic phase transformations. *Acta Mater.* **2002**, *50*, 4255–4274, doi:10.1016/S1359-6454(02)00257-4.

120. Nashrudin, M.N.; Mahmud, A.S.; Mohamad, H. Precipitation-induced of partial annealing of Ni-rich NiTi shape memory alloy. *AIP Conf. Proc.* **2018**, *1958*, doi:10.1063/1.5034545.

121. Drexel, M.; Selvaduray, G.; Pelton, A. The effects of cold work and heat treatment on the properties of Nitinol wire. *Med. Device Mater. IV Proc. Mater. Process. Med. Devices Conf. 2007* **2008**, 114–119, doi:10.1361/cp2007mpmd114.

122. Gherghescu, I.A.; Tarcolea, M.; Jicmon, G.L.; Turcas, C.V. Heat treatment influence upon precipitates chemical composition and transformation temperatures of a NiTi shape memory alloy. *Rev. Chim.* **2013**, *64*, 407–413.

123. Rahim, M.; Frenzel, J.; Frotscher, M.; Pfetzing-Micklich, J.; Steegmüller, R.; Wohlschlögel, M.; Mughrabi, H.; Eggeler, G. Impurity levels and fatigue lives of pseudoelastic NiTi shape memory alloys. *Acta Mater.* **2013**, *61*, 3667–3686, doi:10.1016/j.actamat.2013.02.054.

124. Olier, P.; Barelo, F.; Bechade, J.L.; Brachet, J.C.; Lefevre, E.; Guenin, G. Effects of impurities content (oxygen, carbon, nitrogen) on microstructure and phase transformation temperatures of near equiatomic TiNi shape memory alloys. *J. Phys. IV JP* **1997**, *7*, 1–6, doi:10.1051/jp4:1997522.

125. Kai, W.Y.; Chang, K.C.; Wu, H.F.; Chen, S.W.; Yeh, A.C. Formation mechanism of Ni2Ti4Ox in NITI shape memory alloy. *Materialia* **2019**, *5*, doi:10.1016/j.mtla.2018.100194.

126. Toker, S.M.; Gerstein, G.; Maier, H.J.; Canadinc, D. Effects of microstructural mechanisms on the localized oxidation behavior of NiTi shape memory alloys in simulated body fluid. *J. Mater. Sci.* **2018**, *53*, 948–958, doi:10.1007/s10853-017-1586-4.

127. Hayashida, T.; Uemura, Y.; Kimura, K.; Matsuoka, S.; Morikawa, D.; Hirose, S.; Tsuda, K.; Hasegawa, T.; Kimura, T. Visualization of ferroaxial domains in an order-disorder type ferroaxial crystal. *Nat. Commun.* **2020**, *11*, 1–8, doi:10.1038/s41467-020-18408-6.

128. Otubo, J.; Rigo, O.D.; Coelho, A.A.; Neto, C.M.; Mei, P.R. The influence of carbon and oxygen content on the martensitic transformation temperatures and enthalpies of NiTi shape memory alloy. *Mater. Sci. Eng. A* **2008**, *481–482*, 639–642, doi:10.1016/j.msea.2007.02.137.

129. Wataha, J.C.; Craig, R.G.; Hanks, C.T. The Release of Elements of Dental Casting Alloys into Cell-culture Medium. *J. Dent. Res.* **1991**, *70*, 1014–1018, doi:10.1177/00220345910700060301.

130. Jenko, M.; Godec, M.; Kocijan, A.; Rudolf, R.; Dolinar, D.; Ovsenik, M.; Gorenšek, M.; Zaplotnik, R.; Mozetic, M. A new route to biocompatible Nitinol based on a rapid treatment with H 2 /O 2 gaseous plasma. *Appl. Surf. Sci.* **2019**, *473*, 976–984, doi:10.1016/j.apsusc.2018.12.140.

131. Azizi, A.; Jamilian, A.; Nucci, F.; Kamali, Z.; Hosseinikhoo, N.; Perillo, L. Release of metal ions from round and rectangular NiTi wires. *Prog. Orthod.* **2016**, *17*, doi:10.1186/s40510-016-0123-3.

132. Jinlong, L.; Tongxiang, L.; Chen, W.; Limin, D. Surface corrosion enhancement of

passive films on NiTi shape memory alloy in different solutions. *Mater. Sci. Eng. C* **2016**, *63*, 192–197, doi:10.1016/j.msec.2016.02.066.

133. Toker, S.M.; Canadinc, D.; Maier, H.J.; Birer, O. Evaluation of passive oxide layer formation-biocompatibility relationship in NiTi shape memory alloys: Geometry and body location dependency. *Mater. Sci. Eng. C* **2014**, *36*, 118–129, doi:10.1016/j.msec.2013.11.040.

134. Kaynak, Y. Machining and phase transformation response of room-temperature austenitic NiTi shape memory alloy. *J. Mater. Eng. Perform.* **2014**, *23*, 3354–3360, doi:10.1007/s11665-014-1058-9.

135. Kaynak, Y.; Karaca, H.E.; Noebe, R.D.; Jawahir, I.S. Analysis of Tool-wear and Cutting Force Components in Dry , Preheated , and Cryogenic Machining of NiTi Shape Memory Alloys. *Procedia CIRP* **2013**, *8*, 498–503, doi:10.1016/j.procir.2013.06.140.

136. Wang, Z.Y.; Rajurkar, K.P. Cryogenic machining of hard-to-cut materials. *Wear* **2000**, *239*, 168–175.

137. Bermingham, M.J.; Kirsch, J.; Sun, S.; Palanisamy, S.; Dargusch, M.S. New observations on tool life, cutting forces and chip morphology in cryogenic machining Ti-6Al-4V. *Int. J. Mach. Tools Manuf.* **2011**, *51*, 500–511, doi:10.1016/j.ijmachtools.2011.02.009.

138. Kaynak, Y.; Karaca, H.E.; Noebe, R.D.; Jawahir, I.S. Tool-wear analysis in cryogenic machining of NiTi shape memory alloys: A comparison of tool-wear performance with dry and MQL machining. *Wear* **2013**, *306*, 51–63, doi:10.1016/j.wear.2013.05.011.

139. Pfeifer, R.; Herzog, D.; Hustedt, M.; Barcikowski, S. Pulsed Nd:YAG laser cutting of NiTi shape memory alloys - Influence of process parameters. *J. Mater. Process. Technol.* **2010**, *210*, 1918–1925, doi:10.1016/j.jmatprotec.2010.07.004.

140. Biffi, C.A.; Tuissi, A. Nitinol laser cutting: Microstructure and functional properties of femtosecond and continuous wave laser processing. *Smart Mater. Struct.* **2017**, *26*, doi:10.1088/1361-665X/aa5596.

141. Theisen, W.; Schuermann, A. Electro discharge machining of nickel-titanium shape

memory alloys. *Mater. Sci. Eng. A* **2004**, *378*, 200–204, doi:10.1016/j.msea.2003.09.115.

142. Bisaria, H.; Shandilya, P. Surface integrity aspects for NiTi shape memory alloys during wire electric discharge machining: A review. *J. Mater. Res.* **2020**, *35*, 537–558, doi:10.1557/jmr.2020.32.

143. Soni, H.; Sannayellappa, N.; Rangarasaiah, R.M. An experimental study of influence of wire electro discharge machining parameters on surface integrity of TiNiCo shape memory alloy. *J. Mater. Res.* **2017**, *32*, 3100–3108, doi:10.1557/jmr.2017.137.

144. Li, C.; Nikumb, S.; Wong, F. An optimal process of femtosecond laser cutting of NiTi shape memory alloy for fabrication of miniature devices. *Opt. Lasers Eng.* **2006**, *44*, 1078–1087, doi:10.1016/j.optlaseng.2005.08.003.

145. Velmurugan, C.; Senthilkumar, V.; Dinesh, S.; Arulkirubakaran, D. Machining of NiTi-shape memory alloys-A review. *Mach. Sci. Technol.* **2018**, *22*, 355–401, doi:10.1080/10910344.2017.1365894.

146. Kaya, E.; Kaya, İ. A review on machining of NiTi shape memory alloys: the process and post process perspective. *Int. J. Adv. Manuf. Technol.* **2019**, *100*, 2045–2087, doi:10.1007/s00170-018-2818-8.

147. Hlavacova, I.M.; Geryk, V. Abrasives for water-jet cutting of high-strength and thick hard materials. *Int. J. Adv. Manuf. Technol.* **2017**, *90*, 1217–1224, doi:10.1007/s00170-016-9462-y.

148. Natarajan, Y.; Murugesan, P.K.; Mohan, M.; Liyakath Ali Khan, S.A. Abrasive Water Jet Machining process: A state of art of review. *J. Manuf. Process.* **2020**, *49*, 271–322, doi:10.1016/j.jmapro.2019.11.030.

149. Pal, V.K.; Tandon, P. Identification of the role of machinability and milling depth on machining time in controlled depth milling using abrasive water jet. *Int. J. Adv. Manuf. Technol.* **2013**, *66*, 877–881, doi:10.1007/s00170-012-4373-z.

150. Mahmoudi, M.; Tapia, G.; Franco, B.; Ma, J.; Arroyave, R.; Karaman, I.; Elwany, A. On the printability and transformation behavior of nickel-titanium shape memory alloys

fabricated using laser powder-bed fusion additive manufacturing. *J. Manuf. Process.* **2018**, *35*, 672–680, doi:10.1016/j.jmapro.2018.08.037.

151. Elahinia, M.; Shayesteh Moghaddam, N.; Taheri Andani, M.; Amerinatanzi, A.; Bimber, B.A.; Hamilton, R.F. Fabrication of NiTi through additive manufacturing: A review. *Prog. Mater. Sci.* **2016**, *83*, 630–663, doi:10.1016/j.pmatsci.2016.08.001.

152. Bimber, B.A.; Hamilton, R.F.; Keist, J.; Palmer, T.A. Anisotropic microstructure and superelasticity of additive manufactured NiTi alloy bulk builds using laser directed energy deposition. *Mater. Sci. Eng. A* **2016**, *674*, 125–134, doi:10.1016/j.msea.2016.07.059.

153. Malukhin, K.; Ehmann, K. Material Characterization of NiTi Based Memory Alloys Fabricated by the Laser Direct Metal Deposition Process. *J. Manuf. Sci. Eng.* **2006**, *128*, 691, doi:10.1115/1.2193553.

154. Khademzadeh, S.; Carmignato, S.; Parvin, N.; Zanini, F.; Bariani, P.F. Micro porosity analysis in additive manufactured NiTi parts using micro computed tomography and electron microscopy. *Mater. Des.* **2016**, *90*, 745–752, doi:10.1016/j.matdes.2015.10.161.

155. Marattukalam, J.J.; Singh, A.K.; Datta, S.; Das, M.; Balla, V.K.; Bontha, S.; Kalpathy, S.K. Microstructure and corrosion behavior of laser processed NiTi alloy. *Mater. Sci. Eng. C* **2015**, *57*, 309–313, doi:10.1016/j.msec.2015.07.067.

156. Bormann, T.; Müller, B.; Schinhammer, M.; Kessler, A.; Thalmann, P.; De Wild, M. Microstructure of selective laser melted nickel-titanium. *Mater. Charact.* **2014**, *94*, 189–202, doi:10.1016/j.matchar.2014.05.017.

157. Speirs, M.; Wang, X.; Van Baelen, S.; Ahadi, A.; Dadbakhsh, S.; Kruth, J.-P.; Van Humbeeck, J. On the Transformation Behavior of NiTi Shape-Memory Alloy Produced by SLM. *Shape Mem. Superelasticity* **2016**, *2*, 310–316, doi:10.1007/s40830-016-0083-y.

158. Karamooz-Ravari, M.R.; Taheri Andani, M.; Kadkhodaei, M.; Saedi, S.; Karaca, H.; Elahinia, M. Modeling the cyclic shape memory and superelasticity of selective laser melting fabricated NiTi. *Int. J. Mech. Sci.* **2018**, *138–139*, 54–61,

doi:10.1016/j.ijmecsci.2018.01.034.

159. Zhou, Q.; Hayat, M.D.; Chen, G.; Cai, S.; Qu, X.; Tang, H.; Cao, P. Selective electron beam melting of NiTi: Microstructure, phase transformation and mechanical properties. *Mater. Sci. Eng. A* **2019**, *744*, 290–298, doi:10.1016/j.msea.2018.12.023.

160. Oliveira, J.P.; Cavaleiro, A.J.; Schell, N.; Stark, A.; Miranda, R.M.; Ocana, J.L.; Braz Fernandes, F.M. Effects of laser processing on the transformation characteristics of NiTi: A contribute to additive manufacturing. *Scr. Mater.* **2018**, *152*, 122–126, doi:10.1016/j.scriptamat.2018.04.024.

161. Hamilton, R.F.; Bimber, B.A.; Taheri Andani, M.; Elahinia, M. Multi-scale shape memory effect recovery in NiTi alloys additive manufactured by selective laser melting and laser directed energy deposition. *J. Mater. Process. Technol.* **2017**, *250*, 55–64, doi:10.1016/j.jmatprotec.2017.06.027.

162. Shiva, S.; Palani, I.A.; Mishra, S.K.; Paul, C.P.; Kukreja, L.M. Investigations on the influence of composition in the development of Ni-Ti shape memory alloy using laser based additive manufacturing. *Opt. Laser Technol.* **2015**, *69*, 44–51, doi:10.1016/j.optlastec.2014.12.014.

163. Halani, P.R.; Shin, Y.C. In situ synthesis and characterization of shape memory alloy nitinol by laser direct deposition. *Metall. Mater. Trans. A Phys. Metall. Mater. Sci.* **2012**, *43*, 650–657, doi:10.1007/s11661-011-0890-x.

164. Zhang, B.; Chen, J.; Coddet, C. Microstructure and transformation behavior of in-situ shape memory alloys by selective laser melting Ti-Ni mixed powder. *J. Mater. Sci. Technol.* **2013**, *29*, 863–867, doi:10.1016/j.jmst.2013.05.006.

165. Stoll, P.; Spierings, A.; Wegner, K. SLM processing of elementally blended NiTi shape memory alloy. *Procedia CIRP* **2020**, *95*, 121–126, doi:10.1016/j.procir.2020.02.250.

166. Zhao, C.; Liang, H.; Luo, S.; Yang, J.; Wang, Z. The effect of energy input on reaction , phase transition and shape memory effect of NiTi alloy by selective laser melting. *J. Alloys Compd.* **2020**, *817*, 153288, doi:10.1016/j.jallcom.2019.153288.

167. Zhang, H.; Zhao, Y.; Huang, S.; Zhu, S.; Wang, F.; Li, D. Manufacturing and analysis

of high-performance refractory high-entropy alloy via selective laser melting (SLM). *Materials (Basel).* **2019**, *12*, doi:10.3390/ma12050720.

168. Weller, C.; Kleer, R.; Piller, F. *Economic Implications of 3D printing: Market structure Models in light of additive manufacturing Revisited*; 2015; Vol. 164;.

169. Bandyopadhyay, A.; Bose, S. *Additive Manufacturing*; Bandyopadhyay, A., Bose, S., Eds.; 1st ed.; CRC Press Taylor & Francis Group: Boca Raton, 2015; ISBN 978-1-4822-2360-6.

170. Gibson, I.; Rosen, D.; Stucker, B. *Additive Manufacturing Technologies 3D Printing, Rapid Prototyping, and Direct Digital Manufacturing*; Second Edi.; Springer, 2015; ISBN 9781493921126.

171. Patil, A.N.; Sarje, S.H. Additive manufacturing with shape changing/memory materials: A review on 4D printing technology. *Mater. Today Proc.* **2021**, 11–16, doi:10.1016/j.matpr.2020.11.907.

172. Farber, E.; Zhu, J.N.; Popovich, A.; Popovich, V. A review of NiTi shape memory alloy as a smart material produced by additive manufacturing. *Mater. Today Proc.* **2019**, *30*, 761–767, doi:10.1016/j.matpr.2020.01.563.

173. Khoo, Z.X.; Liu, Y.; An, J.; Chua, C.K.; Shen, Y.F.; Kuo, C.N. A review of selective laser melted NiTi shape memory alloy. *Materials (Basel).* **2018**, *11*, 11–17, doi:10.3390/ma11040519.

174. Hodgson, D.E.; Wu, M.H.; Biermann, R.J. *Shape Memory Alloys*; ASM International: Novelty, OH, USA, 2013; Vol. 2;.

175. Sharma, K.; Srinivas, G. Flying smart : Smart materials used in aviation industry. *Mater. Today Proc.* **2019**, doi:10.1016/j.matpr.2019.10.115.

176. Shabalovskaya, S.; Anderegg, J.; Van Humbeeck, J. Critical overview of Nitinol surfaces and their modifications for medical applications. *Acta Biomater.* **2008**, *4*, 447–467, doi:10.1016/j.actbio.2008.01.013.

177. Chen, X.; Liu, K.; Guo, W.; Gangil, N.; Siddiquee, A.N.; Konovalov, S. The fabrication of NiTi shape memory alloy by selective laser melting: a review. *Rapid Prototyp. J.*

2019, *25*, 1421–1432, doi:10.1108/RPJ-11-2018-0292.

178. Khalil-Allafi, J.; Amin-Ahmadi, B. The effect of chemical composition on enthalpy and entropy changes of martensitic transformations in binary NiTi shape memory alloys. *J. Alloys Compd.* **2009**, *487*, 363–366, doi:10.1016/j.jallcom.2009.07.135.

179. Wei, K.; Lv, M.; Zeng, X.; Xiao, Z.; Huang, G.; Liu, M.; Deng, J. Effect of laser remelting on deposition quality, residual stress, microstructure, and mechanical property of selective laser melting processed Ti-5Al-2.5Sn alloy. *Mater. Charact.* **2019**, *150*, 67–77, doi:10.1016/j.matchar.2019.02.010.

180. Wejrzanowski, T.; Spychalski, W.L.; Rózniatowski, K.; Kurzydłowski, K.J. Image based analysis of complex microstructures of engineering materials. *Int. J. Appl. Math. Comput. Sci.* **2008**, *18*, 33–39, doi:10.2478/v10006-008-0003-1.

181. Wejrzanowski, T.; Lewandowska, M.; Kurzydłowski, K.J. Stereology of nano-materials. *Image Anal. Stereol.* **2010**, *29*, 1–12, doi:10.5566/ias.v29.p1-12.

182. Lu, P.; Cheng-Lin, Z.; Hai-Yi, L.; Liang, W.; Tong, L. A new two-step selective laser remelting of 316L stainless steel: Process, density, surface roughness, mechanical properties, microstructure. *Mater. Res. Express* **2020**, *7*, doi:10.1088/2053-1591/ab8b86.

183. Sato, Y.; Tsukamoto, M.; Shobu, T.; Yamashita, Y.; Yamagata, S.; Higashino, R.; Masuno, S.; Abe, N. Effect of baseplate temperature on sputter-generation for development of SLM in vacuum. In Proceedings of the Lasers in Manufacturing Conference; 2017; p. 4.

184. Wang, Z.; Wang, X.; Zhou, X.; Ye, G.; Cheng, X.; Cheng, X.; Zhang, P. Investigation into spatter particles and their effect on the formation quality during selective laser melting processes. *C. - Comput. Model. Eng. Sci.* **2020**, *124*, 243–263, doi:10.32604/cmes.2020.09934.

185. Li, R.; Liu, J.; Shi, Y.; Wang, L.; Jiang, W. Balling behavior of stainless steel and nickel powder during selective laser melting process. *Int. J. Adv. Manuf. Technol.* **2012**, *59*, 1025–1035, doi:10.1007/s00170-011-3566-1.

186. Liu, S.; Guo, H. Balling behavior of selective laser melting (SLM) magnesium alloy.

Materials (Basel). **2020**, *13*, doi:10.3390/MA13163632.

187. Sun, K.; Peng, W.; Yang, L.; Fang, L. Effect of SLM processing parameters on microstructures and mechanical properties of al0.5 CoCrFeNi high entropy alloys. *Metals (Basel).* **2020**, *10*, doi:10.3390/met10020292.

188. Motemani, Y.; Nili-Ahmadabadi, M.; Tan, M.J.; Bornapour, M.; Rayagan, S. Effect of cooling rate on the phase transformation behavior and mechanical properties of Ni-rich NiTi shape memory alloy. *J. Alloys Compd.* **2009**, *469*, 164–168, doi:10.1016/j.jallcom.2008.01.153.

189. Thomas, F. *The Effect of Various Quenchants on the Hardness and Microstructure of 60-NITINOL;* 2015;

190. Chen, K.C. NiTi - magic or phase transformations? In Proceedings of the ASEE Annual Conference Proceedings; 2003; pp. 2423–2430.

191. Li, B.Q.; Li, Z.; Liu, B. Selective laser remelting of an additive layer manufacturing process on AlSi10Mg. *Results Phys.* **2019**, *12*, 982–988, doi:10.1016/j.rinp.2018.12.018.

192. Griffiths, S.; Rossell, M.D.; Croteau, J.; Vo, N.Q.; Dunand, D.C.; Leinenbach, C. Effect of laser rescanning on the grain microstructure of a selective laser melted Al-Mg-Zr alloy. *Mater. Charact.* **2018**, *143*, 34–42, doi:10.1016/j.matchar.2018.03.033.

193. Chen, H.; Gu, D.; Dai, D.; Xia, M.; Ma, C. A novel approach to direct preparation of complete lath martensite microstructure in tool steel by selective laser melting. *Mater. Lett.* **2018**, *227*, 128–131, doi:10.1016/j.matlet.2018.05.042.

194. Xiong, Z.; Zhang, P.; Tan, C.; Dong, D.; Ma, W.; Yu, K. Selective Laser Melting and Remelting of Pure Tungsten. *Adv. Eng. Mater.* **2020**, *22*, 1–9, doi:10.1002/adem.201901352.

195. Dong, D.; Chang, C.; Wang, H.; Yan, X.; Ma, W.; Liu, M.; Deng, S.; Gardan, J.; Bolot, R.; Liao, H. Selective laser melting (SLM) of CX stainless steel: Theoretical calculation, process optimization and strengthening mechanism. *J. Mater. Sci. Technol.* **2021**, *73*, 151–164, doi:10.1016/j.jmst.2020.09.031.

196. Liu, B.; Fang, G.; Lei, L. An analytical model for rapid predicting molten pool geometry

of selective laser melting (SLM). *Appl. Math. Model.* **2021**, *92*, 505–524, doi:10.1016/j.apm.2020.11.027.

197. Ali, H.; Ma, L.; Ghadbeigi, H.; Mumtaz, K. In-situ residual stress reduction, martensitic decomposition and mechanical properties enhancement through high temperature powder bed pre-heating of Selective Laser Melted Ti6Al4V. *Mater. Sci. Eng. A* **2017**, *695*, 211–220, doi:10.1016/j.msea.2017.04.033.

198. Trapp, J.; Rubenchik, A.M.; Guss, G.; Matthews, M.J. In situ absorptivity measurements of metallic powders during laser powder-bed fusion additive manufacturing. *Appl. Mater. Today* **2017**, *9*, 341–349, doi:10.1016/j.apmt.2017.08.006.

199. Chmielewska, A.; Wysocki, B.; Żrodowski, Ł.; Święszkowski, W. Hybrid solid-porous titanium scaffolds. In Proceedings of the Transactions on Additive Manufacturing Meets Medicine; Infinite Science Publishing: Lubeck, Germany, 2019; Vol. 1, p. 2.

200. Tang, X.; Zhang, S.; Zhang, C.; Chen, J.; Zhang, J.; Liu, Y. Optimization of laser energy density and scanning strategy on the forming quality of 24CrNiMo low alloy steel manufactured by SLM. *Mater. Charact.* **2020**, *170*, 110718, doi:10.1016/j.matchar.2020.110718.

201. Gong, H.; Rafi, K.; Gu, H.; Janaki Ram, G.D.; Starr, T.; Stucker, B. Influence of defects on mechanical properties of Ti-6Al-4V components produced by selective laser melting and electron beam melting. *Mater. Des.* **2015**, *86*, 545–554, doi:10.1016/j.matdes.2015.07.147.

202. Leuders, S.; Thöne, M.; Riemer, A.; Niendorf, T.; Tröster, T.; Richard, H.A.; Maier, H.J. On the mechanical behaviour of titanium alloy TiAl6V4 manufactured by selective laser melting: Fatigue resistance and crack growth performance. *Int. J. Fatigue* **2013**, *48*, 300–307, doi:10.1016/j.ijfatigue.2012.11.011.

203. Shi, X.; Wang, H.; Feng, W.; Zhang, Y.; Ma, S.; Wei, J. The crack and pore formation mechanism of Ti–47Al–2Cr–2Nb alloy fabricated by selective laser melting. *Int. J. Refract. Met. Hard Mater.* **2020**, *91*, 105247, doi:10.1016/j.ijrmhm.2020.105247.

204. Guo, M.; Gu, D.; Xi, L.; Du, L.; Zhang, H.; Zhang, J. Formation of scanning tracks during Selective Laser Melting (SLM) of pure tungsten powder: Morphology, geometric

features and forming mechanisms. *Int. J. Refract. Met. Hard Mater.* **2019**, *79*, 37–46, doi:10.1016/j.ijrmhm.2018.11.003.

205. Shishkovsky, I.; Yadroitsev, I.; Smurov, I. Direct Selective Laser Melting of Nitinol Powder. *Phys. Procedia* **2012**, *39*, 447–454, doi:10.1016/j.phpro.2012.10.060.

206. Wysocki, B.; Maj, P.; Krawczyńska, A.; Rożniatowski, K.; Zdunek, J.; Kurzydłowski, K.J.; Święszkowski, W. Microstructure and mechanical properties investigation of CP titanium processed by selective laser melting (SLM). *J. Mater. Process. Technol.* **2017**, *241*, 13–23, doi:10.1016/j.jmatprotec.2016.10.022.

207. Kwasniak, P.; Garbacz, H.; Kurzydlowski, K.J. Solid solution strengthening of hexagonal titanium alloys: Restoring forces and stacking faults calculated from first principles. *Acta Mater.* **2016**, *102*, 304–314, doi:10.1016/j.actamat.2015.09.041.

208. Sun, B.; Li, S.; Imai, H.; Mimoto, T.; Umeda, J.; Kondoh, K. Fabrication of high-strength Ti materials by in-process solid solution strengthening of oxygen via P/M methods. *Mater. Sci. Eng. A* **2013**, *563*, 95–100, doi:10.1016/j.msea.2012.11.058.

209. Wysocki, B.; Idaszek, J.; Zdunek, J.; Rozniatowski, K.; Pisarek, M.; Yamamoto, A.; Swieszkowski, W. The Influence of Selective Laser Melting (SLM) Process Parameters on In-Vitro Cell Response. *Int. J. Mol. Sci.* **2018**, *19*, doi:10.3390/ijms19061619.

210. Velasco-Castro, M.; Hernández-Nava, E.; Figueroa, I.A.; Todd, I.; Goodall, R. The effect of oxygen pickup during selective laser melting on the microstructure and mechanical properties of Ti–6Al–4V lattices. *Heliyon* **2019**, *5*, doi:10.1016/j.heliyon.2019.e02813.

211. Pauzon, C.; Dietrich, K.; Forêt, P.; Hryha, E.; Witt, G. Mitigating oxygen pick-up during laser powder bed fusion of Ti-6Al-4V by limiting heat accumulation. *Mater. Lett.* **2021**, *288*, 129365, doi:10.1016/j.matlet.2021.129365.

212. Chmielewska, A.; Wysocki, B.; Buhagiar, J.; Michalski, B.; Adamczyk-Cieślak, B.; Gloc, M.; Święszkowski, W. In situ alloying of NiTi: Influence of Laser Powder Bed Fusion (LBPF) scanning strategy on chemical composition. *Mater. Today Commun.* **2021**, *30*, 103007, doi:10.1016/j.mtcomm.2021.103007.

213. Gustmann, T.; Gutmann, F.; Wenz, F.; Koch, P.; Stelzer, R.; Drossel, W.G.; Korn, H. Properties of a superelastic NiTi shape memory alloy using laser powder bed fusion and adaptive scanning strategies. *Prog. Addit. Manuf.* **2020**, *5*, 11–18, doi:10.1007/s40964-020-00118-6.

214. Zhukov, A.; Barakhtin, B.; Shakirov, I.; Bobyr, V. The emergence of inhomogeneity in the chemical composition of powder applicable for manufacturing products by additive technologies. *Procedia Manuf.* **2019**, *36*, 19–25, doi:10.1016/j.promfg.2019.08.004.

215. Sedlak, J.; Rican, D.; Piska, M.; Rozkosny, L. Study of materials produced by powder metallurgy using classical and modern additive laser technology. *Procedia Eng.* **2015**, *100*, 1232–1241, doi:10.1016/j.proeng.2015.01.488.

216. Voiculescu, I.; Geanta, V.; Vasile, I.M.; Binchiciu, E.F.; Winestoock, R. Chemical elements diffusion in the stainless steel components brazed with Cu-Ag alloy. In Proceedings of the IOP Conference Series: Materials Science and Engineering; 2016; Vol. 133, pp. 1–8.

217. Klassen, A.; Scharowsky, T.; Körner, C. Evaporation model for beam based additive manufacturing using free surface lattice Boltzmann methods. *J. Phys. D. Appl. Phys.* **2014**, *47*, 1–12, doi:10.1088/0022-3727/47/27/275303.

218. Doubenskaia, M.; Domashenkov, A.; Smurov, I.; Petrovskiy, P. Study of Selective Laser Melting of intermetallic TiAl powder using integral analysis. *Int. J. Mach. Tools Manuf.* **2018**, *129*, 1–14, doi:10.1016/j.ijmachtools.2018.02.003.

219. Morawiec, H. *Metale z pamięcia kształtu i ich zastosowanie*; Todos-Burny, B., Ed.; Wydawnictwo Uniwersytetu Śląskiego: Katowice, 2014; ISBN 9788322622056.

220. Chmielewska, A.; Jahadakbar, A.; Wysocki, B.; Elahinia, M.; Święszkowski, W.; Dean, D. Chemical Polishing of Additively Manufactured, Porous, Nickel–Titanium Skeletal Fixation Plates. *3D Print. Addit. Manuf.* **2021**, *00*, 10, doi:0.1089/3dp.2020.0209.

221. Ghaini, F.M.; Sheikhi, M.; Torkamany, M.J.; Sabbaghzadeh, J. The relation between liquation and solidification cracks in pulsed laser welding of 2024 aluminium alloy. *Mater. Sci. Eng. A* **2009**, *519*, 167–171, doi:10.1016/j.msea.2009.04.056.

222. Böllinghaus, T.; Herold, H. *Hot Cracking Phenomena in Welds*; Springer: Berlin, 2005; ISBN 3540223320.

223. Aboulkhair, N.T.; Simonelli, M.; Parry, L.; Ashcroft, I.; Tuck, C.; Hague, R. 3D printing of Aluminium alloys: Additive Manufacturing of Aluminium alloys using selective laser melting. *Prog. Mater. Sci.* **2019**, *106*, 100578, doi:10.1016/j.pmatsci.2019.100578.

224. Dadbakhsh, S.; Mertens, R.; Vanmeensel, K.; Vleugels, J.; Van Humbeeck, J.; Kruth, J.P. In situ alloying and reinforcing of Al6061 during selective laser melting. *Procedia CIRP* **2018**, *74*, 39–43, doi:10.1016/j.procir.2018.08.009.

225. Kalentics, N.; Sohrabi, N.; Tabasi, H.G.; Griffiths, S.; Jhabvala, J.; Leinenbach, C.; Burn, A.; Logé, R.E. Healing cracks in selective laser melting by 3D laser shock peening. *Addit. Manuf.* **2019**, *30*, 100881, doi:10.1016/j.addma.2019.100881.

226. Zhang, X.; Chen, H.; Xu, L.; Xu, J.; Ren, X.; Chen, X. Cracking mechanism and susceptibility of laser melting deposited Inconel 738 superalloy. *Mater. Des.* **2019**, *183*, 108105, doi:10.1016/j.matdes.2019.108105.

227. Greiner, C.; Oppenheimer, S.M.; Dunand, D.C. High strength, low stiffness, porous NiTi with superelastic properties. *Acta Biomater.* **2005**, *1*, 705–716, doi:10.1016/j.actbio.2005.07.005.

228. Duering, T.W.; Pelton, A.R. *Materials Properties Handbook: Titanium Alloys*; Welsch, G., Boyer, R., Collings, E.W., Eds.; 1st ed.; ASM International the Materials Information Society: Materials Park, OH, USA, 1994; ISBN ISBN: 978-0-87170-481-8.

229. Wang, X.; Kustov, S.; Van Humbeeck, J. A short review on the microstructure, transformation behavior and functional properties of NiTi shape memory alloys fabricated by selective laser melting. *Materials (Basel).* **2018**, *11*, doi:10.3390/ma11091683.

230. Chmielewska, A.; Wysocki, B.; Buhagiar, J.; Michalski, B.; Adamczyk-Cieślak, B.; Gloc, M.; Święszkowski, W. In situ alloying of NiTi: Influence of Laser Powder Bed Fusion (LBPF) scanning strategy on chemical composition. *Mater. Today Commun.* **2022**, *30*, 1–7, doi:10.1016/j.mtcomm.2021.103007.

231. Lee, J.; Shin, Y.C. Effects of Composition and Post Heat Treatment on Shape Memory Characteristics and Mechanical Properties for Laser Direct Deposited Nitinol. *Lasers Manuf. Mater. Process.* **2019**, *6*, 41–58, doi:10.1007/s40516-019-0079-5.

232. Ibrahim, H.; Dean, D.; Klarner, A.D.; Luo, A.A. The Effect of Heat-Treatment on Mechanical, Microstructural, and Corrosion Characteristics of a Magnesium Alloy With Potential Application in Resorbable Bone Fixation Hardware. *MSEC2016-8822* **2017**, 1–7.

233. Halani, P.R.; Kaya, I.; Shin, Y.C.; Karaca, H.E. Phase transformation characteristics and mechanical characterization of nitinol synthesized by laser direct deposition. *Mater. Sci. Eng. A* **2013**, *559*, 836–843, doi:10.1016/j.msea.2012.09.031.

234. Li, X.; Chen, H.; Guo, W.; Guan, Y.; Wang, Z.; Zeng, Q.; Wang, X. Improved superelastic stability of NiTi shape memory alloys through surface nano-crystallization followed by low temperature aging treatment. *Intermetallics* **2021**, *131*, 8, doi:10.1016/j.intermet.2021.107114.

235. Divinski, S. V.; Stloukal, I.; Kral, L.; Herzig, C. Diffusion of titanium and nickel in B2 NiTi. *Defect Diffus. Forum* **2009**, *289–292*, 377–382, doi:10.4028/www.scientific.net/DDF.289-292.377.

236. Wilkinson, D.S. *Mass transport in solids and fluids*; Cambridge University Press, 2000; ISBN 0521624940.

237. Sitepu, H. Texture and structural refinement using neutron diffraction data from molybdite (MoO 3) and calcite (CaCO 3) powders and a Ni-rich Ni 50.7 Ti 49.30 alloy . *Powder Diffr.* **2009**, *24*, 315–326, doi:10.1154/1.3257906.

238. Kudoh, Y.; Tokonami, M.; Miyazaki, S.; Otsuka, K. Crystal structure of the martensite in Ti-49.2 at.%Ni alloy analyzed by the single crystal X-ray diffraction method. *Acta Metall.* **1985**, *33*, 2049–2056, doi:10.1016/0001-6160(85)90128-2.

239. Mueller, M.H.; Knott, H.W. The crystal structures of Ti2 Cu, Ti2 Ni, Ti4 Ni2 O, and Ti4 Cu2 O. *Trans. Metall. Soc. Aime* **1963**, *227*, 674–678.

240. Laves, F.; Wallbaum, J.H. Die Kristallstruktur von Ni3Ti und Si3Ti, Zeitschrift fuer

Kristallographie, Kristallgeometrie, Kristallphysik, Kristallchemie (−144, 1977). **1939**, *101*, 78–93.

241. Tirry, W.; Schryvers, D.; Jorissen, K.; Lamoen, D. Electron-diffraction structure refinement of Ni4Ti3 precipitates in Ni52Ti48. *Acta Crystallogr. Sect. B Struct. Sci.* **2006**, *62*, 966–971, doi:10.1107/S0108768106036457.

242. Dutkiewicz, J.; Rogal, Ł.; Kalita, D.; Węglowski, M.; Błacha, S.; Berent, K.; Czeppe, T.; Antolak-Dudka, A.; Durejko, T.; Czujko, T. Superelastic Effect in NiTi Alloys Manufactured Using Electron Beam and Focused Laser Rapid Manufacturing Methods. *J. Mater. Eng. Perform.* **2020**, *29*, 4463–4473, doi:10.1007/s11665-020-04938-z.

243. Morris, D.G.; Morris, M.A. NiTi intermetallic by mixing, milling and interdiffusing elemental components. *Mater. Sci. Eng. A* **1989**, *110*, 139–149, doi:10.1016/0921-5093(89)90165-2.

244. Hwang, Y.S.; Levitas, V.I. Internal stress-induced melting below melting temperature at high-rate laser heating. *Appl. Phys. Lett.* **2014**, *104*, doi:10.1063/1.4886799.

245. Zhang, Y.; Cheng, X.; Cai, H. Fabrication, characterization and tensile property of a novel Ti2Ni/TiNi micro-laminated composite. *Mater. Des.* **2016**, *92*, 486–493, doi:10.1016/j.matdes.2015.12.014.

246. Povoden-Karadeniz, E.; Cirstea, D.C.; Lang, P.; Wojcik, T.; Kozeschnik, E. Thermodynamics of Ti-Ni shape memory alloys. *Calphad Comput. Coupling Phase Diagrams Thermochem.* **2013**, *41*, 128–139, doi:10.1016/j.calphad.2013.02.004.

247. Takeshita, H.T.; Tanaka, H.; Kuriyama, N.; Sakai, T.; Uehara, I.; Haruta, M. Hydrogenation characteristics of ternary alloys containing Ti4Ni2X (X = O, N, C). *J. Alloys Compd.* **2000**, *311*, 188–193, doi:10.1016/S0925-8388(00)01118-X.

248. Karlík, M.; Haušild, P.; Klementová, M.; Novák, P.; Beran, P.; Perrière, L.; Kopeček, J. TEM phase analysis of NiTi shape memory alloy prepared by self-propagating high-temperature synthesis. *Adv. Mater. Process. Technol.* **2017**, *3*, 58–69, doi:10.1080/2374068X.2016.1247338.

249. Chmielewska, A.; Dobkowska, A.; Kijeska-Gawrońska, E.; Jakubczak, M.;

Krawczyńska, A.; Choińska, E.; Jastrzębska, A.; Dean, D.; Wysocki, B.; Święszkowski, W. Biological and Corrosion Evaluation of In Situ Alloyed NiTi Fabricated through Laser Powder Bed Fusion (LPBF). *Int. J. Mol. Sci.* **2021**, *22*, 16, doi:10.3390/ijms222413209.

250. Kaserer, L.; Bergmueller, S.; Braun, J.; Leichtfried, G. Vacuum laser powder bed fusion—track consolidation, powder denudation, and future potential. *Int. J. Adv. Manuf. Technol.* **2020**, *110*, 3339–3346, doi:10.1007/s00170-020-06071-6.

251. Cooper, N.; Coles, L.A.; Everton, S.; Maskery, I.; Campion, R.P.; Madkhaly, S.; Morley, C.; O'Shea, J.; Evans, W.; Saint, R.; et al. Additively manufactured ultra-high vacuum chamber for portable quantum technologies. *Addit. Manuf.* **2021**, *40*, doi:10.1016/j.addma.2021.101898.

252. Martins, J.N.R.; Silva, E.J.N.L.; Marques, D.; Belladonna, F.; Simões-Carvalho, M.; Vieira, V.T.L.; Antunes, H.S.; Braz Fernandes, F.M.B.; Versiani, M.A. Design, metallurgical features, mechanical performance and canal preparation of six reciprocating instruments. *Int. Endod. J.* **2021**, *54*, 1623–1637, doi:10.1111/iej.13529.

253. Plotino, G.; Grande, N.M.; Cordaro, M.; Testarelli, L.; Gambarini, G. A Review of Cyclic Fatigue Testing of Nickel-Titanium Rotary Instruments. *J. Endod.* **2009**, *35*, 1469–1476, doi:10.1016/j.joen.2009.06.015.

254. Bhardwaj, A.; Gupta, A.K.; Padisala, S.K.; Poluri, K. Characterization of mechanical and microstructural properties of constrained groove pressed nitinol shape memory alloy for biomedical applications. *Mater. Sci. Eng. C* **2019**, *102*, 730–742, doi:10.1016/j.msec.2019.04.070.

255. Petrini, L.; Migliavacca, F. Biomedical Applications of Shape Memory Alloys. *J. Metall.* **2011**, *2011*, 1–15, doi:10.1155/2011/501483.

256. Ibrahim, H.; Jahadakbar, A.R.; Dehghan, A.; Moghaddam, N.S.; Amerinatanzi, A.; Elahinia, M. In vitro corrosion assessment of additively manufactured porous NiTi structures for bone fixation applications. *Metals (Basel).* **2018**, *8*, doi:10.3390/met8030164.

257. Shayesteh Moghaddam, N.; Saghaian, S.E.; Amerinatanzi, A.; Ibrahim, H.; Li, P.; Toker,

G.P.; Karaca, H.E.; Elahinia, M. Anisotropic tensile and actuation properties of NiTi fabricated with selective laser melting. *Mater. Sci. Eng. A* **2018**, *724*, 220–230, doi:10.1016/j.msea.2018.03.072.

258. Zglobicka, I.; Chmielewska, A.; Topal, E.; Kutukova, K.; Jürgen, G.; Krüger, P.; Kilroy, C.; Swieszkowski, W.; Kurzydlowski, K.J.; Zschech, E. 3D Diatom – Designed and Selective Laser Melting (SLM) Manufactured Metallic Structures. *Sci. Rep.* **2019**, *9*, 1–9, doi:10.1038/s41598-019-56434-7.

259. Westhoff, D.; Skibinski, J.; Šedivý, O.; Wysocki, B.; Wejrzanowski, T.; Schmidt, V. Investigation of the relationship between morphology and permeability for open-cell foams using virtual materials testing. *Mater. Des.* **2018**, *147*, 1–10, doi:10.1016/j.matdes.2018.03.022.

260. Lu, X.; Zhao, T.; Ji, X.; Hu, J.; Li, T.; Lin, X.; Huang, W. 3D printing well organized porous iron-nickel/polyaniline nanocages multiscale supercapacitor. *J. Alloys Compd.* **2018**, *760*, 78–83, doi:10.1016/j.jallcom.2018.05.165.

261. Hussein, A.Y. The Development of Lightweight Cellular Structures for Metal Additive Manufacturing. **2013**, 228.

262. Tran, T.Q.; Chinnappan, A.; Lee, J.K.Y.; Loc, N.H.; Tran, L.T.; Wang, G.; Kumar, V.V.; Jayathilaka, W.A.D.M.; Ji, D.; Doddamani, M.; et al. 3D printing of highly pure copper. *Metals (Basel).* **2019**, *9*, 12–20, doi:10.3390/met9070756.

263. Moghaddam, N.S.; Skoracki, R.; Miller, M.; Elahinia, M.; Dean, D. Three Dimensional Printing of Stiffness-tuned, Nitinol Skeletal Fixation Hardware with an Example of Mandibular Segmental Defect Repair. *Procedia CIRP* **2016**, *49*, 45–50, doi:10.1016/j.procir.2015.07.027.

264. Kamali, P.; Dean, D.; Skoracki, R.; Koolen, P.G.L.; Paul, M.A.; Ibrahim, A.M.S.; Lin, S.J. The Current Role of Three-Dimensional Printing in Plastic Surgery. *Technol. Innov.* **2016**, *137*, 1045–1055, doi:10.1097/01.prs.0000479977.37428.8e.

265. Dabrowski, B.; Swieszkowski, W.; Godlinski, D.; Kurzydlowski, K.J. Highly porous titanium scaffolds for orthopaedic applications. *J. Biomed. Mater. Res. - Part B Appl. Biomater.* **2010**, *95*, 53–61, doi:10.1002/jbm.b.31682.

266. Bram, M.; Ahmad-Khanlou, A.; Heckmann, A.; Fuchs, B.; Buchkremer, H.P.; Stöver, D. Powder metallurgical fabrication processes for NiTi shape memory alloy parts. *Mater. Sci. Eng. A* **2002**, *337*, 254–263, doi:10.1016/S0921-5093(02)00028-X.

267. Hartzband, M.A.; Glassman, A.H.; Goldberg, V.M.; Jordan, L.R.; Crowninshield, R.D.; Fricka, K.B.; Jordan, L.C. Survivorship of a low-stiffness extensively porous-coated femoral stem at 10 years. *Clin. Orthop. Relat. Res.* **2010**, *468*, 433–440, doi:10.1007/s11999-009-0950-3.

268. Wysocki, B.; Idaszek, J.; Szlazak, K.; Strzelczyk, K.; Brynk, T.; Kurzydłowski, K.J.; Swieszkowski, W. Post Processing and Biological Evaluation of the Titanium Scaffolds for Bone Tissue Engineering. *Materials (Basel).* **2016**, *9*, doi:10.3390/ma9030197.

269. Saedi, S.; Shayesteh Moghaddam, N.; Amerinatanzi, A.; Elahinia, M.; Karaca, H.E. On the effects of selective laser melting process parameters on microstructure and thermomechanical response of Ni-rich NiTi. *Acta Mater.* **2018**, *144*, 552–560, doi:10.1016/j.actamat.2017.10.072.

270. Idaszek, J.; Kijeńska, E.; Łojkowski, M.; Swieszkowski, W. How important are scaffolds and their surface properties in regenerative medicine. *Appl. Surf. Sci.* **2016**, *388*, 762–774, doi:10.1016/j.apsusc.2016.03.038.

271. Liu, C.; Xia, Z.; Czernuszka, J.T. Design and development of three-dimensional scaffolds for tissue engineering. *Chem. Eng. Res. Des.* **2007**, *85*, 1051–1064, doi:10.1205/cherd06196.

272. Almirall, A.; Larrecq, G.; Delgado, J.A.; Martínez, S.; Planell, J.A.; Ginebra, M.P. Fabrication of low temperature macroporous hydroxyapatite scaffolds by foaming and hydrolysis of an α-TCP paste. *Biomaterials* **2004**, *25*, 3671–3680, doi:10.1016/j.biomaterials.2003.10.066.

273. Wysocki, B.; Maj, P.; Sitek, R.; Buhagiar, J.; Kurzydłowski, K.J.; Świeszkowski, W. Laser and electron beam additive manufacturing methods of fabricating titanium bone implants. *Appl. Sci.* **2017**, *7*, 0–19, doi:10.3390/app7070657.

274. Lavery, N.P.; Brown, S.G.R.; Sienz, J.; Cherry, J. A review of Computational Modelling of Additive Layer Manufacturing – multi-scale and multi-physics. *Sustain. Des. Manuf.*

2014, *1*, 651–673, doi:10.13140/RG.2.1.3103.0884.

275. Kruth, J.; Badrossamay, M.; Yasa, E.; Deckers, J.; Thijs, L.; Humbeeck, J. Van Part and material properties in selective laser melting of metals. *16th Int. Symp. Electromachining (ISEM XVI)* **2010**, *1*.

276. Pal, S.; Igor, D.; Brajlih, T. Physical Behaviors of Materials in Selective Laser Melting Process. In *DAAAM INTERNATIONAL SCIENTIFIC BOOK 2018*; 2018; pp. 239–256 ISBN 9783902734198.

277. Li, Y.; Gu, D. Parametric analysis of thermal behavior during selective laser melting additive manufacturing of aluminum alloy powder. *Mater. Des.* **2014**, *63*, 856–867, doi:10.1016/j.matdes.2014.07.006.

278. Kadkhodapour, J.; Montazerian, H.; Darabi, A.C.; Anaraki, A.P.; Ahmadi, S.M.; Zadpoor, A.A.; Schmauder, S. Failure mechanisms of additively manufactured porous biomaterials: Effects of porosity and type of unit cell. *J. Mech. Behav. Biomed. Mater.* **2015**, *50*, 180–191, doi:10.1016/j.jmbbm.2015.06.012.

279. Löber, L.; Flache, C.; Petters, R.; Kühn, U.; Eckert, J. Comparison of different post processing technologies for SLM generated 316l steel parts. *Rapid Prototyp. J.* **2013**, *19*, 173–179, doi:10.1108/13552541311312166.

280. Boschetto, A.; Bottini, L.; Macera, L.; Veniali, F. Post-processing of complex SLM parts by barrel finishing. *Appl. Sci.* **2020**, *10*, doi:10.3390/app10041382.

281. Łyczkowska, E.; Szymczyk, P.; Dyba, B.; Chlebus, E. Chemical polishing of scaffolds made of Ti – 6Al – 7Nb alloy by additive manufacturing. **2014**, *4*, doi:10.1016/j.acme.2014.03.001.

282. Yang, Z.; Wei, X.; Cao, P.; Gao, W. Surface modification of nitinol by chemical and electrochemical etching. **2013**, doi:10.1142/S0217984913410121.

283. Vojtech, D.; Fojt, J.; Joska, L.; Novák, P. Surface treatment of NiTi shape memory alloy and its influence on corrosion behavior. *Surf. Coat. Technol.* **2010**, *204*, 3895–3901, doi:10.1016/j.surfcoat.2010.05.010.

284. Shabalovskaya, S.A.; Rondelli, G.C.; Undisz, A.L.; Anderegg, J.W.; Burleigh, T.D.;

Rettenmayr, M.E. The electrochemical characteristics of native Nitinol surfaces. *Biomaterials* **2009**, *30*, 3662–3671, doi:10.1016/j.biomaterials.2009.03.034.

285. Barfeie, A.; Wilson, J.; Rees, J. Implant surface characteristics and their effect on osseointegration. *Br. Dent. J.* **2015**, *218*, doi:10.1038/sj.bdj.2015.171.

286. Junker, R.; Dimakis, A.; Thoneick, M.; Jansen, J.A. Effects of implant surface coatings and composition on bone integration: A systematic review. *Clin. Oral Implants Res.* **2009**, *20*, 185–206, doi:10.1111/j.1600-0501.2009.01777.x.

287. Trigwell, S.; Hayden, R.D.; Nelson, K.F.; Selvaduray, G. Effects of Surface Treatment on the Surface Chemistry of NiTi Alloy for Biomedical Applications. *Surf. INTERFACE Anal.* **1998**, *26*, 483–489.

288. Chu, C.L.; Wang, R.M.; Hu, T.; Yin, L.H.; Pu, Y.P.; Lin, P.H.; Wu, S.L.; Chung, C.Y.; Yeung, K.W.K.; Chu, P.K. Surface structure and biomedical properties of chemically polished and electropolished NiTi shape memory alloys. *Mater. Sci. Eng. C* **2008**, *28*, 1430–1434, doi:10.1016/j.msec.2008.03.009.

289. Shayesteh Moghaddam, N.; Saedi, S.; Amerinatanzi, A.; Hinojos, A.; Ramazani, A.; Kundin, J.; Mills, M.J.; Karaca, H.; Elahinia, M. Achieving superelasticity in additively manufactured NiTi in compression without post-process heat treatment. *Sci. Rep.* **2019**, *9*, 1–11, doi:10.1038/s41598-018-36641-4.

290. Chu, C.L. Graded surface structure in chemically polished NiTi shape memory alloy after NaOH treatment. **2005**, *52*, 1117–1121, doi:10.1016/j.scriptamat.2005.02.002.

291. Wysocki, B.; Idaszek, J.; Buhagiar, J.; Szlązak, K.; Brynk, T.; Kurzydłowski, K.J.; Święszkowski, W. The influence of chemical polishing of titanium scaffolds on their mechanical strength and in-vitro cell response. *Mater. Sci. Eng. C* **2019**, *95*, 428–439, doi:10.1016/j.msec.2018.04.019.

292. Singh, R.; Dahotre, Æ.N.B. Corrosion degradation and prevention by surface modification of biometallic materials. **2007**, 725–751, doi:10.1007/s10856-006-0016-y.

List of figures

List of tables

Acknowledgement

First of all, I would like to acknowledge Professor Wojciech Święszkowski for giving me the opportunity to perform my PhD research and develop my knowledge of materials science under his supervision. I would like to thank him for the trust in my skills and encouraging me to take the lead in my research and laboratory work. I am very grateful for giving me numerous possibilities to attend scientific conferences, workshops, and international internships which undoubtedly expanded my professional experience.

I would like to acknowledge all scientist who helped me in performing experiments and gave me their support, valuable advices, and constructive critic throughout my PhD research: prof. David Dean, prof. Joseph Buhagiar, dr inż. Bogusława Adamczyk-Cieślak, dr inż. Anna Dobkowska, dr inż. Ewa Kijeńska-Gawrońska, mgr. inż. Michał Jakubczak, dr inż. Agnieszka Krawczyńska, dr inż. Emilia Choińska, prof. dr hab. inż. Agnieszka Jastrzębska, dr inż. Piotr Kwaśniak, dr inż. Mirosław Jakub Kruszewski, dr inż. Bartosz Michalski and dr inż. Elżbieta Gadalińska. Most importantly, I would like to thank dr inż. Bartłomiej Wysocki shared with me the fascination for additive manufacturing. I would also like to thank dr inż. Michał Gloc, who has accompanied me in my scientific career from the very beginning of my studies on the Faculty of Materials Science and Engineering.

Last, but not the least, I would like to thank my family and friends for their support, encouragement, and kindness. Most importantly, I would like to thank my mum and my sister for their presence both in the moments of happiness and success and times full of doubts and sadness.

Curriculum Vitae

29 June 1992	Born in Warsaw

Education

2016-2022	Warsaw University of Technology Faculty of Materials Science and Engineering *PhD student*
2015-2016	Warsaw University of Technology Faculty of Power and Aeronautical Engineering *Postgraduate studies: Modern Methods of Design of the application of advanced techniques of CAD / CAM / CAE*
2011-2016	Warsaw University of Technology Faculty of Materials Science and Engineering *Engineer's and Master's Degree*
2008-2011	I Dywizji Kościuszkowskiej Secondary School in Piaseczno

Work

2020-2022	Research Associate at The Ohio State University, Columbus, OH, USA
2014-2022	Researcher at Warsaw University of Technology Faculty of Materials Science and Engineering
2016	Junior Constructor in EDAG Engineering Poland, Warsaw
2016-2022	Researcher in Materialscare LTD, spin off company established at the Faculty of Materials Science and Engineering of the Warsaw University of Technology

Internship

2019	The Ohio State University, Columbus, OH, USA
2015	National Institute for Materials Science Tsukuba, Japan
2013	Sandvik Poland Sp. Z o. o., Warsaw-Katowice, Poland

Awards

2019	Progress Award – A Pearl of Innovation, Warsaw, Poland
2019	Best poster presentation on AMM 2019 (Additive manufacturing Meeting), Wrocław, Poland
2018	Best oral presentation on Young Ceramist Network Workshop, Smolenice, Slovakia

---

National Projects

1. MAZOWSZE/0023/19 „Opracowanie konstrukcji i technologii wytwarzania nowatorskich bioaktywnych implantów stomatologicznych, founder The National Centre for Research and Development; Poland
2. “The innovative additive shaping laser technology LENS for cementless hip implants geometry modification and surface layer biofunctionalization”, grant no. PBS3/A5/53/2015, founder The National Centre for Research and Development, Poland
3. “Method of treatment of large bone defects in oncological patients using in vivo tissue engineering approach- iTE”, grant no. STRATEGMED3/306888/3/NCBR/2017, founder The National Centre for Research and Development; Poland

4. “Development of the first Polish complementary molecular navigation system for surgical oncologic treatment”; grant no. STRATEGMED1/233624/4/NCBR/2014, founder The National Centre for Research and Development; Poland

5. “Synthesis and characterization of novel biomaterials based on three-dimensional (3D) multifunctional titanium substrates”; grant no. NCN OPUS.13 2017/25/B/ST8/01599, founder National Science Centre; Poland

International Projects

1. “3D Printing of Resorbable Mg-1.2Zn-0.5Ca-0.5Mn Mandibular Graft Fixation”, Cross-disciplinary Postdoctoral Scholars Program, College of Engineering and the James Comprehensive Cancer Center- The Ohio State University, Columbus, USA,

2. TVSF grant, #TECG20170372, from the Third Frontier (State of Ohio); RegenFix, LLC (Toledo, OH); the Department of Plastic and Reconstructive Surgery at The Ohio State University.

3. Third Frontier Accelerator Grant (State of Ohio) “Chaotic Lamina for Cell Expansion and Tissue Regeneration”,

List of Publications

Dissertation chapters:

1. A. Chmielewska, B. Wysocki, E. Gadalińska, E. McDonald, B. Adamczyk-Cieślak, D. Dean, W. Święszkowski, *Laser Powder Bed Fusion (LPBF) of NiTi Alloy Using Elemental Powders: The Influence of Remelting on the Printability and Microstructure,* Rapid Prototyping Journal (2022), DOI: 10.1108/RPJ-08-2021-0216

2. A. Chmielewska, B. Wysocki, J. Buhagiar, B. Michalski, B. Adamczyk-Cieślak, M. Gloc, W. Święszkowski, *In situ alloying of NiTi: Influence of Laser Powder Bed Fusion (LBPF) scanning strategy on chemical composition*, Mater. Today Commun. (2021), DOI: 10.1016/j.mtcomm.2021.103007

3. A. Chmielewska, A. Jahadakbar, B. Wysocki, M. Elahinia, W. Święszkowski, D. Dean, *Chemical Polishing of Additively Manufactured, Porous, Nickel–Titanium Skeletal Fixation Plates,* 3D Print. Addit. Manuf. (2021), DOI: 0.1089/3dp.2020.0209

4. A. Chmielewska, A. Dobkowska, E. Kijeńska-Gawrońska, M. Jakubczak, A. Krawczyńska, E. Choińska, A. Jastrzębska, D. Dean, B. Wysocki, W. Święszkowski, *Biological and Corrosion Evaluation of In Situ Alloyed NiTi Fabricated through Laser Powder Bed Fusion (LPBF),* International Journal of Molecular Science (2021), DOI: 10.3390/ijms222413209

Other publications:

1. B. Shaqour, Ż. Górecka, A. Chmielewska, B. Wysocki, M. Heljak, M. Gernaey, B. Verleije, K. Beyers, C. Vervaet, E. Choińska, W. Święszkowski, P. Cos, *Novel design for an additively manufactured nozzle to produce tubular scaffolds via fused filament fabrication,* Addit. Manuf. (2021) 102467, DOI: 10.1016/j.addma.2021.102467.

2. P. Wychowański, A. Starzyńska, P. Adamska, M. Słupecka-Ziemilska, B. K. Sobocki, A. Chmielewska, B. Wysocki, D. Alterio, G. Marvaso, B. A. Jereczek-Fossa, J. Kowalski; *Methods of Topical Administration of Drugs and Biological Active Substances for Dental Implants—A Narrative Review*; Antibiotics 2021, DOI: 10.3390/antibiotics10080919

3. A. Chmielewska, T. Macdonald, H. Ibrahim, T. McManus, J. Lammel Lindemann, P. Smith, L. Rong, A. Luo, R. Advincula, W. Swieszkowski, M. Elahinia, D. Dean, *Biocompatibility of a novel heat-treated and ceramic-coated magnesium alloy (Mg-1.2Zn-0.5Ca-0.5Mn) for resorbable skeletal fixation devices,* MRS Commun. 10 (2020) 467–474, DOI: 10.1557/mrc.2020.46

4. I. Zglobicka, A. Chmielewska, E. Topal, K. Kutukova, J. Gluch, P. Kruger, C. Kilroy, W. Święszkowski, K.J. Kurzydłowski, E. Zsechech, *3D Diatom–Designed and Selective Laser Melting (SLM) Manufactured Metallic Structures*. Sci Rep 9, 19777 (2019) DOI: 10.1038/s41598-019-56434-7

5. A. Chmielewska, B. Wysocki, K. Szlązak, W. Święszkowski*, Druk 3D w leczeniu ludzi i zwierząt,* Polski Przemysł, 2017

6. B. Wysocki, A. Chmielewska, K. Szlązak, Druk 3D implantów na wymiar metodami FDM i SLM, Tworzywa Sztuczne w Przemyśle, 2017

Conference Proceedings:

1. A. Chmielewska, B. Wysocki, Ł. Żrodowski, W. Święszkowski; *Hybrid solid-porous titanium scaffolds*, Additive Manufacturing Meets Medicine at 3D Week 2019, Infinite Science Publishing (2019)

2. A. Chmielewska, B.A. Wysocki, K. Szlązak, J. Sterna, W. Święszkowski, K. J. Kurzydłowski; *Fabrication of custom designed spinal disc replacement for veterinary applications*; Engineering of Biomaterials, vol. 143, str. 40, (2017)

List of Patents

Granted

1. Pat. 239353 (P.425508//PCT/PL2019/050063//WO/2021/091406) (PL)- *Bioaktywny śródkostny implant stomatologiczny*; A. Chmielewska, B. Wysocki, P. Wychowański, W. Święszkowski, J. Mizera
2. Pat. 238391 (P.428410) (PL)- *Sposób wytwarzania kompozytów na bazie szkieł metalicznych o planowanych właściwościach metodą selektywnego przetapiania proszków*; Ł. Żrodowski, A. Chmielewska, B. Wysocki, A. Krawczyńska, R. Wróblewski, W. Swięszkowski, B. Morończyk
3. Pat. 233190 (P.423442) (PL) *Sposób wytwarzania addytywnego trójwymiarowych obiektów*; B. Wysocki, Ł. Żrodowski, A. Chmielewska, W. Święszkowski, A. Supeł, K. Kurzydłowski, K. Czarnecka

Submitted

1. P.437316 (PL)- *Implant stomatologiczny*; A. Chmielewska, B. Wysocki, M. Gloc, P. Wychowański, W. Święszkowski, J. Mizera;

List of conference presentations

Oral presentations

1. *Optimization of SLM parameters for 3D printing pure magnesium*, A. Chmielewska, B. Wysocki, K. Bogdanowicz, Ł. Żrodowski, W. Święszkowski, A. Luo D. Dean, 13th Symposium on Biodegradable Metals for Biomedical Applications, 23-26.08.2021

2. *Post-fabrication processing of 3D printed metal parts*, E-MRS 2019 Fall Meeting, A. Chmielewska, B. Wysocki, W. Święszkowski, Warsaw Poland, 16-19.09.2019

3. *Hybrid solid-porous titanium scaffolds*, Additive Manufacturing Meets Medicine at 3D Week 2019, A. Chmielewska, B. Wysocki, Ł. Żrodowski, W. Święszkowski, Lübeck, Germany, 12-13.09.2019

4. *Chemical and Electrochemical Polishing of 3D Printed Metal Parts*, AMM 2019, A. Chmielewska, B. Wysocki, W. Święszkowski, Wrocław, Poland, 8-9.09.2019

5. *Mechanical Properties Of Pure Titanium Enriched With Oxygen Processed By Selective Laser Melting*, EUROMAT 2019, A. Chmielewska, B. Wysocki, W. Święszkowski, Stockholm, Sweden, 1-5.09.2019

6. *The influence of chemical polishing of titanium scaffolds on their mechanical strength and in-vitro cell response*, EUROMAT 2019, B. Wysocki, A. Chmielewska, W. Święszkowski, Stockholm, Sweden, 1-5.09.2019

7. *Fabrication of Stiffness Matched, 3D Printed, and Regenerative Nitinol Skeletal Fixation Plates*, Military Health System Research Symposium, D.Dean, A. Jahadakbar, A. Chmielewska, M. Elahinia, Kissimmee, FL, USA, 19-22.08.2019

8. *Spersonalizowane implanty weterynaryjne*, A. Chmielewska, B. Wysocki, W. Święszkowski, Implanty 2018- Od idei do komercjalizacji, Gdańsk, Poland 28.06.2018

9. *Calcium phosphate coatings on 3D printed titanium implants*, Young Ceramist Network Workshop, A. Chmielewska, B. Wysocki, W. Święszkowski, Smolenice, Slovakia 2-4.10.2018

10. *Modeling of the patient-specific cutting guides and surgical instruments*, A. Chmielewska, B. Wysocki, K. Szlązak, M. Rysz, W. Święszkowski, 7th European Young Engineers Conference; Warsaw. Poland, 23-25.04.2018

11. *Post processing and biological evaluation of the titanium implants fabricated by Selective Laser Melting*, A. Chmielewska, B. Wysocki, K. Szlązak, J. Idaszek, Wojciech Święszkowski, 7th European Young Engineers Conference, Warsaw, Poland, 23-25.04.2018

12. *Modelowanie oraz drukowanie 3D spersonalizowanych szablonów do rekonstrukcji żuchwy*, A. Chmielewska, B. Wysocki, M. Rysz, K. Szlązak, W. Święszkowski, Diagnostyka Materiałów Polimerowych 2018, Male, Italy, 21-27.01.2018

Poster presentation:

1. *Chemical Polishing Postprocessing of 3D Printed Titanium Alloys*, A.Chmielewska, B.Wysocki, D. Dean, W. Święszkowski, 1st InterBioMed Young Scientists Forum, Warszawa, 14-15.10.2019

2. *Mechanical properties, microstructure and cell behavior of CP titanium processed by Selective Laser Melting (SLM)*, AMM 2019, B. Wysocki, P. Maj, J. Idaszek, K. Szlązak, A. Krawczyńska, A. Chmielewska, W. Święszkowski, Wroclaw Poland, 8-19.09.2019

3. *Biocompatibility Of A Work Hardened Mg-1.2zn-0.5ca-0.5mn Alloy For Skeletal Fixation Devices*, 11th Symposium on Biodegradable Metals, A. Chmielewska, T. Avey, A. Luo, D.Dean, Alicante, Spain, 25-30.08.2019

4. *Postprocessing of Stifness Mathed 3D Printed NiTi Skeletal Fixation Plates*, OSU Materials Week, A. Chmielewska, D. Dean, A. Jahadakbar, M. Elahinia, W. Święszkowski, Columbus, OH, USA, 7-9.05.2019

5. *Modeling and fabrication of custom designed veterinary implants*, A. Chmielewska, B. Wysocki, K. Szlązak, J. Gawor, W. Święszkowski, 7th European Young Engineers Conference, Warsaw, Poland, 23-25.04.2018

6. *Functionalisation of titanium implants by electrodeposition of composite calcium-phosphate (Ca-P) coatings strengthened with Carbon Nanotubes (CNTs)*, A.

Chmielewska, B. Wysocki, A. Supeł, W. Święszkowski, D. Leszczyńska, 25th Conference on Current Trends in Computional Chemistry 2017, Jackson, USA, 10-11.11.2017

7. *Fabrication of custom designed spinal disc replacement for veterinary applications*, A. Chmielewska, B.A. Wysocki, Ł. Żrodowski, K. Szlązak, J. Sterna, W. Święszkowski, 26th Conference on Biomaterials in Medicine and Veterinary Medicine, Rytro, Poland, 12-15.10.2017

8. *Titanium foams modified with carbon nanoparticles for automotive catalytic converter*, A. Chmielewska, B. Wysocki, W. Święszkowski, D. Leszczyńska, 14th International Symposium on Recent Advances in Environmental Health Research, Jackson, USA, 10-13.09.2017

9. *Calcium-phosphate coatings fabricated by electrodeposition method studied with electron microscopies*, A. Chmielewska, B.A. Wysocki, T. Durejko, A. Supeł, A. Brojanowska, K. J. Kurzydłowski, W. Święszkowski, XVI International Conference on Electron Microscopy, Jachranka, Poland, 10-13.09.2017

10. *Reducing air pollution: fabrication of composite titanium foams modified with carbon nanopareticles for automotive catalytic converters*, A. Chmielewska, B. Wysocki, W. Święszkowski, D. Leszczyńska, 17th Southern School on Computational Chemistry and Materials Science Conference, Jackson, USA, 27-28.07.2017